

On the Transport and Radiative Properties of Plasmas with Small-Scale Electromagnetic Fluctuations

By

Brett D. Keenan

Submitted to the Department of Physics & Astronomy and the
Graduate Faculty of the University of Kansas
in partial fulfillment of the requirements for the degree of
Doctor of Philosophy

Mikhail V. Medvedev, Chairperson

Thomas E. Cravens

Committee members

Gregory H. Rudnick

Hume A. Feldman

David E. Lerner

Date defended: January 25, 2016

ProQuest Number: 10129375

All rights reserved

INFORMATION TO ALL USERS

The quality of this reproduction is dependent upon the quality of the copy submitted.

In the unlikely event that the author did not send a complete manuscript and there are missing pages, these will be noted. Also, if material had to be removed, a note will indicate the deletion.



ProQuest 10129375

Published by ProQuest LLC (2016). Copyright of the Dissertation is held by the Author.

All rights reserved.

This work is protected against unauthorized copying under Title 17, United States Code
Microform Edition © ProQuest LLC.

ProQuest LLC.
789 East Eisenhower Parkway
P.O. Box 1346
Ann Arbor, MI 48106 - 1346

The Dissertation Committee for Brett D. Keenan certifies
that this is the approved version of the following dissertation :

On the Transport and Radiative Properties of Plasmas with Small-Scale Electromagnetic
Fluctuations

Mikhail V. Medvedev, Chairperson

Date approved: _____ January 25, 2016 _____

Abstract

Plasmas with sub-Larmor-scale (“small-scale”) electromagnetic fluctuations are a feature of a wide variety of high-energy-density environments, and are essential to the description of many astrophysical/laboratory plasma phenomena. Radiation from particles, whether they be relativistic or non-relativistic, moving through small-scale electromagnetic turbulence has spectral characteristics distinct from both synchrotron and cyclotron radiation.

The radiation, carrying information on the statistical properties of the turbulence, is also intimately related to the particle diffusive transport. We investigate, both theoretically and numerically, the transport of non-relativistic and trans-relativistic particles in plasmas with high-amplitude isotropic sub-Larmor-scale magnetic turbulence – both with and without a mean field component – and its relation to the spectra of radiation simultaneously produced by these particles.

Furthermore, the transport of particles through small-scale electromagnetic turbulence – under certain conditions – resembles the random transport of particles – via Coulomb collisions – in collisional plasmas. The pitch-angle diffusion coefficient, which acts as an effective “collision” frequency, may be substantial in these, otherwise, collisionless environments. We show that this effect, colloquially referred to as the plasma “quasi-collisionality”, may radically alter the expected radiative transport properties of candidate plasmas. We argue that the modified magneto-optic effects in these plasmas provide an attractive, novel, diagnostic tool for the exploration and characterization of small-scale electromagnetic turbulence. Lastly, we speculate upon the manner in which quasi-collisions may

affect inertial confinement fusion (ICF), and other laser-plasma experiments.

Finally, we show that mildly relativistic jitter radiation, from laser-produced plasmas, may offer insight into the underlying electromagnetic turbulence. Here we investigate the prospects for, and demonstrate the feasibility of, such direct radiative diagnostics for mildly relativistic, solid-density laser plasmas produced in lab experiments.

In effect, we demonstrate how the diffusive and radiative properties of plasmas with small-scale, turbulent, electromagnetic fluctuations may serve as a powerful tool for the diagnosis of laboratory, astrophysical, and space plasmas.

In memory of my big brother and hero, Andrew Kerr Keenan.

Acknowledgements

This is the product of a many year endeavor, which would not have been possible without considerable support along the way. In particular, my research advisor, Misha Medvedev, has been an invaluable mentor; through his instruction and guidance, I have achieved much more than I had ever imagined I would.

Additionally, I wish to thank my committee. They have been nothing but helpful throughout this entire ordeal, and I greatly appreciate their cooperation. I would like to thank, particularly, Tom Cravens and Hume Feldman. Not only have they served on my committee, but they have supported – via recommendation letters – my journey ahead.

I want to say thank you to my fellow graduate students, as well. Alex Ford, in particular, was a loyal friend and colleague throughout the entirety of grad school. While we weren't working on physics problems together, our discussions on non-physics related things – like philosophy – provided an occasional [needed] distraction. It has been a joy to share an office with Alex, as well as Nesar Ramachandra, these last few years.

I would like to thank all of my friends and family. Their unwavering faith in my abilities was instrumental to my success. Obviously, none of this would be possible without my parents, Gloria and Terry Keenan. They supported me from the beginning; never once did they discourage my aspirations, and the same goes for my sister, Jill Keenan.

Finally, I would like to acknowledge a newcomer in my life. Stephanie Zielaskowski, my beloved, was very supportive in the last few moments of my graduate career. I look forward to our future together; which is slated to be a bright one – in part – because of the hard work embodied here.

Contents

1 General Introduction	1
1.1 GRB Collisionless Shocks and Jitter Radiation	2
1.2 Research Overview	4
1.2.1 Non-Relativistic Jitter Radiation	5
1.2.2 Small-Scale Fields in Magnetized Plasmas	5
1.2.3 Jitter Radiation in Laser-Plasma Experiments	6
1.2.4 Small-Scale Turbulence and Quasi-Collisionality	8
1.3 Chapter Organization	9
2 Theoretical Background	10
2.1 The Classical Plasma	10
2.1.1 The Boltzmann Transport Equation	12
2.1.2 The Vlasov Equations	15
2.1.3 The Debye Length	18
2.1.4 The “Good” Plasma	21
2.1.5 The Plasma Dielectric Tensor	22
3 The Characterization of Waves, Turbulence, and Instabilities in Collisionless Plasmas	25
3.1 Introduction	25
3.2 The Permittivity of an Isotropic Collisionless Plasma	26

3.2.1	Landau Damping	28
3.2.2	Langmuir Oscillations	29
3.3	The Dielectric Properties of Magnetized Plasmas	30
3.3.1	The Motion of a Charge in an External Magnetic Field	31
3.3.2	The “Linearized” Vlasov Solution for Magnetized Plasmas	32
3.3.3	The “Cold” Plasma Approximation	33
3.3.4	Whistler-Mode Waves in Cold Plasmas	35
3.3.5	The Validity of the “Cold” Plasma Approximation	36
3.4	Weibel-like Instabilities	38
3.4.1	The “Classic” Weibel Instability	38
3.4.2	Generalizations of the Weibel Instability	40
3.4.3	Weibel-like Instabilities in Real Plasmas	43
3.5	The Meaning of Turbulence	45
3.5.1	The Two-Point Autocorrelation Tensor	46
4	The Simulation of Test Particle Dynamics in Small-Scale Electromagnetic Turbulence	50
4.1	Overview	50
4.2	The Numerical Generation of the Electromagnetic Field	51
4.2.1	Generating the Fields: Lattice Approach	51
4.2.2	Generating the Fields: Continuous Wave Approach	52
4.3	Calculating the Radiation Spectrum	53
4.4	Initial Tests	54
5	Transport Properties of Small-Scale Electromagnetic Turbulence	59
5.1	Introduction	59
5.2	Analytic Theory	59
5.2.1	Pitch-Angle Diffusion in Small-Scale Magnetic Turbulence	61

5.2.2	Pitch-Angle Diffusion in Small-Scale Electric Turbulence	63
5.2.3	Energy Diffusion in Small-Scale Electric Turbulence	66
5.2.4	Particle Transport in Magnetized Plasmas with Electric Fluctuations	72
5.2.5	Energy Diffusion in Small-Scale Whistler Turbulence	74
5.3	Simulation Results	77
5.3.1	Magnetic Pitch-Angle Diffusion	77
5.3.2	Transport in Magnetized Plasmas	85
5.3.3	Langmuir Turbulence	94
5.4	Discussion of Results	96
6	Radiation From Charged Particles Moving Through Small-Scale Electromagnetic Turbulence	98
6.1	Introduction	98
6.2	The Classic Jitter Theory	98
6.3	Generalizations of Jitter Radiation	101
6.3.1	Pseudo-Cyclotron Radiation	101
6.3.2	Jitter Radiation From Mildly Relativistic Particles	105
6.3.3	The Jitter Parameter and the Gyro-number	107
6.3.4	Jitter Radiation From Magnetized Plasmas	108
6.4	Simulation Results	109
6.4.1	Trans-Relativistic Jitter Radiation	109
6.4.2	Jitter Radiation From Monopoles	115
6.4.3	Jitter Radiation From Magnetized Plasmas	118
6.4.4	Jitter Radiation and Small-Scale Langmuir Turbulence	121
6.5	The Jitter/Synchrotron Spectrum of a Thermal Distribution of Particles . .	123
6.5.1	Plasma Dispersion	126
6.6	Discussion of Results	127

7 Small-Scale Magnetic Turbulence And (Quasi-)Collisionality	129
7.1 Introduction	129
7.2 General Discussion	129
7.3 The Lorentz Collision Model of Electron-Ion Collisions	130
7.4 Pitch-angle Diffusion as Effective Collisionality	131
7.5 A Phenomenological Interpretation	133
7.6 Magneto-optic Effects with Small-Scale Magnetic Fields	135
7.7 “Quasi-collisional” Faraday Effect	136
7.8 Ordinary and Extraordinary Mode Propagation in “Quasi-collisional” Solid-density Laser Plasmas	140
7.9 Discussion of Results	149
8 (Quasi-)collisionality and Small-scale Electric Fields	151
8.1 Introduction	151
8.2 Pitch-Angle Diffusion in Small-Scale Langmuir-like Turbulence	151
8.3 A Phenomenological Definition of the [Electric] Quasi-Collision Frequency .	152
8.4 “Quasi-collisional” Faraday Effect in Electric Turbulence	153
8.5 Small-Scale Electric Turbulence in Real Plasmas	157
8.6 Discussion of Results	158
9 Jitter Radiation and Solid-Density Laser-Plasma Experiments	159
9.1 Introduction	159
9.2 The Weibel Instability in Laser-Plasma Experiments	159
9.3 Jitter Radiation	160
9.3.1 The Jitter Frequency	162
9.3.2 The Jitter Power	163
9.4 Thermal Bremsstrahlung	164
9.5 Radiative Cooling	166

9.6	The Radiation Power Spectrum	167
9.7	Discussion of Results	171
10	General Conclusions	172
10.1	Assumptions Concerning Turbulence	172
10.2	The Applicability of the Radiation Perturbation Theory	173
10.3	Plasma Dispersion and Pseudo-Cyclotron Radiation	174
10.4	Small-Scale Whistler/Langmuir Turbulence and “Cold” Plasmas	176
10.5	Quasi-collisions in Real Plasmas	178
10.6	Jitter Radiation and Laser-Plasmas	179
10.7	Future Studies	180
10.8	Final Remarks	181
A	The Spectral Tail	190
B	Interpolation of the Magnetic Field	192
C	The Effect of Plasma Dispersion on the Radiation Spectra	195

List of Figures

2.1	Approximate magnitudes of characteristic parameters in some typical plasmas. Source: The NRL Plasma Formulary (2013 Revision).	13
3.1	Image adapted from: http://www.icra.it/MG/mg12/talks/anm8_medvdedev.pdf . Counter-streaming currents pass through the plane with an initial magnetic perturbation.	42
3.2	The magnetic field of the non-relativistic Weibel instability at saturation (with periodic boundary conditions). The energy density of the field is indicated by the blue iso-surfaces. The magnitude of B^2 along the x1-direction is the x2-x3-plane projection. Peaks in B^2 are indicated with red.	44
4.1	Radiation spectrum (i.e., the total radiated energy, dW per unit solid angle, $d\Omega$ per unit frequency, $d\omega$ vs. frequency, ω) of a single relativistic charge moving through a uniform magnetic field. The total simulation time was $10T_g$, where $T_g = 2\pi/\omega_B$ is the gyroperiod. The numerical solution is indicated in blue, the red line is the analytical solution, and they agree very well. The spectrum is peaked at the synchrotron frequency $\omega_c = (3/2)\gamma_e^2\omega_B$, where $\omega_B = eB_\perp/\gamma_e m_e c$ is the electron gyrofrequency. In this and other spectral plots, the radiation power is arbitrarily normalized.	55

4.2	The trajectories of 50 monoenergetic ($\gamma_e = 3$) particles through a turbulent magnetic field projected on to the x - y plane. Each particle (denoted by 50 shades of gray) starts from an origin with a random initial velocity. The axes are x and y positions in arbitrary simulation units.	56
4.3	Velocity space of a single particle ($\gamma_e = 5$) moving through isotropic magnetic turbulence. The axes are the components of the velocity, which are in units of c . Notice that, although the velocity vector of the particle varies randomly (and, over enough time, visits all possible directions), its magnitude is constant.	57
5.1	Average square pitch-angle vs. time (in simulation units). Relevant parameters are $N_p = 2000$, $k_{\min} = 4\pi/5$, $k_{\max} = 8\pi$, $\langle \delta B^2 \rangle^{1/2} = 0.01$, and $\mu = 3$. The particle velocities in each case range from $\frac{1}{8}c$ to $\frac{1}{512}c$ (by multiples of two). The curves appear with increasing average slope as β decreases. As β decreases, eventually $\rho \sim 1$ (at $\beta = \frac{c}{128}$, i.e. the fifth most sloped, “green” line), after which the deflection angle becomes large, and pitch-angle diffusion breaks down.	79
5.2	Average square pitch-angle vs. time (in simulation units). Relevant parameters are $N_p = 2000$, $k_{\min} = \pi$, $k_{\max} = 8\pi$, and $\mu = 3$. $\langle \delta B^2 \rangle^{1/2}$ ranges from 5×10^{-4} to 0.032, by multiples of two. The particle velocities range (in the opposite order) from $\frac{1}{256}c$ to $\frac{1}{4}c$. These two parameters, $\langle \delta B^2 \rangle$ and β , vary in such a way as to keep $\rho = 24.5$. The curves appear with increasing slope as β decreases. Clearly, the linear form of the curves is retained in all seven cases.	80
5.3	Magnetic pitch-angle diffusion coefficient, $D_{\alpha\alpha}$ vs the logarithm (base 2) of the inverse normalized particle velocity, $\log_2(\beta^{-1})$. The (blue) empty “squares” indicate the $D_{\alpha\alpha}$ obtained directly from simulation (as the slope of $\langle \alpha^2 \rangle$ vs. time), while the (red) filled “triangles” are the analytical, given by Eq. (5.7), pitch-angle diffusion coefficients. Simulation parameters are identical to those used in Figure 5.2.	81

5.4 Magnetic pitch-angle diffusion coefficient, $D_{\alpha\alpha}$ vs the magnetic spectral index, μ . The (blue) empty “squares” indicate the $D_{\alpha\alpha}$ obtained directly from simulation, while the (red) filled “triangles” are the analytical, given by Eq. (5.7), pitch-angle diffusion coefficients. Relevant parameters are $N_p = 2000$, $k_{\min} = \pi$, $k_{\max} = 8\pi$, $\langle \delta B^2 \rangle^{1/2} = 0.064$, $\beta = 0.5$, and $\rho = 24.5$. The magnetic spectral indexes are 2, 3, 4, and 5. Notice that the numerical results have nearly the same functional dependence on μ as the analytical triangles, as given by Eq. (5.7).	82
5.5 Numerical [magnetic] pitch-angle diffusion coefficient vs the analytical [magnetic] pitch-angle diffusion coefficient, for three different cases. In each case, the magnetic spectral index has been varied from 2 to 5, by intervals of unity. Relevant parameters are $k_{\min} = \pi/2$ (red) “circles” and (blue) “triangles”, π (green) “diamonds”, $k_{\max} = 5.12\pi$ (red) “circles”; $k_{\max} = 8\pi$ (green) “diamonds” and (blue) “triangles”; $\langle \delta B^2 \rangle^{1/2} = 0.016$ (red) “circles”, 0.032 (blue) “triangles”; 0.064 (green) “diamonds”; $\beta = 0.25$ (red) “circles”, 0.5 (blue) “triangles” and (green) “diamonds”. In each case, a line of best fit is applied. The slopes are 0.979 (circles), 0.972 (diamonds), and 1.06 (triangles)	83
5.6 Magnetic pitch-angle diffusion coefficient, $D_{\alpha\alpha}$ vs the total number of simulation particles, N_p . The “blue squares” indicate the $D_{\alpha\alpha}$ obtained directly from simulation, while the red dotted line is the analytical result, given by Eq. (5.7). Relevant parameters are $k_{\min} = \pi/2$, $k_{\max} = 8\pi$, $\langle \delta B^2 \rangle^{1/2} = 0.032$, $\beta = 0.5$, and $\rho = 24.5$. There appears to be no strong dependence of the numerical pitch-angle diffusion coefficient upon the total number of simulation particles; nevertheless, there appears to be some convergence to the analytical result.	84

5.7	Average square pitch-angle vs. normalized time for electrons moving through small-scale Whistler-mode turbulence. Relevant parameters are $\beta = 0.25$, (number of simulation particles) $N_p = 5000$, $k_{\min} = 32\pi$, $k_{\max} = 10k_{\min}$, $\langle \delta B^2 \rangle^{1/2}/B_0 = 0.1$, $\Omega_{ce} = 1$, $\rho \approx 400$, $\chi \approx 0.04$, and $\mu = 4$. The linear nature of the curve (solid, “red”) confirms the diffusive nature of the pitch-angle transport. Here, the dashed (“blue”) line indicates a line of best fit (simple linear regression) with Pearson correlation coefficient: 0.9998.	86
5.8	Average square change in electron energy (in simulation units) vs. normalized time for electrons moving through small-scale Whistler-mode turbulence. Relevant parameters are $\beta = 0.25$, (number of simulation particles) $N_p = 5000$, $k_{\min} = 64\pi$, $k_{\max} = 10k_{\min}$, $\langle \delta B^2 \rangle^{1/2}/B_0 = 0.1$, $\Omega_{ce} = 1$, $\rho \approx 400$, $\chi \approx 0.04$, and $\mu = 4$. The linear nature of the curve (solid, “red”) confirms the diffusive nature of the energy transport. Here, the dashed (“blue”) line indicates a line of best fit (simple linear regression) with Pearson correlation coefficient: 0.9999.	87
5.9	Magnetic pitch-angle diffusion coefficient, $D_{\alpha\alpha}$ vs the normalized electron velocity, β . Relevant simulation parameters include: $N_p = 5000$, $k_{\min} = 32\pi$, $k_{\max} = 10k_{\min}$, $\langle \delta B^2 \rangle^{1/2}/B_0 = 0.1$, $\Omega_{ce} = 1$, $\chi \approx 0.02$, and $\mu = 4$. The (purple) empty “squares” indicate the $D_{\alpha\alpha}$ ’s obtained directly from simulation data (as the slope of $\langle \alpha^2 \rangle$ vs. time), while the (green) filled “circles” are the analytical pitch-angle diffusion coefficients, given by Eq. (5.7).	88
5.10	Energy diffusion coefficient, D_{WW} vs the normalized electron velocity, β . Relevant simulation parameters include: $N_p = 5000$, $k_{\min} = 32\pi$, $k_{\max} = 10k_{\min}$, $\langle \delta B^2 \rangle^{1/2}/B_0 = 0.1$, $\Omega_{ce} = 1$, $\chi \approx 0.02$, and $\mu = 4$. The (blue) empty “squares” indicate the D_{WW} ’s obtained directly from simulation (as the slope of $\langle \Delta W_e^2 \rangle$ vs. time), while the (red) filled “circles” are the analytical energy diffusion coefficients, given by Eq. (5.50).	89

5.11 Magnetic pitch-angle diffusion coefficient, $D_{\alpha\alpha}$ vs the inverse of magnetic field correlation scale, λ_B^{-1} . Relevant simulation parameters include: $\gamma_e = 3$, $N_p = 1000$, $k_{\min} = 8\pi$, 16π , 32π , 64π , and 128π , $k_{\max} = 10k_{\min}$ (for each k_{\min}), $\langle \delta B^2 \rangle^{1/2}/B_0 = 0.1$, $\Omega_{ce} = 1$, $\chi \approx 0.02$, and $\mu = 4$. For each data point, the theoretical and numerical results differ only by a small factor of $\mathcal{O}(1)$.	90
5.12 Energy diffusion coefficient, D_{WW} vs the inverse of magnetic field correlation scale, λ_B^{-1} . Relevant simulation parameters include: $\gamma_e = 3$, $N_p = 1000$, $k_{\min} = 8\pi$, 16π , 32π , 64π , and 128π , $k_{\max} = 10k_{\min}$ (for each k_{\min}), $\langle \delta B^2 \rangle^{1/2}/B_0 = 0.1$, $\Omega_{ce} = 1$, $\chi \approx 0.02$, and $\mu = 4$. The theoretical and numerical results differ only by a small factor of $\mathcal{O}(1)$.	91
5.13 Magnetic pitch-angle diffusion coefficient, $D_{\alpha\alpha}$ vs the magnetic spectral index, μ . Relevant parameters are $N_p = 2000$, $k_{\min} = 32\pi$, $k_{\max} = 10k_{\max}$, $\langle \delta B^2 \rangle^{1/2}/B_0 = 0.1$, $\Omega_{ce} = 1$, and $\chi \approx 0.05$. Notice that the numerical results have nearly the same functional dependence on μ as the analytical squares, as given by Eq. 5.7.	92
5.14 Energy diffusion coefficient, D_{WW} vs the magnetic spectral index, μ . Relevant parameters are $N_p = 2000$, $k_{\min} = 32\pi$, $k_{\max} = 10k_{\max}$, $\langle \delta B^2 \rangle^{1/2}/B_0 = 0.1$, $\Omega_{ce} = 1$, and $\chi \approx 0.05$.	93
5.15 Electric pitch-angle diffusion coefficient, $D_{\alpha\alpha}^{\text{elec.}}$ vs the normalized electron velocity, β for small-scale Langmuir turbulence. Relevant simulation parameters include: $k_{\min} = 8\pi$, $k_{\max} = 10k_{\min}$, $\langle \Omega_E^2 \rangle = 4.0$, $\chi \approx 666.67$, $\delta_j \approx 0.08$, and $\mu = 5$. The (purple) empty “squares” indicate the $D_{\alpha\alpha}^{\text{elec.}}$ ’s obtained directly from simulation data, while the (green) filled “circles” are the analytical pitch-angle diffusion coefficients, given by Eq. (5.11). Notice that the small deflection approximation, which is the foundational assumption behind Eq. (5.11), holds well for velocities that are mildly relativistic ($\gamma \sim 2$).	95

6.1	Radiation regimes. (a) Large-angle jitter regime, $1 < \delta < \gamma_e$; radiation is only seen along certain segments of the particle path, thus resulting in the spectrum that is synchrotron-like at and above the peak but differing from synchrotron at low frequencies. (b) Small-angle jitter regime, $\delta < 1$; radiation is seen from the entire trajectory, thus the spectrum depends on the underlying spectrum of electromagnetic turbulence.	100
6.2	Radiation spectra given variable k_{\min} , with all other parameters fixed. The number of simulation particles, N_p , is 2000, and $v = 0.5c$ in each case. In each trial, the particles moved for a total simulation time of $T = T_g$, where $T_g \equiv 2\pi\gamma_e m_e c / e\langle\delta B^2\rangle^{1/2}$ is the “gyroperiod”. Here, the axes are in arbitrary, simulation units. We see that the frequency scales as k_{\min} and $dW/d\omega$ scales as λ_B	110
6.3	Radiation spectra given variable v . In each trial, 1000 particles move for a total simulation time of $T = 10T_g$, where $T_g \equiv 2\pi\gamma_e m_e c / e\langle\delta B^2\rangle^{1/2}$ is the “gyroperiod”. We see that the overall shape of the spectra is not appreciably altered with decreasing v . The spectra are normalized by $T\gamma_e^2 v$, vertically. Given Figure 6.2, we may conclude that the peak frequency of these spectra is $\omega \sim \gamma_e^2 k_{\min} v$ – cf. Eq. (6.37).	112
6.4	Radiation spectra given two different values of the magnetic spectral index: $\mu = 5$ (red) “thick” line and $\mu = 4$ (blue) “thin” line. Included are the analytical solutions given by Eq. (6.20). Note that the $\mu = 5$ solution has been multiplied by an overall factor of two for easier visualization. For frequencies near $\omega \sim \gamma_e^2 k_{\min} v$, the numerical spectra agree decently with the analytical results. However, for frequencies near the break, $\omega \sim \gamma_e^2 k_{\max} v$, there is considerable deviation between the predicted and numerical spectra – for both values of the magnetic spectral index. The origin of this discrepancy is explored in Appendix B.	113

6.5 Radiation spectra with differing k_{\max} . Some other relevant parameters are $v = 0.25c$, $\rho = 6.34$, $N_p = 2000$, and $\mu = 5$ (for a complete listing, see Table 6.1). The two spectra differ by a factor of 2 in k_{\max} , with k_{\min} the same between them. Roughly, the spectra transition to the “tail” feature near $\omega \sim \gamma_e^2 k_{\max} v = \omega_{bn}$	114
6.6 Radiation spectrum with $\mu = 100$ ($\beta = 0.125c$). Evidently, the spectral feature presented directly prior to ω_{jn} has a functional form given by $A + D\omega^2$ (dashed line). This is consistent with Eq. (6.20).	115
6.7 Radiation spectrum of non-relativistic electrons moving through small-scale magnetic turbulence generated by a distribution of magnetic monopoles (“thick”, blue), superimposed with the radiation spectrum given a magnetic spectrum (“thin”, red) produced by standard means (i.e. Ampere’s Law). For each run, $\mu = 4$ and $\beta = 0.125c$. Each curve is accompanied by its corresponding analytical solutions (“dashed”, black). The spectral shape for frequencies less than ω_{jn} is $A + D\omega^2$ and $A - D\omega^2$ for the “divergenceless” field and “monopolar” field, respectively.	116
6.8 Average square pitch-angle growth as a function of time for non-relativistic electrons moving through small-scale magnetic turbulence generated by a distribution of magnetic monopoles “dashed” (blue), superimposed with the otherwise equivalent curve “solid” (red) produced by standard means (i.e. Ampere’s Law). For each run, $\mu = 6$, $N_p = 15420$, $\langle \delta B^2 \rangle^{1/2} = 0.032$, $k_{\min} = \pi$, $k_{\max} = 8\pi$, and $\beta = 0.125c$. Note that the slope of the “monopolar” curve is very nearly twice the slope of the standard curve – in accordance with Eq. (6.43).	117

- 6.9 Radiation spectrum for a monoenergetic, isotropic distribution of $\gamma_e = 5$ ($\chi \sim 1$; $\rho \approx 928$; $\langle \delta B^2 \rangle^{1/2} / B_0 = 0.1$) electrons moving through small-scale Whistler turbulence. The frequency is normalized by $\omega_{jn} = \gamma_e^2 k_{\min} \beta c$ – the relativistic jitter frequency. The solid (“red”) curve is from simulation data, whereas the dashed (“blue”) curve is the analytic estimate. Clearly, the spectrum is well represented by a superposition of synchrotron+jitter components. 119
- 6.10 Radiation spectrum for a monoenergetic, isotropic distribution of $\beta = 0.125$ electrons ($\chi \sim 0.04$; $\rho \approx 160$; $\langle \delta B^2 \rangle^{1/2} / B_0 = 0.2$; $\Omega_{ce} = 2$; $k_{\min} = 64\pi$; $k_{\max} = 10k_{\min}$; $\mu = 5$; $T = 50T_g$); superimposed with a spectrum given a population of $\gamma_e = 4$ electrons ($\chi \sim 1$; $\rho \approx 367$; $\langle \delta B^2 \rangle^{1/2} / B_0 = 0.1$; $\Omega_{ce} = 0.512$; $k_{\min} = \pi$; $k_{\max} = 10\pi$; $\mu = 4$; $T = 5T_g$). The normalization on the y -axis is arbitrary, whereas the x -axis is normalized to the $\beta = 0.125$ population’s cyclotron frequency, i.e. $\Omega_{ce} = 2$. The “thick” solid (“red”) curve is from simulation data for the $\beta = 0.125$ population, the dashed (“blue”) curve is the corresponding analytic estimate for “pure” psuedo-cyclotron radiation, the “thin” solid line is the simulation data for the $\gamma_e = 4$ population, and the “dot-dashed” (“black”) line is the $\gamma_e = 4$ analytic estimate. Notice, for the $\beta = 0.125$ spectrum, that the spectrum peaks near the cyclotron frequency, Ω_{ce} – hence we see the signature of cyclotron radiation. The additional harmonics, which are purely a relativistic effect, are the signature of emerging synchrotron radiation. . . . 120
- 6.11 Langmuir Radiation spectra for the $\gamma_e = 2$ and $v = 0.125c$ electrons (see Figure 5.15 for details on the simulation parameters). The frequency is normalized by the characteristic jitter frequency, i.e. $\omega_{jn} \equiv \gamma_e^2 k_{\min} \beta c$. The lower (“red”) curve is from simulation data, and it corresponds to the $v = 0.125c$ electron. The upper (“blue”) curve is the simulation result for the $\gamma_e = 2$ electron, and the dashed curve is the analytic estimate. Clearly, the mildly relativistic spectrum is well represented by the (Langmuir) jitter result. . . . 122

6.12 Emission coefficient vs. frequency for a thermal distribution of electrons moving through “magnetized”, sub-Larmor-scale magnetic turbulence. Relevant parameters: $n_e = 1 \text{ cm}^{-3}$, $\delta B = B_0 = 1 \text{ G}$, $\gamma_{T_e} = 12$, $k_{\max} = 50k_{\min}$, and $k_{\min}^{-1} = d_e^{\text{rel.}}$ – where $d_e^{\text{rel.}} \equiv c\sqrt{\gamma_{T_e}}/\omega_{pe}$ is the relativistic skin-depth. The jitter component – dashed (“blue”) line – overpowers the synchrotron portion – three-dot-dashed (“red”) line – at frequencies below $\omega_{bn} \sim \gamma_{T_e}^2 k_{\max} v_{T_e}$. This produces a distinctly non-synchrotron feature, at low frequencies, in the total (summed) spectrum, solid (“purple”) line.	124
6.13 Emission coefficient vs. frequency for a thermal distribution of electrons moving through “magnetized”, sub-Larmor-scale magnetic turbulence. Relevant parameters: $n_e = 1 \text{ cm}^{-3}$, $\delta B = B_0 = 1 \text{ G}$, $\gamma_{T_e} = 1.6$, $k_{\max} = 50k_{\min}$, and $k_{\min}^{-1} = d_e^{\text{rel.}}$. Despite the presence of noticeable thermal spread, the jitter component – dashed (“blue”) line – still overpowers the synchrotron portion – three-dot-dashed (“red”) line – at frequencies below $\omega_{bn} \sim \gamma_{T_e}^2 k_{\max} v_{T_e}$. The summed spectrum, solid (“purple”) line, remains distinctly non-synchrotron-like at low frequencies.	125
7.1 Normalized Faraday rotation angle vs. the normalized collision frequency. Notice that at $Z \equiv \nu_{\text{eff}}^*/\omega = 1$ zero Faraday rotation occurs. Collisions have effectively nullified Faraday Rotation.	139
7.2 Index of refraction for the O -mode as a function of depth (in terms of the electron density). Displayed here are five solutions, all differing by the ratio, $\delta B/B_0$. Notice that for $\delta B/B_0 = 0.001$, $\nu_{ei} \gg D_{\alpha\alpha}^{ssc}$, and the expected weakly-collisional dependence is realized; i.e., a steep approach of the index of refraction towards zero at n_c . In contrast, $\delta B = B_0$ leads to a virtually transparent target. Included in this plot is the solution for $\nu_{\text{eff}} = \nu_{ei}$ — the dashed black line.	143

7.3 Index of refraction for the X -mode as a function of depth (in terms of the electron density). Displayed here are five solutions, all differing by the ratio, $\delta B/B_0$. Notice that for $\delta B/B_0 = 0.001$, $\nu_{ei} \gg D_{\alpha\alpha}^{ssc}$, and the expected weakly-collisional dependence is realized; i.e., a steep approach of the index of refraction towards zero at ω_R , a resonance at ω_{UH} , and another cutoff at ω_L . Collisions effectively connect the cutoff frequencies to the resonance, allowing access to ω_{UH} and ω_L . Nonetheless, for $\delta B \sim B_0$, the cutoffs and resonance disappear completely. Included in this plot is the solution for $\nu_{eff} = \nu_{ei}$ — the dashed black line.	145
7.4 Index of refraction for the X -mode as a function of depth (in terms of the electron density). Here, three solutions for which $\delta B/B_0 = 0.1$ are plotted with a variable B_0 . As expected, the solution approaches the O -mode profile for $B_0 \rightarrow 0$	146
7.5 X -mode laser intensity as a function of the target depth (in terms of the electron density). Despite the relative transparency for $\delta B \sim B_0$, the laser intensity quickly decays beyond the critical surface. Interestingly, the laser intensity is relatively fixed from ω_{UH} to ω_L , for low- Z . Additionally, there is initial drop near ω_{UH} that is not present in the high- Z case. Included in this plot is the solution for $\nu_{eff} = \nu_{ei}$ — the dashed black line.	147
7.6 O -mode laser intensity as a function of the target depth (in terms of the electron density). Once more, we see a relatively fixed laser intensity up to the critical surface, for low- Z . The high- Z curve is identical to the X -mode equivalent. Included in this plot is the solution for $\nu_{eff} = \nu_{ei}$ — the dashed black line.	148

8.1 Normalized Faraday rotation angle – i.e. Eq. (7.27) – vs. the electric fluctuation strength for various electron densities. The electron number densities are (from right to left): $n_e = 1, 10^2, 10^4, 10^6$, and 10^8 cm^{-3} ; the electron temperature is 0.511 MeV (or $\gamma_e \sim 2$), and $\omega/2\pi = 10 \text{ GHz}$. These curves exhibit a universal feature; namely, the rotation angle will reverse sign when the electric fluctuation field is sufficiently strong. As $\langle E^2 \rangle^{1/2} \rightarrow \infty$, the rotation is completely nullified.	155
8.2 Quasi-collisional absorption e-folding distance vs. the ambient magnetic field. The instance depicted here is the $n_e = 10^8 \text{ cm}^{-3}$ case from Figure 8.1. We see that the “collisional” absorption occurs on a many kilometer length scale. With $B_0 = 10 \text{ G}$, the signal would be reduced to a factor of 0.01 around 44 km.	156
9.1 Spectral flux (differential flux per differential frequency) of the total emitted radiation vs normalized frequency. The frequency is normalized to the jitter frequency, i.e. Eq. (9.2). The total power (“purple”, solid line) is the sum of the individual jitter (“blue”, upper-left dashed line) and Bremsstrahlung (“red”, lower-left dashed line) components. Clearly, the jitter component dominants near the jitter frequency (here defined as $f = \omega/2\pi$).	169
9.2 The photon flux at each frequency; i.e. Figure 9.1 divided by the the photon energy, $\hbar\omega$. We see that the majority of the jitter flux is at frequencies slightly below the jitter frequency, ω_{jn}	170
A.1 Radiation spectra of Figure 6.2, with linear abscissa. We see that the power spectrum quickly approaches zero around the “break” frequency, $\gamma^2 k_{max} v$ – in accord with Eq. (6.20). This numerical approach to zero, since it is not instantaneous, appears readily in a log-log plot which magnifies features on an orders of magnitude scale.	191

List of Tables

6.1 Table of parameters used for the radiation spectra figures. Here, and elsewhere, Δt is the simulation time step, the simulation time is denoted in multiples of the “gyroperiod” (i.e. $T_g = 2\pi\gamma_e m_e c / e\langle\delta B^2\rangle^{1/2}$), and N_p is the total number of simulation particles.	111
---	-----

Chapter 1

General Introduction

Electromagnetic turbulence is an ubiquitous phenomenon. In the laboratory setting, understanding and controlling electromagnetic turbulence is critical to fusion energy science and the inertial confinement concept (Ren et al., 2004; Tatarakis et al., 2003). Plasma/electromagnetic turbulence is a critical element in the development and evolution of supernovae blast waves (Fan et al., 2011), shocks in the interplanetary medium (Gurnett et al., 1979), jets of quasars (Mao & Wang, 2007; Gurnett et al., 1979), and solar flares (McAteer et al., 2009).

Turbulence in electromagnetic fields is the byproduct of instability. Many plasma processes are susceptible to exponential (sometimes, non-linear) growth when sufficient free-energy is available (Treumann et al., 1997). High-energy-density (HED) environments can readily provide this energy, as these conditions are often the product of forces driving the system towards great extremes of pressure, density, temperature, etc. Many of these environments are, in fact, “collisionless”. A plasma is collisionless if the spatial and time scales which characterize the system are much less than the Coulomb mean free path and time, respectively. Collisionless plasmas evolve in time, not by hydrodynamic-like binary Coulomb interactions, but by collective plasma effects (i.e. plasma waves, macroscopic electromagnetic fields, etc.). This often requires a full kinetic treatment.

1.1 GRB Collisionless Shocks and Jitter Radiation

One particular, fully kinetic, plasma instability known as the “Weibel-filamentation instability” (Weibel, 1959; Fried, 1959) garnered renewed interest when it was proposed that the instability may play an essential role in the explanation of the enigmatic, gamma-ray burst (GRB). GRB’s are intensely energetic explosions, $\sim 10^{51} - 10^{54}$ ergs, of cosmological origin (Medvedev & Loeb, 1999). These events have been shrouded in mystery ever since their serendipitous discovery during the heart of the Cold War in the 1960’s. The “standard model” of GRB’s considers a particularly violent astrophysical event (e.g. neutron star merger or black hole birth) as a “progenitor” for the creation of a “fireball”. These fireballs are thought to consist principally of radiation and electron-positron pairs. The fireball accompanies the creation of internal and external (i.e. the upstream is the surrounding interstellar medium) relativistic collisionless shocks. It is believed that the GRB event (i.e. the observed gamma-rays) and “afterglow” effect (in x-rays, all the way down to radio emissions) are produced by the Compton scattering and synchrotron emission of relativistic electrons moving in the “post-shocked” magnetic field. The acceleration of these electrons is thought to occur via first-order Fermi acceleration, mediated by multiple crossings with the shock barrier. The shock, itself, must be the site of an intense magnetic field. Indeed, observations suggest that strong magnetic fields must exist in the up and downstream of the shock. To explain the origin of these strong magnetic fields, Medvedev & Loeb proposed a relativistic generalization of the Weibel instability as a mechanism. In this proposal, the counter-streaming electrons (in the shock frame) will mediate the shock by the creation of a strong magnetic field.

“Weibel fields” possess a number of favorable properties. First, Weibel magnetic fields are created spontaneously – without the need for the existence of a “pre-magnetized” environment. All that is needed to create these fields is an initial perturbation (seed field), which naturally arises from simple thermal fluctuations of the plasma. Next, the strength of these magnetic fields is owed to the Weibel instability’s inherently non-resonant nature. The Weibel instability involves the participation of the plasma as a whole, i.e. there is no partic-

ular sub-population of plasma particles that are responsible for maintaining the instability. Consequently, the Weibel instability can transform a significant fraction of the particle kinetic energy into magnetic field energy. Additionally, the randomness of the initial seed field ensures that the resulting magnetic field is turbulent; thus, the fields may effectively scatter particles at the shock front. Finally, the Weibel instability is approximately aperiodic. This indicates that its saturation requires the influence of non-linear processes – i.e. kinetic effects, such as Landau-like damping, cannot stop its growth (Medvedev & Loeb, 1999).

Large-scale, state of the art, particle-in-cell (PIC) codes have confirmed that the Weibel instability, indeed, plays a role in the formation of relativistic (Silva et al., 2003; Nishikawa et al., 2003; Frederiksen et al., 2004; Spitkovsky, 2005, 2008) and nonrelativistic collisionless shocks (Medvedev, 2006b; Fiúza et al., 2012).

Medvedev, subsequently, considered the radiation from particles moving in this “Weibel turbulence”. Weibel generated magnetic turbulence has a small correlation length – a few orders of the plasma skin-depth. Since the skin-depth is, typically, of comparable order to the Larmor curvature radius, this has immediate implications for particle transport – and therefore – radiation production in these plasmas.

The Synchrotron Shock Model (SSM) posits that the basic radiation mechanism involved in GRB’s is synchrotron radiation emitted by relativistic electrons. This treatment is valid for magnetic fields with correlation lengths greater than the electron’s average Larmor/gyro-radius. However, the Weibel-mediated magnetic fields have correlation lengths comparable to, or less than, the Larmor-scale; they are sub-Larmor-scale or “small-scale” fields. Thus, the radiation these electrons emit is distinct from synchrotron radiation.

The radiation from relativistic electrons in sub-Larmor-scale magnetic turbulence is called *jitter radiation* (Medvedev, 2000). Unlike synchrotron radiation, which is principally determined only by the strength of the magnetic field (which, in turn, determines the Larmor curvature radius), the spectral characteristics of jitter radiation are directly related to the statistical properties of the magnetic spectral distribution and particle distribution functions.

Three-dimensional jitter radiation has been observed in connection to the Weibel instability in PIC simulations (Medvedev et al., 2011; Mizuno et al., 2008; Frederiksen et al., 2010). Additionally, there is considerable observational support for the jitter mechanism as an explanation of the GRB “afterglow” (Medvedev, 2006). It was the Burst and Transient Source Experiment (BATSE) on the Compton Gamma Ray Observatory that first discovered a discrepancy in the SSM from GRB light curves. The SSM places a strict upper limit on the photon number spectral index, α , for low energies. The model considers the photon spectrum, $dN/dE \propto E^a$, where N is the number of photons with energy, E . The, so called, “synchrotron line of death” requires $a \lesssim -2/3$. According to BATSE’s initial measurements, 23 of the 100 observed bright GRB’s violated the $-2/3$ limit (Preece et al., 1998). In contrast, the jitter mechanism can account for this discrepancy. Moreover, the jitter theory explains the abundance of a specific spectral index (namely, $a \sim 1$) in the observational data; which, by no means, is favored by the SSM (Medvedev et al., 2009).

1.2 Research Overview

The intimate connection between jitter radiation and the transport of electrons/ions through the turbulence may be exploited as well. The first-order Fermi acceleration mechanism must appeal to the magnetic fields near shocks as the driving factor. Consequently, understanding the transport of plasma particles in the turbulent magnetic fields, via pitch-angle diffusion and energy diffusion, is essential to probing the particle acceleration. It is the elucidation of this inter-connection between transport and radiation production in small-scale magnetic turbulence that has directed our initial research efforts (Keenan & Medvedev, 2013). Our main interest has been the exploitation of this connection for general plasma diagnostic purposes.

1.2.1 Non-Relativistic Jitter Radiation

Nonetheless, electrons and ions in many suitable environments are non-relativistic (or mildly relativistic). The jitter theory is, formally, applicable to ultrarelativistic particles; thus, it may not adequately capture the transport/radiative properties of laboratory collisionless shocks, laser-plasmas, etc. The major component of this work includes the development of the non-relativistic, small-angle, jitter theory. Specifically, we derived the non-relativistic jitter (“pseudo-cyclotron”) radiation spectrum and precise analytic estimates for the non-relativistic generalization of the pitch-angle diffusion coefficient. Additionally, we confirmed our analytic results with first-principle numerical simulations (Keenan et al., 2015).

1.2.2 Small-Scale Fields in Magnetized Plasmas

Our initial studies strictly considered a “Weibel-like” magnetic turbulence. This means that we treated the electromagnetic turbulence as static, i.e. with zero real frequency. Additionally, we extended our model to include sub-Larmor-scale electromagnetic turbulence in plasmas with ambient magnetic fields. The instabilities, in this case, are usually driven with non-zero real frequency, and thus, they induce random electric fields. For this reason, we not only considered stochastic transport via (magnetic) pitch-angle diffusion, but transport via (electric) energy diffusion as well. We showed that the energy diffusion coefficient is proportional to the (sub-Larmor-scale) pitch-angle diffusion coefficient (Keenan et al., 2016). The exploitation of the inter-relation between the transport and radiative properties of these plasmas may provide a powerful diagnostic tool for examination of small-scale turbulence in “magnetized” plasmas.

We, furthermore, considered the transport of, and radiation production by, relativistic electrons moving through “small-scale” electric turbulence (Keenan et al., 2016). We, principally, focused on realizations of Whistler-mode turbulence, because Whistler waves are regularly seen in a very wide variety of magnetized environments. Given certain conditions, the (temperature anisotropy) Weibel instability – in pre-magnetized plasmas – may evolve

into a Whistler-mode instability (Palodhi et al., 2010); thus, for example, Whistler-modes may spontaneously appear in environments where Weibel-like instabilities may take hold.

Many examples of Whistler waves in space and astrophysical plasmas exist. Whistler waves near collisionless shocks in the solar system, in particular, have been observed *in situ* for decades. These wave-modes have, additionally, been strongly associated with interplanetary shocks – appearing both in the upstream and downstream regions (Fairfield, 1974; Tsurutani et al., 1983; Ramírez Vélez et al., 2012). The solar wind turbulence, as well, appears to host Whistler-modes (Lengyel-Frey et al., 1996; Lin et al., 1998).

1.2.3 Jitter Radiation in Laser-Plasma Experiments

An obvious application of mildly relativistic jitter radiation is offered by laser-plasma experiments. For over a decade, the production of strong ($>$ megaGauss) magnetic fields/turbulence in solid-density plasmas, generated by the irradiation of a target with high-intensity lasers, has been observed in a diverse set of laboratory experiments (Sandhu et al., 2002; Sarri et al., 2012; Wagner et al., 2004; Gopal et al., 2013; Mondal et al., 2012). Understanding and controlling electromagnetic turbulence in these environments is critical to studies in the fusion energy sciences, and for the inertial confinement concept (Ren et al., 2004; Tatarakis et al., 2003), in particular.

These magnetic fields can be generated by a number of mechanisms – e.g., by the misalignment in plasma temperature and density gradients (Biermann Battery), or by an induction field produced by the flux of fast electrons via the ponderomotive acceleration (Belyaev et al., 2008). At relativistic intensities ($> 10^{18} W/cm^2$) and ultrashort pulse durations ($< 1 ps$), magnetic fields can also be generated via an electron-driven Weibel-filamentation instability (Belyaev et al., 2008; Sarri et al., 2012). The instability is initiated by counterstreaming electron beams consisting of a “hot” beam (arising immediately following the target’s interaction with the high-intensity laser) and a returning (shielding) “cold” electron beam. Initially, the net current is zero; however, the Weibel-like instability subsequently grows, leading to

the formation of separated current filaments – the source of a quasi-static magnetic field configuration. The current filaments may further evolve, as they may in the astrophysical setting, via coalescence/tearing/screw instabilities, into current channels (Medvedev et al., 2005; Polomarov et al., 2008; Shvets et al., 2009), which further initiate filamentary magnetic structures (Mondal et al., 2012).

It is worth noting that there is considerable overlap between astrophysics and laboratory plasma physics. For example, the creation of a collisionless shock in the laboratory setting is a major goal of experimental astrophysics. It is strongly believed that presently existing laser facilities, such as OMEGA/OMEGA EP and NIF, will eventually observe these Weibel-mediated shocks in the laboratory – i.e. to make a “gamma-ray burst in a lab” (Medvedev, 2007, 2008; Medvedev & Spitkovsky, 2009). In contrast to the aforementioned solid-density plasmas, these plasmas flow freely in-between laser ablated metal plates (Fox et al., 2013; Sakawa et al., 2013; Bret et al., 2014; Huntington et al., 2015; Park et al., 2015). This is achieved via weaker laser intensities and longer pulse durations ($\sim 10^{14} \text{ W/cm}^2$ and $\sim 1 \text{ ns}$, for a recent Omega laser experiment) – although higher intensities are believed to be required for the creation of a shock (Sakawa et al., 2013; Huntington et al., 2015). Recently, the formation of filamentary structures indicative of ion-driven Weibel-like magnetic fields has been observed in a scaled laboratory experiment at the Omega Laser Facility (Fox et al., 2013; Huntington et al., 2015; Park et al., 2015).

We showed that the direct observation of mildly relativistic jitter radiation may be feasible in the laboratory setting (Keenan & Medvedev, 2015b). We focused our attention upon the 2012 Mondal experiment (Mondal et al., 2012). This experiment provides a concrete example of an applicable laser-plasma. Additionally, the Mondal experiment constructed, directly from data, the magnetic (spatial) power spectrum – an estimate of which is necessary to predict the jitter radiation spectra. A considerable amount of what is explored here is applicable to (short duration) relativistic laser-plasma experiments, in general.

1.2.4 Small-Scale Turbulence and Quasi-Collisionality

Despite much variation in the origin of the electromagnetic turbulence (e.g., the Weibel or filamentation instabilities), most of these plasmas have one thing in common: their configuration is such that binary Coulomb collisions are negligible; i.e., the plasmas are “collisionless”. Nonetheless, some of these environments, such as plasmas at “collisionless” shocks, display phenomena that resemble conventional collisional interactions. Hereafter, we colloquially refer to these phenomena as “quasi-collisional”.

We showed that sub-Larmor-scale (“small-scale”) magnetic turbulence (Keenan et al., 2015a), and small-scale electric turbulence (Keenan et al., 2016a), induces particle dynamics reminiscent of binary Coulomb interactions. In fact, the random small-angle deflections of electrons by small-scale magnetic and electric fields leads to an effective collisionality with the effective “collision” frequency being equal to the (small-angle) pitch-angle diffusion coefficient.

Random magnetic fields are known to lead to effective diffusion. Particularly, braided fields, for example, can cause anomalous transport in tokamaks near destroyed rational magnetic surfaces (Rechester & Rosenbluth, 1978) and in turbulent plasmas inside galaxy clusters (Chandran & Cowley, 1998; Narayan & Medvedev, 2001; Malyshkin & Kulsrud, 2001; Malyshkin, 2001; Medvedev, 2007b). The key difference in our work, from previous works, is that they considered that the correlation length of the field (or equivalently the chaotic Lyapunov exponent) is substantially larger than the Larmor scale (hence the term “braided”), whereas we considered the case of the fluctuating field having a correlation length smaller than the Larmor scale.

This “quasi-collisional” effect, if real, would produce a distinct (anomalous) signature in Faraday rotation measures of astrophysical magnetic fields (that is, if they contain any non-negligible small-scale component). This effect significantly alters the reflection and absorption coefficients of laser-plasmas with small-scale fields, as well. In fact, if the effect is sufficiently large, it may effectively render the plasma medium transparent; i.e. the “critical

surface”, at which absorption/reflection principally occurs, disappears (or, at the very least, is pushed further into the material). This may be important for inertial confinement fusion (ICF), in particular. The deposition of momentum within the target is required for implosion to occur; thus, this deposition depends upon the reflection coefficient. Additionally, excess absorption, with its accompanying increase in temperature, may be problematic.

1.3 Chapter Organization

This work is organized as follows. In Chapters 2 & 3, we provide the theoretical background needed to understand the proper context of our research efforts. Many of the concepts discussed, therein, will appear throughout this work. In Chapter 4, we present details on the first-principle numerical simulations employed. Chapters 5 & 6 present the analytic theory, and simulation results, for the transport and radiation production of particles moving through small-scale electromagnetic turbulence. In Chapters 7 & 8, we discuss quasi-collisionality in small-scale magnetic and electric turbulence, respectively. Chapter 9 presents our work on the possible observation of jitter radiation in laser-plasma experiments. Finally, Chapter 10 presents our general conclusions. All equations are in cgs units.

Chapter 2

Theoretical Background

In this Chapter, we discuss the basic concepts underlying the kinetic theory of collisionless plasmas. These concepts, in one form or another, will appear throughout this work.

2.1 The Classical Plasma

Colloquially, a *plasma* is a rarefied gas of fully ionized electrically charged particles. However, for our purposes, we will need a more specific, i.e. formal, definition. This require some development.

The plasmas we will consider are governed by *classical physics*. Essentially, the particles that compose a plasma behave like “particles”, i.e. their field and wave-like properties are suppressed. This means that the characteristic spatial scales of plasmas are much larger than length scales at which quantum phenomena become important. We will now estimate these characteristic scales. We will treat the electron scales only, since the equivalent ion scales are far shorter.

The shortest electron length is that for which “renormalization” becomes important in Quantum Electrodynamics (QED); this is, roughly, the *classical electron radius* (Landau & Lifshitz, 1975). This scale is connected to the electron’s, so called, self-energy. In classical physics, the idea of a point-like electron is actually a source of contradiction, since the

electron's self-energy must be infinite if it were the size of a point. One may reach this conclusion by considering an electron as a distribution of charge. If we bring in the bits of charge to form the electron from infinity, then work must be done against these bits' mutual electrostatic (Coulomb) repulsion. That work then becomes the rest mass energy of the electron, $m_e c^2$ (where m_e is the electron mass and c is the speed of light in a vacuum). Thus, since the electron mass is finite, the electron radius must be finite as well. Consequently, the electron's radius must be given by the equality: $e^2/r_e = m_e c^2$ – where e^2/r_e , the Coulomb potential energy (zeroed at infinity), which is the work required to assemble a charge of e with radius, r_e . Thus, the classical electron radius is defined as:

$$r_e \equiv \frac{e^2}{m_e c^2}. \quad (2.1)$$

This is a very short length; $r_e \approx 2.82 \times 10^{-15} \text{ m}$. The average separation between plasma particles, \bar{d} is much, much greater than this length scale.

Next, the spatial scale at which QED, itself, becomes important is dictated by the *Compton wavelength*. This is the wavelength of a photon with sufficient energy, W_{ph} , to produce an electron or positron, i.e. $W_{\text{ph}} = m_e c^2$. The energy of a photon is given by: $W_{\text{ph}} = hc/\lambda$ – where h is Planck's constant and λ is the photon's wavelength. Thus, the Compton wavelength follows as:

$$\lambda_{\text{compton}} \equiv \frac{\hbar}{m_e c}, \quad (2.2)$$

where $\hbar \equiv h/2\pi$ is the reduced Planck's constant. The Compton wavelength, $\lambda_{\text{compton}} \approx 2.43 \times 10^{-12} \text{ m}$, defines the characteristic spatial scale at which electron and positron creation and annihilation become important; equivalently, it dictates the energy-scale at which QED is necessary for the complete description of the plasma.

The final quantum scale is dictated by the wavelength of an electron. If the characteristic length of the plasma (which is, presumably, larger than \bar{d}) is much greater than the quantum wavelength, then we may legitimately treat the electrons and ions as point-like “particles”.

The wavelength of an electron is, roughly, given by its *de Broglie wavelength*, i.e. $\lambda_{\text{debroglie}} = h/p$ – where p is the electron’s momentum. Thus, we require that:

$$\frac{h}{p} \ll \bar{d}. \quad (2.3)$$

The de Broglie wavelength will depend upon the plasma temperature, i.e. the average kinetic energy of each particle, $\bar{W}_e \sim k_B T$ – where k_B is the Boltzmann constant and T is the absolute temperature. We may relate \bar{d} to the average electron number density, n_e , by noting that: $n_e \sim \bar{d}^{-3}$. Thus, the inequality may be expressed, alternatively, as:

$$n_e^{-1/3} \sqrt{m_e k_B T} / h \gg 1, \quad (2.4)$$

where we have used $p^2/m_e \sim \bar{W}_e^1$ A more convenient representation is given by:

$$n_e^{-1/3} \sqrt{\theta_{\text{eV}}} \gg 2 \times 10^{-7} \text{ cm eV}^{1/2}, \quad (2.5)$$

where the electron temperature, θ_{eV} , is in electron-volts. In Figure 2.1 (where $n \equiv n_e$), we see parameter values for some typical plasmas (we will discuss the nature of each parameter in the following sections). For each plasma setup, Eq. (2.5) holds well – up to, at least, an order of magnitude. Thus, many plasmas permit the classical prescription. For this reason, we will presuppose the classical picture for everything to follow.

2.1.1 The Boltzmann Transport Equation

Eq. (2.3) implies that electrons and ions in a plasma behave like particles. This means that each particle has a rather well-defined position and momentum. The complete description of their motion is given by the Hamilton, H ; which is a function of generalized coordinates

¹Strictly, this applies only for non-relativistic plasmas. Relativistic plasmas, on the other hand, will more easily satisfy the general inequality. Although, when the energy-scales exceed the Compton limit, quantum processes like pair production may become important.

APPROXIMATE MAGNITUDES IN SOME TYPICAL PLASMAS

Plasma Type	$n \text{ cm}^{-3}$	$T \text{ eV}$	$\omega_{pe} \text{ sec}^{-1}$	$\lambda_D \text{ cm}$	$n\lambda_D^3$	$\nu_{ei} \text{ sec}^{-1}$
Interstellar gas	1	1	6×10^4	7×10^2	4×10^8	7×10^{-5}
Gaseous nebula	10^3	1	2×10^6	20	8×10^6	6×10^{-2}
Solar Corona	10^9	10^2	2×10^9	2×10^{-1}	8×10^6	60
Diffuse hot plasma	10^{12}	10^2	6×10^{10}	7×10^{-3}	4×10^5	40
Solar atmosphere, gas discharge	10^{14}	1	6×10^{11}	7×10^{-5}	40	2×10^9
Warm plasma	10^{14}	10	6×10^{11}	2×10^{-4}	8×10^2	10^7
Hot plasma	10^{14}	10^2	6×10^{11}	7×10^{-4}	4×10^4	4×10^6
Thermonuclear plasma	10^{15}	10^4	2×10^{12}	2×10^{-3}	8×10^6	5×10^4
Theta pinch	10^{16}	10^2	6×10^{12}	7×10^{-5}	4×10^3	3×10^8
Dense hot plasma	10^{18}	10^2	6×10^{13}	7×10^{-6}	4×10^2	2×10^{10}
Laser Plasma	10^{20}	10^2	6×10^{14}	7×10^{-7}	40	2×10^{12}

Figure 2.1: Approximate magnitudes of characteristic parameters in some typical plasmas.
Source: The NRL Plasma Formulary (2013 Revision).

and canonical momenta. The particles obey Hamilton's Equations:

$$\begin{cases} \partial H / \partial \mathbf{q}_i = -\dot{\mathbf{p}}_i, \\ \partial H / \partial \mathbf{p}_i = \dot{\mathbf{q}}_i, \end{cases} \quad (2.6)$$

where \mathbf{p}_i and \mathbf{q}_i are the i^{th} particle's momentum and position, respectively. Thus, for a collection of N particles, we have $6N$ equations. Since these particles obey Hamilton's equations, the $6N$ -dimensional phase space volume element:

$$\Pi_{i=1}^N d\mathbf{q}_i d\mathbf{p}_i, \quad (2.7)$$

is a conserved quantity when the Hamiltonian is not an explicit function of time – a fact which underlies *Liouville's Theorem* (Lifshitz & Pitaevskii, 1981). In principle, these $6N$ equations wholly determine the state of the system. Nonetheless, they are too numerous to deal with in practice, so we require something simpler. We may reduce the complexity by moving from this $6N$ -dimensional phase space to that of a single particle. We define the single particle distribution function as:

$$f(\mathbf{x}, \mathbf{p}, t) \equiv \frac{d^2 N}{d\mathbf{x} d\mathbf{p}}, \quad (2.8)$$

where $d\mathbf{x} d\mathbf{p}$ is the volume element of the 6-dimensional phase space for one particle. Thus, f specifies the number of particles within an infinitesimal volume of phase space. Integration of f over all of phase space then gives the total number of particles. There will be, in fact, a distribution function for each plasma species, but we will consider (for simplicity) just one species at this time. Implicit in this definition is the assertion that the plasma contains a very large number of particles, and that their physical separation is sufficiently small enough that we may treat the distribution function as a continuous function of \mathbf{x} and \mathbf{p} .

Next, the evolution equation for f may be conceptualized by first considering the lim-

iting case of zero “interactions”. If each particle may be treated as its own “sub-system”, it will individually obey Liouville’s theorem. Thus, the number of particles occupying an infinitesimal volume of phase space is conserved; hence:

$$\frac{d}{dt} [f(\mathbf{x}, \mathbf{p}, t) d\mathbf{q} d\mathbf{p}] = \frac{df(\mathbf{x}, \mathbf{p}, t)}{dt} d\mathbf{q} d\mathbf{p} + f(\mathbf{x}, \mathbf{p}, t) \frac{d}{dt} [d\mathbf{q} d\mathbf{p}] = 0. \quad (2.9)$$

Thus, because $\frac{d}{dt} [d\mathbf{q} d\mathbf{p}] = 0$:

$$\frac{df}{dt} = 0. \quad (2.10)$$

With the introduction of “collisions”, this condition fails. We correct Eq. (2.10) for collisions with:

$$\frac{df}{dt} = \left(\frac{\partial f}{\partial t} \right)_{\text{coll}}, \quad (2.11)$$

where the functional form of $(\partial f / \partial t)_{\text{coll}}$ depends upon the collisional model chosen. Thus, we write the *Boltzmann transport equation* by expanding df/dt , i.e.

$$\frac{\partial f}{\partial t} + \frac{\partial f}{\partial \mathbf{x}} \cdot \dot{\mathbf{x}} + \frac{\partial f}{\partial \mathbf{p}} \cdot \dot{\mathbf{p}} = \left(\frac{\partial f}{\partial t} \right)_{\text{coll}}, \quad (2.12)$$

Next, we must interpret the $\dot{\mathbf{p}}$ term in Eq. (2.12) and the meaning of “collisional” interaction in the transport equation. Unless otherwise stated, we will assume a non-relativistic plasma for the following derivations.

2.1.2 The Vlasov Equations

In essence, Liouville’s theorem states that the total energy of a closed system is conserved. Thus, Eq. (2.10), which asserts that a single particle acts as “closed” sub-system, implies that the total energy of a single plasma particle must be conserved. Consequently, the only “forces” acting on the particle must be conservative.

Since a plasma is composed of electric charges, it responds to the application of electric and magnetic fields. We interpret the $\dot{\mathbf{p}}$ term in Eq. (2.12) as a force applied to each plasma

particle by external fields – which conserve particle energy. The equation of motion of a charged particle in external electromagnetic fields is given by the Lorentz force, i.e.

$$\dot{\mathbf{p}} = e \left(\mathbf{E} + \frac{\mathbf{v}}{c} \times \mathbf{B} \right), \quad (2.13)$$

where \mathbf{E} , \mathbf{B} , and \mathbf{v} are the external electric field, magnetic field, and particle velocity, respectively.² The electric field, if it does not possess any explicit time-dependence, conserves the total (single) particle energy. Thus, the application of \mathbf{E} does not violate Eq. (2.12). In general, a force-field that depends explicitly upon the particle velocity is non-conservative. However, since $\mathbf{v}/c \times \mathbf{B}$ is always perpendicular to \mathbf{v} , the magnetic field will always impose a transverse acceleration. As a result, the particle speed, v , remains constant; therefore, the kinetic energy is unaffected by \mathbf{B} .

Thus, since the Lorentz force does not affect the total energy of a single particle, it does not violate Eq. (2.10). Collisions, on the other hand, are conceptually distinct. When a particle “encounters” another particle, we say that they will have a Coulomb interaction. This interaction is, generally, non-conservative (for a single particle) – since it may involve an exchange of energy from one particle to another.

The notion of an “external” field, as we have discussed, implicitly entails that the “self-field” of the plasma particle has no effect on the “source” of the external fields – thus, no exchange of energy between the particle and the “source” occurs.³ As we will show in the next section, the Coulomb fields of each plasma particle cannot be completely “screened out”. Rather, they effectively add to produce an overall “macroscopic” field. It is these fields which we treat as external, because a single plasma particle has very little influence on the fields

²Formally, the momentum variable should be the canonical momentum, $\mathbf{P} = \mathbf{p} - e/c\mathbf{A}(\mathbf{x}, t)$ – where $\mathbf{A}(\mathbf{x}, t)$ is the magnetic vector potential and $\mathbf{p} = m\mathbf{v}$ is the “kinetic momentum”. However, the action of \mathbf{A} is simply to change the zero of momentum at each point in space and time. This leaves the phase space volume unchanged; in other words, $d\mathbf{P}d\mathbf{x} = d\mathbf{p}d\mathbf{x}$. Thus, we legitimately make the switch: $f(\mathbf{x}, \mathbf{P}, t) \rightarrow f(\mathbf{x}, \mathbf{p}, t)$ (Lifshitz & Pitaevskii, 1981)

³Technically, a charge loses energy in an external field too – since the particle radiates electromagnetic waves whenever it experiences acceleration. Nonetheless, if the radiated energy is much less than the total particle energy, then we may safely ignore radiative losses.

produced by the plasma as a whole.

Formally, if the average distance a particle travels before “colliding”, i.e. the *mean-free path*, is much greater than the characteristic size of the plasma, then we can ignore collisions. Likewise, we may ignore collisions if the plasma processes of interest happen on a time-scale, Ω^{-1} , which is much less than the collisional mean-free time, τ_{mfp} . We call plasmas which meet any of these criteria *collisionless*.

Many plasmas, especially those considered in this work, fit the collisionless criteria; thus, they will be our main focus. We will formalize the notion of a collisionless plasma in the following sections, but first we will define the fundamental equations that govern their distribution function. First, since the plasmas are collisionless, the *RHS* of Eq. (2.12) is zero. Thus, we write the *Collisionless Boltzmann equations* as such:

$$\sum_s \frac{\partial f_s}{\partial t} + \sum_s \frac{\partial f_s}{\partial \mathbf{x}} \cdot \dot{\mathbf{x}} + e \left[\mathbf{E} + \frac{\mathbf{v}}{c} \times \mathbf{B} \right] \cdot \sum_s Z_s \frac{\partial f_s}{\partial \mathbf{p}} = 0, \quad (2.14)$$

where s denotes the plasma species (e.g. electron or proton) and Z_s is the ratio of the particle’s charge to e (i.e. 1 for a proton, -1 for an electron, 2 for a Helium nucleus, and so forth).

Next, these external fields must be calculated from Maxwell’s Equations using the plasma charge density, ρ , and the current density, \mathbf{J} . In *cgs* units, we write:

$$\nabla \cdot \mathbf{E} = 4\pi\rho \quad (2.15a)$$

$$\nabla \times \mathbf{E} = -\frac{1}{c} \frac{\partial \mathbf{B}}{\partial t} \quad (2.15b)$$

$$\nabla \cdot \mathbf{B} = 0 \quad (2.15c)$$

$$\nabla \times \mathbf{B} = \frac{4\pi}{c} \mathbf{J} + \frac{1}{c} \frac{\partial \mathbf{E}}{\partial t} \quad (2.15d)$$

We wish to obtain solutions that are consistent with a distribution function, f , and Eq. (2.14). To this end, we take “moments” of the distribution function to define effective current

and charge densities; these are:

$$\rho(\mathbf{x}, t) = e \sum_s Z_s \int f_s(\mathbf{x}, \mathbf{p}, t) d\mathbf{p} \quad (2.16a)$$

$$\mathbf{J}(\mathbf{x}, t) = e \sum_s Z_s \int f_s(\mathbf{x}, \mathbf{p}, t) \mathbf{v} d\mathbf{p} \quad (2.16b)$$

Eqs. (2.14)-(2.16) form a complete, self-consistent, set of equations for the solution of the distribution functions, f_s (Lifshitz & Pitaevskii, 1981). As a set, these are called the *Vlasov equations* – although, the literature sometimes applies the term exclusively to Eq. (2.14).

With the Vlasov Equations, we have very nearly defined what we mean by a *plasma*; nonetheless, there is still much to discuss.

2.1.3 The Debye Length

Consider a collisionless plasma that is in “thermal equilibrium”. That is to say, the plasma species possess a definite temperature, T_s , that is fixed in time. Let us, further, assume that the plasma is *isotropic*; i.e. $f(\mathbf{p}) = f(p)$ – where $p \equiv |\mathbf{p}|$. One solution to Eq. (2.14) which fits these criteria is the *Maxwell-Boltzmann distribution* (Cravens, 1997):

$$f_{sM}(\mathbf{x}, p) \propto \exp \left[-\frac{W_s}{k_B T_s} \right], \quad (2.17)$$

where W_s is the total energy of a single particle of species, s . Let us suppose that the plasma is permeated by a macroscopic electrostatic field, $\mathbf{E}(\mathbf{x}) = -\nabla\Phi(\mathbf{x})$. For electrons, $W_e = p^2/2m_e + e\Phi(\mathbf{x})$; thus:

$$f_{eM}(\mathbf{x}, p) \propto \exp \left[-\frac{p^2}{2m_e k_B T} \right] \exp \left[-\frac{e\Phi(\mathbf{x})}{k_B T_s} \right]. \quad (2.18)$$

The physical meaning of the potential term becomes clear when we consider the difference between an equilibrium plasma and the standard ideal gas. Consider, for simplicity, a plasma

composed exclusively of electrons and protons. Furthermore, assume that the protons are relatively immobile, and that the electrons move freely.

The equilibrium configuration of this plasma will be such that the electrons “bunch” together into clouds surrounding nearest protons. Eq. (2.18) suggests the electron number density, $n_e(\mathbf{x})$, that this equilibrium position will assume; namely:

$$n_e(\mathbf{x}) = n_{e0} \exp \left[-\frac{e\Phi(\mathbf{x})}{k_B T_e} \right], \quad (2.19)$$

where $n_{e0} \equiv n_e(\Phi = 0)$. We assume that the plasma is composed of, roughly, an equal number of protons and electrons; thus, $n_p = n_{e0}$ – where n_p is the proton number density. Since the protons are relatively immobile, their number density will largely not be affected by the macroscopic field.

Next, if the plasma is homogeneous, then we may choose the origin of our coordinate system at the center of a single proton and use the radius vector, \mathbf{r} . Thus, the total charge density surrounding a proton will be:

$$\rho(\mathbf{r}) = e [n_p - n_e] = en_{e0} \left[1 - \exp \left(-\frac{e\Phi(\mathbf{r})}{k_B T_e} \right) \right]. \quad (2.20)$$

Now that we have the charge density, we may solve for the potential using:

$$\nabla \cdot \mathbf{E} = -\nabla^2 \Phi = 4\pi\rho. \quad (2.21)$$

Applying Eq. (2.20) yields:

$$\nabla^2 \Phi(\mathbf{r}) = -4\pi en_{e0} \left[1 - \exp \left(-\frac{e\Phi(\mathbf{r})}{k_B T_e} \right) \right]. \quad (2.22)$$

Since the plasma is isotropic, $\Phi(\mathbf{r}) = \Phi(r)$. Hence, in spherical coordinates, we may write:

$$\nabla^2\Phi(\mathbf{r}) = \frac{1}{r^2}\frac{d}{dr}\left(r^2\frac{d\Phi}{dr}\right) = -4\pi en_{e0} \left[1 - \exp\left(-\frac{e\Phi}{k_B T_e}\right)\right]. \quad (2.23)$$

Next, let us assume that the electrons' kinetic energy,

$$W_e \sim k_B T_e \gg e|\Phi|. \quad (2.24)$$

With this assumption, the argument of the exponential in Eq. (2.23) is much less than unity. For this reason, we may expand the exponential; keeping only the first-order term. This considerably simplifies the expression, leading to:

$$\frac{1}{r^2}\frac{d}{dr}\left(r^2\frac{d\Phi}{dr}\right) \approx \left(\frac{4\pi e^2 n_{e0}}{k_B T_e}\right)\Phi. \quad (2.25)$$

Finally, the solution of Eq. (2.25) is given by (Cravens, 1997):

$$\Phi(r) = \frac{e}{r} \exp\left(-\frac{r}{\lambda_D}\right), \quad (2.26)$$

where,

$$\lambda_D \equiv \sqrt{\frac{k_B T_e}{4\pi n_{e0} e^2}} \quad (2.27)$$

is the electron *Debye length*.

Eq. (2.26) admits a simple physical interpretation – in its limits. As $r \rightarrow \infty$, the potential tends to zero. Hence, the electric field of the plasma is completely “screened out” at spatial infinity. In the opposite limit, i.e. $r \rightarrow 0$, the potential resembles the standard Coulomb potential: $\Phi = e/r$.

The Debye length is the characteristic spatial scale that roughly divides these two regimes. In other words, the large-scale electric fields in an equilibrium plasma only dominate spatial scales comparable to λ_D . For this reason, it is an important plasma parameter; one which

is critical to the definition of a “good” plasma – a term we will formally define in the next section.

2.1.4 The “Good” Plasma

The Debye length is a valid concept if the plasma contains a sufficiently large number of particles. This ensures that we may define an average particle number density that is actually statistically meaningful. It is, especially, important that the number of particles within a Debye radius is large. This motivates the introduction of N_D – which we define as the number of particles occupying a sphere of radius, λ_D . Hence:

$$N_D \approx n_{e0} \frac{4\pi}{3} \lambda_D^3. \quad (2.28)$$

We now define a new *plasma parameter*:

$$g_{\text{plasma}} \equiv 1/N_D. \quad (2.29)$$

Thus, we require that $g_{\text{plasma}} \ll 1$ to ensure the meaningfulness of λ_D .

Recall that $n_e^{-1/3} \sim \bar{d}$, where \bar{d} is average separation between plasma particles. With this relation, an alternative interpretation of g_{plasma} is given by:

$$g_{\text{plasma}} \sim \frac{3}{4\pi} \left(\frac{\bar{d}}{\lambda_D} \right)^3. \quad (2.30)$$

Hence, $g_{\text{plasma}} \ll 1$ implies that $\lambda_D \gg \bar{d}$.

Next, the plasmas we will consider are typically characterized by *quasi-neutrality*. This is the concept that, on the largest scales of plasma, the system is basically neutral. In other words, no electric fields exist on the scale of the system as a whole, L . This condition holds if the system size is much greater than the Debye length.

Finally, we define a plasma as “good” [for our purposes] if it satisfies the Vlasov Equations,

and these criteria:

$$\left\{ \begin{array}{l} \lambda_D \ll L \rightarrow (\text{Quasi-Neutrality}) \\ g_{\text{plasma}} \ll 1 \rightarrow (\text{Statistical Validity}) \\ \Omega\tau_{\text{mfp}} \gg 1 \rightarrow (\text{Collisionless Plasma}) \end{array} \right. \quad (2.31)$$

We have included the latter condition because our plasmas are typically collisionless. We will, nonetheless, relax this condition in Chapter 7.

Referring back to Figure 2.1, $n\lambda_D^3$ is approximately N_D – whereas, ν_{ei} is the electron-ion collision frequency. From the table, we see that a few plasmas are obviously not “good”. Laser-plasmas, in particular, violate both the *Statistical Validity* condition and quasi-neutrality. They are, additionally, weakly collisional. Nonetheless, most *Space and Astrophysical plasmas* (e.g. interstellar gas) are “good”.

2.1.5 The Plasma Dielectric Tensor

Sources of free energy can drive a plasma away from equilibrium. This may promote the growth of instabilities, electromagnetic fluctuations/waves, and turbulence. Even in isotropic plasma, there are fluctuation processes, e.g. Langmuir oscillations, that would go unnoticed if we restricted our attention to the “good” plasma description. To fully appreciate the non-equilibrium dynamics of plasmas, we must utilize the *plasma dielectric tensor*.

We may derive the dielectric tensor by considering the response of a plasma due to the application of an external electric field, \mathbf{E} . To that end, we define the polarization vector, \mathbf{P} , thusly:

$$\left\{ \begin{array}{l} \partial\mathbf{P}/\partial t = \mathbf{J}, \\ \nabla \cdot \mathbf{P} = -\rho. \end{array} \right. \quad (2.32)$$

These implicit relations for \mathbf{P} are compatible, since they follow immediately from the charge continuity equation (Lifshitz & Pitaevskii, 1981).

Next, we define the displacement field, $\mathbf{D} \equiv \mathbf{E} + 4\pi\mathbf{P}$. This may be interpreted as the field produced by the plasma in response to \mathbf{E} . This definition, additionally, allows the expression

of Maxwell's Equations symmetrically (i.e. without the presence of currents and charge densities which underlies the distinction between the “homogeneous” and “inhomogeneous” equations). With these relations, Eqs. (2.15) become (Lifshitz & Pitaevskii, 1981):

$$\nabla \cdot \mathbf{D} = 0 \quad (2.33a)$$

$$\nabla \times \mathbf{E} = -\frac{1}{c} \frac{\partial \mathbf{B}}{\partial t} \quad (2.33b)$$

$$\nabla \cdot \mathbf{B} = 0 \quad (2.33c)$$

$$\nabla \times \mathbf{B} = \frac{1}{c} \frac{\partial \mathbf{D}}{\partial t} \quad (2.33d)$$

We wish to write a general expression for the plasma response. To do this, we must realize that the plasma does not respond instantaneously to the applied field. Consequently, $\mathbf{D}(\mathbf{r}, t)$ will depend upon the development of \mathbf{E} throughout all of its history.

Furthermore, we wish to treat the plasma self-consistently. For this reason, we treat the “external” electric field as emanating from the plasma itself. This means that \mathbf{D} will depend upon \mathbf{E} in a non-local way; thus, \mathbf{D} at \mathbf{r} will be determined by \mathbf{E} throughout the entirety of the plasma.

With these stipulations, the most general expression that we may write for the relation between \mathbf{E} and \mathbf{D} – at the point, \mathbf{r} , during time, t – will have the component form (Lifshitz & Pitaevskii, 1981):

$$D_\alpha(\mathbf{r}, t) = E_\alpha(\mathbf{r}, t) + \int_{-\infty}^t \int_V K_{\alpha\beta}(\mathbf{r}, t | \mathbf{r}', t') E_\beta(\mathbf{r}', t') dt' d\mathbf{r}', \quad (2.34)$$

where V is the volume of the space, and $K_{\alpha\beta}$ is a kernel function which depends upon the dielectric properties of the plasma under consideration.

If the plasma is spatially homogeneous, then the lack of a preferred coordinate origin implies that K will only depend upon $\mathbf{r} - \mathbf{r}'$. Likewise, temporal homogeneity implies that the response of the plasma will depend upon the duration from t' to t , i.e. $t - t'$. Thus,

assuming homogeneity in time and space, we may write (Lifshitz & Pitaevskii, 1981):

$$D_\alpha(\mathbf{r}, t) = E_\alpha(\mathbf{r}, t) + \int_0^\infty \int_V K_{\alpha\beta}(\boldsymbol{\rho}, \tau) E_\beta(\mathbf{r} - \boldsymbol{\rho}, t - \tau) d\tau d\boldsymbol{\rho}, \quad (2.35)$$

where $\boldsymbol{\rho} \equiv \mathbf{r} - \mathbf{r}'$ and $\tau \equiv t - t'$.

Let us suppose plane wave solutions for \mathbf{E} and \mathbf{D} ; namely:

$$\begin{cases} \mathbf{D}(\mathbf{r}, t) = \mathbf{D}(\Omega, \mathbf{k}) \exp(i\mathbf{k} \cdot \mathbf{r} - i\Omega t), \\ \mathbf{E}(\mathbf{r}, t) = \mathbf{E}(\Omega, \mathbf{k}) \exp(i\mathbf{k} \cdot \mathbf{r} - i\Omega t). \end{cases} \quad (2.36)$$

With these expressions, Eq. (2.35) is:

$$\mathbf{D}(\Omega, \mathbf{k}) e^{i\mathbf{k} \cdot \mathbf{r} - i\Omega t} = \mathbf{E}(\Omega, \mathbf{k}) e^{i\mathbf{k} \cdot \mathbf{r} - i\Omega t} + \left[\int_0^\infty \int_V K_{\alpha\beta}(\boldsymbol{\rho}, \tau) e^{i\Omega\tau - i\mathbf{k} \cdot \boldsymbol{\rho}} d\tau d\boldsymbol{\rho} \right] \mathbf{E}(\Omega, \mathbf{k}) e^{i\mathbf{k} \cdot \mathbf{r} - i\Omega t}. \quad (2.37)$$

We define the plasma dielectric (permittivity) tensor, $\epsilon_{\alpha\beta}(\Omega, \mathbf{k})$, such that:

$$D_\alpha(\Omega, \mathbf{k}) = \epsilon_{\alpha\beta}(\Omega, \mathbf{k}) E_\beta(\Omega, \mathbf{k}), \quad (2.38)$$

so, from Eq. (2.37), the dielectric tensor must be defined by:

$$\epsilon_{\alpha\beta}(\Omega, \mathbf{k}) \equiv \delta_{\alpha\beta} + \int_0^\infty \int_V K_{\alpha\beta}(\boldsymbol{\rho}, \tau) e^{i\Omega\tau - i\mathbf{k} \cdot \boldsymbol{\rho}} d\tau d\boldsymbol{\rho}, \quad (2.39)$$

where $\delta_{\alpha\beta}$ is the Kronecker delta.

The dielectric tensor encapsulates the fundamental response of a plasma to instability, waves, etc. Specifically, the solution to Eq. (2.38) – which is found, non-trivially, by solving the characteristic equation which results from taking the determinant of $\epsilon_{\alpha\beta}$ – gives us a dispersion relation, which is an expression that relates Ω and \mathbf{k} . Thus, to examine waves and instabilities in plasmas, we must construct the dielectric tensor. To that end, we solve the Vlasov Equations, under assumptions appropriate for the “disturbance” in question.

Chapter 3

The Characterization of Waves, Turbulence, and Instabilities in Collisionless Plasmas

3.1 Introduction

In this Chapter, we will use the tools we developed to describe the plasma processes (waves, instabilities, and turbulence) which will play an important role in the plasmas that we will consider later. Once completed, our unique contribution to the study of small-scale electromagnetic turbulence, as detailed in the Chapters to follow, may be sufficiently grasped.

Unless otherwise specified, the dynamics of the plasmas we will explore are dominated by electrons. That is to say, the electrons will principally respond to changes in the fields, distribution, etc. – whereas, any ion populations present will be largely unresponsive; they will merely provide a neutralizing, fixed background. Such a plasma is, colloquially, known as an *electron plasma*.

3.2 The Permittivity of an Isotropic Collisionless Plasma

The simplest plasma is isotropic, homogeneous, collisionless, and *non-magnetized*. The latter term refers to the lack of a large-scale, i.e. “external”, magnetic field in the plasma. As we will see later, this is a rather imprecise definition, but it will service our immediate needs.

Let us consider small electromagnetic perturbations to the plasma, $\delta\mathbf{E}$ and $\delta\mathbf{B}$. The response of the plasma to these fields is to perturb the electron distribution function by δf . Thus, we write the new distribution function as $f = f_0 + \delta f$ – where f_0 is the initial, “equilibrium” distribution.

Thus, with these substitutions, and dropping terms second-order and above, Eq. (2.14) becomes:

$$\frac{\partial(\delta f)}{\partial t} + \frac{\partial(\delta f)}{\partial \mathbf{x}} \cdot \dot{\mathbf{x}} = e \left[\delta\mathbf{E} + \frac{\mathbf{v}}{c} \times \delta\mathbf{B} \right] \cdot \frac{\partial f_0}{\partial \mathbf{p}}. \quad (3.1)$$

Since $f_0(\mathbf{v}) = f_0(v)$, for an isotropic plasma, the $\partial f_0 / \partial \mathbf{p}$ term is in the same direction as \mathbf{v} . Consequently, $\partial f_0 / \partial \mathbf{p} \cdot (\mathbf{v} \times \delta\mathbf{B}) = 0$. Thus, the magnetic perturbation has no effect on the distribution.

Assuming, once more, plane wave solutions in δf and $\delta\mathbf{E}$, we have the result (Lifshitz & Pitaevskii, 1981):

$$\delta f = \frac{e\delta\mathbf{E}}{i(\mathbf{k} \cdot \mathbf{v} - \Omega)} \cdot \frac{\partial f_0}{\partial \mathbf{p}}. \quad (3.2)$$

Next, we wish to obtain the dielectric tensor, *à la* Eq. (2.38). We presume that the initial distribution is, on the whole, electrically neutral and devoid of any currents (i.e. “quasi-neutral”). Additionally, the new current and charge density is the result of the perturbed electron distribution. Thus, using Eq. (2.16), we may write:

$$\rho = -e \int \delta f \, d\mathbf{p}, \quad (3.3a)$$

$$\mathbf{J} = -e \int \mathbf{v} \delta f \, d\mathbf{p}. \quad (3.3b)$$

Since δf is a plane wave function, \mathbf{J} and ρ will also be proportional to $\exp(i\mathbf{k} \cdot \mathbf{r} - i\Omega t)$.

Thus, using Eq. (2.32), The polarization vector is indicated by the relations:

$$i\mathbf{k} \cdot \mathbf{P} = -\rho, \quad (3.4a)$$

$$-i\Omega\mathbf{P} = \mathbf{J}. \quad (3.4b)$$

To proceed, we must address a problem. Eq. (3.2) has a pole when $\Omega = \mathbf{k} \cdot \mathbf{v}$. Since δf blows up at this point, it clearly violates our assumption that the perturbation is small (which permitted our initial “linearization” of the Boltzmann equation).

To deal with this pole, we may employ the Landau prescription which opts for the substitution: $\Omega \rightarrow \Omega + i\delta$ – followed by taking the limit: $\delta \rightarrow 0$. This rule is used for solving integrals of the form (Lifshitz & Pitaevskii, 1981):

$$I = \int_{-\infty}^{\infty} \frac{f(z)}{z - i\delta} dz, \quad (3.5)$$

where $\delta > 0$. The contour integration is done below the pole at $z = i\delta$. For $\delta \rightarrow 0$, we write the result as:

$$\int_{-\infty}^{\infty} \frac{f(z)}{z - i0} dz = P \int_{-\infty}^{\infty} \frac{f(z)}{z} dz + i\pi f(0), \quad (3.6)$$

wherein P signifies the “principal value” of the, formally, divergent integral of $f(z)/z$.

Next, using Eqs. (3.2)-(3.4), we write:

$$i\mathbf{k} \cdot \mathbf{P} = -e^2 \delta \mathbf{E} \cdot \int \frac{\partial f_0}{\partial \mathbf{p}} \frac{1}{(\mathbf{k} \cdot \mathbf{v} - \Omega - i0)} d\mathbf{p}. \quad (3.7)$$

Consider a purely longitudinal mode, i.e. $\delta \mathbf{E} \parallel \mathbf{k}$. In this case, the dielectric tensor assumes a scalar value, ϵ_l . Thus, $4\pi\mathbf{P} = (\epsilon_l - 1)\mathbf{E}$. With these considerations, the scalar permittivity for a purely longitudinal “wave-mode” is (Lifshitz & Pitaevskii, 1981):

$$\epsilon_l = 1 - \frac{4\pi e^2}{k^2} \int \mathbf{k} \cdot \frac{\partial f_0}{\partial \mathbf{p}} \frac{1}{(\mathbf{k} \cdot \mathbf{v} - \Omega - i0)} d\mathbf{p}. \quad (3.8)$$

Next, we will interpret the complex nature of this expression.

3.2.1 Landau Damping

Let us examine the imaginary part of Eq. (3.8); using Eq. (3.6), we find (Lifshitz & Pitaevskii, 1981):

$$\Im[\epsilon_l] = -\frac{4\pi e^2}{k^2} \int \mathbf{k} \cdot \frac{\partial f_0}{\partial \mathbf{p}} \delta(\Omega - \mathbf{k} \cdot \mathbf{v}) d\mathbf{p}. \quad (3.9)$$

Choosing \mathbf{k} along the x -axis, we may write this as:

$$\Im[\epsilon_l] = -\frac{4\pi^2 e^2 m_e}{k^2} \left[\frac{df(p_x)}{dp_x} \right]_{v_x=\Omega/k}, \quad (3.10)$$

where $p_x = m_e v$ and

$$f(p_x) \equiv \int f(p_x, p_y, p_z) dp_y dp_z, \quad (3.11)$$

is the one-dimensional distribution function.

An imaginary permittivity implies dissipation, or the growth, of energy in the electric fluctuations. The mean energy loss per unit time, Q , experienced by a plane electric wave, \mathbf{E} , moving through an anisotropic medium is given by the general expression (Lifshitz & Pitaevskii, 1981):

$$Q = \frac{i\Omega}{16\pi} [\epsilon_{\beta\alpha}^*(\Omega, \mathbf{k}) - \epsilon_{\alpha\beta}(\Omega, \mathbf{k})] E_\alpha^* E_\beta. \quad (3.12)$$

If $\epsilon_{\alpha\beta}$ is symmetric, which it must be in this longitudinal case, then:

$$Q = \frac{\Omega}{8\pi} \Im[\epsilon_l] |\mathbf{E}|^2 = -|\mathbf{E}|^2 \frac{\pi m_e e^2 \Omega}{2k^2} \left[\frac{df(p_x)}{dp_x} \right]_{v_x=\Omega/k}. \quad (3.13)$$

It may be shown that $df(p_x)/dp_x = -2\pi p_x f(p_x^2)$, when the plasma is isotropic (Lifshitz & Pitaevskii, 1981). Consequently, Eq. (3.13) must always be positive, indicating a damping of the wave when the electron velocity is equal to the wave phase velocity, Ω/k . This dissipation, which happens even in collisionless media, is known as *Landau damping*.

Landau damping, naturally, works to stabilize the plasma by removing energy from longitudinal fluctuations. Interestingly, if the distribution is anisotropic, then $Q < 0$ is possible; a negative Q implies the growth of plasma waves. This is a recipe for plasma *instability*.

Intuitively, damping or growth of these longitudinal modes depends upon the relative velocity between the electrons and the waves. Much like a surfer on an ocean wave, if $v_x < \Omega/k$, then the electron gains energy from the wave. In contrast, if $v_x > \Omega/k$, then the electron losses energy to the wave. The relative abundance of these electron populations, faster or slower than the phase velocity, determines whether the effect, on the average, dissipates wave energy or grows it (Lifshitz & Pitaevskii, 1981).

In the next subsection, we will investigate the real part of the permittivity for a Maxwell-Boltzmann distribution of electrons.

3.2.2 Langmuir Oscillations

Assume a Maxwell-Boltzmann (Maxwellian) electron distribution in the x -direction:

$$f(p_x) = \frac{n_e}{(2\pi m_e k_B T_e)^{1/2}} \exp\left(-\frac{p_x^2}{2m_e k_B T_e}\right). \quad (3.14)$$

Substitution of this function into Eq. (3.8) gives the result (Lifshitz & Pitaevskii, 1981):

$$\epsilon_l(\Omega, k) = 1 + \frac{1}{(k\lambda_D)^2} \left[1 + F\left(\frac{\Omega}{\sqrt{2}kv_{T_e}}\right) \right], \quad (3.15)$$

where $v_{T_e} \equiv \sqrt{k_B T_e / m_e}$ is the electron *thermal speed* and the $F(x)$ is given by:

$$F(x) = \frac{x}{\sqrt{\pi}} \int_{-\infty}^{\infty} \frac{e^{-z^2}}{z - x - i0} dz. \quad (3.16)$$

With $\Omega/kv_{T_e} \gg 1$, it may be shown that (Lifshitz & Pitaevskii, 1981):

$$\epsilon_l = 1 - \frac{\omega_{pe}^2}{\Omega^2} \left(1 + \frac{3k^2 v_{T_e}^2}{\Omega^2} \right) + i\sqrt{\frac{\pi}{2}} \frac{\Omega \omega_{pe}^2}{(kv_{T_e})^3} \exp\left(-\frac{\Omega^2}{2k^2 v_{T_e}^2}\right), \quad (3.17)$$

where

$$\omega_{pe} \equiv v_{Te}/\lambda_D = \sqrt{4\pi n_e e^2/m_e}, \quad (3.18)$$

is the electron *plasma frequency* or *Langmuir frequency*. This is, in general, a very important plasma parameter – as we will see later.

The generalization of Eq. (3.15), accounting for the ion contribution, nicely meets our expectations; it is (Lifshitz & Pitaevskii, 1981):

$$\epsilon_l = 1 + \frac{1}{(k\lambda_D)^2} \left[1 + F \left(\frac{\Omega}{\sqrt{2}kv_{Te}} \right) \right] + \sum_s \frac{1}{(k\lambda_{Ds})^2} \left[1 + F \left(\frac{\Omega}{\sqrt{2}kv_{Ts}} \right) \right], \quad (3.19)$$

where $v_{Ts} \equiv \sqrt{k_B T_s / m_s}$, $\omega_{ps} \equiv \sqrt{4\pi n_s Z_s^2 e^2 / m_s}$, and $\lambda_{Ds} \equiv v_{Ts} / \omega_{ps}$.

Allowing $k \rightarrow 0$, Eq. (3.17) becomes simply: $\Omega \approx \omega_{pe}$ – note that we have used $\Re[\sqrt{\epsilon}] = n = kc/\Omega$, where n is the index of refraction. Thus, isotropic plasmas admit non-propagating longitudinal wave-modes; these are known as plasma oscillations or *Langmuir oscillations*. Incidentally, the same oscillations appear in the limit of $v_{Ts} \rightarrow 0$ – thus, the solution is also $\Omega \approx \omega_{pe}$ in the limit of negligible thermal speed. In Chapter 8, we will explore the motion of relativistic electrons moving through, so called, small-scale Langmuir turbulence with precisely this dispersion relation.

3.3 The Dielectric Properties of Magnetized Plasmas

When an “external” magnetic field, \mathbf{B}_0 , is introduced in a plasma, new degrees of freedom may appear. The plasma is, by construction, no longer isotropic, since the response of the plasma perpendicular and parallel to \mathbf{B}_0 may be different. We will now investigate the richness that this differential response entails.

3.3.1 The Motion of a Charge in an External Magnetic Field

To understand the plasma response, we examine the magnetic component of the Lorentz force equation; i.e., $\mathbf{v}/c \times \mathbf{B}_0$. If we write \mathbf{v} in terms of components perpendicular, \mathbf{v}_\perp , and parallel, \mathbf{v}_\parallel , to the magnetic field, then we immediately see the result of the magnetic Lorentz force on species, s :

$$\mathbf{F}_{\text{mag}} = Z_s e(\mathbf{v}_\perp + \mathbf{v}_\parallel) \times \mathbf{B}_0/c = Z_s e \mathbf{v}_\perp / c \times \mathbf{B}_0. \quad (3.20)$$

Hence, the parallel component of the velocity is unaltered by the magnetic field. The perpendicular velocity, however, is constantly acted upon. The cross product between the magnetic field and the perpendicular velocity indicates that the magnetic Lorentz force is perpendicular to both \mathbf{B}_0 and \mathbf{v}_\perp .

If \mathbf{B}_0 is uniform, then \mathbf{F}_{mag} will behave as a (perpendicular) centripetal force. The resulting trajectory is helical in shape, with an axis along the magnetic field. In the frame moving with \mathbf{v}_\parallel , the particle traces a circle. The radius of this circle, known as the *Larmor radius*, is a characteristic spatial scale. We obtain this length by equating the centripetal force with the magnetic Lorentz force, i.e.

$$\frac{m_s v_\perp^2}{r_L} = Z_s e v_\perp B_0 / c, \quad (3.21)$$

where $|\mathbf{v}_\perp| \equiv v_\perp$, $|\mathbf{B}_0| \equiv B_0$, and r_L is the Larmor radius. Thus,

$$r_L \equiv \frac{m_s v_\perp c}{Z_s e B_0}. \quad (3.22)$$

The corresponding *Larmor frequency* or *gyro-frequency* is:

$$\Omega_{\text{cs}} \equiv v_\perp / r_L = \frac{Z_s e B_0}{m_s c}. \quad (3.23)$$

It is noteworthy that the relativistic generalizations of these expressions is given by the substitution: $m_s \rightarrow \gamma_s m_s$ – where $\gamma_s \equiv 1/(1 - v^2/c^2)$ is the Lorentz “gamma” factor for species, s .

3.3.2 The “Linearized” Vlasov Solution for Magnetized Plasmas

Now that we understand the basic plasma response to \mathbf{B}_0 , we may discern the proper equilibrium distribution function, f_{s0} . The division of motions perpendicular and parallel to the external, or “ambient”, magnetic field suggest that:

$$f_{s0}(\mathbf{p}) = f_{s0}(p_\perp, p_\parallel). \quad (3.24)$$

Thus, assuming once more that the equilibrium distribution is slightly perturbed by $\delta f(\mathbf{r}, \mathbf{p}, t)$, the Boltzmann equation, for each species, simplifies to:

$$\frac{d(\delta f_s)}{dt} = \frac{\partial(\delta f_s)}{\partial t} + \frac{\partial(\delta f_s)}{\partial \mathbf{x}} \cdot \dot{\mathbf{x}} + eZ_s \left(\frac{\mathbf{v}}{c} \times \mathbf{B}_0 \right) \cdot \frac{\partial(\delta f_s)}{\partial \mathbf{p}} = -eZ_s \left[\delta \mathbf{E} + \frac{\mathbf{v}}{c} \times \delta \mathbf{B} \right] \cdot \frac{\partial f_{s0}}{\partial \mathbf{p}}. \quad (3.25)$$

Notice that since the initial distribution function is not isotropic, the magnetic terms are not zero. Thus, the magnetic field, and its perturbation, will influence the new distribution.

If we suppose that $\mathbf{B}_0 \gg \delta \mathbf{B}$, then the “unperturbed” motion of plasma particles will be characterized by the helical trajectories described in the previous section. Thus, we consider a new set of coordinates – \mathbf{r}' , \mathbf{v}' , and t' – defined by the solution to the “unperturbed” motion, i.e.

$$\frac{dv'}{dt'} = \frac{eZ_s}{m_s} \left(\frac{\mathbf{v}'}{c} \times \mathbf{B}_0 \right), \quad (3.26)$$

with $d\mathbf{r}'/dt' = \mathbf{v}'$. We may solve Eq. (3.25) by treating the problem in these new coordinates; in other words, by integrating along the path of the unperturbed particle “orbits”. Assuming that the perturbations grow from infinitesimally small values in the distant past,

the prescribed solution will have the form (Brambilla, 1998):

$$\delta f_s(\mathbf{r}, \mathbf{p}, t) = \int_{-\infty}^t \left[\delta \mathbf{E}(\mathbf{r}', t') + \frac{\mathbf{v}'}{c} \times \delta \mathbf{B}(\mathbf{r}', t') \right] \cdot \frac{\partial f_{s0}}{\partial \mathbf{p}'} dt', \quad (3.27)$$

where $\mathbf{r}'(t' = t) = \mathbf{r}$, $\mathbf{v}'(t' = t) = \mathbf{v}$, and $\mathbf{p}'(t' = t) = \mathbf{p}$.

The dielectric tensor for this magnetized plasma may be obtained by following a procedure similiar to that used in Section 3.2. Rather than repeat the cumbersome solution, we will merely report the result (Brambilla, 1998):

$$\epsilon_{ij}(\Omega, \mathbf{k}) = \delta_{ij} - \sum_s \frac{\Omega_{ps}^2}{\Omega^2} \int_0^\infty v_\perp dv_\perp \int_{-\infty}^\infty dv_\parallel \left[\sum_{n=-\infty}^\infty \frac{2\pi\Omega}{\Omega - n\Omega_{cs} - k_\parallel v_\parallel} Q_{ij}^{s,n}(v_\perp, v_\parallel, \mathbf{k}, \Omega) \right], \quad (3.28)$$

where \parallel and \perp refer to the directions parallel and perpendicular to \mathbf{B}_0 (respectively), and $Q_{ij}^{s,n}(v_\perp, v_\parallel, \mathbf{k}, \Omega)$ is a function of f_{s0} and its derivatives.

One noteworthy property of this tensor is that it satisfies the *Onsager symmetry relations*; which are (Brambilla, 1998):

$$\begin{cases} \epsilon_{xy} = -\epsilon_{yx}, \\ \epsilon_{xz} = \epsilon_{zx}, \\ \epsilon_{yz} = -\epsilon_{zy}. \end{cases} \quad (3.29)$$

These relations are an important feature of the limiting case of Eq. (3.28) called the *Cold Plasma Approximation* – which we will now address.

3.3.3 The “Cold” Plasma Approximation

For a Maxwellian plasma, two parameters characterize the dielectric tensor for a magnetized plasma. These are:

$$\begin{cases} \lambda_s = \frac{k_\perp^2 v_{Ts}^2}{2\Omega_{cs}^2} \\ x_{n,s} = \frac{\Omega - n\Omega_{cs}}{k_\parallel v_{Ts}}, \end{cases} \quad (3.30)$$

The “cold” plasma approximation assumes the limits to these parameters which occurs when $v_{Ts} \rightarrow 0$; that is, $\lambda_s \rightarrow 0$ and $|x_{n,s}| \rightarrow \infty$. Given these limits, the non-vanishing components of the dielectric tensor simplify to (Brambilla, 1998):

$$\begin{cases} \epsilon_{xx} = \epsilon_{yy} = S = \frac{1}{2}(R + L) \\ \epsilon_{xy} = -\epsilon_{yx} = -iD = \frac{1}{2i}(R - L), \\ \epsilon_{zz} = P, \end{cases} \quad (3.31)$$

where:

$$S = 1 - \sum_s \frac{\Omega_{ps}^2}{\Omega^2 - \Omega_{cs}^2}, \quad (3.32a)$$

$$D = \sum_s \frac{\Omega_{cs}}{\Omega} \frac{\Omega_{ps}^2}{\Omega^2 - \Omega_{cs}^2}, \quad (3.32b)$$

$$P = 1 - \sum_s \frac{\Omega_{ps}^2}{\Omega^2}, \quad (3.32c)$$

and where

$$L = 1 - \sum_s \frac{\Omega_{ps}^2}{\Omega^2} \frac{\Omega}{\Omega - \Omega_{cs}}, \quad (3.33a)$$

$$R = 1 - \sum_s \frac{\Omega_{ps}^2}{\Omega^2} \frac{\Omega}{\Omega + \Omega_{cs}}, \quad (3.33b)$$

signify the components corresponding to left- and right-circular polarizations of the electric field perpendicular to the magnetic field (these representations will prove useful in Chapter 7).

Next, we will consider a solution to these equations which we will make use of in Chapters 5 and 6.

3.3.4 Whistler-Mode Waves in Cold Plasmas

Consider a “cold”, magnetized, electron plasma in the frequency range:

$$\Omega_{ci} \ll \Omega_r \ll \Omega_{ce} \quad (3.34)$$

where Ω_{ci} is the gyro-frequency for ion species, i , Ω_r is the “real” wave frequency, and Ω_{ce} is the electron gyro-frequency. The inequality is understood to hold for all ion species. If, additionally, we assume that $\omega_{pe} \gg \Omega_{ce}$, then one possible solution to the cold plasma equations is given by (Sazhin, 1993):

$$\Omega_r(k) = \Omega_{ce} \frac{k^2 c^2}{k^2 c^2 + \omega_{pe}^2} \cos(\theta_k), \quad (3.35)$$

where $\theta_k \in (0, \pi/2)$, is the angle between the wave-vector, \mathbf{k} , and the ambient magnetic field, \mathbf{B}_0 . These wave-modes are known as *Whistler waves*.

Additionally, the equations specify the polarization of the wave-modes. Given obliquely (with respect to the ambient magnetic field) propagating whistler waves, the magnetic component will be right-circularly polarized with the following relations among its components (Sazhin, 1993)

$$\delta B_x = -\frac{1}{\tan(\theta_k)} \delta B_z = i \cos(\theta_k) \delta B_y, \quad (3.36)$$

where \mathbf{B}_0 is along the z -direction, and the wave-vector is in the x - z plane. Because the magnetic field is divergenceless, $\mathbf{k} \perp \delta\mathbf{B}$. Given these conditions, the magnetic field will rotate about the direction of the wave-vector.

Next, the Whistler electric field is (generally) elliptically polarized. It obeys the following relations (Sazhin, 1993; Verkhoglyadova et al., 2010) :

$$\begin{cases} E_x/E_y = -i\Theta_1 \\ E_z/E_x = \Theta_2, \end{cases} \quad (3.37)$$

where

$$\begin{cases} \Theta_1 \equiv \frac{k^2 c^2 \sin(\theta_k) \cos(\theta_k)}{\omega_{pe}^2 + k^2 c^2 \sin^2(\theta_k)} \\ \Theta_2 \equiv \frac{\Omega_r^2 \omega_{pe}^2 + (\Omega_r^2 - \Omega_{ce}^2) k^2 c^2}{\Omega_r \omega_{pe}^2 \Omega_{ce}}. \end{cases} \quad (3.38)$$

These equations suggest that the electric field parallel to the ambient magnetic field may be expressed in terms of the magnetic fluctuations via the relation (Sazhin, 1993):

$$E^{\parallel} = \frac{\Omega_r^2}{\Omega_{ce} k c} |\mathbf{B}| \tan(\theta_k). \quad (3.39)$$

With these equations, the wave pattern of a Whistler-like disturbance can be completely specified. As we will argue later, *electromagnetic turbulence* may be conceived as a superposition of various wave-modes with random relative phases and polarizations. Thus, we may construct a turbulent spectrum of Whistler waves by adding a large number of Whistler wave-modes – which are specified by their unique polarization and wave dispersion relation – with random wave-vectors and phases.

3.3.5 The Validity of the “Cold” Plasma Approximation

Since we rely heavily upon the cold plasma approximation throughout this work, we are beholden to justify its validity. As mentioned before, these are conditions sufficient for the proper application of the approximation:

$$\begin{cases} \frac{k_{\perp}^2 v_{Ts}^2}{\Omega_{cs}^2} \ll 1 \\ \left| \frac{\Omega - n \Omega_{cs}}{k_{\parallel} v_{Ts}} \right| \gg 1. \end{cases} \quad (3.40)$$

The meaning of the first condition will become clearer as we develop the notion of a “small-scale”, or “sub-Larmor-scale”, magnetic field. For now, we will only say that this condition implies magnetic fluctuations that are “super-Larmor-scale” (in the perpendicular plane) with respect to the “fluctuation-generating” population of plasma particles – since the condition is equivalent to $r_{L_{th.}}^2 k_{\perp}^2 \ll 1$, where $r_{L_{th.}} \equiv v_{Ts}/\Omega_{cs}$ is the “thermal” Larmor radius.

The last condition is more complicated, since n is any integer. Fortunately, the influence of terms with $|n| > 2$, when the first condition holds, are negligible – thus, we will only consider 0, 1, 2.

If $n = 0$, the condition (in part) implies that the wave phase velocity is much greater than the thermal speed, v_{T_s} . This condition is equivalent to the statement that the cold plasma approximation ignores *spatial dispersion*. Spatial dispersion refers to the dependence of the dielectric tensor on the spatial history of constituent plasma particles; i.e. it refers to the \mathbf{k} -dependence of $\epsilon_{\alpha\beta}$.

As we saw before with electrostatic (longitudinal) waves in isotropic plasmas, resonances can occur when the particle velocity is in phase with the wave. The same is true here, but additional resonances occur with $n = 1, 2$; this is because resonance effects between the gyration of the plasma particles and the waves is now possible (cyclotron resonance). Thus, the latter condition in Eq. (3.41) implies that an exponentially small number of plasma particles have velocities comparable to any “wave-particle resonance” velocities (Brambilla, 1998). This suggests that wave-particle energy exchange is negligible.

Despite these, more obvious, conditions for valid usage of the cold plasma approximation, there exists another set for frequencies higher than the gyro-frequency. These are (Brambilla, 1998):

$$\left\{ \begin{array}{l} \frac{k_\perp v_{T_s}}{\Omega_{cs}} \gg 1, \\ \frac{\Omega}{k_\perp v_{T_s}} \gg 1, \\ \frac{\Omega}{k_\parallel v_{T_s}} \gg 1. \end{array} \right. \quad (3.41)$$

The latter two conditions, as before, ensure that spatial dispersion is negligible. The first, on the other hand, implies quite the opposite condition as presumed before. With $r_{L_{th.}} k_\perp \gg 1$, the plasma particles move in a manner that is largely unresponsive to the magnetic field. In this sense, we say that plasma particles which satisfy this condition are “unmagnetized” or “weakly magnetized”. In fact, these plasma particles are sub-Larmor-scale with respect to the magnetic field. As we will see later, these particles do respond to the magnetic field –

but it is in a manner which is very distinct from the basic gyro-motions of old.

3.4 Weibel-like Instabilities

It is clear from our initial discussion of Debye shielding, and later Laudau damping, that plasmas largely resist the creation of electric fields on electron spatial scales. Magnetic fields, on the other hand, are not so easily removed. But the question remains: how are plasmas magnetized in the first place?

Although there are a number different mechanisms for creating and/or strengthening pre-existing magnetic fields in plasmas (e.g. turbulent dynamos), *Weibel-like instabilities* will be the principal focus of this work. For this reason, we will discuss the creation of “Weibel-like” magnetic fields next.

3.4.1 The “Classic” Weibel Instability

In 1959, Weibel proposed a novel mechanism for generating “transverse”, self-excited, electron-driven, wave-modes in anisotropic plasmas. This is analogous to the self-excitation of longitudinal modes in isotropic plasmas that we saw earlier, and the procedure for identifying them is very similar. As before, we first turn our attention to the linearized Boltzmann Equation, Eq. (3.25).

Next, Weibel supposed plane wave solutions in all fluctuating variables, and used Maxwell’s equations to eliminate $\delta\mathbf{B}$. The result of this procedure was (Weibel, 1959):

$$i(\Omega + \mathbf{k} \cdot \mathbf{v})\delta f - \frac{e\mathbf{B}_0}{m_e c} \cdot \left[\mathbf{v} \times \frac{\partial(\delta f)}{\partial \mathbf{v}} \right] = -\frac{e}{m_e \Omega} \left[\Omega \mathbf{E}_{\mathbf{k},\Omega} \cdot \frac{\partial f_0}{\partial \mathbf{v}} + (\mathbf{k} \times \mathbf{E}_{\mathbf{k},\Omega}) \cdot \left(\mathbf{v} \times \frac{\partial f_0}{\partial \mathbf{v}} \right) \right], \quad (3.42)$$

where $\mathbf{v} = \mathbf{p}/m_e$ and $\mathbf{E}_{\mathbf{k},\Omega}$ is the component of $\delta\mathbf{E}$ with frequency, Ω , and wave-number, \mathbf{k} .

The essential term in Eq. (3.42) is: $(\mathbf{k} \times \mathbf{E}_{\mathbf{k},\Omega}) \cdot (\mathbf{v} \times \partial f_0 / \partial \mathbf{v})$. The cross product between the wave-vector and the electric field, in essence, selects transverse electric modes (i.e. modes

perpendicular to \mathbf{k}). Thus, quite independently of \mathbf{B}_0 , these modes exist if $\mathbf{v} \times \partial f_0 / \partial \mathbf{v}$ is non-zero.

Weibel then selected a distribution of the form:

$$f_0(\mathbf{v}) = f(v_0, v_z), \quad (3.43)$$

where $v_0 = \sqrt{v_x^2 + v_y^2}$, and both \mathbf{B}_0 and \mathbf{k} are along the z -direction. Additionally, the electric field was chosen to be purely transverse – i.e. $\mathbf{E}_{\mathbf{k},\Omega} \perp \mathbf{k}$.

Under these conditions, Weibel obtained the general dispersion relation (Weibel, 1959):

$$k^2 c^2 - \Omega^2 = \frac{\pi e^2 c}{m_e} \int_0^\infty v_0^2 dv_0 \int_{-\infty}^\infty dv_z \frac{(\Omega + kv_z) \partial f_0 / \partial v_0 - v_0 k \partial f_0 / \partial v_z}{(\Omega + kv_z) \pm (eB_0/m_e c)}. \quad (3.44)$$

Suppose an initial distribution with an anisotropic temperature profile, namely:

$$f_0 = \frac{n_e}{v_{T_0}^2 v_{T_z} (2\pi)^{3/2}} \exp \left[- \left(\frac{v_0^2}{2v_{T_0}^2} + \frac{v_z^2}{2v_{T_z}^2} \right) \right], \quad (3.45)$$

where $v_{T_0}^2 \equiv k_B T_{e0}/m_e$ and $v_{T_z}^2 \equiv k_B T_{ez}/m_e$ are the thermal speeds in the perpendicular plane and parallel direction, respectively. The solution to Eq. (3.44) for this distribution is given by (Weibel, 1959):

$$k^2 c^2 - \Omega^2 = \omega_{pe}^2 \left[A - \left(A \frac{\Omega \pm \Omega_{ce}}{v_{T_z} k} + \frac{\Omega}{v_{T_z} k} \right) \phi \left(\frac{\Omega \pm \Omega_{ce}}{v_{T_z} k} \right) \right], \quad (3.46)$$

where:

$$\phi(z) = \exp \left(\frac{1}{2} z^2 \right) \int_{-i\infty}^z \exp \left(\frac{1}{2} \psi^2 \right) d\psi, \quad (3.47)$$

and $A = (v_{T_0}/v_{T_z})^2 - 1$. In the limit that spatial dispersion may be ignored in the z -direction,

i.e. $v_{T_z} \ll \Omega/k^1$, there exists a $B_0 = 0$ solution (Weibel, 1959):

$$\Omega = -\sqrt{\frac{1}{2} \left[\omega_{pe}^2 + k^2 c^2 - \left((\omega_{pe}^2 + k^2 c^2)^2 + 4v_{T_0}^2 \omega_{pe}^2 k^2 \right)^{1/2} \right]}, \quad (3.48)$$

such that Ω is purely imaginary, and negative; which is more apparent in the approximation:

$$\Omega \approx -i \frac{v_{T_0} k}{(1 + k^2 d_e^2)^{1/2}}, \quad (3.49)$$

where $d_e \equiv c/\omega_{pe}$ is the electron *skin-depth*. Thus, Eq. (3.49) implies the growth of transverse wave-modes with zero real frequency (i.e. $\Omega_r = 0$).

Via Faraday's law, i.e.

$$i\mathbf{k} \times \mathbf{E}_{\mathbf{k},\Omega} = -i\Omega \mathbf{B}_{\mathbf{k},\Omega}/c, \quad (3.50)$$

we know that magnetic modes must, also, exist here. Using Eq. (3.49), we can express the ratio of the electric and magnetic fields as:

$$\frac{|\mathbf{E}_{\mathbf{k},\Omega}|^2}{|\mathbf{B}_{\mathbf{k},\Omega}|^2} \approx \frac{v_{T_0}^2/c^2}{1 + k^2 d_e^2}. \quad (3.51)$$

The thermal speed, $v_{T_0} \ll c$ – since we are considering the non-relativistic regime. Thus, $|\mathbf{B}_{\mathbf{k},\Omega}|^2 \gg |\mathbf{E}_{\mathbf{k},\Omega}|^2$. Therefore, the Weibel instability, via a temperature anisotropy, can grow magnetic fluctuations spontaneously. Next, we will explore the generalizations of the Weibel instability.

3.4.2 Generalizations of the Weibel Instability

In the same year that Weibel wrote his seminal paper, Fried (Fried, 1959) proposed an alternative – yet analogous – mechanism for generating spontaneous magnetic fields in, previously, unmagnetized media. This *Weibel-Filamentation instability*, as it may be called, offers an

¹This condition implies that $v_{T_0} \gg v_{T_z}$.

attractive mechanism for the mediation of collisionless shocks – both in the laboratory and astrophysical settings.

Consider counter-streaming electrons moving across a fixed ion background with an initial seed magnetic field in the plane perpendicular to the streaming particles. The seed field (which may be imagined, for simplicity, as sinusoidal) reinforces the tenuous streaming particle “filaments” by way of the Lorentz force (see Figure 3.1). These larger filaments then proceed to grow the initial magnetic perturbation, which then increases the current density of the filaments, which grows the magnetic field, and so on. The magnetic field can acquire great strength by way of the Weibel-Filamentation instability. Saturation will occur when the transverse deflections of the particles become too large to support their free streaming. This occurs when the electrons become trapped by the field, i.e. when $kr_L \sim 1$. The relativistic Weibel instability may undergo saturation later in a non-linear stage of development in which the current filaments coalesce (Medvedev et al., 2006); eventually, the ions may participate as well (Medvedev & Loeb, 1999).

Referring back to Eq. (3.49), if $k d_e \gg 1$, then $\Omega \sim (v_{T_0}/c)\omega_{pe}$. Remarkably, by selecting an appropriate anisotropic electron distribution, this (maximum) growth rate is retained for the relativistic regime, with the substitution $\omega_{pe} \rightarrow \omega_{pe}/\sqrt{\gamma_e}$ – where γ_e is the electron lorentz factor (Yoon & Davidson, 1987). Similarly, the maximum fluctuation wave-number, k_{max} , is indicated by the skin-depth. The relativistic expression for k_{max} is given by (Yoon & Davidson, 1987):

$$k_{max} \sim \frac{\omega_{pe}}{\sqrt{\gamma_e} c} (1 - v_{\perp}^2/c^2)^{1/4}, \quad (3.52)$$

where \perp refers to the plane hosting the initial magnetic perturbation, i.e. the plane perpendicular to the particle streaming direction. This result assumes that $p_{\parallel} \gg p_{\perp}$. Consequently, $k_{max} \sim d_e^{-1}/\sqrt{\gamma_e}$ – which is the relativistic skin-depth.

Finally, the instability’s saturation condition, $kr_L \sim 1$, suggests that the Weibel magnetic fields contain fluctuations on sub-Larmor-scales.

(Medvedev & Loeb, 1999, ApJ)

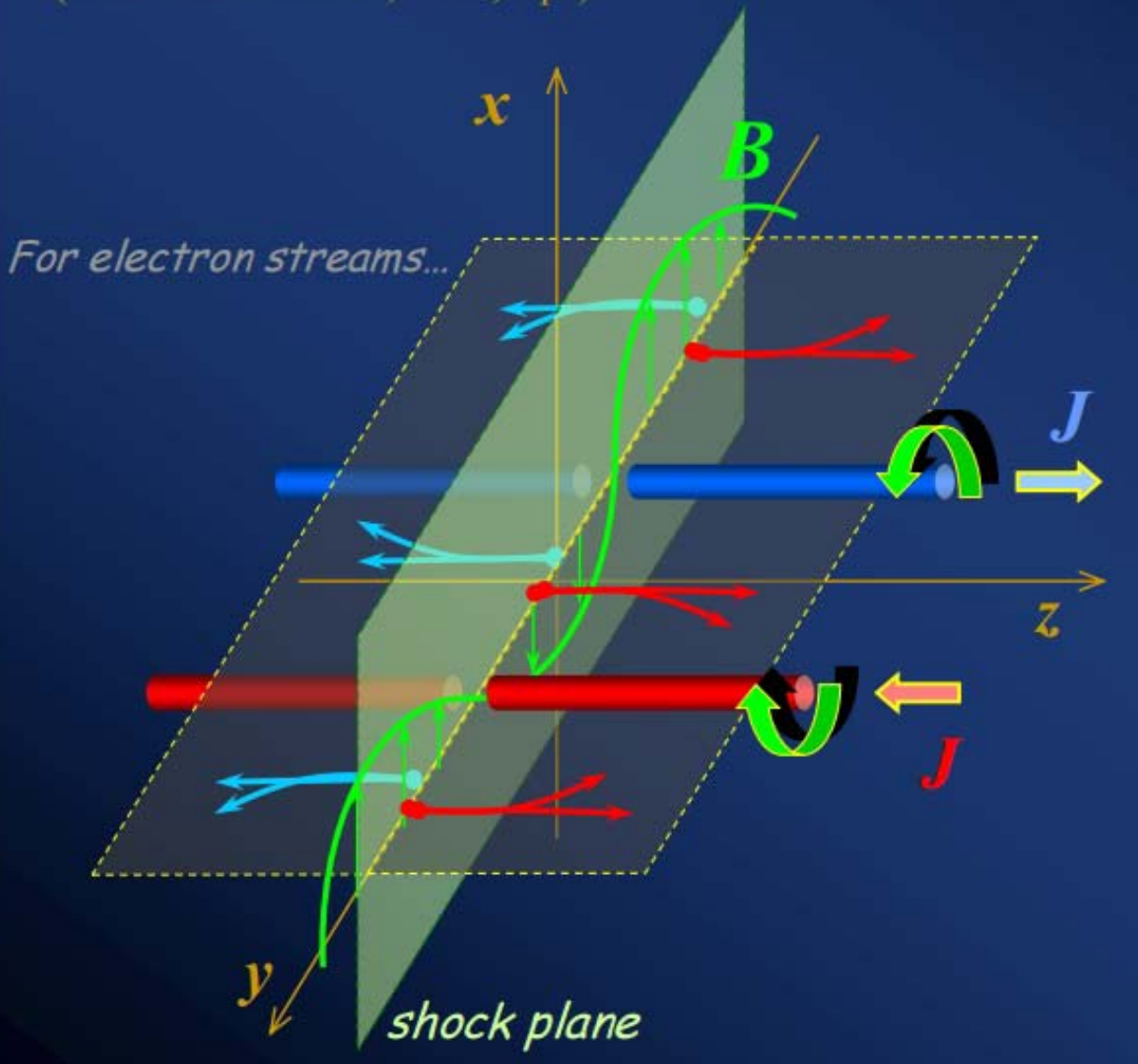


Figure 3.1: Image adapted from: http://www.icra.it/MG/mg12/talks/anm8_medvedev.pdf. Counter-streaming currents pass through the plane with an initial magnetic perturbation.

3.4.3 Weibel-like Instabilities in Real Plasmas

Environments where the formation of Weibel-like instabilities is very favorable include Gamma-ray bursts, relativistic pulsar winds, supernovae shocks, sites of magnetic reconnection, relativistic jets from quasars, plasmas generated via high-intensity lasers, and many more. All these diverse HED environments share a propensity for the development of spontaneous magnetic fields. The generation and evolution of the Weibel instability has been studied extensively with particle-in-cell (PIC) codes which agree very closely with theory. An example of the complicated magnetic fields that emerge from the Weibel instability can be seen in Figure 3.2. This plot, obtained from Medvedev, Silva, Kamionkowski (Medvedev et al., 2006), shows the three-dimensional structure of the self-generated magnetic field that originates from the saturated non-relativistic Weibel instability. PIC simulations additionally reveal, in confirmation of the theory first developed by Medvedev & Loeb, the role of the Weibel instability in collisionless relativistic shocks – like those believed to be created in gamma-ray burst (GRB) events. These shocks are “collisionless” because the scale of the shock system is much smaller than the coulomb mean-free-path. As Figure 3.2 indicates, the structure of the Weibel generated magnetic field is quite random. Indeed, since the initial perturbation (seed) field is random – since it is the product of random thermal fluctuations – Weibel magnetic fields are, also, very random. In fact, these fields are *turbulent*.

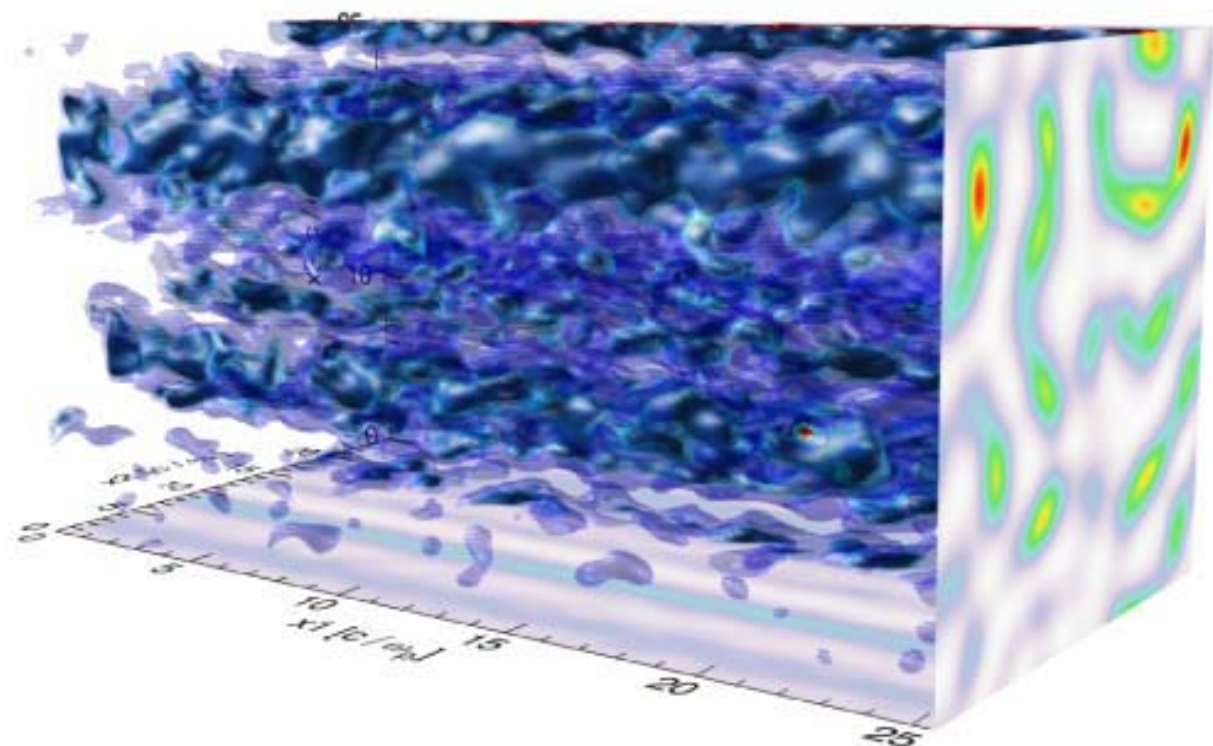


Figure 3.2: The magnetic field of the non-relativistic Weibel instability at saturation (with periodic boundary conditions). The energy density of the field is indicated by the blue iso-surfaces. The magnitude of B^2 along the x_1 -direction is the x_2 - x_3 -plane projection. Peaks in B^2 are indicated with red.

3.5 The Meaning of Turbulence

Turbulence in fluids may be conceived as a state in which the collective degrees of freedom of constituent particles are random and strongly excited (Tsytovich, 1977). The key feature of turbulence, which distinguishes it from regular random fluid fluctuations, is this stipulation that the degrees of freedom are strongly excited – i.e. the energy possessed in these fluctuations must be well above their average statistical equilibrium values. The macroscopic identifiers of the state of a turbulent fluid are sensitive to the initial conditions of these particles – thus, fluid turbulence is directly related to the chaotic trajectories of individual fluid particles.

The concept of turbulence may be generalized to include plasmas. *Magnetohydrodynamics* (MHD) is an approach to plasmas which treats them, essentially, as fluids. Of course, this picture is complicated by the existence of the electromagnetic nature of plasmas; for this reason, MHD fluids include a richer variety of phenomena than “neutral” fluids. In fact, MHD turbulence is two-fold. The plasma fluid, itself, may assume a turbulent configuration, and the electromagnetic fields in the plasma – as they are often “tied” to individual fluid elements in this approximation – will be turbulent as well.

As we saw in the previous section, however, random magnetic and electric fluctuations are possible in plasmas that are not themselves turbulent. Random magnetic fields produced by the Weibel instability, for example, are random of their own accord. Furthermore, this form of turbulence is distinct from MHD turbulence, since the MHD approximation breaks down on spatial scales comparable to the skin-depth (which is the characteristic domain of Weibel magnetic fields). We will refer to these realizations of *electromagnetic turbulence* as *kinetic-scale turbulence*. They will be the principal focus of this work.

The mathematical description of turbulence, nonetheless, is largely the same for kinetic-scale, MHD, etc. One useful statistical quantity, which we will use extensively, is the *two-point Autocorrelation Tensor*.

3.5.1 The Two-Point Autocorrelation Tensor

Turbulent fields are only random at some characteristic spatial and temporal scales. This is evident by the simple fact that turbulent motions are maintained by discrete, non-continuous, particles. Thus, there exists some correlation between field points in turbulent electromagnetic fields.

Let us consider a random magnetic field, $\delta\mathbf{B}$. We define a two-point autocorrelation tensor:

$$R^{ij}(\mathbf{r}, t) \equiv \langle \delta B^i(\mathbf{x}, \tau) \delta B^j(\mathbf{x} + \mathbf{r}, \tau + t) \rangle_{\mathbf{x}, \tau}. \quad (3.53)$$

Essentially, this quantity specifies the degree of correlation between the magnetic field at (\mathbf{r}, t) and all other field points. Spatially, the correlation will, largely, be zero beyond a characteristic length, which we call the *correlation length*. We formally define the path and time-dependent “correlation length tensor” as:

$$\lambda_B^{ij}(\hat{\mathbf{r}}, t) \equiv \int_0^\infty \frac{R^{ij}(\mathbf{r}, t)}{R^{ij}(0, 0)} dr. \quad (3.54)$$

Note that we make no distinction between co-variant and contra-variant components; the usage of upper and lower indices is only for convenience.

To evaluate Eq. (3.54), we must consider the physics involved. In magnetic deflections, only the component of the magnetic field transverse to the particle velocity is involved in the acceleration. Thus, for magnetic fields, we only consider fields transverse to the direction of motion. In contrast, electric fields will have a “longitudinal” and “transverse” correlation length. The former is important for energy diffusion – whereas, the latter governs pitch-angle diffusion, since transverse deflections do no work.

Since only the component of the magnetic field perpendicular to the particle trajectory alters the motion, we may choose an integration path along \mathbf{v}_\perp and only consider a transverse magnetic field component. In accord with standard practice (Batchelor, 1982), we choose

$\mathbf{r} = z\hat{\mathbf{z}}$ and $i = j = x$. Thus, we define the magnetic field correlation length as:

$$\lambda_B \equiv \lambda_B^{xx}(\hat{\mathbf{z}}, t) = \int_0^\infty \frac{R^{xx}(z\hat{\mathbf{z}}, t)}{R^{xx}(0, 0)} dz. \quad (3.55)$$

The correlation length has a convenient representation in Fourier “ k -space” and “ Ω -space”.

Let $\mathbf{B}_{\mathbf{k}, \Omega}$ be the spatial and temporal Fourier transform of the magnetic field, i.e.

$$\mathbf{B}_{\mathbf{k}, \Omega} = \int \mathbf{B}(\mathbf{x}, t) e^{-i(\mathbf{k} \cdot \mathbf{x} - \Omega t)} d\mathbf{x} dt, \quad (3.56)$$

where \mathbf{k} and Ω are the corresponding wave vector and frequency, respectively. We may define a complementary spectral correlation tensor $\Phi_{ij}(\mathbf{k}, \Omega)$, such that:

$$R_{ij}(\mathbf{r}, t) = (2\pi)^{-4} \int \Phi_{ij}(\mathbf{k}, \Omega) e^{i\mathbf{k} \cdot \mathbf{r} - i\Omega t} d\mathbf{k} d\Omega, \quad (3.57)$$

We will assume isotropy, homogeneity, and time-independence. In this case, the spectral correlation tensor may only be constructed from the isotropic tensor, δ_{ij} , and the components of the wave-vector, \mathbf{k} (rotational invariance). Thus, the only tensor structure that meets these requirements is:

$$\Phi_{ij} \propto \left[\left(\delta_{ij} - \hat{k}_i \hat{k}_j \right) |\mathbf{B}_k^t|^2 + \hat{k}_i \hat{k}_j |\mathbf{B}_k^l|^2 \right], \quad (3.58)$$

where $|\mathbf{B}_k^t|^2$ and $|\mathbf{B}_k^l|^2$ are the transverse and longitudinal components of the magnetic spectrum, respectively. Since the magnetic field is divergenceless, $|\mathbf{B}_k^l|^2 = 0$; thus, $|\mathbf{B}_k|^2 = |\mathbf{B}_k^t|^2$. The spectral correlation tensor must then be of the form (Tsytovich, 1977):

$$\Phi_{ij}(\mathbf{k}, \Omega) = \frac{1}{2V} |\mathbf{B}_k|^2 \left(\delta_{ij} - \hat{k}_i \hat{k}_j \right) 2\pi\delta(\Omega), \quad (3.59)$$

where V is the volume of the space considered and $\hat{\mathbf{k}}$ is the unit vector in the direction of the wave vector. The normalization has been chosen such that $\sum R_{ii}(0, 0) = \langle B^2 \rangle_{\mathbf{x}, \tau} = \langle B^2 \rangle$.

Given Eq. (3.57) and Eq. (3.59), the correlation length may be reformulated as:

$$\lambda_B = \int_0^\infty \frac{\int |\mathbf{B}_k|^2 k^{-2} (k^2 - k_x^2) e^{ik_z z} d\mathbf{k}}{\int |\mathbf{B}_k|^2 k^{-2} (k^2 - k_x^2) d\mathbf{k}} dz. \quad (3.60)$$

By assuming isotropic turbulence, the magnetic field has azimuthal and polar symmetry in k -space, hence \mathbf{B}_k is only a function of $|\mathbf{k}| \equiv k$. After the integration over z and all solid-angles in Fourier space, Eq. (3.60) becomes:

$$\lambda_B = \frac{3\pi}{8} \frac{\int_0^\infty k |\mathbf{B}_k|^2 dk}{\int_0^\infty k^2 |\mathbf{B}_k|^2 dk}. \quad (3.61)$$

It may be noted that $\lambda_B \approx k_B^{-1}$, where k_B is the characteristic (dominant) wave number of turbulence.

For much of this work, we will assume isotropic three-dimensional magnetic turbulence that is a static, i.e. time-independent, power-law turbulent spectrum of the form:

$$\begin{cases} |\delta \mathbf{B}_k|^2 = C k^{-\mu}, & k_{min} \leq k \leq k_{max} \\ |\delta \mathbf{B}_k|^2 = 0, & \text{otherwise} \end{cases} \quad (3.62)$$

Here the magnetic spectral index, μ is a real number, and

$$C \equiv \frac{2\pi^2 V \langle \delta B^2 \rangle}{\int_{k_{min}}^{k_{max}} k^{-\mu+2} dk}, \quad (3.63)$$

is a normalization, such that:

$$V^{-1} \int \delta \mathbf{B}^2(\mathbf{x}) d\mathbf{x} = (2\pi)^{-3} \int |\delta \mathbf{B}_k|^2 d\mathbf{k}. \quad (3.64)$$

In physically realistic settings, anisotropy will likely be present. Thus, the applicability of an isotropic power-law may, rightfully, be questioned. Nevertheless, we assume isotropy for simplicity. The comparison between our theoretical and numerical results is aided by

this choice, since the analytical expressions for anisotropic distributions are generally very complicated.

In the next Chapter, we will discuss the simulation of electron “test” particles moving through magnetic turbulence – specified by the spectral distribution, Eq. (3.62).

Chapter 4

The Simulation of Test Particle Dynamics in Small-Scale Electromagnetic Turbulence

4.1 Overview

Our goal was to explore, via simulations of particle dynamics in electromagnetic turbulence, the diffusive and radiative properties of plasmas with small-scale electromagnetic fluctuations, and how these phenomena are connected. Our approach was from first-principles. Electrons were test particles moving in preset electromagnetic fields, and they did not interact with each other, nor did they induce any fields. Radiative energy losses were considered negligible compared to the energies of individual particles. Motion of each electron was, thus, solely determined by the Lorentz force equation, which we express here as:

$$\frac{d\beta}{dt} = -\frac{1}{\gamma_e} [\Omega_E + \beta \times \Omega_B - \beta (\beta \cdot \Omega_E)]. \quad (4.1)$$

where $\gamma_e \equiv (1 - \beta^2)^{-1/2}$ is the electron's Lorentz factor, and $\beta \equiv \mathbf{v}/c$ is the dimensionless particle velocity. The quantities $\Omega_B \equiv e\mathbf{B}/m_ec$ and $\Omega_E \equiv e\mathbf{E}/m_ec$ are the “normalized”

magnetic and electric fields, respectively. For simplicity, we defined our simulation fields as $\mathbf{B} \equiv \boldsymbol{\Omega}_B$ and $\mathbf{E} \equiv \boldsymbol{\Omega}_E$. In this manner, our arbitrary simulation units were always related to physical fields via these definitions.

4.2 The Numerical Generation of the Electromagnetic Field

Our principal assumption, in generating electromagnetic turbulence, was that these stochastic electromagnetic fields are the linear superposition of a large number of wave-modes with randomized propagation direction and relative phase. Given this assumption, we can construct the turbulent fields directly from the plasma waves characteristic of the underlying instability. In general, the properties of these electromagnetic wave-modes, and their dispersion relation, are derived from the plasma dielectric tensor – the determinant, of which, provides a system of characteristic equations.

4.2.1 Generating the Fields: Lattice Approach

The first approach starts with the spectral distribution in Fourier space. We first considered purely magnetic fields. We began with a 3-dimensional lattice of points over a box of finite length (these will then form the identical “cubes” that fill the “infinitely” sized box used in the simulation). Given this constraint, the representable wave numbers of the magnetic field range anywhere from $2\pi/L_{\text{box}}$ to the Nyquist frequency. Furthermore, to ensure that the magnetic field obeys Gauss’s Law, we applied the Gram-Schmidt process to each \mathbf{k} , \mathbf{B}_k pair. Next, each \mathbf{B}_k was oriented in a random direction, and then multiplied by a random phase factor. The inverse Fourier transform of \mathbf{B}_k ought to yield a purely real \mathbf{B} -field; for this reason, we imposed field “hermiticity”. Finally, the field was normalized to fit a predefined spectral distribution, and we performed the inverse Fast Fourier Transform (FFT) on the lattice of points.

The field lattice was interpolated, as needed, so that a “continuous” field may be represented. The interpolation was implemented by way of divergenceless matrix-valued radial basis functions (McNally, 2011). This method begins with a radial function – in our case, one of the simplest, $\phi(\mathbf{r}) = e^{-\epsilon r^2}$ (where ϵ is a scaling factor, and $r^2 = x^2 + y^2 + z^2$). Then, a set of divergence-free matrix-valued radial basis functions was obtained from the transformation (McNally, 2011):

$$\Phi(\mathbf{r}) = (\nabla \nabla^T - \mathbb{I}_{3 \times 3} \nabla^2) \phi(\mathbf{r}), \quad (4.2)$$

where $\nabla \nabla^T$ is the second-order, 3×3 -matrix differential operator and $\mathbb{I}_{3 \times 3}$ is the 3×3 identity matrix. These interpolants were applied to the interior of each lattice “cube” (i.e. the space between a single lattice point and the five immediately adjacent points). The end results was a numerical representation of the magnetic field for each point in space.

4.2.2 Generating the Fields: Continuous Wave Approach

The lattice approach is not feasible for the general case of electromagnetic turbulence, since the fields may vary in time. An alternative generation of the electromagnetic field – which is grid-less and, therefore, not requiring interpolation – employs a large sum of sinusoidal wave modes which are evaluated at each time step (as needed). Thus, the electromagnetic field is effectively “continuous” in this representation. Each wave mode is constructed with a random phase and an appropriate polarization vector (e.g. one that occupies the plane transverse to \mathbf{k} , for magnetic fields). Concerning purely isotropic magnetic turbulence, the polarization vector may be generated by a variety of methods, but we chose the implementation described by Tautz (Tautz & Dosch, 2013). This representation of the polarization vectors is designed specifically to simultaneously satisfy the required properties of isotropic, homogeneous, and divergence-free magnetic turbulence. Lastly, the wave-numbers, ranging from k_{\min} to k_{\max} , were logarithmically spaced.

In Appendix B, we compare the lattice and continuous methods for the case of the pure

magnetic turbulence. We find that the continuous approach is superior; we suspect that this is likely due to computational limitations.

Nevertheless, there is a computational price to pay for the use of this approach. Whereas the lattice field may be generated only once, this “sum” approach must be applied for every time-step. Hence, the computational complexity – for solving the equation of motion for each particle – is $\sim \mathcal{O}(N_m N_{\text{steps}})$, where N_{steps} is the number of time-steps and N_m is the number of wave-modes applied. Fortunately, the summation is trivially parallelizable; hence, our parallelized code ran fairly quickly on a multi-core machine.

4.3 Calculating the Radiation Spectrum

The next stage in the simulation was the numerical solution of the equation of motion, Eq. (4.1). This was done via a fixed step 4th-order Runge-Kutta-Nyström method, or a (symplectic) 2nd-order Boris method. In our test runs, we found little variation between these two methods – barring numerical instability due to using an insufficiently small step-size in time. This is likely because our simulation time was limited by actual computational time, and thus, we were unable to realize the slow accumulation of errors in the total energy characteristic of non-symplectic numerical integrators.

With all the particle positions, velocities, and accelerations calculated, the radiation spectrum (which is the radiative spectral energy, dW per unit frequency, $d\omega$, and per unit solid-angle, $d\eta$) seen by a distant observer is obtained from the equation (Landau & Lifshitz, 1975; Jackson, 1998):

$$\frac{d^2W}{d\omega d\eta} = \frac{e^2}{4\pi^2 c} \left| \int_{-\infty}^{\infty} \mathbf{A}_{\kappa}(t) e^{i\omega t} dt \right|^2, \quad (4.3)$$

where

$$\mathbf{A}_{\kappa}(t) \equiv \frac{\hat{\mathbf{n}} \times [(\hat{\mathbf{n}} - \boldsymbol{\beta}) \times \dot{\boldsymbol{\beta}}]}{(1 - \hat{\mathbf{n}} \cdot \boldsymbol{\beta})^2} e^{-i\kappa \cdot \mathbf{r}(t)}. \quad (4.4)$$

In this equation, $\mathbf{r}(t)$ is the particle’s position at the retarded time t , $\kappa \equiv \hat{\mathbf{n}}\omega/c$ is the wave

vector which points along $\hat{\mathbf{n}}$ from $\mathbf{r}(t)$ to the observer and $\dot{\beta} \equiv d\beta/dt$. Since the observer is assumed to be distant, $\hat{\mathbf{n}}$ is approximated as fixed in time to the origin of the coordinate system.

Next, the total radiation spectrum is obtained by “summing” over the spectra of the individual particles. For the moment, we will only consider mean-free, small-scale magnetic turbulence in the following discussion.

Given an isotropically distributed (in velocity-space) ensemble of electrons, the “summed” spectrum will be equivalent to the angle-averaged, i.e. $dW/d\omega$, spectrum for a single electron. There are two, usually equivalent, methods for doing this “summation”. First, one may add the spectra coherently by summing over each particle’s \mathbf{A}_κ , and then performing a single integration via Eq. (4.3). This method is more physical. Alternatively, we may add the spectra incoherently (i.e., by integrating each particle’s \mathbf{A}_κ separately, and then summing the results of each integration). As discussed in (Hedeland, 2005), both methods will result in the same spectra, since the wave phases are uncorrelated. However, an incoherent sum will produce a spectrum that is less noisy (for a given number of simulation particles) than the coherently summed spectrum. For this reason, we employed the incoherent approach.

Lastly, the simulation run time was largely dominated by this integration, since it was performed directly (i.e. via a Riemann sum) over many time-steps. This means that the runtime scales roughly as $\sim \mathcal{O}(N_{\text{step}}^2)$. Since the particle runs are decoupled from each other, the total runtime also scaled as $\sim \mathcal{O}(N_p)$, where N_p is the number of particles.

4.4 Initial Tests

Our initial (lattice) code for pure magnetic turbulence was tested in various set-ups. In one, we considered motion of a single relativistic particle in a uniform magnetic field. Figure 4.1 shows the obtained radiation spectrum and the corresponding theoretical synchrotron spectrum. Here, the blue curve represents the numerically resolved synchrotron harmonics

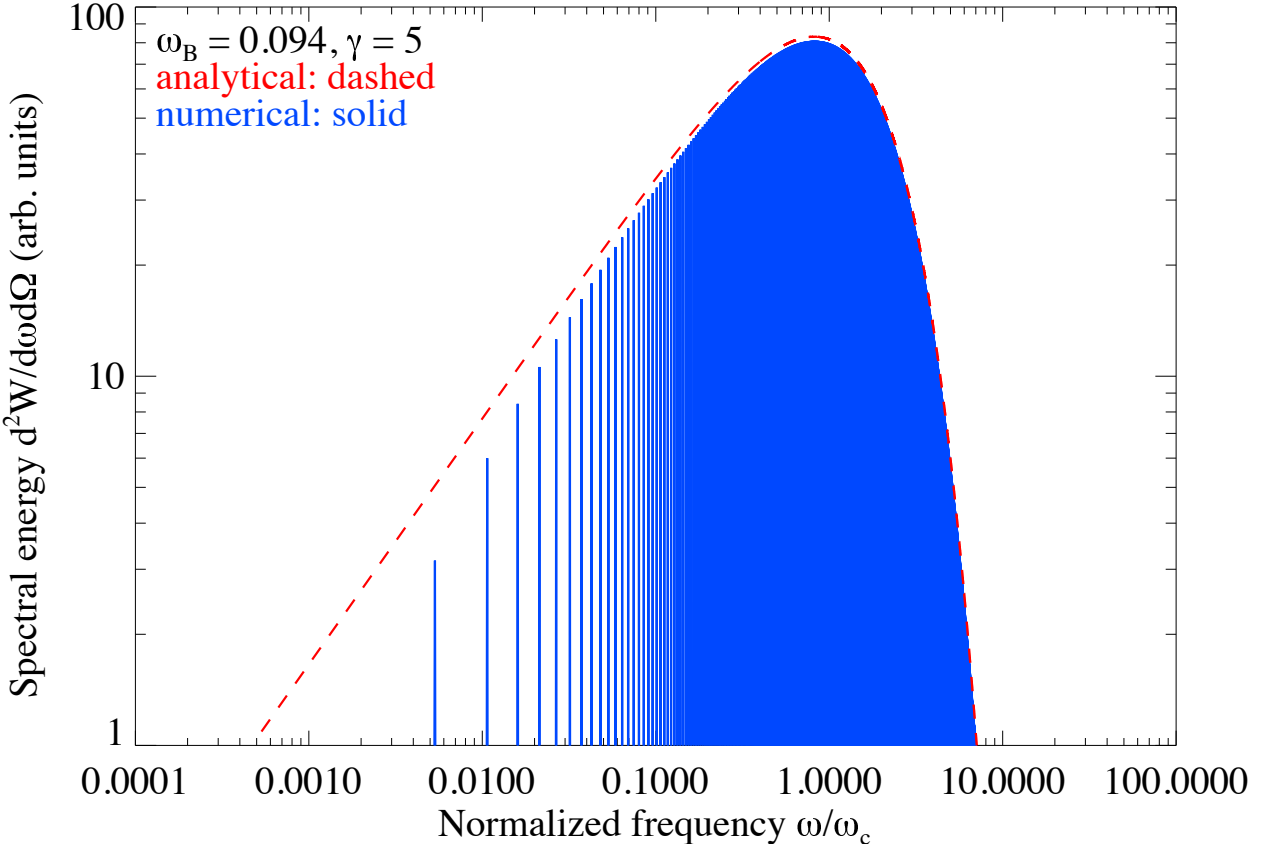


Figure 4.1: Radiation spectrum (i.e., the total radiated energy, dW per unit solid angle, $d\Omega$ per unit frequency, $d\omega$) of a single relativistic charge moving through a uniform magnetic field. The total simulation time was $10T_g$, where $T_g = 2\pi/\omega_B$ is the gyroperiod. The numerical solution is indicated in blue, the red line is the analytical solution, and they agree very well. The spectrum is peaked at the synchrotron frequency $\omega_c = (3/2)\gamma_e^2\omega_B$, where $\omega_B = eB_\perp/\gamma_e m_e c$ is the electron gyrfrequency. In this and other spectral plots, the radiation power is arbitrarily normalized.

(which are integer multiples of the gyrfrequency, $\omega_B = eB_\perp/\gamma_e m_e c$). We see excellent agreement with the analytical result, indicated in red.

Finally, we also verified that motion of a particle in small-scale random magnetic fields is chaotic. This is illustrated in Figure 4.2. Here, 50 monoenergetic ($\gamma_e = 3$) particles are sent out from an origin in random directions. The variability in the particle motion is seen after shortly leaving the origin. The diffusive nature of the particle motion is evident from Figure 4.3. In Figure 4.3, the velocity space of a single relativistic particle ($\gamma_e = 5$) is plotted over a very large simulation time. Notice that the particle velocity is confined to a sphere (i.e.,

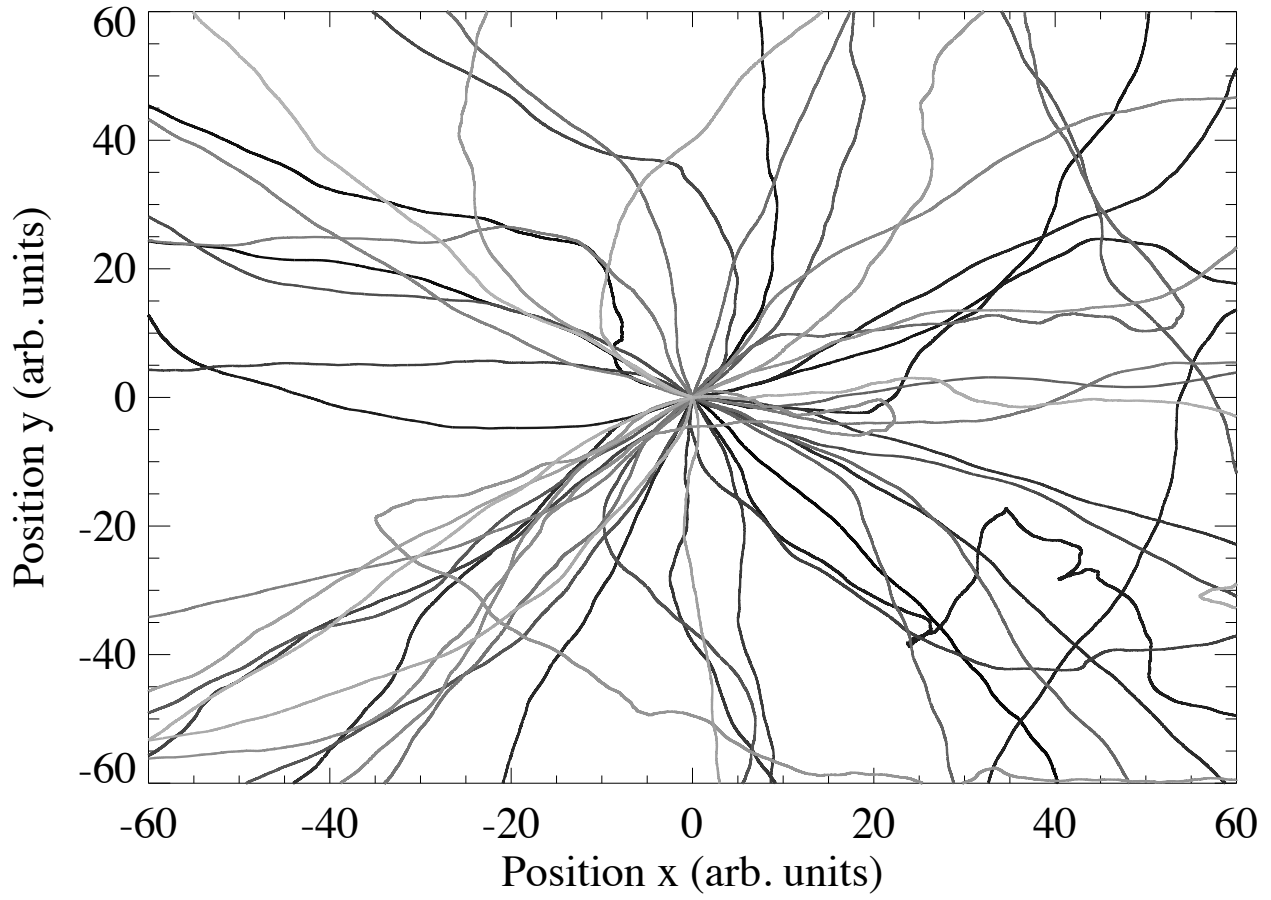


Figure 4.2: The trajectories of 50 monoenergetic ($\gamma_e = 3$) particles through a turbulent magnetic field projected on to the x - y plane. Each particle (denoted by 50 shades of gray) starts from an origin with a random initial velocity. The axes are x and y positions in arbitrary simulation units.

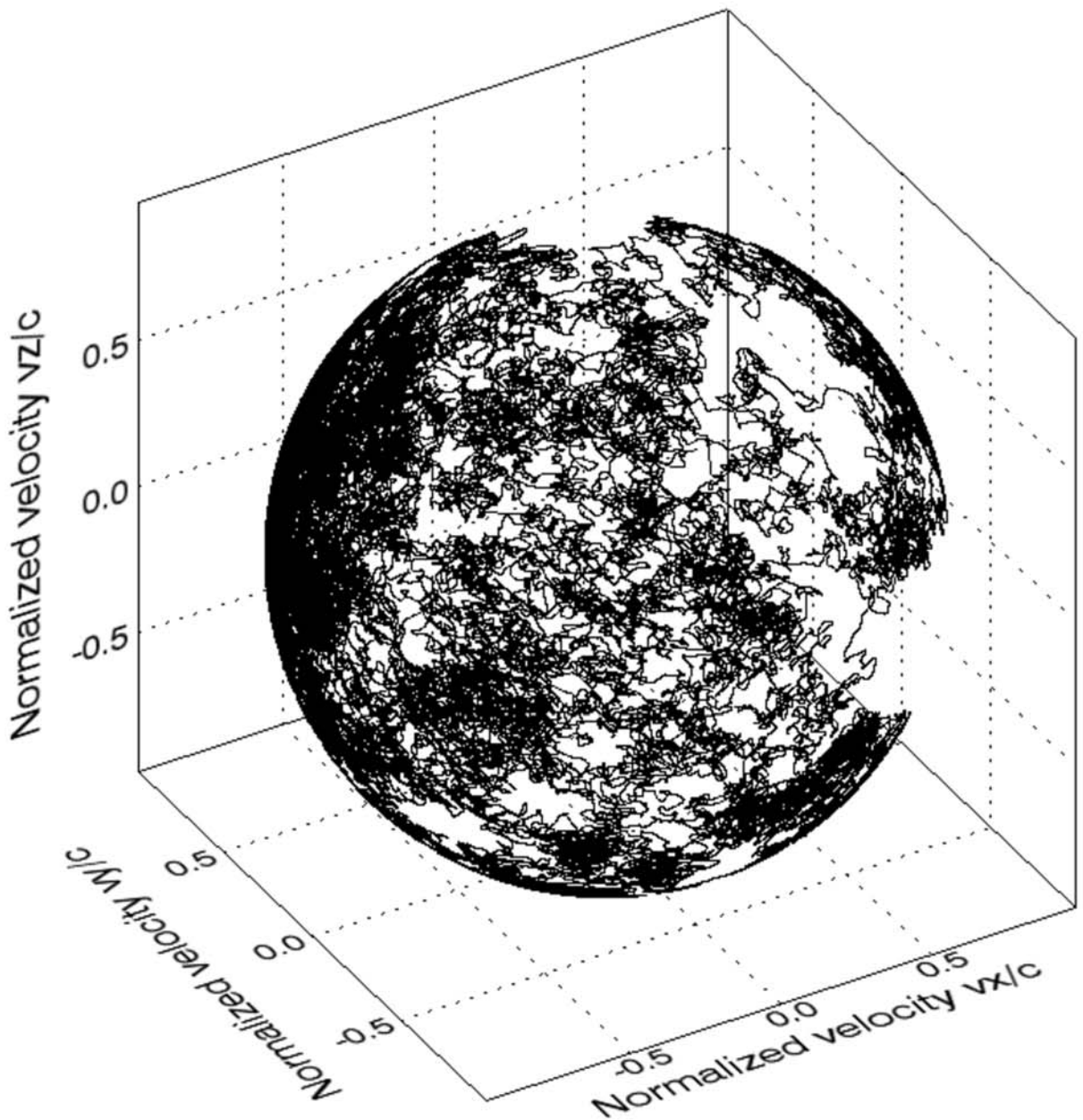


Figure 4.3: Velocity space of a single particle ($\gamma_e = 5$) moving through isotropic magnetic turbulence. The axes are the components of the velocity, which are in units of c . Notice that, although the velocity vector of the particle varies randomly (and, over enough time, visits all possible directions), its magnitude is constant.

γ_e is constant), and that the velocity vector diffusively visits various directions in the course of the particle's motion.

Chapter 5

Transport Properties of Small-Scale Electromagnetic Turbulence

5.1 Introduction

In this Chapter, we develop the first-principle transport theory for charge particles moving through small-scale magnetic and electric turbulence. Specifically, we derive the (small-scale) pitch-angle and energy diffusion coefficients, and test them against our simulation results.

5.2 Analytic Theory

Consider a test particle (electron) moving through a non-uniform, random magnetic field with velocity, \mathbf{v} . Assume that the magnetic field has the mean value, $\langle \mathbf{B} \rangle$, where $\langle \cdot \rangle$ is an appropriately chosen average over space and, possibly, time. Consequently, we write the total random magnetic field as:

$$\mathbf{B}(\mathbf{x}, t) = \mathbf{B}_0 + \delta\mathbf{B}(\mathbf{x}, t), \quad (5.1)$$

where $\mathbf{B}_0 \equiv \langle \mathbf{B} \rangle$ is the mean field and $\delta\mathbf{B}(\mathbf{x}, t)$ is the mean-free “fluctuation” field, that is $\langle \delta\mathbf{B} \rangle = 0$ but $\delta B \equiv \langle \delta B^2 \rangle^{1/2} \neq 0$.

Next, the motion of an electron in a random magnetic field is, in general, very complicated. It is the spatial scale of inhomogeneity, i.e., the correlation length of the field fluctuation, that fundamentally determines the dynamics. These magnetic fluctuations are deemed sub-Larmor-scale (or “small-scale”) when the electron’s *fluctuation* Larmor radius, $r_L \equiv \gamma\beta m_e c^2 / e\delta B$ (where $\beta = v/c$ is the dimensionless particle velocity, m_e is the electron mass, c is the speed of light, e is the electric charge, and γ is the electron’s Lorentz factor) is greater than, or comparable to, the correlation length of the field, λ_B , i.e., $r_L \gtrsim \lambda_B$. We introduce the “gyro-number”, which fully characterizes the small-scale regime, follows as:

$$\rho \equiv r_L \lambda_B^{-1}. \quad (5.2)$$

Notice that we are considering only the *fluctuation* component of the magnetic field, $\delta\mathbf{B}$. This is because the motion can be separated into two components: the regular gyro-motion about the mean magnetic field, and the random deflections due to the small-scale random component. In the discussion to follow, we will presuppose that $\rho \gg 1$.

Next, because the *fluctuation* Lorentz force on the electron is random, the electron velocity and acceleration vectors vary stochastically, leading to a random (diffusive) trajectory. Additionally, the magnetic Lorentz force acts only upon the component of velocity transverse to the local magnetic field, leading only to energy-conserving (i.e., $\beta = \text{constant}$) deflections. Only an electric field can change the particle energy. When this electric field is random, transport via energy diffusion may occur – we will explore this later.

This picture is, of course, only correct if any present electric fields are ignored. Electric turbulence, likewise, can induce transport via pitch-angle diffusion – as we will show later. However, the contribution to the total transport due to electric fields in small-scale Whistler turbulence, specifically, is negligible.

Ignoring, for the moment, the presence of any electric fields: the electron motion has two limiting regimes – depending upon the relative strength of the magnetic fluctuations with respect to the mean field. These are a “straight line” trajectory with random (transverse) deflections (i.e., $\delta\mathbf{B} \gg \mathbf{B}_0$), and a slightly “perturbed” helical motion about the mean magnetic field (i.e., $\delta\mathbf{B} \ll \mathbf{B}_0$). In the latter case, we will ignore the regular component of the motion. Doing so allows us to consider only the transport in mean-free, small-scale, magnetic turbulence.

5.2.1 Pitch-Angle Diffusion in Small-Scale Magnetic Turbulence

For small deflections, the deflection angle of the velocity (with respect to the particle’s initial direction of motion) is approximately the ratio of the change in the electron’s transverse momentum to its initial transverse momentum. The former is $\sim F_L \tau_\lambda$, where $\mathbf{F}_L = (e/c) \mathbf{v} \times \delta\mathbf{B}$ is the transverse Lorentz force, and τ_λ is the transit time, which is the time required to traverse the scale of the field’s inhomogeneity, i.e., the field correlation length, λ_B . This is, $\tau_\lambda \sim \lambda_B / v_\perp$ – where v_\perp is the component of the velocity perpendicular to the magnetic field. The change in the transverse momentum is thus, $\Delta p_\perp \sim F_L \tau_\lambda \sim e(\delta B/c)\lambda_B$. Given that the particle’s total transverse momentum is $p_\perp \sim \gamma_e m_e v_\perp$, the deflection angle over the field correlation length will be $\alpha_\lambda \approx \Delta p_\perp / p_\perp \sim e(\delta B/c)\lambda_B / \gamma_e m_e v_\perp$. The subsequent deflection will be in a random direction, because the field is uncorrelated over scales greater than λ_B , hence the particle motion is diffusive. As for any diffusive process, the ensemble-averaged squared deviation grows linearly with time. Hence, for the pitch-angle deviation, we have:

$$\langle \alpha^2 \rangle = D_{\alpha\alpha} t. \quad (5.3)$$

The pitch-angle diffusion coefficient is, by definition, the ratio of the square of the deflection angle in a coherent patch to the transit time over this patch, that is:

$$D_{\alpha\alpha} \sim \frac{\alpha_\lambda^2}{\tau_\lambda} \sim \left(\frac{e^2}{m_e^2 c^3} \right) \frac{1}{\langle \beta_\perp^2 \rangle^{1/2}} \frac{\lambda_B}{\gamma_e^2} \langle \delta B^2 \rangle, \quad (5.4)$$

$\langle \delta B^2 \rangle$ and the perpendicular rms velocity, $\langle \beta_\perp^2 \rangle^{1/2}$, have been substituted for δB^2 and $\beta_\perp \equiv v_\perp/c$, respectively. Note that the diffusion coefficient depends on both statistical properties of the magnetic field, namely its strength and the typical correlation scale.

Although the assumption that $\alpha_\lambda \ll 1$ is certainly valid in the ultra-relativistic limit, it is not evident that it holds for trans-relativistic and non-relativistic velocities. As we demonstrated via numerical simulation, pitch-angle diffusion does occur in accordance with Eq. (5.4), so long as the magnetic turbulence is sub-Larmor-scale, i.e. $r_L \gtrsim \lambda_B$.

The average square fluctuation magnetic field, $\langle \delta B^2 \rangle$ is related to $\langle \delta B_\perp^2 \rangle$ by a multiplicative factor. For isotropic magnetic turbulence, $\langle \delta B_x^2 \rangle = \langle \delta B_y^2 \rangle = \langle \delta B_z^2 \rangle$. Thus, $\frac{1}{3}\langle \delta B^2 \rangle = \langle \delta B_x^2 \rangle$. Alternatively, $\delta \mathbf{B}$ may be expressed as a linear combination of parallel and perpendicular components. Given isotropy, $\langle \delta B_\perp^2 \rangle = \langle \delta B_x^2 \rangle + \langle \delta B_y^2 \rangle$, so

$$\langle \delta B_\perp^2 \rangle = \frac{2}{3} \langle \delta B^2 \rangle. \quad (5.5)$$

Recognizing that $v_\perp \delta B = v \delta B_\perp$ allows the expression of the rms perpendicular velocity as

$$\langle \beta_\perp^2 \rangle^{1/2} = \sqrt{\frac{2}{3}} \beta, \quad (5.6)$$

Next, the correlation length, λ_B is obtained from Eq. (3.61) – which follows from the two-point auto-correlation tensor. Thus, with Eqs. (5.4), (5.6), and (3.61), the pitch-angle diffusion coefficient is

$$D_{\alpha\alpha} \equiv \frac{3\pi}{8} \sqrt{\frac{3}{2}} \left(\frac{e^2}{m_e^2 c^3} \right) \frac{\int_0^\infty k |\delta \mathbf{B}_k|^2 dk}{\int_0^\infty k^2 |\delta \mathbf{B}_k|^2 dk} \frac{\langle \delta B^2 \rangle}{\gamma_e^2 \beta}. \quad (5.7)$$

To continue, we must specify a magnetic spectral distribution. To this end, we will choose

the simple isotropic power-law given by Eq. (3.62).

It is worth mentioning that statistically isotropic magnetic turbulence has a single correlation length, for all directions. Anisotropy in the fluctuation field, on the other hand, would induce a path-dependent correlation length. Thus, the diffusion coefficient along an axis of anisotropy (which is usually demarcated by the direction of the mean magnetic field, \mathbf{B}_0) may differ from that across the transverse plane.

However, since our magnetic turbulence is assumed to be statistically homogeneous and isotropic, the pitch-angle diffusion coefficient will be the same along all directions; thus, we may arbitrary define the axis of the deflection angle, α . Without loss of generality, therefore, we may define α in conventional terms as the angle of the velocity vector with respect to the mean (ambient) magnetic field, \mathbf{B}_0 .

Lastly, we have assumed that all relevant time-scales (e.g., the time to transit λ_B) are much smaller than the magnetic field variability time-scale — thus, the magnetic turbulence may be considered in the static approximation. For this reason, we may safely ignore any time-dependence in the correlation length, and therefore in $D_{\alpha\alpha}$.

5.2.2 Pitch-Angle Diffusion in Small-Scale Electric Turbulence

The derivation for pitch-angle diffusion in general small-scale electric turbulence follows in a similar fashion. Suppose an electron test particle is moving, with speed v , through an external random electric field. This may be an electrostatic field (i.e., Langmuir-like turbulence), or – as in the more general case – it may be the electric component of electromagnetic turbulence (e.g. Whistler-mode turbulence). We will assume that the electric field fluctuates very slowly – such that the particle dynamics, on relevant time-scales, are largely unaffected by the field’s time-variability. Furthermore, we will ignore any present magnetic fields – for the moment.

For “small-scale” turbulence, the principal time-scale which governs particle transport is the time to transit a single electric field correlation length, λ_E^t – where the “ t ” superscript indicates that the correlation length is specified along the path with a “transverse” component

of the electric field (which we did with the magnetic field). If the (pitch-angle) transit time, $\tau_E^t \sim \lambda_E^t/v$, is much less than the field-variability time-scale, Ω^{-1} , then we may treat the electric field as approximately time-independent.

To proceed, it will be instructive to first discuss the radiation produced by an electron moving through an external random field. First, regardless of the acceleration mechanism, the radiation of an ultrarelativistic electron will be beamed along a narrow cone with opening angle, $\Delta\theta \sim 1/\gamma$. In a random electromagnetic field, the acceleration occurs principally along the extent of a correlation length. Since the electron is moving ultrarelativistically, it will undergo a slight deflection, $\delta\alpha_E$, as it traverses a correlation length. If $\delta\alpha_E \ll \Delta\theta$, then the electron will move approximately rectilinearly, undergoing only slight random deflections along its path; the radiation will then be beamed along the extent of the electron's relatively fixed direction of motion. Consequently, an observer on axis would see a signal for the entire trajectory of the electron. Furthermore, the radiation spectrum will be wholly determined by the statistical properties of the underlying acceleration mechanism (Landau & Lifshitz, 1975). When the acceleration mechanism is a random (static) magnetic field, the electron emits radiation in the small-angle jitter regime (Medvedev, 2000, 2006; Medvedev et al., 2011; Reville & Kirk, 2010; Teraki & Takahara, 2011; Keenan & Medvedev, 2013). The radiation produced by ultrarelativistic electrons moving through electrostatic turbulence, in this small deflection angle regime, is nearly identical – which has lead to its designation as a subclass of small-angle jitter radiation (Teraki & Takahara, 2014).

We have previously shown that these random deflections initiate pitch-angle diffusion in sub-Larmor-scale magnetic turbulence, and that this diffusion coefficient is intimately related to the radiation spectrum. We expect that an electric field analog of this diffusion exists for the (small-angle) jitter regime in small-scale electric turbulence. Here, we consider an

electric field as “small-scale”, with respect to the test electrons, if:

$$\Omega^{-1} \gg \tau_E^t, \quad (5.8a)$$

$$\Delta\theta \gg \delta\alpha_E. \quad (5.8b)$$

Since the electron is moving ultrarelativistically, the component of its acceleration transverse to its direction of motion will be far larger than the longitudinal component. Thus, its motion occupies the small deflection angle regime – which is the reason its radiation spectrum resembles the jitter spectrum. Additionally, transverse accelerations leave the particle’s kinetic energy fixed. For this reason, we will assume a constant v .

Next, since the deflections are small, $\delta\alpha_E \sim \Delta p_t/p$ – as previously noted for magnetic deflections. Since $\Delta p_t/\tau_E^t \sim eE_t$, where E_t is the component of the electric field perpendicular (transverse) to the electron’s direction of motion, $\Delta p_t/p \sim eE_t/\gamma m_e v$; thus:

$$\delta\alpha_E \sim \frac{eE_t}{\gamma m_e v} \tau_E^t. \quad (5.9)$$

Consequently, the electric diffusion coefficient must be:

$$D_{\alpha\alpha}^{\text{elec.}} \sim \delta\alpha_E^2/\tau_E^t \sim \frac{e^2 E_t^2}{\gamma^2 m_e^2 v^2} \left(\frac{\lambda_E^t}{v} \right). \quad (5.10)$$

Finally, the exact numerical coefficients depend upon the statistical properties of the turbulent fluctuations. Given statistically isotropic and homogeneous turbulence, $\langle E_t^2 \rangle = \frac{2}{3} \langle E^2 \rangle$. Thus, the diffusion coefficient follows as:

$$D_{\alpha\alpha}^{\text{elec.}} = \frac{2}{3} \frac{\lambda_E^t}{\gamma^2 c \beta^3} \langle \Omega_E^2 \rangle, \quad (5.11)$$

where:

$$\Omega_E \equiv eE/m_e c. \quad (5.12)$$

When a magnetic field is introduced, the (small-scale) pitch-angle diffusion coefficient will be the sum of the magnetic and electric components – i.e. Eq. (5.11) and Eq. (5.7).

As we mentioned previously, and will demonstrate later, the electric pitch-angle diffusion is negligibly small compared to the magnetic equivalent in small-scale Whistler-mode turbulence. For this reason, the electric contribution to the radiation production is, also, insignificant. Nonetheless, the electric field will still uniquely affect the particle motion via energy diffusion.

5.2.3 Energy Diffusion in Small-Scale Electric Turbulence

All electromagnetic turbulence results from instabilities, dynamo-action, etc. with some finite growth rate. So long as the growth (or dissipation) time-scale is much greater than the correlation length transit time, we can ignore the time-dependence of the magnetic field in our model.

In contrast to Weibel magnetic fields in (initially) unmagnetized plasmas, however, MHD/kinetic instabilities – which require an ambient magnetic field – may grow random fields with non-negligible real frequency, Ω_r . That is to say, these magnetic fields will possess oscillating wave-modes, whose time-dependence may not be completely ignored. The Faraday-induced electric fields, \mathbf{E} , may influence the particle motion on relevant time-scales, e.g., the gyro-period time-scale in the regular (ambient) magnetic field.

These random electric fields may induce transport via energy diffusion. Although diffusive energy transport in electromagnetic turbulence has long been a topic of investigation (Stix, 1992), energy diffusion in strictly sub-Larmor-scale electromagnetic fields has yet to be – to the best of our knowledge – explored. This topic has proved to be richly complicated, so we have limited ourselves to a particularly simple regime.

Furthermore, we emphasize that the “energy” diffusion coefficient – rather than the “velocity-space” analog – is a more useful quantity for our purposes. Although it possesses a number of favorable properties, its prominent feature is that it is directly proportional to the elec-

tric field's correlation length. This feature is not present in the “velocity-space” coefficient, however.

Next, we must consider the time-scales involved. There are two such characteristic time-scales: the “acceleration” time, τ_E^l and the electric field “auto-correlation” time, τ_{ac} . The latter time-scale characterizes the temporal inhomogeneity of the electric field. Diffusive (energy) transport may arise not only from spatial stochasticity in the electric field but temporal randomness as well.

The former quantity, τ_E^l , characterizes the spatial stochasticity. This is the time required to transit an electric field correlation length, λ_E^l – with the “ l ” superscript indicating the “longitudinal” transit time; i.e. the time required to transverse a “longitudinal” electric correlation length, λ_E^l , which is along the direction of motion. Assuming that $a_\lambda \tau_E^l \ll v_E$, where a_λ is the acceleration over λ_E^l , and v_E is the component of the electron velocity parallel to the electric field, the transit time is:

$$\tau_E^l \sim \frac{\lambda_E^l}{v_E}. \quad (5.13)$$

While transiting a single correlation length, the electron is subject to a nearly uniform electric field. These “accelerations” are uncorrelated on a spatial-scale dictated by the electric field correlation length.

The diffusion regime we will explore will consider the “spatial” diffusion to be the dominant process, i.e.,

$$\tau_E^l \ll \tau_{ac}. \quad (5.14)$$

Furthermore, to ensure that the energy change is random on the time-scale of consideration, we require that:

$$\tau_E^l \ll t. \quad (5.15)$$

Next, an equation for the electron energy, W_e , may be obtained directly from the Lorentz Force Equation of Motion. It is:

$$\frac{dW_e}{dt} = e(\mathbf{v} \cdot \mathbf{E}). \quad (5.16)$$

Since the electron energy changes over the characteristic time-scale, τ_E^l , we may write:

$$\frac{\Delta W_\lambda}{\tau_E^l} \sim ev_E E. \quad (5.17)$$

If the random process is, indeed, diffusive:

$$D_{WW} \equiv \frac{\langle W_e^2 \rangle}{t}. \quad (5.18)$$

Thus:

$$D_{WW} \sim \frac{(\Delta W_\lambda)^2}{\tau_E^l} \sim e^2 v_E E^2 \lambda_E^l, \quad (5.19)$$

where we have used Eq. (5.13). With the usual assumptions of statistical homogeneity/isotropy and an initially mono-energetic distribution of electrons, we may write the energy diffusion coefficient, thusly:

$$D_{WW} = \sqrt{\frac{1}{3}} e^2 \langle E^2 \rangle v \lambda_E^l. \quad (5.20)$$

This result may be contrasted with the “temporal”, i.e. *resonant*, energy diffusion coefficient. The physics of this type of diffusion may be understood by considering the, so called, “Quasilinear” energy diffusion coefficient. As before, we will consider only small corrections to the electron’s initial velocity – hence, we will assume the zero-order trajectory:

$$\mathbf{r}(t) = \mathbf{v}t + \mathbf{r}_0, \quad (5.21)$$

where \mathbf{r}_0 is the electron’s initial position. Let us suppose that the electric field assumes a simple sinusoidal profile, i.e.

$$\mathbf{E}(\mathbf{x}, t) = \mathbf{E}_0 \cos(\mathbf{k} \cdot \mathbf{x} - \Omega t). \quad (5.22)$$

Thus, using Eqs. (5.16) and (5.22), we have:

$$\frac{dW_e}{dt} = e(\mathbf{v} \cdot \mathbf{E}_0) \cos(\mathbf{k} \cdot \mathbf{v}t + \mathbf{k} \cdot \mathbf{r}_0 - \Omega t). \quad (5.23)$$

Integrating Eq. (5.23), averaging over all possible initial positions, and squaring the result, gives the energy variance:

$$\langle \Delta W_e^2 \rangle = \left[\frac{e(\mathbf{v} \cdot \mathbf{E}_0)}{(\Omega - \mathbf{k} \cdot \mathbf{v})} \right]^2 \sin^2 \left[\frac{(\Omega - \mathbf{k} \cdot \mathbf{v})t}{2} \right]. \quad (5.24)$$

Finally, with $\Omega t \gg 1$, we may employ the relation (Stix, 1992):

$$\sin^2 \left[\frac{(\Omega - \mathbf{k} \cdot \mathbf{v})t}{2} \right] \sim \pi \delta(\Omega - \mathbf{k} \cdot \mathbf{v}), \quad (5.25)$$

Thus the (Quasilinear) diffusion coefficient is:

$$D_{WW}^{\text{res.}} \equiv \frac{\langle \Delta W_e^2 \rangle}{t} \sim \pi \left[\frac{e(\mathbf{v} \cdot \mathbf{E}_0)}{(\Omega - \mathbf{k} \cdot \mathbf{v})} \right]^2 \delta(\Omega - \mathbf{k} \cdot \mathbf{v}). \quad (5.26)$$

In general, turbulence will contain a spectrum of waves; hence, an integration of Eq. (5.26) over $|\mathbf{E}_{\mathbf{k},\Omega}|^2$ is required to produce the complete diffusion equation.

Nevertheless, much can be gathered by examining the functional form of this simplified expression. For example, owing to the dependence on the quantity, $\delta(\Omega - \mathbf{k} \cdot \mathbf{v})$, only particles that are in resonance with the wave participate in the diffusive process.

Moreover, since $\Omega t \gg 1$, this “temporal” diffusion process occurs on a much greater time-scale than τ_E^l (when the electric field is small-scale). For this reason, the non-resonant energy diffusion coefficient – Eq. (5.19) – is much greater than the resonant equivalent – at least, for the “small-scale” population of electrons.

As an important side note, the “Quasilinear” diffusion equation derived here applies for non-magnetized plasmas. When an ambient magnetic field, \mathbf{B}_0 , is present, the “resonance”

condition generalizes to (Stix, 1992):

$$\Omega - k_{\parallel} v_{\parallel} = n \Omega_{ce} / \gamma, \quad (5.27)$$

where $\Omega_{ce} \equiv eB_0/m_e c$ is the non-relativistic gyro-frequency, the “parallel” direction is along the ambient (mean) magnetic field, and n is an integer. This result, we may expect, follows from the relativistic generalization of the denominator term in Eq. (3.28) – which establishes the resonance condition for the “hot” dielectric tensor in a magnetized plasma.

As we mentioned previously, electrons moving through electromagnetic turbulence are not “magnetized” – in the formal sense – with respect to the “small-scale” fluctuation fields. Hence, the small-scale fields do not contribute to the higher-order (magnetic) resonances – such as the Cherenkov resonance at $n = 1$. Thus, with regard to the “small-scale” sub-population of electrons, we may disregard resonant diffusion in general.

Finally, to evaluate the (non-resonant) energy diffusion coefficient – Eq. (5.20) – we need an expression for the electric field, $\langle E^2 \rangle$, and its “longitudinal” correlation length, λ_E^l . To this end, we must relate the electric field to the underlying magnetic turbulence that produces it, i.e., we need to specify the wave turbulence dispersion relation, $\Omega_r(\mathbf{k})$.

In general, this may be done via the dielectric tensor, $\overset{\leftrightarrow}{\epsilon}_{\mathbf{k},\Omega}$. Using Ampère’s law, and the definition of the dielectric tensor, we write (Brambilla, 1998):

$$\mathbf{k} \times \delta \mathbf{B}_{\mathbf{k},\Omega} = -\frac{\Omega}{c} \overset{\leftrightarrow}{\epsilon}_{\mathbf{k},\Omega} \cdot \mathbf{E}_{\mathbf{k},\Omega}. \quad (5.28)$$

Suppressing the time-dependence in the field amplitudes, i.e. ignoring wave growth/damping, the electric spectral distribution may be expressed as:

$$|\mathbf{E}_{\mathbf{k}}|^2 = \left| \overset{\leftrightarrow}{\epsilon}_{\mathbf{k},\Omega}^{-1} \cdot \hat{b}_{\mathbf{k}}^t \right|^2 n^2 |\delta \mathbf{B}_{\mathbf{k}}|^2, \quad (5.29)$$

where $\hat{b}_{\mathbf{k}}^t$ is the unit vector in the direction of $\mathbf{k} \times \delta \mathbf{B}_{\mathbf{k},\Omega}$, and $n \equiv kc/\Omega$ is the index of

refraction.

Next, using Eq. (5.29) and Parseval's theorem, $\langle E^2 \rangle$ becomes:

$$\langle E^2 \rangle = \frac{\int \left| \overset{\leftrightarrow}{\epsilon}_{\mathbf{k},\Omega}^{-1} \cdot \hat{b}_{\mathbf{k}}^t \right|^2 n^2 |\delta \mathbf{B}_{\mathbf{k}}|^2 d\mathbf{k}}{\int |\delta \mathbf{B}_{\mathbf{k}}|^2 d\mathbf{k}} \langle \delta B^2 \rangle. \quad (5.30)$$

Finally, the general expression which relates the (electric) energy diffusion and (magnetic) pitch-angle diffusion coefficients follows from Eqs. (5.30), (5.20), and (5.7). It is:

$$D_{WW} = \frac{\sqrt{2}}{3} W_e^2 \beta^2 \frac{\int \left| \overset{\leftrightarrow}{\epsilon}_{\mathbf{k},\Omega}^{-1} \cdot \hat{b}_{\mathbf{k}}^t \right|^2 n^2 |\delta \mathbf{B}_{\mathbf{k}}|^2 d\mathbf{k}}{\int |\delta \mathbf{B}_{\mathbf{k}}|^2 d\mathbf{k}} \left(\frac{\lambda_E^l}{\lambda_B} \right) D_{\alpha\alpha}, \quad (5.31)$$

where $W_e \equiv \gamma m_e c^2$ is the electron's total energy, and we have assumed statistical isotropy and homogeneity to produce the numerical prefactor.

Eq. (5.31), despite its apparent complication, offers a fairly simple interpretation when the dielectric tensor assumes a scalar value, ϵ . Recalling that $\sqrt{\epsilon} = n$, so that $\epsilon^{-1} = 1/n^2$, Eq. (5.31) simplifies to:

$$D_{WW} = \frac{\sqrt{2}}{3} W_e^2 \beta^2 \langle \beta_{ph}^2 \rangle_{\text{dist.}} \left(\frac{\lambda_E^l}{\lambda_B} \right) D_{\alpha\alpha}, \quad (5.32)$$

where $\langle \beta_{ph}^2 \rangle_{\text{dist.}}$ is the distributional average, over the magnetic spectrum, of the normalized wave phase velocity, $\beta_{ph} \equiv \Omega/kc$. Thus,

$$D_{WW} \propto (m_e^2 v^2 \langle v_{ph}^2 \rangle_{\text{dist.}}) D_{\alpha\alpha}, \quad (5.33)$$

which is what we would expect, given the general relation between the “velocity space” diffusion coefficient, D_{vv} , and the pitch-angle diffusion coefficient; i.e. $D_{vv} \sim v_{ph}^2 D_{\alpha\alpha}$ (Cravens, 1997).

5.2.4 Particle Transport in Magnetized Plasmas with Electric Fluctuations

As mentioned previously, the combined effect of electric and magnetic fields can lead to fairly complicated particle dynamics. Particle *drifts*, for example, involving both the electric and magnetic fields, should be considered. Here, we present two realizations of the drift phenomenon. We will, subsequently, argue that these effects are of negligible importance for diffusion in small-scale fields.

We argued that sub-Larmor-scale magnetic fluctuations result in trajectories that occupy the small deflection angle regime. For this reason, the “guiding center approximation”, that underlies the drift theory, breaks down. Consequently, the notions of *curvature drift* and *Grad-B drift* lose all meaning in this regime.

Nonetheless, a magnetized plasma contains a large-scale magnetic field – which is, by construction, “super-Larmor-scale”. Hence, drifts that involve the electric field and the ambient (mean) field are, in principle, important to consider.

The first of these that we will explore is the, so called, *E cross B drift*. We will, once more, assume a sinusoidal electric field. In this case, however, we assume that an ambient magnetic field, \mathbf{B}_0 , is present. Furthermore, we suppress the time-dependence; hence:

$$\mathbf{E}(x) = E_0 \cos(kx) \hat{x}, \quad (5.34)$$

where the x -direction is along \mathbf{k} . Assuming non-relativistic velocities, the y -component of the electron, in the ambient magnetic field, will have the solution (Chen, 1984):

$$\frac{d^2 v_y}{dt^2} = -\Omega_{ce}^2 v_y - \Omega_{ce}^2 \frac{c E_0}{B_0} \cos [kx_0 + kr_{L0} \sin(\Omega_{ce} t)] \quad (5.35)$$

where x_0 is the initial position, and $r_{L0} = m_e \beta c^2 / e B_0$ is the (ambient) Larmor radius. This solution presupposes that the electric field will only perturb the electron orbit about the

ambient field. Hence, our substitution of the zeroth-order solution.

Next, we average Eq. (5.35) over a gyro-period. Thus,

$$\langle v_y \rangle + \frac{cE_0}{B_0} \langle \cos [kx_0 + kr_{L0} \sin(\Omega_{ce} t)] \rangle = 0, \quad (5.36)$$

since $\langle dv_y/dt \rangle = 0$ – i.e. the drift velocity is constant.

Next, assuming that $kr_{L0} \ll 1$, we may write the solution for $\langle v_y \rangle$ as (Chen, 1984):

$$\langle v_y \rangle / c = -\frac{E(x)}{B_0} \left(1 - \frac{1}{4} k^2 r_{L0}^2 \right). \quad (5.37)$$

Finally, recognizing that, in the general case, $i\mathbf{k} \rightarrow \nabla$, we write the solution for an arbitrary electric field as (Chen, 1984):

$$\mathbf{v}_{\mathbf{E} \times \mathbf{B}} = c \left(1 + \frac{1}{4} r_{L0}^2 \nabla^2 \right) \frac{\mathbf{E} \times \mathbf{B}_0}{B_0^2}, \quad (5.38)$$

where $\mathbf{v}_{\mathbf{E} \times \mathbf{B}}$ is the drift velocity. The second term, i.e. that which involves the Laplacian operator, is a correction known as a *finite-Larmor-radius effect*. When $kr_{L0} \gg 1$, the Larmor radius is much larger than the field wavelength. In this case, the particle is acted upon, by the electric field, on a time-scale much shorter than the gyroperiod. Consequently, the drift approximation is not appropriate for “small-scale” fields, since the perturbation is implicitly assumed to act on a time-scale of many gyroperiods.

A similar drift phenomenon occurs when we consider the time-dependence of the electric field. Assuming that $\Omega^2 \ll \Omega_{ce}^2$, the particle will drift with velocity (Chen, 1984):

$$\mathbf{v}_p = \pm \frac{c}{\Omega_{ce} B_0} \frac{d\mathbf{E}}{dt}, \quad (5.39)$$

The quantity, \mathbf{v}_p , is known as the *polarization drift* velocity. Similarly, the small-scale processes – by construction – occur on time-scales much shorter than Ω^{-1} . Hence, the polar-

ization drift time-scale will be far greater than either τ_E^l or τ_E^t . For this reason, polarization drift is not significant on the time-scales of immediate interest.

In the next subsection, we will consider the case of small-scale energy diffusion in isotropic, small-scale Whistler turbulence.

5.2.5 Energy Diffusion in Small-Scale Whistler Turbulence

Next, to evaluate Eq. (5.20), we consider a concrete example of electromagnetic turbulence in a magnetized plasma. Whistler-mode turbulence in a “cold” plasma admits the simple dispersion relation given by Eq. (3.35) – i.e. $\Omega_r(k) = \Omega_{ce} \cos(\theta_k) [k^2 d_e^2 / (1 + k^2 d_e^2)]$.

We will assume a (nearly) steady-state, so that the instability is non-linearly saturated, that is the instability growth rate, Ω_i , is much less than all relevant frequency-scales, and thus is negligible. This treatment assumes that the turbulence is “linear”, i.e. $\delta B \ll B_0$. We will further assume that:

$$\frac{\gamma v}{\Omega_{ce}} > \lambda_B, \quad (5.40)$$

where Ω_{ce}/γ is the relativistic gyro-frequency.

Eq. (5.40) implies that $\rho \gg 1$, since $\delta B \ll B_0$ – thus, the test electrons are sub-Larmor-scale with respect to the fluctuation magnetic field, $\delta\mathbf{B}$.

It is worth mentioning that, formally, the cold plasma approximation requires that $kv/\Omega_{ce} \ll 1$ (Verkhoglyadova et al., 2010). This condition would imply that the electron population is “super-Larmor-scale” with respect to the magnetic field, since $\lambda_B \sim k_B^{-1}$, where k_B is the wave-number of the dominant wave-mode. For this reason, our model implicitly presupposes the existence of a cold population of super-Larmor-scale electrons which support the Whistler-modes. Consequently, our test particles will be comprised of a “hot”, albeit smaller, population of sub-Larmor-scale electrons.

An examination of Eq. (3.35) reveals that $\Omega_r(k) \ll \Omega_{ce}$ in the regime where $kc \ll \omega_{pe}$. Restricting ourselves to this regime motivates the introduction of a new parameter, which

we call the “skin-number”. It is:

$$\chi \equiv d_e \lambda_B^{-1}. \quad (5.41)$$

Thus, the regime of interest is characterized by $\chi \ll 1$.

It is noteworthy that, in principle, the test electron velocities may be large enough so that $\Omega_{ce}/\gamma \sim \Omega_r$. By restricting the electron velocities to the mildly relativistic regime, we may safely presuppose that the field-variability time, Ω_r^{-1} , is sufficiently greater than the time to transit a magnetic correlation length, thus permitting the static field treatment for the magnetic field and avoiding the wave-particle resonance treatment.

Next, in the $\chi \ll 1$ regime, the electric field perpendicular to \mathbf{B}_0 is much greater than the component parallel to the ambient magnetic field; i.e. $E_\perp \gg E_\parallel$ (Sazhin, 1993). Furthermore, it can be shown that in the frame moving along the direction of \mathbf{B}_0 with velocity equal to the parallel phase velocity, $v_{ph}^\parallel \equiv \Omega_r/k_\parallel$, the perpendicular electric field is approximately zero (Sazhin, 1993). Consequently, this allows us, via Lorentz transformation of the electromagnetic fields, to relate the magnetic spectral distribution to the electric distribution. It is, thusly:

$$|\mathbf{E}_k|^2 \approx |\mathbf{E}_k^\perp|^2 \approx \beta_{ph}^2 |\delta\mathbf{B}_k^\perp|^2, \quad (5.42)$$

where \perp refers to the spectrum perpendicular to the mean magnetic field, and

$$\beta_{ph} \equiv \frac{v_{ph}^\parallel}{c} = \frac{\Omega_r(\mathbf{k})}{k_\parallel c}. \quad (5.43)$$

Given isotropic/homogeneous magnetic turbulence:

$$|\delta\mathbf{B}_k^\perp|^2 = |\delta\mathbf{B}_k|^2 \cos^2(\theta_k). \quad (5.44)$$

This relation then allows us to express $\langle E^2 \rangle$ in terms of the magnetic field as:

$$\langle E^2 \rangle = \frac{2}{3} \frac{\int \beta_{ph}^2 |\delta\mathbf{B}_k|^2 d\mathbf{k}}{\int |\delta\mathbf{B}_k|^2 d\mathbf{k}} \langle \delta B^2 \rangle. \quad (5.45)$$

Next, the electric field correlation length may be obtained from the electric field correlation tensor. For isotropic turbulence, one may write the general expression for the Fourier image of the electric field two-point auto-correlation tensor as:

$$\Phi_{ij}(\mathbf{k}) = |\mathbf{E}_k^t|^2 (\delta_{ij} - \frac{k_i k_j}{k^2}) + |\mathbf{E}_k^l|^2 \frac{k_i k_j}{k^2}. \quad (5.46)$$

Isotropy is an approximation here, given the polar asymmetry indicated by Eq. (5.44). Using Maxwell's Equations, we may relate the longitudinal, $|\mathbf{E}_k^l|^2$ and transverse, $|\mathbf{E}_k^t|^2$ distributions to $|\delta\mathbf{B}_k|^2$ (where "longitudinal" and "transverse" are with respect to the wave-vector, not the electron velocity). To wit:

$$\begin{cases} |\mathbf{E}_k^t|^2 = \frac{\Omega_r^2}{k^2 c^2} |\delta\mathbf{B}_k|^2 \\ |\mathbf{E}_k^l|^2 = |\mathbf{E}_k|^2 - |\mathbf{E}_k^t|^2 \end{cases} \quad (5.47)$$

In the $\chi \ll 1$ regime, we may substitute Eq. (5.42) to express the tensor completely in terms of the magnetic spectrum. The trace of the correlation tensor is then given by:

$$Tr \left[\overset{\leftrightarrow}{\Phi}(\mathbf{k}) \right] = 2\beta_{ph}^2 |\delta\mathbf{B}_k|^2 \cos^2(\theta_k). \quad (5.48)$$

While integrating Eq. (5.48) along a selected path, we only consider the component of the electric field parallel to the trajectory, owing to the dot product with velocity in Eq. (5.16). This allows us to draw an analogy to the "monopolar" (magnetic) correlation length that we will explore in the next Chapter – permitting us to write the expression immediately as:

$$\lambda_E^l \equiv \lambda_E^{Tr}(x\hat{x}) = \frac{3\pi}{4} \frac{\int (v_{ph}^{\parallel})^2 k |\delta\mathbf{B}_k|^2 dk}{\int (v_{ph}^{\parallel})^2 k^2 |\delta\mathbf{B}_k|^2 dk}, \quad (5.49)$$

where the integration path was chosen to be along the x-axis. By comparing Eq. (3.61) to Eq. (5.49), we see that the electric correlation length differs from the magnetic correlation length only by a factor of a few. For this reason, we may conclude that τ_E^l is less than

$\tau_{ac} \sim \Omega_r^{-1}$. Consequently, the energy diffusion will be dominated by the electric field's "spatial" stochasticity, as per Eq. (5.14).

Additionally, $\chi \ll 1$ and $\Omega_{ce} \ll \omega_{pe}$ demand that $v_{ph}^{\parallel} \ll c$. This implies that $\langle \delta B^2 \rangle \gg \langle E^2 \rangle$. Consequently, the pitch-angle diffusion will be dominated by the magnetic deflections, and thus we may neglect the contribution due to the electric field.

Finally, given Eq. (5.45), the energy diffusion coefficient may be related directly to the (magnetic) pitch-angle diffusion coefficient via the relation:

$$D_{WW} = \frac{2\sqrt{2}}{9} W_e^2 \beta^2 \frac{\int (\beta_{ph}^{\parallel})^2 |\delta \mathbf{B}_k|^2 d\mathbf{k}}{\int |\delta \mathbf{B}_k|^2 d\mathbf{k}} \frac{\lambda_E^l}{\lambda_B} D_{\alpha\alpha}. \quad (5.50)$$

Eq. (5.50) will be confirmed, given isotropic small-scale Whistler turbulence, via first-principle numerical simulation in Section 5.3.2.

5.3 Simulation Results

In the previous sections, we made a number of theoretical predictions concerning the transport properties of plasmas with small-scale turbulent magnetic and electric fields. Here we check our predictions: first, for pitch-angle diffusion in purely small-scale magnetic fields with $B_0 = 0$.

5.3.1 Magnetic Pitch-Angle Diffusion

First of all, we explored how the pitch-angle diffusion coefficient depends on various parameters, cf. Eq. (5.7), namely the particle's velocity, β , the magnetic field strength, $\langle \delta B^2 \rangle$, the field correlation scale, λ_B , and the "gyro-number", ρ .

To start, we tested our fundamental assumption that the particle velocity vector only varies slightly over a correlation length, λ_B . This is the key assumption that underlies our theoretical predictions for pitch-angle diffusion. If this assumption were to not hold (i.e. if

$\alpha_\lambda \ll 1$) then pitch-angle diffusion would break down, and the plot of $\langle \alpha^2 \rangle$ vs time would deviate from linear behavior. In Figure 5.1, $\langle \alpha^2 \rangle$ is plotted as a function of time for seven different cases. In each run, $\langle \delta B^2 \rangle$, k_{\min} , and N_p (number of simulation particles) are fixed to the values of 0.01, $4\pi/5$ (both in arbitrary simulation units), and 2000, respectively. The particles are monoenergetic, and are isotropically distributed in their initial velocities. Each case differs in particle velocities; which range from $\frac{1}{512}c$ to $\frac{1}{8}c$. As can be seen, the curves begin as straight lines that increase with slope as β decreases. Eventually, the linear behavior breaks down as β decreases. A decrease in ρ occurs concurrently, in accordance with Eq. (5.2). As expected, the breakdown in linear behavior, and hence diffusion, occurs when $\rho \sim 1$. Later, we did the same experiment, only this time we varied $\langle \delta B^2 \rangle$ in such a way as to keep ρ constant ($\rho = 24.5$). In this way, each case is securely in the small-scale regime. In Figure 5.2, we see that the linear behavior of $\langle \alpha^2 \rangle$ vs time is preserved for all velocities, as anticipated. Consequently, our assumption of a small α_λ is valid, as long as $\rho > 1$. With the existence of pitch-angle diffusion established, we then proceeded to compare the slope of $\langle \alpha^2 \rangle$ vs time (the numerical pitch-angle diffusion coefficient) to Eq. (5.7). In Figure 5.3, the numerically obtained diffusion coefficients from Figure 5.2 are compared to the analytical result of Eq. (5.7). In each, the theoretical and numerical results differ only by a small factor of $\mathcal{O}(1)$. Next, we tested the correlation length dependence, i.e. whether or not the numerical simulations agree with Eq. (3.60). With $k_{\min} = \pi$ and $k_{\max} = 8\pi$, we varied the magnetic spectral index, μ from 2 to 5. This is plotted in Figure 5.4, where the numerical diffusion coefficient closely matches the analytical result. In Figure 5.5, the numerical (magnetic) diffusion coefficient is plotted against the analytical coefficient for the same range of μ values, but now the k_{\min} , k_{\max} , and β values differ among the three (with ρ fixed to 24.5). Included are the results of Figure 5.4. All three cases give a nearly linear relationship between the numerical and analytical coefficients, with slopes approximately equal to unity. Another concern worth addressing is the dependence of the numerical diffusion coefficient on the total number of simulation particles. In Figure 5.6, a test case

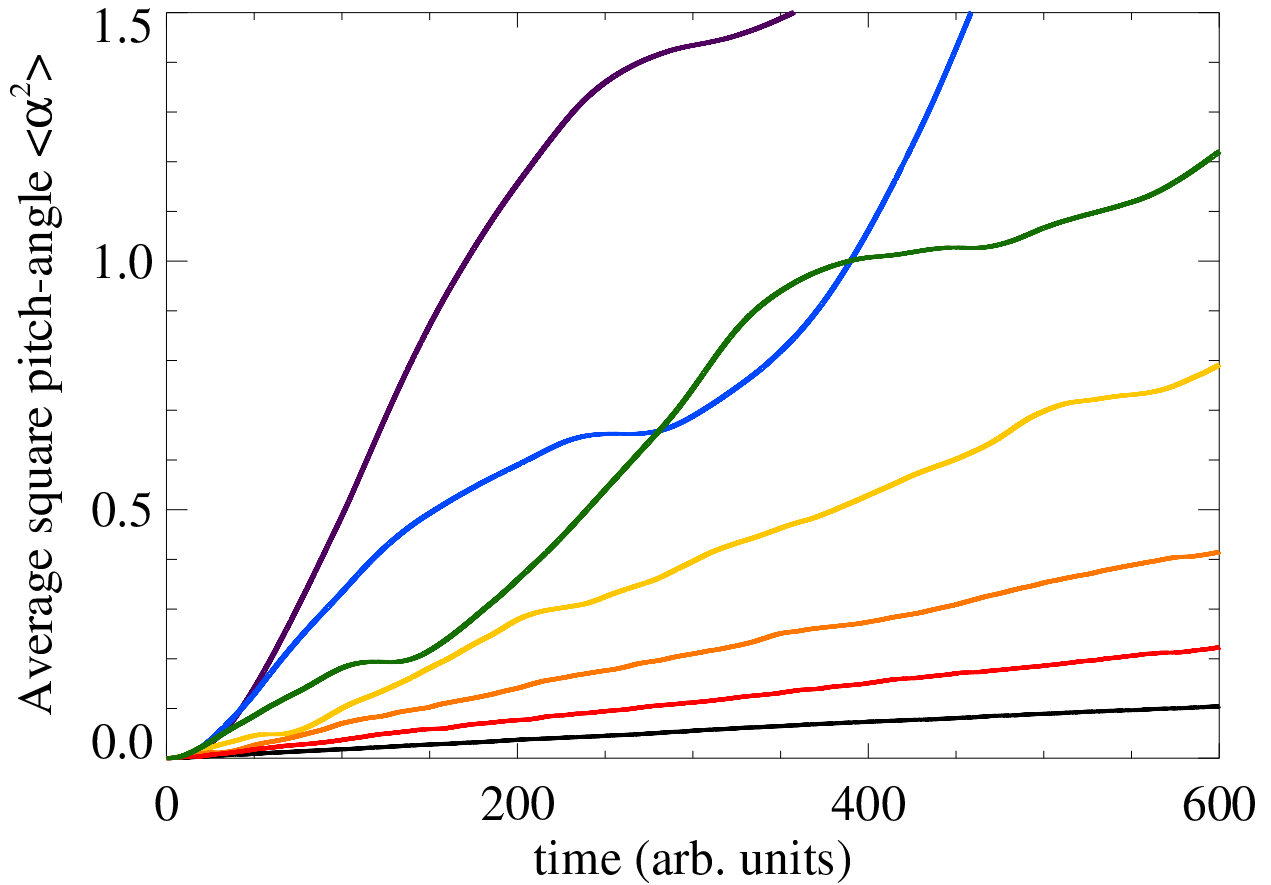


Figure 5.1: Average square pitch-angle vs. time (in simulation units). Relevant parameters are $N_p = 2000$, $k_{\min} = 4\pi/5$, $k_{\max} = 8\pi$, $\langle \delta B^2 \rangle^{1/2} = 0.01$, and $\mu = 3$. The particle velocities in each case range from $\frac{1}{8}c$ to $\frac{1}{512}c$ (by multiples of two). The curves appear with increasing average slope as β decreases. As β decreases, eventually $\rho \sim 1$ (at $\beta = \frac{c}{128}$, i.e. the fifth most sloped, “green” line), after which the deflection angle becomes large, and pitch-angle diffusion breaks down.

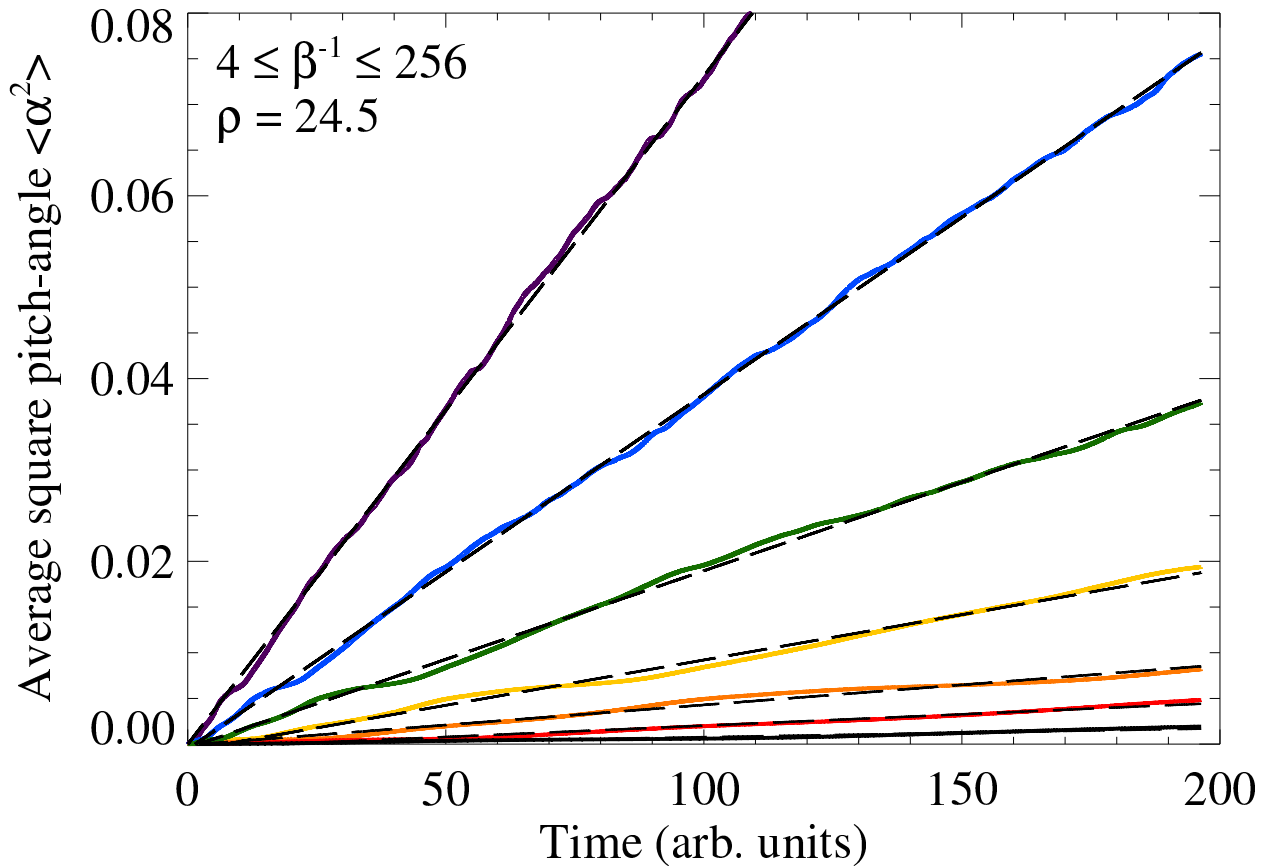


Figure 5.2: Average square pitch-angle vs. time (in simulation units). Relevant parameters are $N_p = 2000$, $k_{\min} = \pi$, $k_{\max} = 8\pi$, and $\mu = 3$. $\langle \delta B^2 \rangle^{1/2}$ ranges from 5×10^{-4} to 0.032 , by multiples of two. The particle velocities range (in the opposite order) from $\frac{1}{256}c$ to $\frac{1}{4}c$. These two parameters, $\langle \delta B^2 \rangle$ and β , vary in such a way as to keep $\rho = 24.5$. The curves appear with increasing slope as β decreases. Clearly, the linear form of the curves is retained in all seven cases.

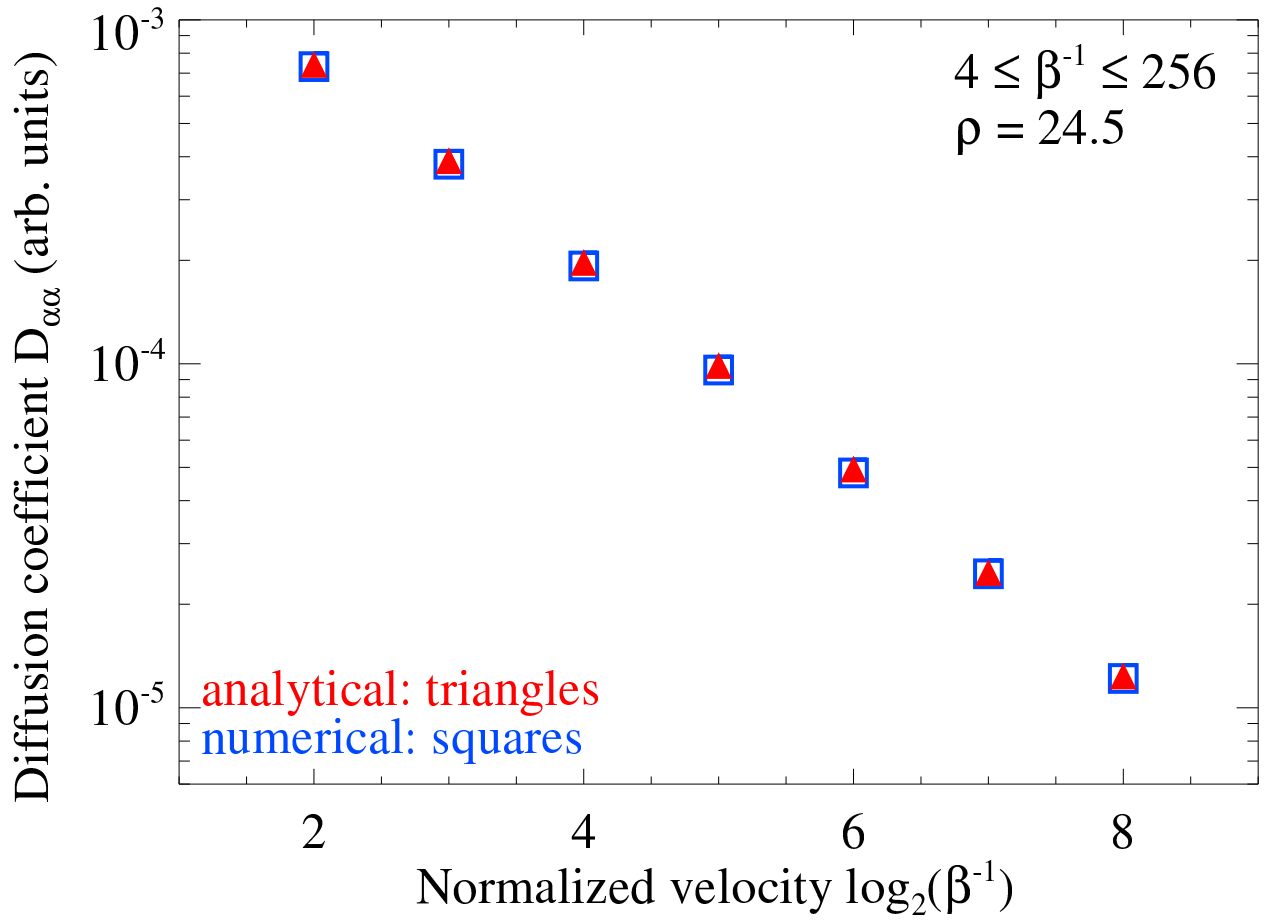


Figure 5.3: Magnetic pitch-angle diffusion coefficient, $D_{\alpha\alpha}$ vs the logarithm (base 2) of the inverse normalized particle velocity, $\log_2(\beta^{-1})$. The (blue) empty “squares” indicate the $D_{\alpha\alpha}$ obtained directly from simulation (as the slope of $\langle \alpha^2 \rangle$ vs. time), while the (red) filled “triangles” are the analytical, given by Eq. (5.7), pitch-angle diffusion coefficients. Simulation parameters are identical to those used in Figure 5.2.

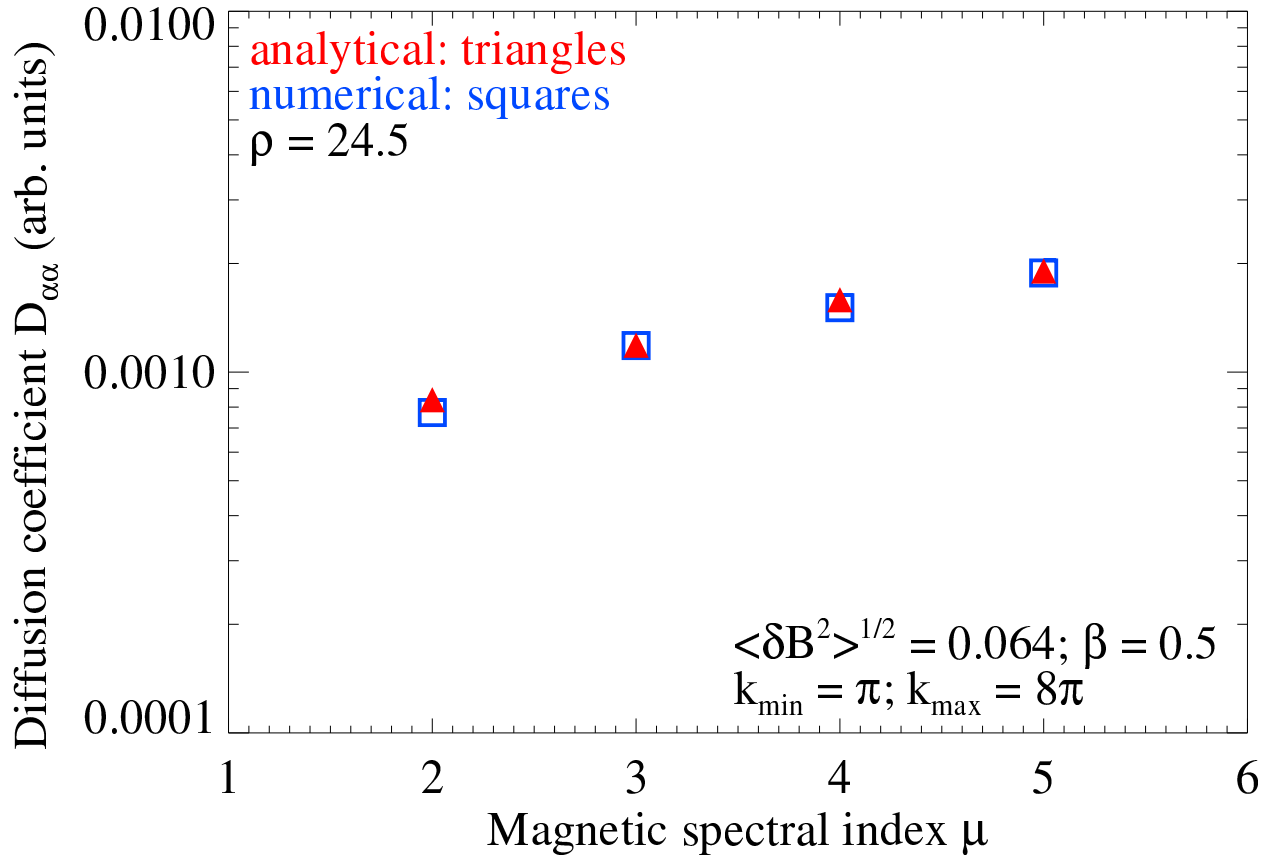


Figure 5.4: Magnetic pitch-angle diffusion coefficient, $D_{\alpha\alpha}$ vs the magnetic spectral index, μ . The (blue) empty “squares” indicate the $D_{\alpha\alpha}$ obtained directly from simulation, while the (red) filled “triangles” are the analytical, given by Eq. (5.7), pitch-angle diffusion coefficients. Relevant parameters are $N_p = 2000$, $k_{\min} = \pi$, $k_{\max} = 8\pi$, $\langle \delta B^2 \rangle^{1/2} = 0.064$, $\beta = 0.5$, and $\rho = 24.5$. The magnetic spectral indexes are 2, 3, 4, and 5. Notice that the numerical results have nearly the same functional dependence on μ as the analytical triangles, as given by Eq. (5.7).

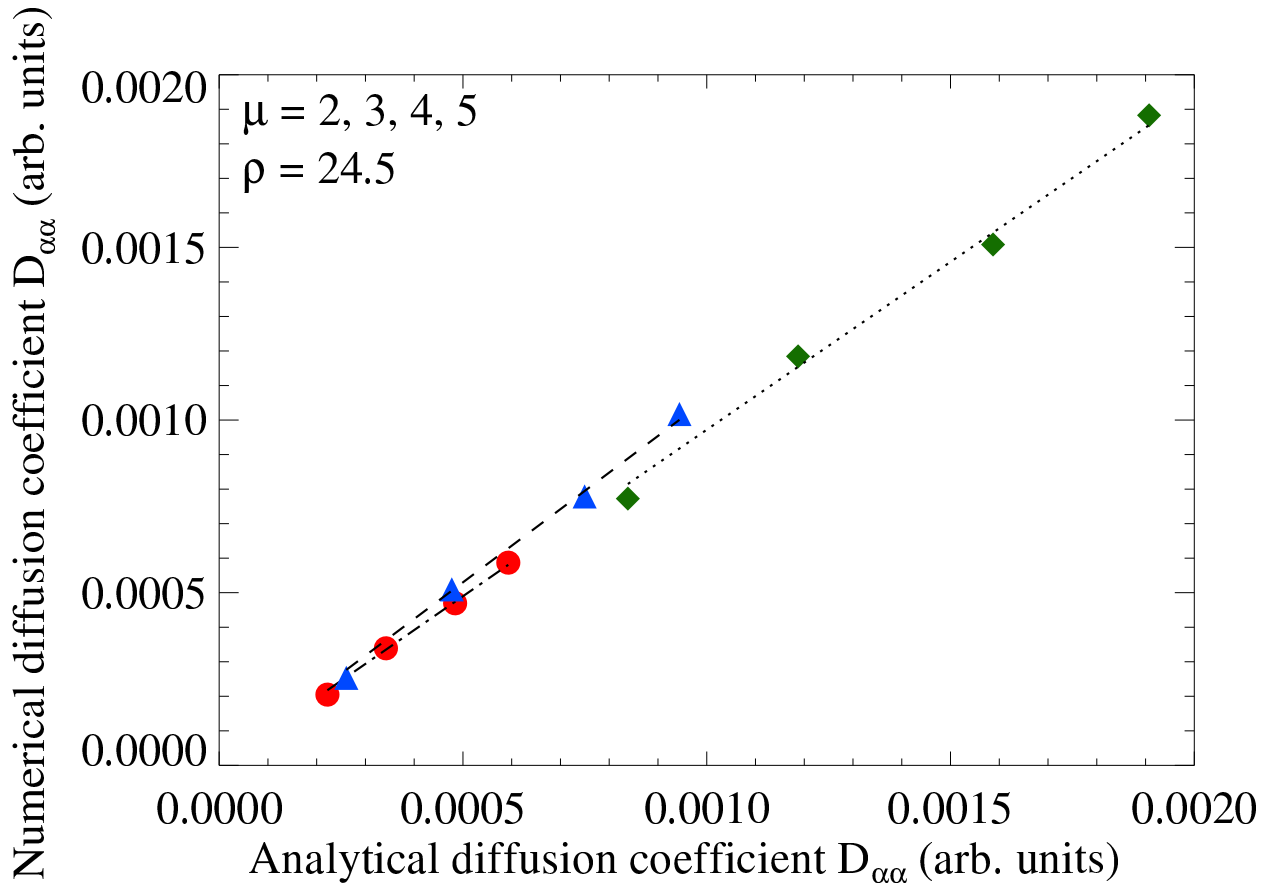


Figure 5.5: Numerical [magnetic] pitch-angle diffusion coefficient vs the analytical [magnetic] pitch-angle diffusion coefficient, for three different cases. In each case, the magnetic spectral index has been varied from 2 to 5, by intervals of unity. Relevant parameters are $k_{\min} = \pi/2$ (red) “circles” and (blue) “triangles”, π (green) “diamonds”, $k_{\max} = 5.12\pi$ (red) “circles”; $k_{\max} = 8\pi$ (green) “diamonds” and (blue) “triangles”; $\langle \delta B^2 \rangle^{1/2} = 0.016$ (red) “circles”, 0.032 (blue) “triangles”; 0.064 (green) “diamonds”; $\beta = 0.25$ (red) “circles”, 0.5 (blue) “triangles” and (green) “diamonds”. In each case, a line of best fit is applied. The slopes are 0.979 (circles), 0.972 (diamonds), and 1.06 (triangles)

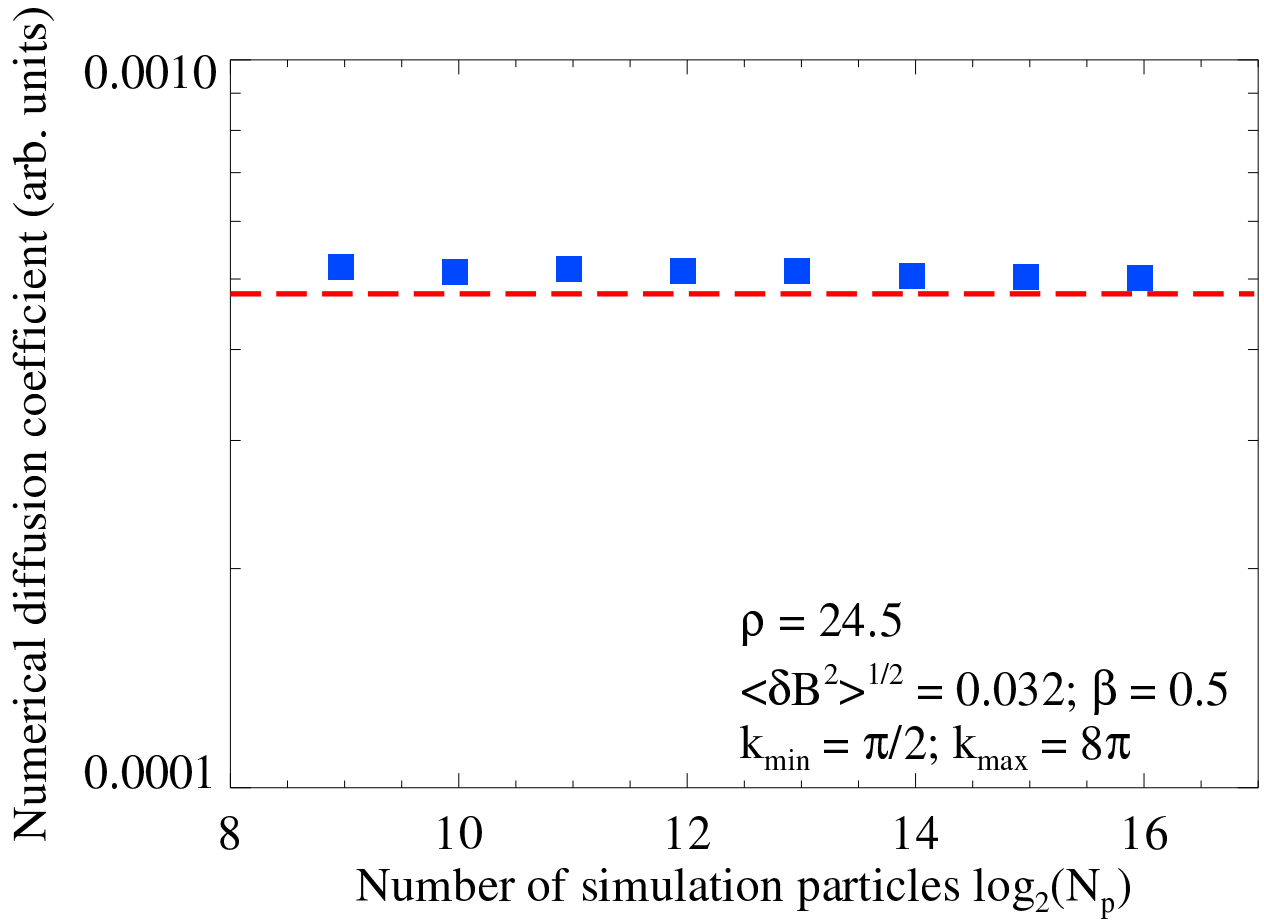


Figure 5.6: Magnetic pitch-angle diffusion coefficient, $D_{\alpha\alpha}$ vs the total number of simulation particles, N_p . The “blue squares” indicate the $D_{\alpha\alpha}$ obtained directly from simulation, while the red dotted line is the analytical result, given by Eq. (5.7). Relevant parameters are $k_{\min} = \pi/2$, $k_{\max} = 8\pi$, $\langle \delta B^2 \rangle^{1/2} = 0.032$, $\beta = 0.5$, and $\rho = 24.5$. There appears to be no strong dependence of the numerical pitch-angle diffusion coefficient upon the total number of simulation particles; nevertheless, there appears to be some convergence to the analytical result.

was repeated with an increasing number of simulation particles. The number of particles was increased from 500 to 64000, by factors of 2. There is little variation to be seen in the numerical result, as the number of particles is increased.

5.3.2 Transport in Magnetized Plasmas

We made the claim in Section 5.2.1 that the presence of a mean magnetic field will not affect the pitch-angle diffusion (in isotropic turbulence), as long as we choose a reference direction along the axis of \mathbf{B}_0 . We confirm this assumption here.

First, however, we consider energy diffusion. As stated previously, a diffusive process requires that both $\langle \Delta W_e^2 \rangle$ and $\langle \alpha^2 \rangle$ increase linearly in time – at least, on some characteristic time-scale of the system. With $\delta B/B_0 \ll 1$, the “gyro-period”

$$T_g \equiv \frac{2\pi}{\Omega_{B_0}} = 2\pi \frac{\gamma_e m_e c}{e B_0}, \quad (5.51)$$

is such a characteristic, “macro” time-scale. On a multiple gyro-period time-scale, the electron velocities will change very slightly. Consequently, we may treat the magnitude of the electron velocity as approximately constant.

To establish diffusion, 5000 mono-energetic electrons ($\beta = 0.25$) were injected into Whistler turbulence with $k_{\min} = 32\pi$ (arbitrary simulation units), $k_{\max} = 10k_{\min}$, $\langle \delta B^2 \rangle^{1/2}/B_0 = 0.1$, $\Omega_{ce} = 1$, $\rho \approx 400$, $\chi \approx 0.04$, and $\mu = 4$. The simulation time included several gyro-periods; $T = 10T_g$. Additional simulation parameters include: the time-step $\Delta t = 0.00125$ (arbitrary units), and the number of Whistler wave-modes $N_m = 10000$. In Figure 5.7, we see that the average square pitch-angle (as measured with respect to the z -axis, i.e. the mean field direction) does, indeed, grow linearly with time. Figure 5.8 confirms that the electron energy undergoes a classical diffusive process as well.

With the existence of pitch-angle and energy diffusion established, we then proceeded

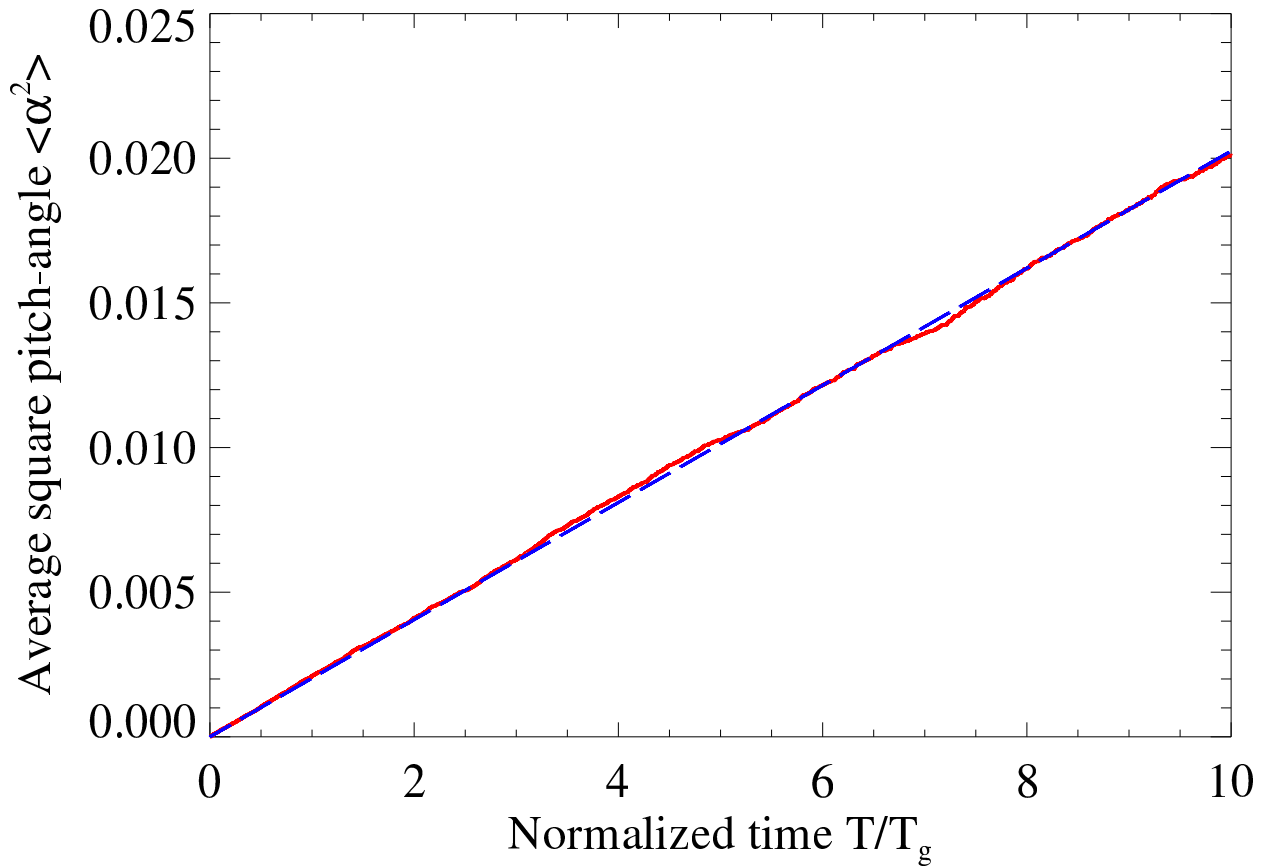


Figure 5.7: Average square pitch-angle vs. normalized time for electrons moving through small-scale Whistler-mode turbulence. Relevant parameters are $\beta = 0.25$, (number of simulation particles) $N_p = 5000$, $k_{\min} = 32\pi$, $k_{\max} = 10k_{\min}$, $\langle \delta B^2 \rangle^{1/2}/B_0 = 0.1$, $\Omega_{ce} = 1$, $\rho \approx 400$, $\chi \approx 0.04$, and $\mu = 4$. The linear nature of the curve (solid, “red”) confirms the diffusive nature of the pitch-angle transport. Here, the dashed (“blue”) line indicates a line of best fit (simple linear regression) with Pearson correlation coefficient: 0.9998.

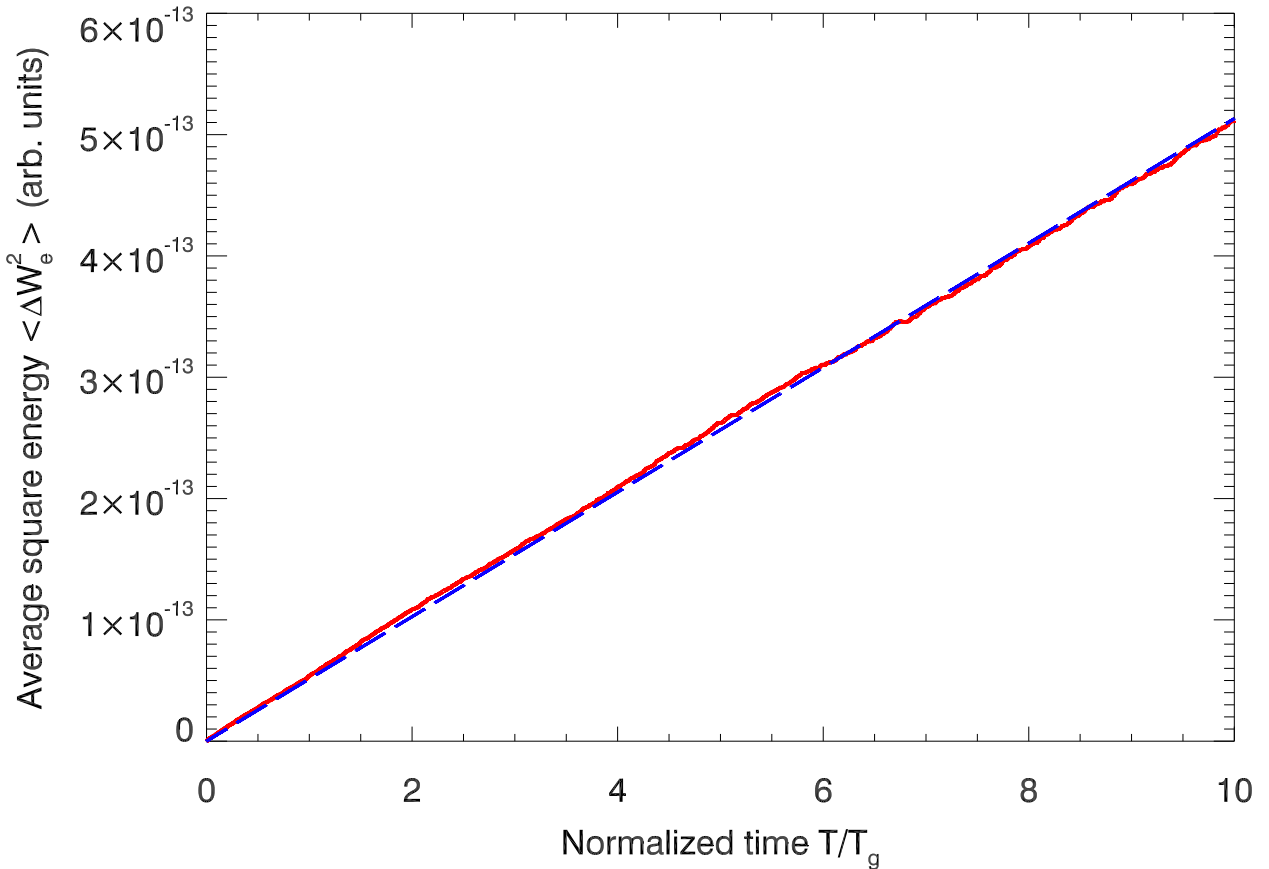


Figure 5.8: Average square change in electron energy (in simulation units) vs. normalized time for electrons moving through small-scale Whistler-mode turbulence. Relevant parameters are $\beta = 0.25$, (number of simulation particles) $N_p = 5000$, $k_{\min} = 64\pi$, $k_{\max} = 10k_{\min}$, $\langle \delta B^2 \rangle^{1/2}/B_0 = 0.1$, $\Omega_{ce} = 1$, $\rho \approx 400$, $\chi \approx 0.04$, and $\mu = 4$. The linear nature of the curve (solid, “red”) confirms the diffusive nature of the energy transport. Here, the dashed (“blue”) line indicates a line of best fit (simple linear regression) with Pearson correlation coefficient: 0.9999.

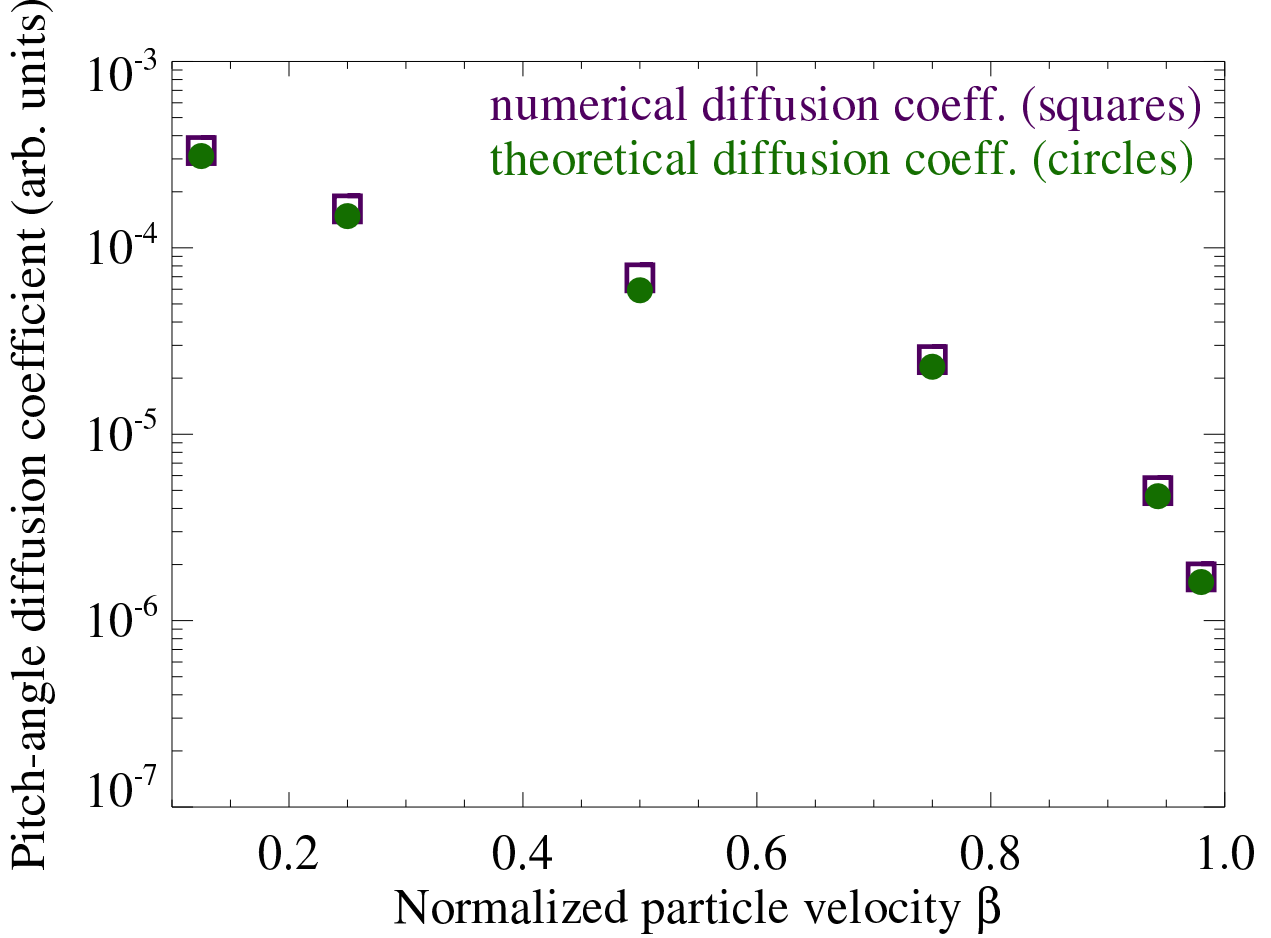


Figure 5.9: Magnetic pitch-angle diffusion coefficient, $D_{\alpha\alpha}$ vs the normalized electron velocity, β . Relevant simulation parameters include: $N_p = 5000$, $k_{\min} = 32\pi$, $k_{\max} = 10k_{\min}$, $\langle \delta B^2 \rangle^{1/2}/B_0 = 0.1$, $\Omega_{ce} = 1$, $\chi \approx 0.02$, and $\mu = 4$. The (purple) empty “squares” indicate the $D_{\alpha\alpha}$ ’s obtained directly from simulation data (as the slope of $\langle \alpha^2 \rangle$ vs. time), while the (green) filled “circles” are the analytical pitch-angle diffusion coefficients, given by Eq. (5.7).

to compare the slope of $\langle \alpha^2 \rangle$ and $\langle \Delta W_e^2 \rangle$ vs time (the numerical [magnetic] pitch-angle and energy diffusion coefficients) to Eqs. (5.7) and (5.50). In Figure 5.9, the numerically obtained pitch-angle diffusion coefficients are compared to Eq. (5.7) for a range of possible electron velocities. In each, the theoretical and numerical results differ only by a small factor of $\mathcal{O}(1)$. Next, in Figure 5.10, we see decent agreement with Eq. (5.50) and the numerical energy diffusion coefficients. Figures 5.9 and 5.10, furthermore, confirm that our theoretical diffusion coefficients are valid for all electron velocities – including relativistic speeds.

Another important parameter which strongly influences the diffusive transport is the

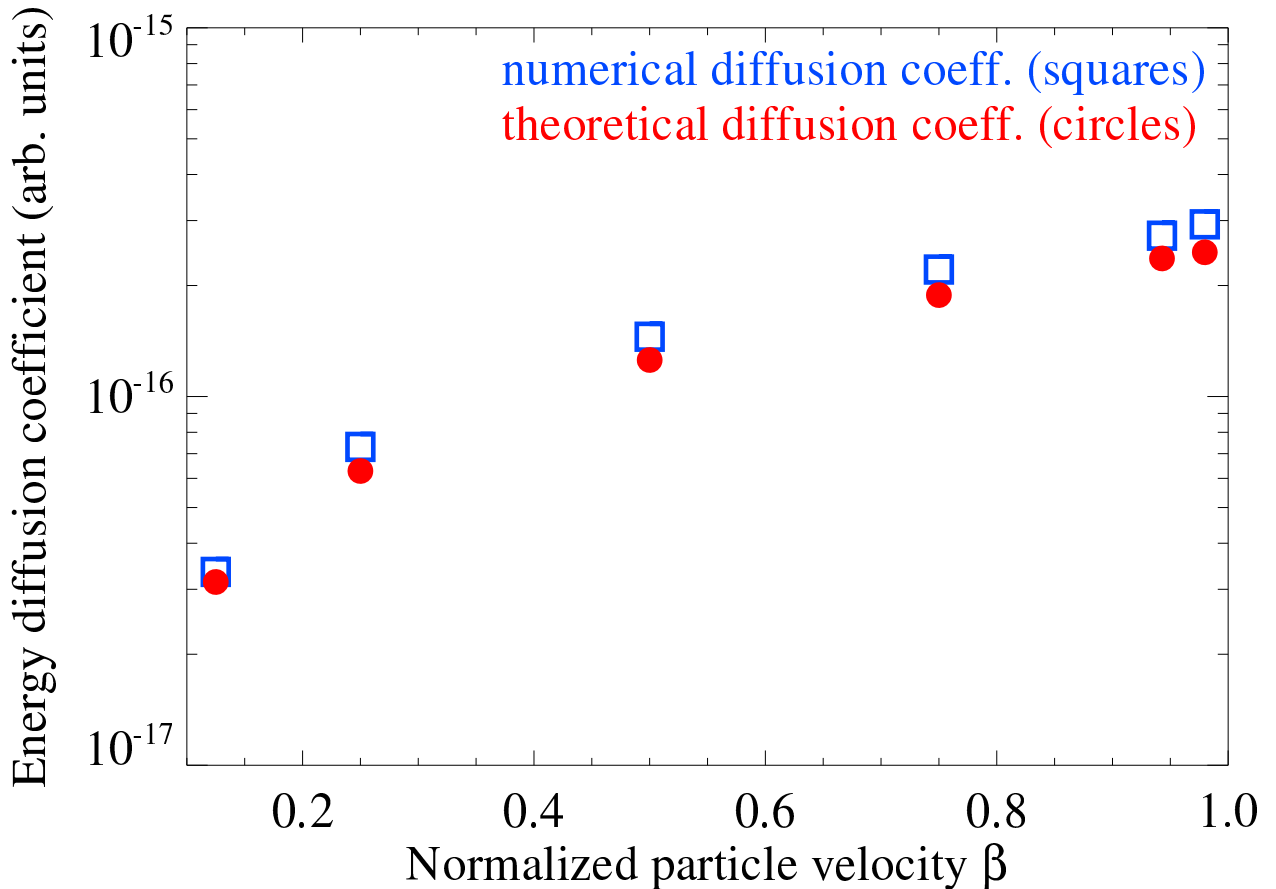


Figure 5.10: Energy diffusion coefficient, D_{WW} vs the normalized electron velocity, β . Relevant simulation parameters include: $N_p = 5000$, $k_{\min} = 32\pi$, $k_{\max} = 10k_{\min}$, $\langle \delta B^2 \rangle^{1/2}/B_0 = 0.1$, $\Omega_{ce} = 1$, $\chi \approx 0.02$, and $\mu = 4$. The (blue) empty “squares” indicate the D_{WW} ’s obtained directly from simulation (as the slope of $\langle \Delta W_e^2 \rangle$ vs. time), while the (red) filled “circles” are the analytical energy diffusion coefficients, given by Eq. (5.50).

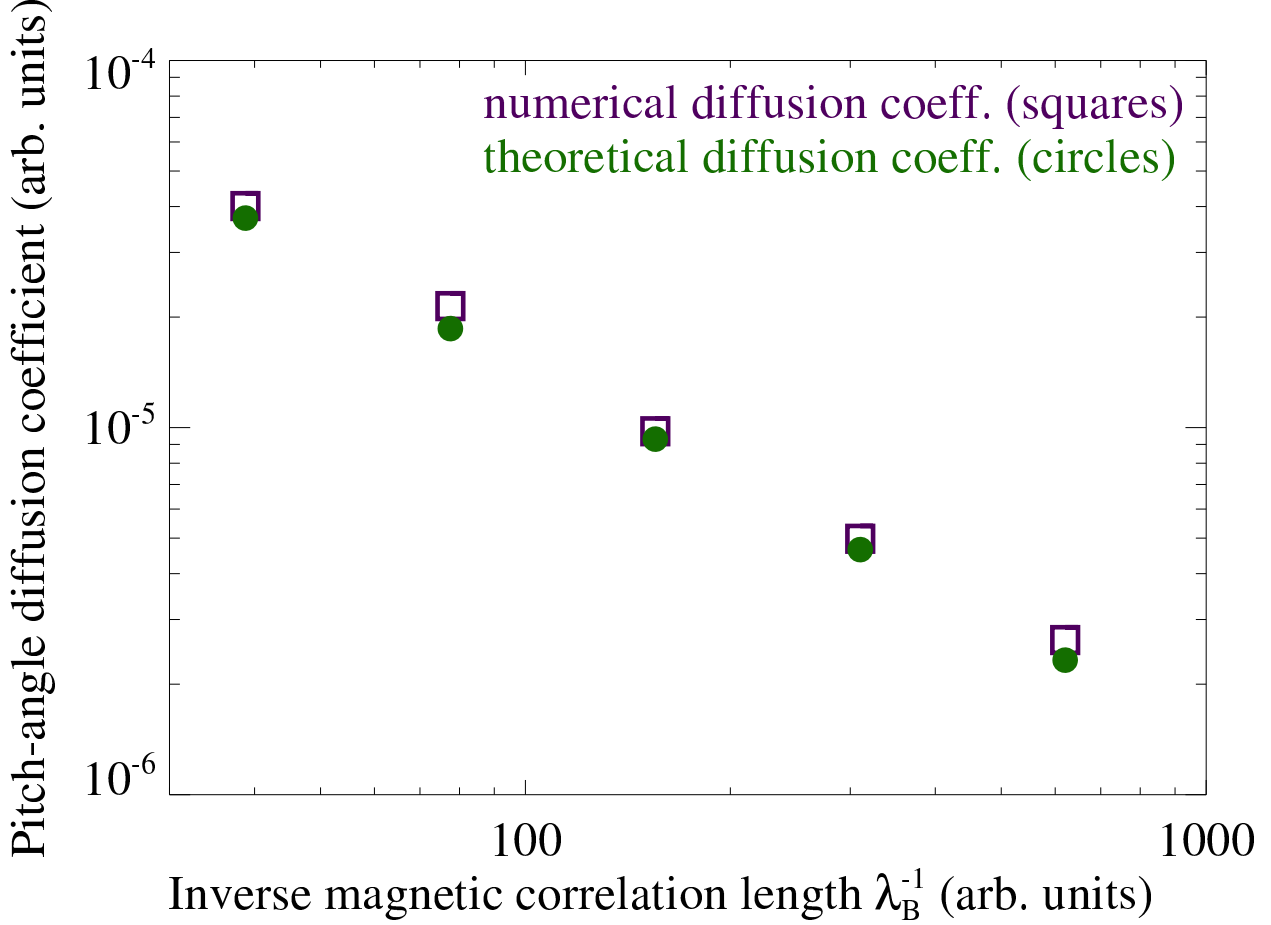


Figure 5.11: Magnetic pitch-angle diffusion coefficient, $D_{\alpha\alpha}$ vs the inverse of magnetic field correlation scale, λ_B^{-1} . Relevant simulation parameters include: $\gamma_e = 3$, $N_p = 1000$, $k_{\min} = 8\pi$, 16π , 32π , 64π , and 128π , $k_{\max} = 10k_{\min}$ (for each k_{\min}), $\langle \delta B^2 \rangle^{1/2}/B_0 = 0.1$, $\Omega_{ce} = 1$, $\chi \approx 0.02$, and $\mu = 4$. For each data point, the theoretical and numerical results differ only by a small factor of $\mathcal{O}(1)$.

magnetic field correlation length. In Figure 5.11, the correlation length was varied by changing k_{\min} , while keeping all other parameters fixed. Once more, we see close agreement with Eq. (5.7). Similarly, the numerical and theoretical energy diffusion coefficients continue to show decent agreement – see Figure 5.12.

Lastly, we consider the magnetic spectral index, μ – i.e. the power-law exponent in Eq. (3.62). With $k_{\min} = 32\pi$ and $k_{\max} = 10k_{\min}$, we varied the magnetic spectral index, μ from -3 to 9 . In Figure 5.13, we see that the numerical pitch-angle diffusion coefficient closely

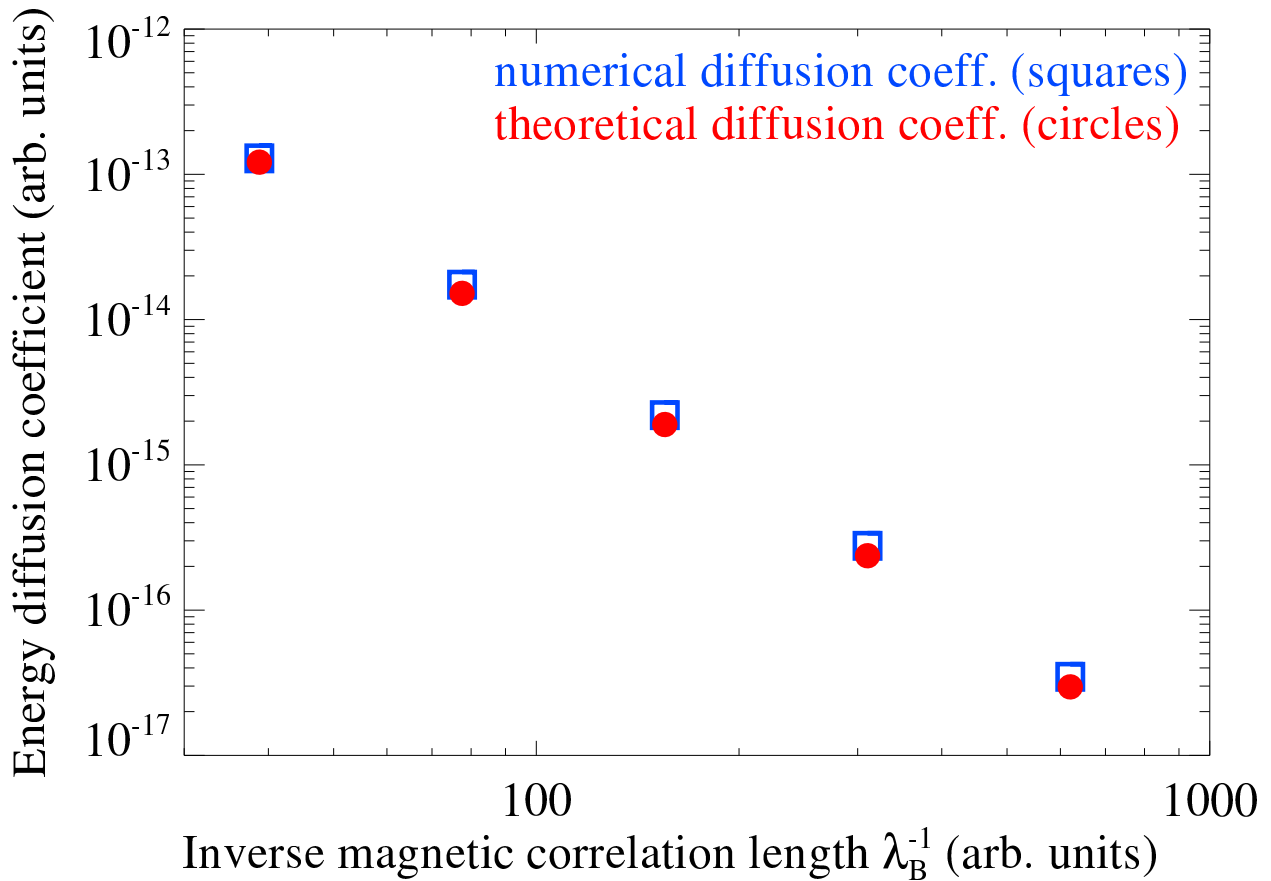


Figure 5.12: Energy diffusion coefficient, D_{WW} vs the inverse of magnetic field correlation scale, λ_B^{-1} . Relevant simulation parameters include: $\gamma_e = 3$, $N_p = 1000$, $k_{\min} = 8\pi, 16\pi, 32\pi, 64\pi$, and 128π , $k_{\max} = 10k_{\min}$ (for each k_{\min}), $\langle \delta B^2 \rangle^{1/2}/B_0 = 0.1$, $\Omega_{ce} = 1$, $\chi \approx 0.02$, and $\mu = 4$. The theoretical and numerical results differ only by a small factor of $\mathcal{O}(1)$.

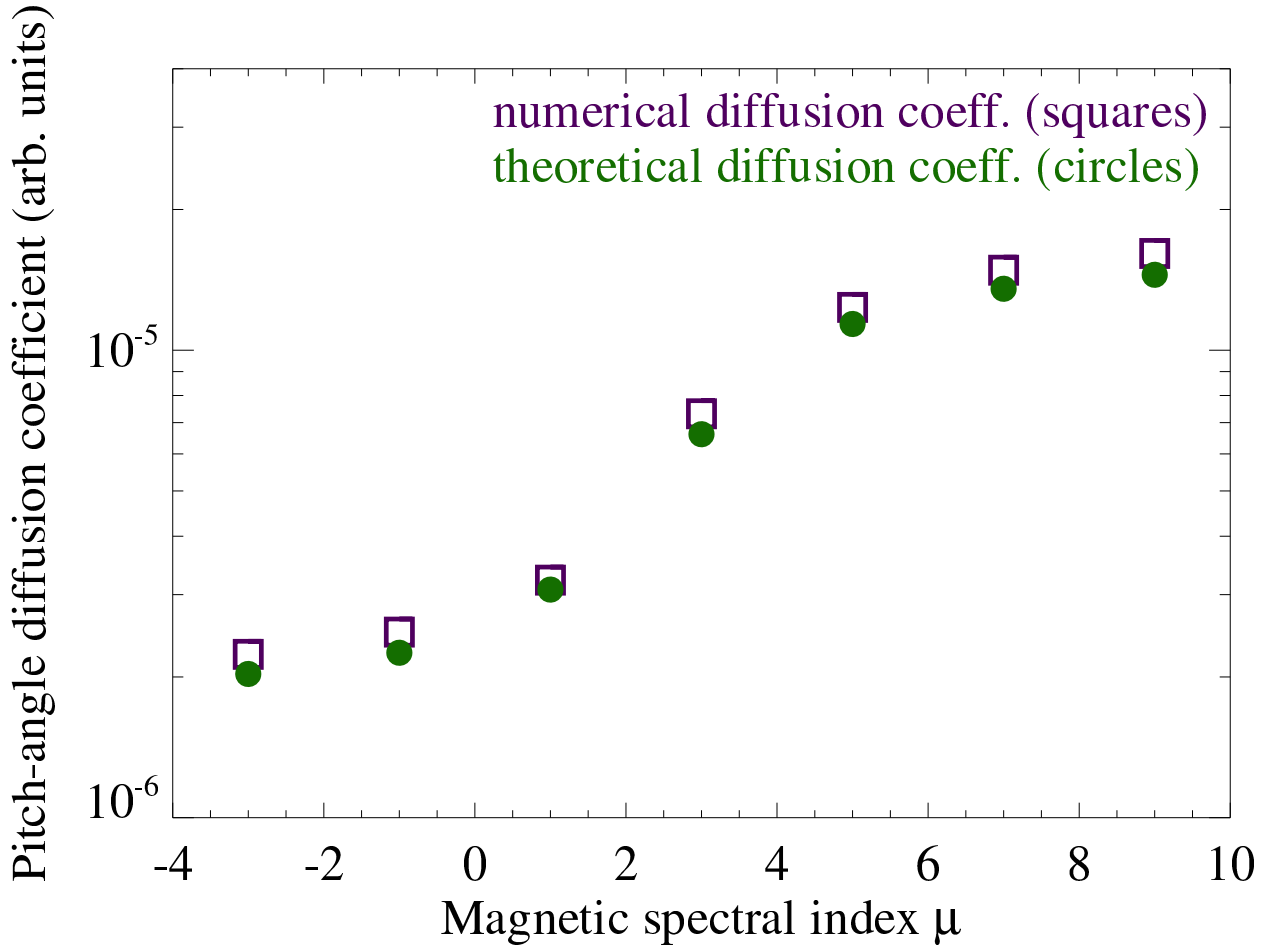


Figure 5.13: Magnetic pitch-angle diffusion coefficient, $D_{\alpha\alpha}$ vs the magnetic spectral index, μ . Relevant parameters are $N_p = 2000$, $k_{\min} = 32\pi$, $k_{\max} = 10k_{\max}$, $\langle \delta B^2 \rangle^{1/2}/B_0 = 0.1$, $\Omega_{ce} = 1$, and $\chi \approx 0.05$. Notice that the numerical results have nearly the same functional dependence on μ as the analytical squares, as given by Eq. 5.7.

matches the analytical result. Similarly close agreement was, once again, realized between the energy diffusion coefficients; as may be seen in Figure 5.14.

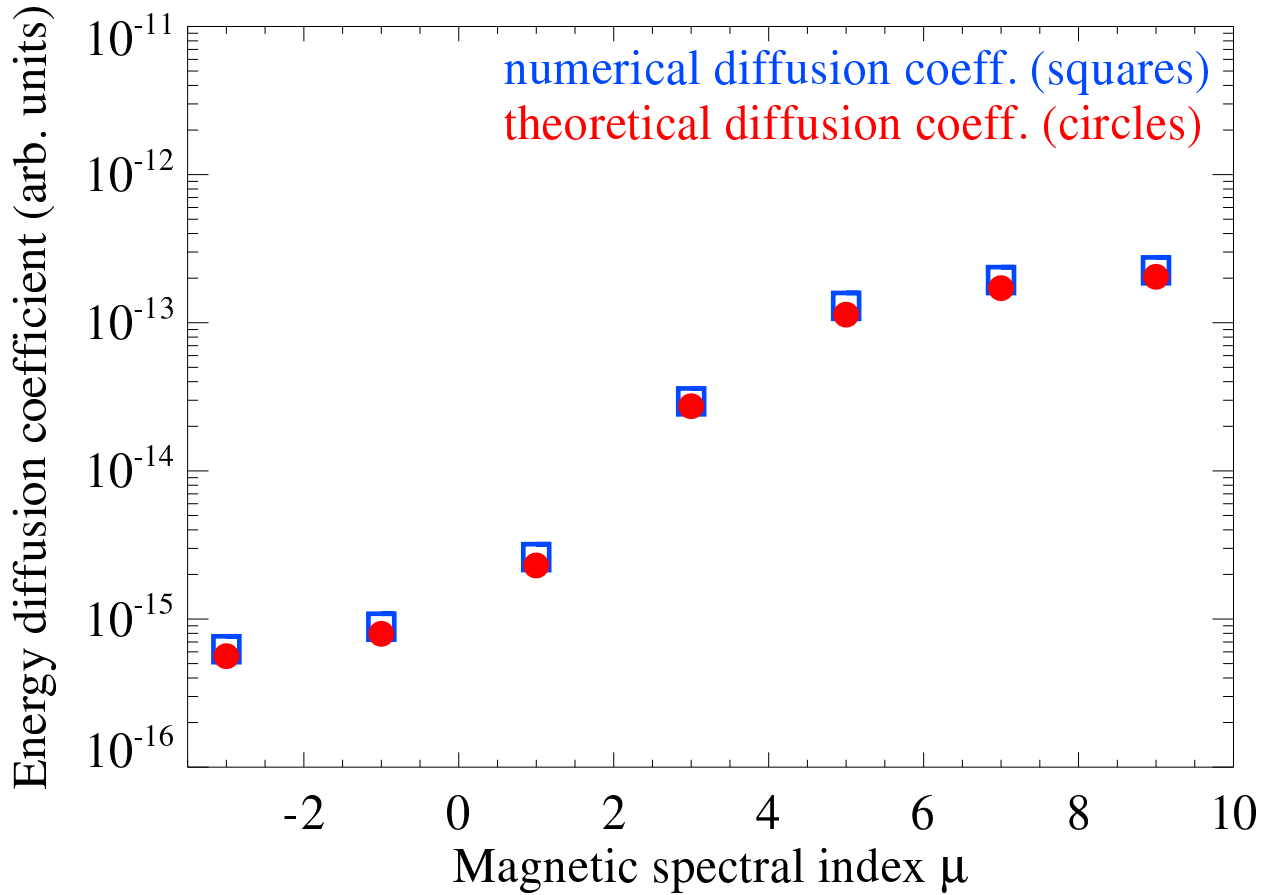


Figure 5.14: Energy diffusion coefficient, D_{WW} vs the magnetic spectral index, μ . Relevant parameters are $N_p = 2000$, $k_{\min} = 32\pi$, $k_{\max} = 10k_{\max}$, $\langle \delta B^2 \rangle^{1/2}/B_0 = 0.1$, $\Omega_{ce} = 1$, and $\chi \approx 0.05$.

5.3.3 Langmuir Turbulence

In Section 5.2.2, we predicted the pitch-angle diffusion coefficient for ultrarelativistic electrons moving in small-scale electric turbulence. Here, we will numerically confirm Eq. (5.11) – via our first-principle simulations. We will treat the electric field as quasi-static, i.e. $\mathbf{k} \times \mathbf{E}_k \approx \mathbf{0}$. To this end, we employ a model identical to that used by (Teraki & Takahara, 2014) for the numerical generation of the electrostatic (Langmuir) turbulence. Essentially, a background of “cold” langmuir wave-modes are assumed to be present, with $\Omega_r \sim \omega_{pe}$.

It was assumed that the Langmuir oscillations are “cold”, i.e. possessing real frequency, $\Omega_r(\mathbf{k}) \approx \omega_{pe}$ (where ω_{pe} is the electron plasma frequency). In this case, the parameters which characterize the radiation/transport regime are the jitter parameter (Teraki & Takahara, 2014):

$$\delta_j \equiv \frac{\delta\alpha_E}{\Delta\theta} \sim \frac{eE_\perp\lambda_E}{m_e c^2} \quad (5.52)$$

and the “skin-number”:

$$\chi \equiv \frac{d_e}{\lambda_E^t} = \frac{c}{\omega_{pe}\lambda_E^t}. \quad (5.53)$$

Additionally, we considered an electric field with a spectral distribution identical to Eq. (3.62) – with $\delta\mathbf{B}_k \rightarrow \mathbf{E}_k$. Furthermore, the simulation procedure was identical – with the exception that $\mathbf{E} \parallel \mathbf{k}$, rather than perpendicularly to the wave-vector.

This form of turbulence may be realized in a number of ways. “Cold” Whistler turbulence with $\chi \gg 1$ – i.e. the opposite regime to that considered in the previous sections – has an electric field which is approximately electrostatic; i.e. resembling an anisotropic realization of Langmuir turbulence (ignoring the magnetic field), with $\Omega_r(\mathbf{k}) \approx \Omega_{ce} \cos(\theta_k)$. For strictly sub-Larmor-scale magnetic fields, the correlation length transit time is much shorter than the average gyro-period – hence the electric field is effectively time-independent. Conceptually, the electric field may be comparable in strength to the magnetic field in this regime. Consequently, it may be necessary to include its contribution. Figure 5.15 shows the electric pitch-angle diffusion coefficient as a function of particle velocity. In each scenario, 10000

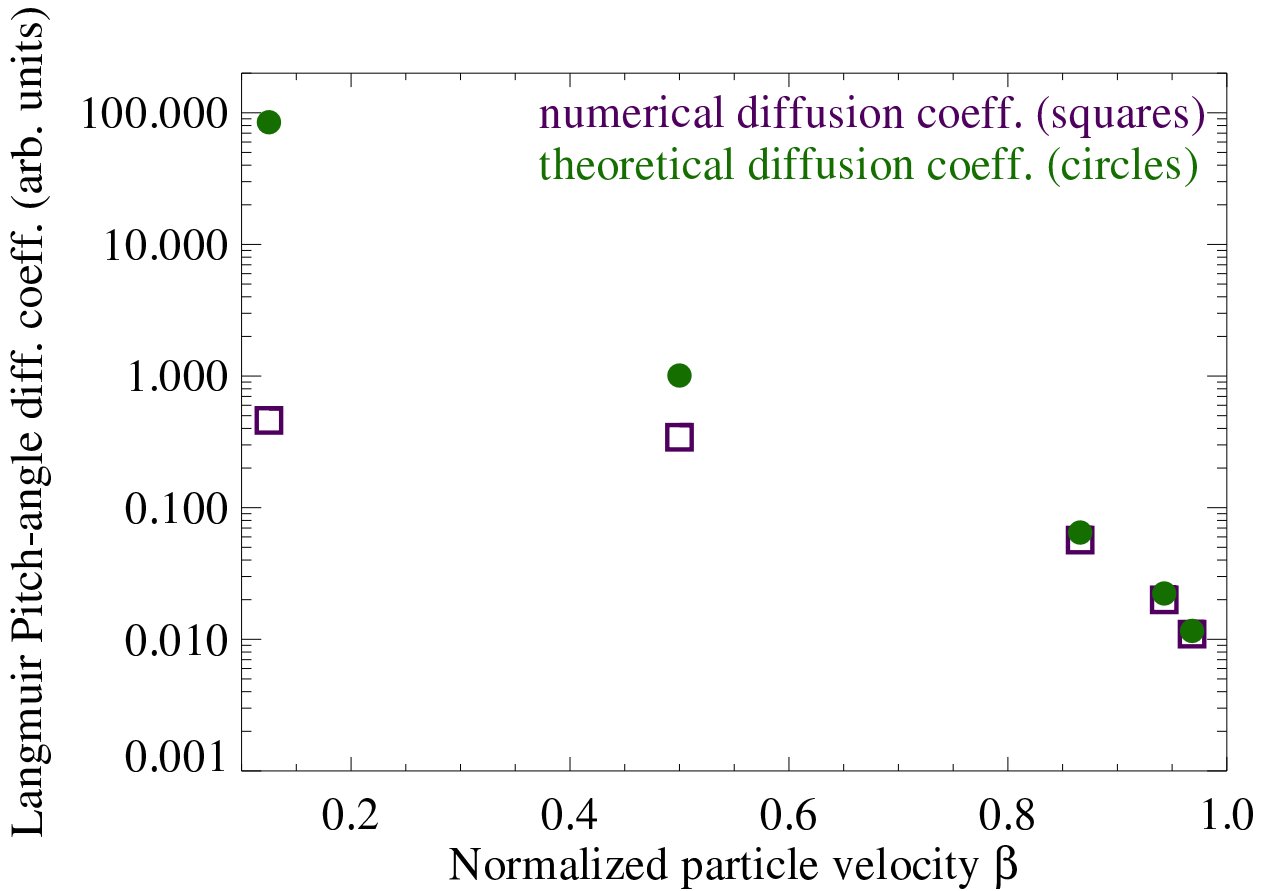


Figure 5.15: Electric pitch-angle diffusion coefficient, $D_{\alpha\alpha}^{\text{elec.}}$ vs the normalized electron velocity, β for small-scale Langmuir turbulence. Relevant simulation parameters include: $k_{\min} = 8\pi$, $k_{\max} = 10k_{\min}$, $\langle \Omega_E^2 \rangle = 4.0$, $\chi \approx 666.67$, $\delta_j \approx 0.08$, and $\mu = 5$. The (purple) empty “squares” indicate the $D_{\alpha\alpha}^{\text{elec.}}$ ’s obtained directly from simulation data, while the (green) filled “circles” are the analytical pitch-angle diffusion coefficients, given by Eq. (5.11). Notice that the small deflection approximation, which is the foundational assumption behind Eq. (5.11), holds well for velocities that are mildly relativistic ($\gamma \sim 2$).

monoenergetic electrons were injected into Langmuir turbulence with $\delta_j \approx 0.08$, $\chi \approx 666.67$, $k_{\min} = 8\pi$, $k_{\max} = 10k_{\min}$, and $\langle \Omega_E^2 \rangle = 4.0$ (all simulation units are arbitrary). The electron velocities vary for each run. We see that the numerical pitch-angle diffusion coefficient approaches the ultrarelativistic result as $v \rightarrow c$. Furthermore, we see fairly close agreement, even in the mildly relativistic ($\gamma \sim 2$) regime. The large discrepancy seen from the most leftward data points may be attributed to the breakdown of the small deflection angle approximation, which accompanies the existence of a comparable longitudinal acceleration.

5.4 Discussion of Results

In this Chapter, we explored test particle transport (diffusion) in magnetized plasmas with small-scale electromagnetic turbulence. Principally, in the case of pure (mean-free) magnetic turbulence, we demonstrated that in the regime of small deflections, i.e. when the particle's deflection angle over a correlation length is small $\alpha_\lambda \ll 1$, the pitch-angle diffusion coefficient is wholly determined by the particle velocity and the statistical/spectral properties of the magnetic turbulence; which is a result most transparently offered by Eqs. (3.61). Additionally, we showed that the condition of a small deflection angle is satisfied if $\rho > 1$, i.e. if the magnetic turbulence is small-scale. These results generalize the ultra-relativistic regime first discussed by Keenan and Medvedev (Keenan & Medvedev, 2013).

In fact, the pitch-angle diffusion coefficient, Eq. (5.7), remains unchanged by the addition of a mean field – so long as the pitch-angle, α assumes its conventional meaning, i.e. as the angle between the electron velocity vector and the ambient (mean) magnetic field. Since magnetized plasmas characterized by instability often include random electric fields, as is the case for the Whistler turbulence considered here, we additionally considered test particle energy diffusion. We showed that the energy diffusion coefficient in small-scale Whistler turbulence is directly proportional to the (magnetic) pitch-angle diffusion coefficient – see Eq. (5.50). Thus, it is also intimately related to the field's statistical properties. Consequently,

transport via energy diffusion may provide, yet another, powerful diagnostic tool for the investigation of small-scale electromagnetic fluctuations in magnetized plasmas.

Whistler turbulence, as conceived here, is dominated by the magnetic field. In contrast, the purely electrostatic Langmuir turbulence is characterized by random electric fields. We showed that a generalization of the magnetic pitch-angle diffusion coefficient exists for the case of relativistic electrons moving through small-scale electric turbulence. We, further, confirmed our analytic result via first-principle numerical simulations of Langmuir turbulence.

Chapter 6

Radiation From Charged Particles Moving Through Small-Scale Electromagnetic Turbulence

6.1 Introduction

In this Chapter, we develop the general theory of radiation production in small-scale electromagnetic turbulence. This is an extension to the “jitter” radiation theory originated by (Medvedev, 2000). The jitter theory, strictly, applies to the ultrarelativistic regime. Here, we generalize the jitter regime to all velocities. Additionally, we present results for the case of small-scale magnetic fields with a mean value. Finally, we confirm these theoretical derivations with our first-principle numerical simulations.

6.2 The Classic Jitter Theory

The ultra-relativistic radiation regime in sub-Larmor-scale magnetic turbulence is well understood. As mentioned in the previous Chapter, this regime is characterized by a single parameter, the ratio of the deflection angle, α_λ , to the relativistic beaming angle, $\Delta\theta \sim 1/\gamma_e$.

The ratio (Medvedev, 2000; Medvedev et al., 2011; Keenan & Medvedev, 2013):

$$\frac{\alpha_\lambda}{\Delta\theta} \sim \frac{eB_\perp\lambda_B}{m_e c^2} \sim 2\pi \frac{e\langle B^2 \rangle^{1/2}}{m_e c^2 k_{\text{mag}}} \equiv \delta_j \quad (6.1)$$

is known as the *jitter parameter*. From this, we recover four distinct radiation regimes. Firstly, if $\delta_j \rightarrow \infty$, the regime is the classical synchrotron radiation regime; the particle orbits are circular in the plane orthogonal to a perfectly homogeneous magnetic field. Secondly, with $\delta_j > \gamma_e$, the regime is very similar to synchrotron, but the particle's guiding center is slowly drifting, due to slight inhomogeneity in the magnetic field. The produced spectrum is well represented by the synchrotron spectrum, and it evolves slowly in time due to the particle diffusion through regions of differing field strength. This regime may be referred to as the diffusive synchrotron regime.

Thirdly, when $1 < \delta_j < \gamma_e$, the particle does not complete its Larmor orbit because the B -field varies on a shorter scale. In this case, which is depicted in Figure 6.1, an onlooking observer would see radiation from only short intervals of the particle's trajectory (i.e., whenever the trajectory is near the line-of-sight), as in synchrotron, but these intervals are randomly distributed. This is the case of the large-angle jitter regime. The radiation is similar to synchrotron radiation near the spectral peak and above, but differs significantly from it at lower frequencies (Medvedev et al., 2011). Finally, If $\delta_j \ll 1$, which is also depicted in Figure 6.1, a distant observer on the line-of-sight will see the radiation along, virtually, the entire trajectory of the particle (which will be approximately straight with small, random, transverse deviations. This is known as small-angle jitter radiation (Medvedev, 2000, 2006; Medvedev et al., 2011). The resulting radiation markedly differs from synchrotron radiation, although the total radiated power of radiation, $P_{\text{tot}} \equiv dW/dt$, produced by a particle in all these regimes, e.g., jitter and synchrotron, is identical:

$$P_{\text{tot}} = \frac{2}{3} r_e^2 c \gamma_e^2 \langle \delta B_\perp^2 \rangle. \quad (6.2)$$

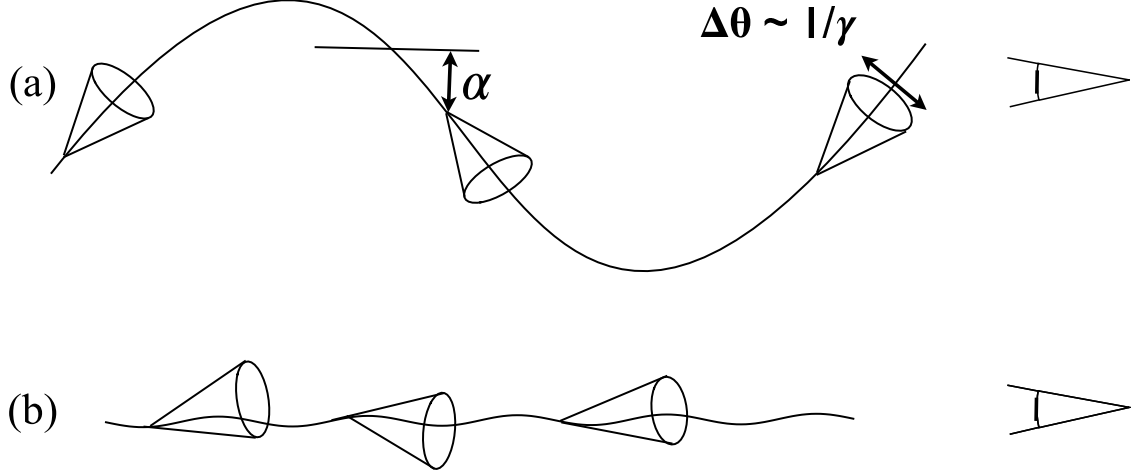


Figure 6.1: Radiation regimes. (a) Large-angle jitter regime, $1 < \delta < \gamma_e$; radiation is only seen along certain segments of the particle path, thus resulting in the spectrum that is synchrotron-like at and above the peak but differing from synchrotron at low frequencies. (b) Small-angle jitter regime, $\delta < 1$; radiation is seen from the entire trajectory, thus the spectrum depends on the underlying spectrum of electromagnetic turbulence.

For ultra-relativistic electrons, the radiation spectra are wholly determined by δ_j and the magnetic spectral distribution. It has been shown (Medvedev, 2006; Medvedev et al., 2011; Reville & Kirk, 2010; Teraki & Takahara, 2011) that monoenergetic relativistic electrons in the sub-Larmor-scale magnetic turbulence given by Eq. (3.62) produce a flat angle-averaged spectrum below the spectral break and a power-law spectrum above the break, that is:

$$P(\omega) \propto \begin{cases} \omega^0, & \text{if } \omega < \omega_j, \\ \omega^{-\mu+2}, & \text{if } \omega_j < \omega < \omega_b, \\ 0, & \text{if } \omega_b < \omega, \end{cases} \quad (6.3)$$

where the spectral break is:

$$\omega_j = \gamma_e^2 k_{\min} c, \quad (6.4)$$

which is called the jitter frequency. Similarly, the high-frequency break is:

$$\omega_b = \gamma_e^2 k_{\max} c. \quad (6.5)$$

6.3 Generalizations of Jitter Radiation

6.3.1 Pseudo-Cyclotron Radiation

In contrast, radiation from non-relativistic particles is not beamed along a narrow cone of opening angle, $\Delta\theta$. The jitter parameter is, consequently, without meaning in the non-relativistic radiation regime. Instead, the “dimensionless scale” (or “gyro-number”), i.e. ρ , is the only meaningful parameter. Given the magnetic spectral distribution exhibited by Eq. (3.62), $k_{\text{mag}} \sim k_{\min}$, so:

$$\rho = k_{\min} r_L. \quad (6.6)$$

As we shall see below, the radiation spectrum in this regime markedly differs from the single-harmonic cyclotron spectrum. We call this radiation, when it is produced by particles moving through **mean-free** magnetic turbulence, “pseudo-cyclotron” radiation or “non-relativistic jitter” radiation.

Regardless of the regime, the radiation spectrum seen by a distant observer is obtained from Eq. (4.3); which, If $v \ll c$, simplifies to:

$$\frac{d^2W}{d\omega d\eta} = \frac{e^2}{4\pi^2 c} \left| \int_{-\infty}^{\infty} \hat{\mathbf{n}} \times (\hat{\mathbf{n}} \times \dot{\beta}) e^{i\omega t} dt \right|^2, \quad (6.7)$$

Next, integrating Eq. (6.7) over all solid-angles gives the radiated energy per frequency, i.e.

$$\frac{dW}{d\omega} = \frac{2e^2}{3\pi c^3} |\mathbf{w}_\omega|^2, \quad (6.8)$$

where \mathbf{w}_ω is the Fourier component of the electron’s acceleration with frequency, ω . Eq. (6.8), valid for $v \ll c$, is known as the dipole approximation (Landau & Lifshitz, 1975). This expression may also be obtained from the Larmor formula, i.e.

$$P_{\text{tot}} = \frac{2}{3} \frac{e^2}{c^3} |\mathbf{w}|^2, \quad (6.9)$$

using the identity (Landau & Lifshitz, 1975):

$$\frac{1}{2} \int_{-\infty}^{\infty} |\mathbf{w}(t)|^2 dt = (2\pi)^{-1} \int_0^{\infty} |\mathbf{w}_\omega|^2 d\omega. \quad (6.10)$$

To proceed further, we use our previous assumption that the particle deflection angle over a field correlation length is small (i.e. $\alpha_\lambda \ll 1$). This condition implies the validity of the “perturbative” approach, whereby the particle trajectory is approximated as a straight line. For a particle moving in a magnetic field, $|\mathbf{w}_\omega|^2$ is given by the Lorentz force. In this limiting case of small deflections, we may write:

$$|\mathbf{w}_\omega|^2 = \left(\frac{e\beta}{m_e} \right)^2 (\delta_{ij} - \hat{v}_i \hat{v}_j) \delta B_\omega^{i*} \delta B_\omega^j, \quad (6.11)$$

where $\delta \mathbf{B}_\omega$ is the temporal variation of the magnetic field along the trajectory of the electron, i.e.

$$\delta \mathbf{B}_\omega = (2\pi)^{-4} \int e^{i\omega t} dt \int \delta \mathbf{B}_{\mathbf{k},\Omega} e^{i\mathbf{k}\cdot\mathbf{r}(t)-i\Omega t} d\mathbf{k} d\Omega. \quad (6.12)$$

Since the trajectory is approximately straight, $\mathbf{r}(t) \approx \mathbf{r}_0 + \mathbf{v}t$, consequently:

$$\delta \mathbf{B}_\omega = (2\pi)^{-4} \int e^{i\mathbf{k}\cdot\mathbf{r}_0} \delta \mathbf{B}_{\mathbf{k},\Omega} d\mathbf{k} d\Omega \int e^{i(\omega+\mathbf{k}\cdot\mathbf{v}-\Omega)t} dt, \quad (6.13)$$

After the time integration, this becomes:

$$\delta \mathbf{B}_\omega = (2\pi)^{-3} \int \delta(\omega + \mathbf{k} \cdot \mathbf{v} - \Omega) e^{i\mathbf{k}\cdot\mathbf{r}_0} \delta \mathbf{B}_{\mathbf{k},\Omega} d\mathbf{k} d\Omega. \quad (6.14)$$

Now, since the magnetic turbulence is assumed to be homogeneous (at least over a time scale greater than the particle transit time) the product of $\delta B_\omega^{i*} \delta B_\omega^j$ along a particular trajectory starting at \mathbf{r}_0 is representative of the magnetic field as a whole (Medvedev et al., 2011). Thus, we may consider only the volume-average of $\delta B_\omega^{i*} \delta B_\omega^j$. Performing the integration

leads to:

$$\langle \delta B_{\omega}^{i*} \delta B_{\omega}^j \rangle_{\mathbf{r}_0} = (2\pi)^{-3} V^{-1} \int \delta(\omega + \mathbf{k} \cdot \mathbf{v} - \Omega) \delta B_{\mathbf{k}, \Omega}^i \delta B_{\mathbf{k}, \Omega}^{j*} d\mathbf{k} d\Omega. \quad (6.15)$$

The quantity, $\delta B_{\mathbf{k}, \Omega}^{i*} \delta B_{\mathbf{k}, \Omega}^j$, is proportional to the Fourier image of the two-point auto-correlation tensor – i.e. Eq. (3.59). Thus, with Eqs. (6.8), (6.11), (6.15), and (3.59), the angle-averaged radiation spectrum of a non-relativistic electron moving in static, statistically homogeneous and isotropic sub-Larmor-scale magnetic turbulence is:

$$\frac{dW}{d\omega} = \left(\frac{Tr_e^2 \beta^2 c}{12\pi^3 V} \right) \int \delta(\omega + \mathbf{k} \cdot \mathbf{v}) \left[1 + (\hat{\mathbf{k}} \cdot \hat{\mathbf{v}})^2 \right] |\delta \mathbf{B}_k|^2 d\mathbf{k}, \quad (6.16)$$

where T is the duration of the observation, and where we have used:

$$\delta(\omega + \mathbf{k} \cdot \mathbf{v}) = \int \delta(\omega + \mathbf{k} \cdot \mathbf{v} - \Omega) \delta(\Omega) d\Omega. \quad (6.17)$$

We see that the radiation spectrum is fully determined by the magnetic spectral distribution, $|\delta \mathbf{B}_k|^2$. It is instructive to consider one of the simplest such distributions – the isotropic spectrum of a magnetic field at a single scale, k_{mag} , i.e.

$$|\delta \mathbf{B}_k|^2 = (2\pi)^3 V \langle \delta B^2 \rangle \frac{\delta(k - k_{\text{mag}})}{4\pi k_{\text{mag}}^2}. \quad (6.18)$$

Substitution of Eq. (6.18) into Eq. (6.16) produces the radiation spectrum:

$$\frac{dW}{d\omega} = \begin{cases} \frac{T}{3k_{\text{mag}}} r_e^2 \beta \langle \delta B^2 \rangle \left(1 + \frac{\omega^2}{\omega_{\text{jn}}^2} \right), & \text{if } \omega \leq \omega_{\text{jn}} \\ 0, & \text{if } \omega > \omega_{\text{jn}}, \end{cases} \quad (6.19)$$

where $\omega_{\text{jn}} = k_B v$. Given the magnetic spectral distribution of Eq. (3.62), the corresponding

non-relativistic jitter spectrum, is:

$$\frac{dW}{d\omega} \propto \begin{cases} A + D\omega^2, & \text{if } \omega \leq \omega_{jn} \\ F\omega^{-\mu+2} + G\omega^2 + K, & \text{if } \omega \leq \omega_{bn} \\ 0, & \text{if } \omega > \omega_{bn}, \end{cases} \quad (6.20)$$

where $\mu \neq 2$ and

$$A \equiv \frac{v}{2-\mu} (k_{\max}^{-\mu+2} - k_{\min}^{-\mu+2}), \quad (6.21)$$

$$D \equiv -\frac{1}{v\mu} (k_{\max}^{-\mu} - k_{\min}^{-\mu}), \quad (6.22)$$

$$F \equiv \frac{v^\mu}{v} \left(\frac{1}{\mu-2} + \frac{1}{\mu} \right), \quad (6.23)$$

$$G \equiv -\frac{1}{v\mu} k_{\max}^{-\mu}, \quad (6.24)$$

$$K \equiv \frac{v}{2-\mu} k_{\max}^{-\mu+2}, \quad (6.25)$$

with the jitter frequency given by the characteristic, and largest, spatial scale:

$$\omega_{jn} = k_{\min} v. \quad (6.26)$$

Finally, the break frequency is indicated by the smallest spatial scale, i.e. the maximum wave number:

$$\omega_{bn} = k_{\max} v. \quad (6.27)$$

Notice the structural similarity between the spectrum at frequencies less than ω_{jn} and the delta function spectrum in Eq. (6.19).

Next, the total radiated power may be obtained by integrating Eq. (6.16) over all frequencies and dividing by the total observation time, yielding:

$$P_{tot} = \frac{2}{3} r_e^2 \beta^2 c \langle \delta B_\perp^2 \rangle, \quad (6.28)$$

where we have used Eq. (5.5). Compare this to the total power radiated by a non-relativistic electron moving through a uniform magnetic field,

$$P_{tot} = \frac{2}{3} r_e^2 \beta^2 c \delta B_\perp^2, \quad (6.29)$$

which follows directly from Eq. (6.9). Evidently, the total power of non-relativistic jitter radiation is identical to the total power of cyclotron radiation – with $B_0^2 \rightarrow \langle \delta B^2 \rangle$; this is exactly analogous to the relation between synchrotron and relativistic jitter radiation.

6.3.2 Jitter Radiation From Mildly Relativistic Particles

The radiation spectrum, generalized to any velocity, may be obtained by a formal Lorentz transformation to the electron rest frame. Consider a relativistic electron moving with velocity β in the (unprimed) laboratory frame. By employing the Lorentz invariant phase space volume, $d^3k/\omega(k)$ – the radiation spectra between the two frames can readily be related by the equality (Jackson, 1998):

$$\frac{1}{\omega^2} \frac{d^2W}{d\omega d\eta} = \frac{1}{\omega'^2} \frac{d^2W'}{d\omega' d\eta'}. \quad (6.30)$$

Thus, the angle-averaged laboratory radiation spectrum is obtained by integration over all solid-angles (in the lab frame) of the electron rest frame spectrum, i.e.

$$\frac{dW}{d\omega} = \int \frac{\omega^2}{\omega'^2} \frac{d^2W'}{d\omega' d\eta'} d\eta. \quad (6.31)$$

We consider, once more, that the electron moves along a straight path, experiencing only small deviations in its trajectory. Consequently, we consider a Lorentz boost of the laboratory coordinates along the trajectory (z-axis). In the electron's rest frame, the field turbulence has both a time-dependent magnetic and electric component. However, since the electron is at rest in this frame, only the electric field contributes to the instantaneous particle acceleration.

Via Lorentz transformation of the laboratory magnetic field, the co-moving electric field is simply:

$$\mathbf{E}'(\mathbf{x}', t') = \gamma_e \boldsymbol{\beta} \times \delta\mathbf{B}(\mathbf{r}), \quad (6.32)$$

where $\mathbf{r}(t) = \mathbf{r}_0 + \mathbf{v}t$. Since the electron is instantaneously at rest in this frame, we may choose $\mathbf{x}' = 0$; thus, $t = \gamma_e t'$. The corresponding equation of motion, for the electron, is then:

$$m_e \mathbf{w}'(t') = e \mathbf{E}'(0, t') = e \gamma_e \boldsymbol{\beta} \times \delta\mathbf{B}(\mathbf{r}). \quad (6.33)$$

As before, the radiation spectrum in the rest frame is given by the Dipole approximation, Eq. (6.7). Substitution of these results into Eq. (6.31) leads to:

$$\frac{dW}{d\omega} = \frac{e^2}{4\pi^2 \gamma_e^2 c^3} \int \frac{|\mathbf{w}'_{\omega'}|^2 \sin^2 \Theta'}{(1 - \beta \cos \theta)^2} d(\cos \theta) d\phi, \quad (6.34)$$

where Θ' is the angle between the wave and acceleration vectors in the electron rest frame, and we have used the relativistic Doppler formula $\omega' = \gamma_e \omega (1 - \hat{\mathbf{n}} \cdot \boldsymbol{\beta})$. Next, given the equivalent form of Eq. (6.33) to the lab frame equation of motion, Eq. (6.11), the acceleration term is given by the non-relativistic jitter spectrum with the substitution, $\omega' \rightarrow \omega'/\gamma_e = \omega(1 - \beta \cos \theta)$.

The final task is to perform the integration. However, the angle Θ' must first be related to the laboratory θ and ϕ coordinates – which are derived from the angle between the wave vector and the velocity, and the azimuthal angle with respect to the boost axis, respectively. With a transverse acceleration, these angles are related by (Rybicki & Lightman, 1986):

$$\sin^2 \Theta' = 1 - \frac{\sin^2 \theta \cos^2 \phi}{\gamma_e^2 (1 - \beta \cos \theta)^2}, \quad (6.35)$$

with $\phi' = \phi$. Thus, the angle-averaged (velocity-independent) jitter spectrum is given by the

following integration of the non-relativistic jitter spectrum:

$$\frac{dW}{d\omega} = \frac{3}{8\gamma_e^2} \int_{-1}^1 dx \left[\frac{1}{(1-\beta x)^2} + \frac{(x-\beta)^2}{(1-\beta x)^4} \right] I(\omega_0), \quad (6.36)$$

where $I(\omega_0)$ is the non-relativistic jitter spectrum, e.g. Eq. (6.16), evaluated at $\omega_0 \equiv \omega(1 - \beta x)$. This result leads to the traditional, ultra-relativistic, jitter spectrum in the limit of $\beta \rightarrow 1$ (or, equivalently, $\gamma_e \rightarrow \infty$). In the trans-relativistic regime, the characteristic frequencies, Eqs. (6.4) and (6.5), generalize to:

$$\omega_{jn} \equiv \gamma_e^2 k_{\min} v, \quad (6.37)$$

and

$$\omega_{bn} \equiv \gamma_e^2 k_{\max} v, \quad (6.38)$$

which are the (trans-relativistic) jitter and break frequencies, respectively. It is noteworthy that ω_{bn} is not a proper break frequency in the mildly relativistic regime. The spectrum quickly falls to zero following ω_{bn} ; however, the drop is not instantaneous (as it is in the ultra-relativistic limit). In the trans-relativistic regime, $\gamma_e \simeq 1$, of course. With this in mind, and for the sake of convenience, we retain the n subscript for both the trans-relativistic and non-relativistic expressions.

6.3.3 The Jitter Parameter and the Gyro-number

What is the relationship between the jitter parameter, δ_j , and the gyro-number, ρ , at relativistic velocities? While the condition that $\delta_j < 1$ implies that $\rho > 1$, the converse is not necessarily true. Consider, for example, the following:

$$r_L < \lambda_B < \gamma_e r_L, \quad (6.39)$$

where r_L is the non-relativistic Larmor radius. This is a situation in which the correlation length is less than the relativistic Larmor radius, $\gamma_e r_L$, but greater than the non-relativistic Larmor analog. Thus, since $\delta_j = 1/\rho$ (with $\gamma_e = 1$), this describes the situation in which $\rho > 1$, but the jitter parameter is greater than unity. Equivalently:

$$1 < \delta_j < \gamma_e, \quad (6.40)$$

which implies that we are in the large-angle jitter regime.

6.3.4 Jitter Radiation From Magnetized Plasmas

The introduction of a mean magnetic field will complicate this picture. The topic of radiation production by ultrarelativistic electrons in magnetized plasmas with small-scale magnetic fluctuations has previously been considered (Toptygin & Fleishman, 1987; Reville & Kirk, 2010). In the case of strictly sub-Larmor-scale magnetic turbulence, with a mean field, the spectrum will simply be the sum of a synchrotron/cyclotron component (corresponding to the mean magnetic field) and the jitter contribution from the small-scale fluctuations, i.e.

$$P(\omega) = P_{\text{jitter}}(\omega) + P_{\text{synch}}(\omega). \quad (6.41)$$

When the electric field is stronger, or comparable, to the magnetic field, its contribution must be included. As discussed in the previous Chapter, the radiation from ultrarelativistic particles in the “small-scale” regime resembles jitter radiation. At non-relativistic velocities, however, the deflection angle may be fairly large – since the parallel acceleration on the electron cannot be neglected in this regime. Consequently, the radiation – in the non-relativistic case – may fall outside the small-angle jitter prescription.

Fortunately, since $\langle E^2 \rangle \ll \langle \delta B^2 \rangle$ for small-scale Whistler turbulence, we can completely ignore this electric contribution.

6.4 Simulation Results

In the previous sections, we made a number of theoretical predictions concerning the radiation properties of plasmas with small-scale turbulent electromagnetic fields. Here we check our predictions.

6.4.1 Trans-Relativistic Jitter Radiation

We first explored the (mean-free) trans-relativistic jitter radiation regime by calculating the radiation spectra, using Eq. (4.3), with variable simulation parameters. We aimed to test the radiation spectra's dependence upon the key turbulent parameters: k_{\min} , k_{\max} , $\langle \delta B^2 \rangle$, and μ , as well as the particle velocity, v . To start, we considered the k_{\min} dependence. In Figure 6.2, we have plotted spectra for an initially isotropically distributed, monoenergetic, ensemble of trans-relativistic electrons ($v = 0.5c$) moving through sub-Larmor-scale magnetic turbulence with three different values of k_{\min} . The key parameters are: $\rho = 18.1$, 36.3 , and 72.6 , with $k_{\min} = \pi/5$, $2\pi/5$, and $4\pi/5$, respectively (see Table 6.1 for a complete listing of simulation parameters used in every figure). The spectra of Figure 6.2, at least superficially, resemble our theoretical prediction; cf. Eq. (6.20). We have normalized the $dW/d\omega$ and ω axes by λ_B and k_{\min} , respectively. As expected, the frequency of the spectral peak scales by k_{\min} . The precise scaling of the peak frequency is revealed in Figure 6.3. In this figure, we have varied the particle velocities, keeping all other parameters fixed. Three velocities appear: $v = 0.125c$, $0.25c$, and $0.5c$. Clearly, the overall shape of the spectra is not strongly dependent upon the particle velocities. We have identified the proper scaling on the horizontal axis. With this result, and Figure 6.2, we may conclude that the frequency of the peak of the radiation spectrum is $\omega \sim \gamma_e^2 k_{\min} v = \omega_{jn}$. This is jitter frequency given in Eq. (6.20).

Next, we tested the μ dependence. In Figure 6.4, $\mu = 4, 5$. For each spectrum, $v = 0.125c$, and the total simulation time was T_g , where $T_g = e\langle \delta B^2 \rangle^{1/2}/\gamma_e m_e c$ is the gyroperiod. The numerical and analytical spectra show close agreement for frequencies less than the break

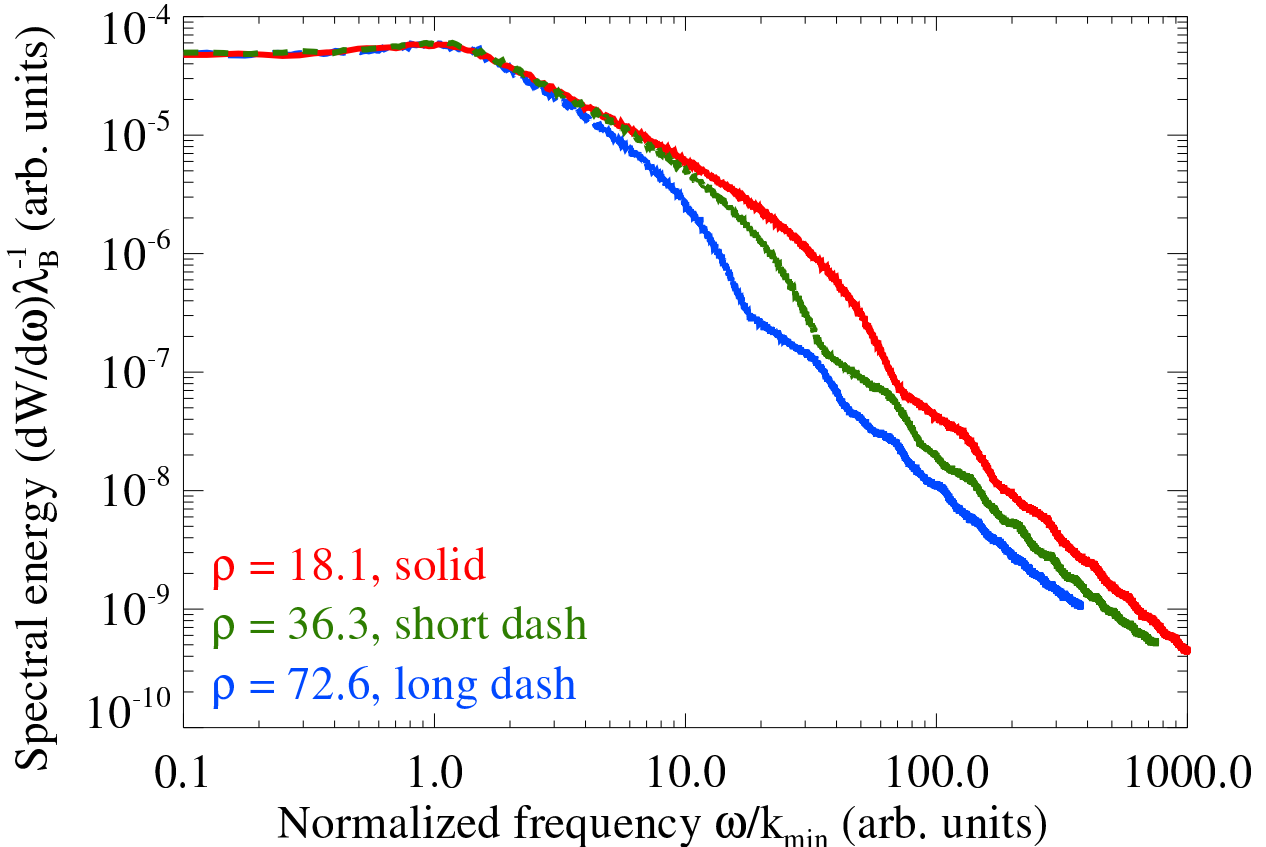


Figure 6.2: Radiation spectra given variable k_{\min} , with all other parameters fixed. The number of simulation particles, N_p , is 2000, and $v = 0.5c$ in each case. In each trial, the particles moved for a total simulation time of $T = T_g$, where $T_g \equiv 2\pi\gamma_e m_e c/e\langle\delta B^2\rangle^{1/2}$ is the “gyroperiod”. Here, the axes are in arbitrary, simulation units. We see that the frequency scales as k_{\min} and $dW/d\omega$ scales as λ_B .

#	ρ	Δt	β	μ	k_{\min}	k_{\max}	$\sqrt{\langle \delta B^2 \rangle}$	N_p	T_g
6.2	18.1	0.005	0.5	3	$\pi/5$	10.24π	0.02	2000	1
6.2	36.3	0.005	0.5	3	$2\pi/5$	10.24π	0.02	2000	1
6.2	72.6	0.005	0.5	3	$4\pi/5$	10.24π	0.02	2000	1
6.3	15.8	0.050	0.125	3	$4\pi/5$	10.24π	0.02	1000	10
6.3	32.4	0.050	0.25	3	$4\pi/5$	10.24π	0.02	1000	10
6.3	72.6	0.050	0.5	3	$4\pi/5$	10.24π	0.02	1000	10
6.4	6.18	0.005	0.125	4	π	8π	0.064	8000	1
6.4	6.18	0.005	0.125	5	π	8π	0.064	8000	1
6.5	6.34	0.005	0.25	5	$\pi/2$	4π	0.064	2000	1
6.5	6.34	0.005	0.25	5	$\pi/2$	8π	0.064	2000	1
6.6	12.4	0.05	0.125	100	π	8π	0.032	8000	10
6.7	7.9	0.05	0.125	4	$2\pi/5$	8π	0.02	4000	10
B.1	6.2	0.005	0.125	5	π	8π	0.064	5000	1
C.1	14.2	0.00125	0.5	4	8π	400π	1.024	1000	10
C.2	14.2	0.00125	0.5	4	8π	400π	1.024	1000	10

Table 6.1: Table of parameters used for the radiation spectra figures. Here, and elsewhere, Δt is the simulation time step, the simulation time is denoted in multiples of the “gyroperiod” (i.e. $T_g = 2\pi\gamma_e m_e c/e\langle \delta B^2 \rangle^{1/2}$), and N_p is the total number of simulation particles.

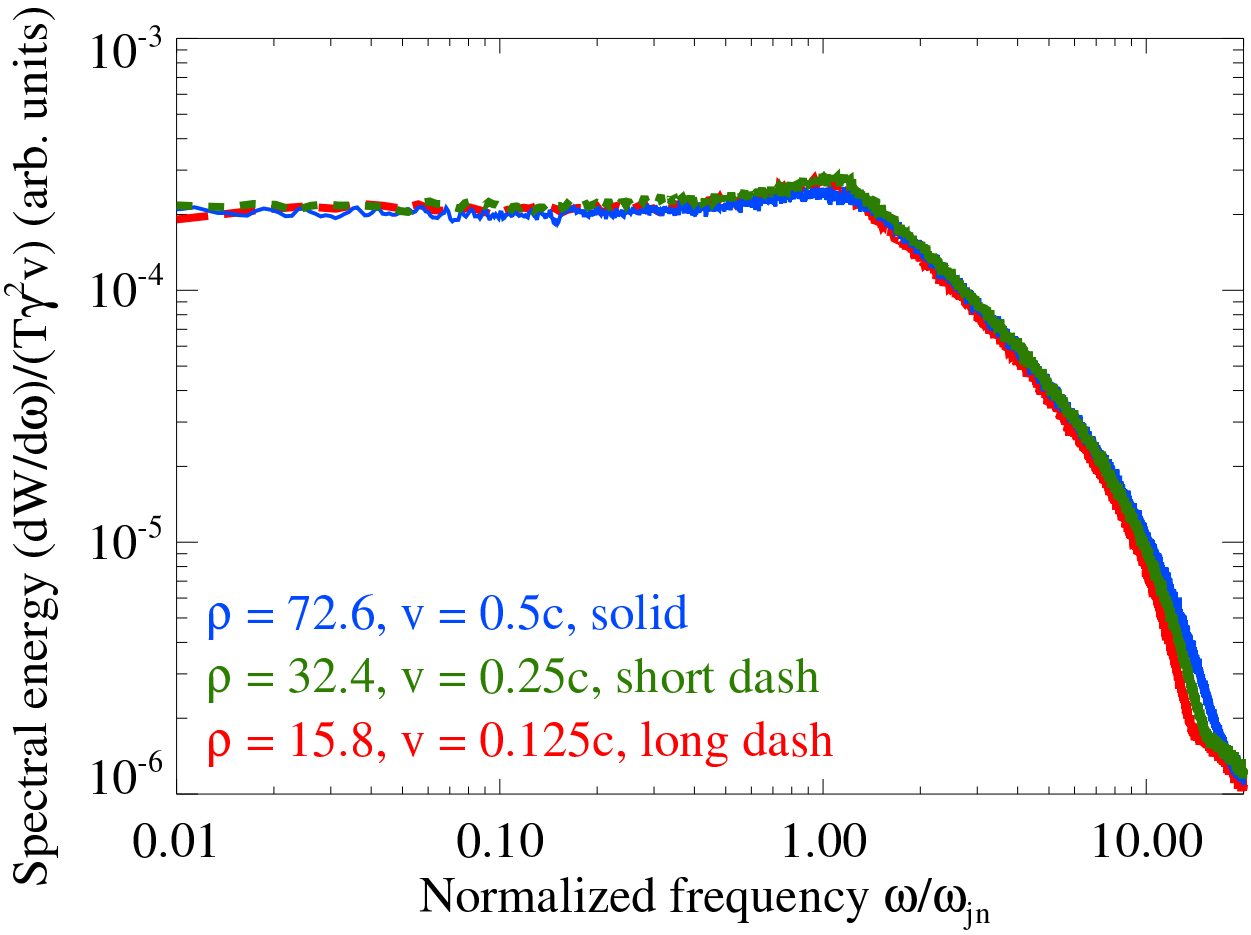


Figure 6.3: Radiation spectra given variable v . In each trial, 1000 particles move for a total simulation time of $T = 10T_g$, where $T_g \equiv 2\pi\gamma_e m_e c / e\langle\delta B^2\rangle^{1/2}$ is the “gyroperiod”. We see that the overall shape of the spectra is not appreciably altered with decreasing v . The spectra are normalized by $T\gamma_e^2 v$, vertically. Given Figure 6.2, we may conclude that the peak frequency of these spectra is $\omega \sim \gamma_e^2 k_{min} v$ – cf. Eq. (6.37).

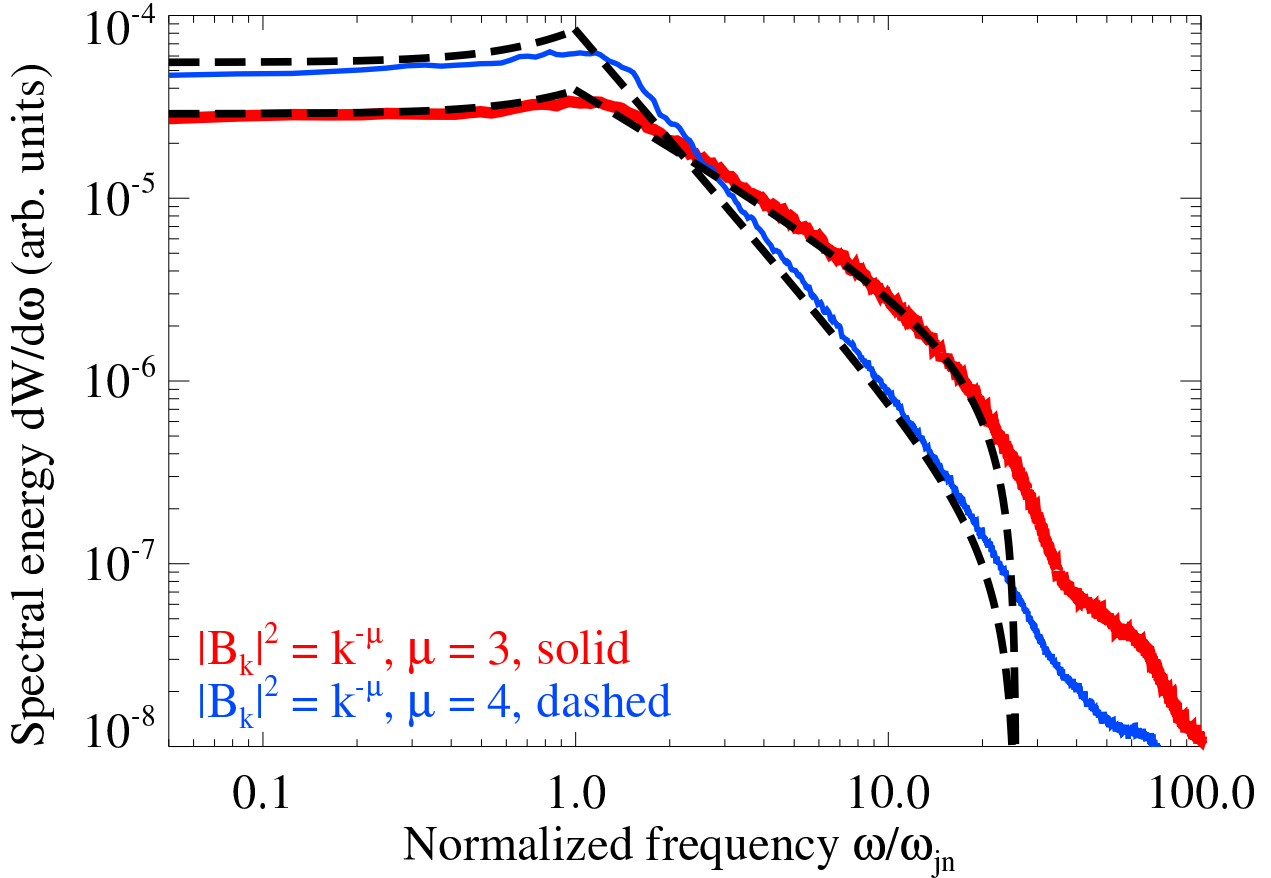


Figure 6.4: Radiation spectra given two different values of the magnetic spectral index: $\mu = 5$ (red) “thick” line and $\mu = 4$ (blue) “thin” line. Included are the analytical solutions given by Eq. (6.20). Note that the $\mu = 5$ solution has been multiplied by an overall factor of two for easier visualization. For frequencies near $\omega \sim \gamma_e^2 k_{\min} v$, the numerical spectra agree decently with the analytical results. However, for frequencies near the break, $\omega \sim \gamma_e^2 k_{\max} v$, there is considerable deviation between the predicted and numerical spectra – for both values of the magnetic spectral index. The origin of this discrepancy is explored in Appendix B.

frequency, $\omega \sim \gamma_e^2 k_{\max} v$. In Figure 6.5, we have plotted two spectra that differ in their k_{\max} values (all other parameters kept fixed). The k_{\max} values employed differ by a factor of 2. We see that, roughly, the spectra approach zero near $\omega \sim \gamma_e^2 k_{\max} v$. The proceeding power law “tail” feature is a numerical artifact that arises from a steep drop to zero power (this fact is more readily apparent in a linear plot – see Appendix A). Next, we examined the apparent structure in the radiation spectra for $\omega < \omega_{jn}$. This is most clearly seen in Figure 6.3, where it appears as a distinctive “bump”. According to Eq. (6.20), this bump-like feature has a functional form of $A + D\omega^2$. To assure that this form is correctly identified, we considered

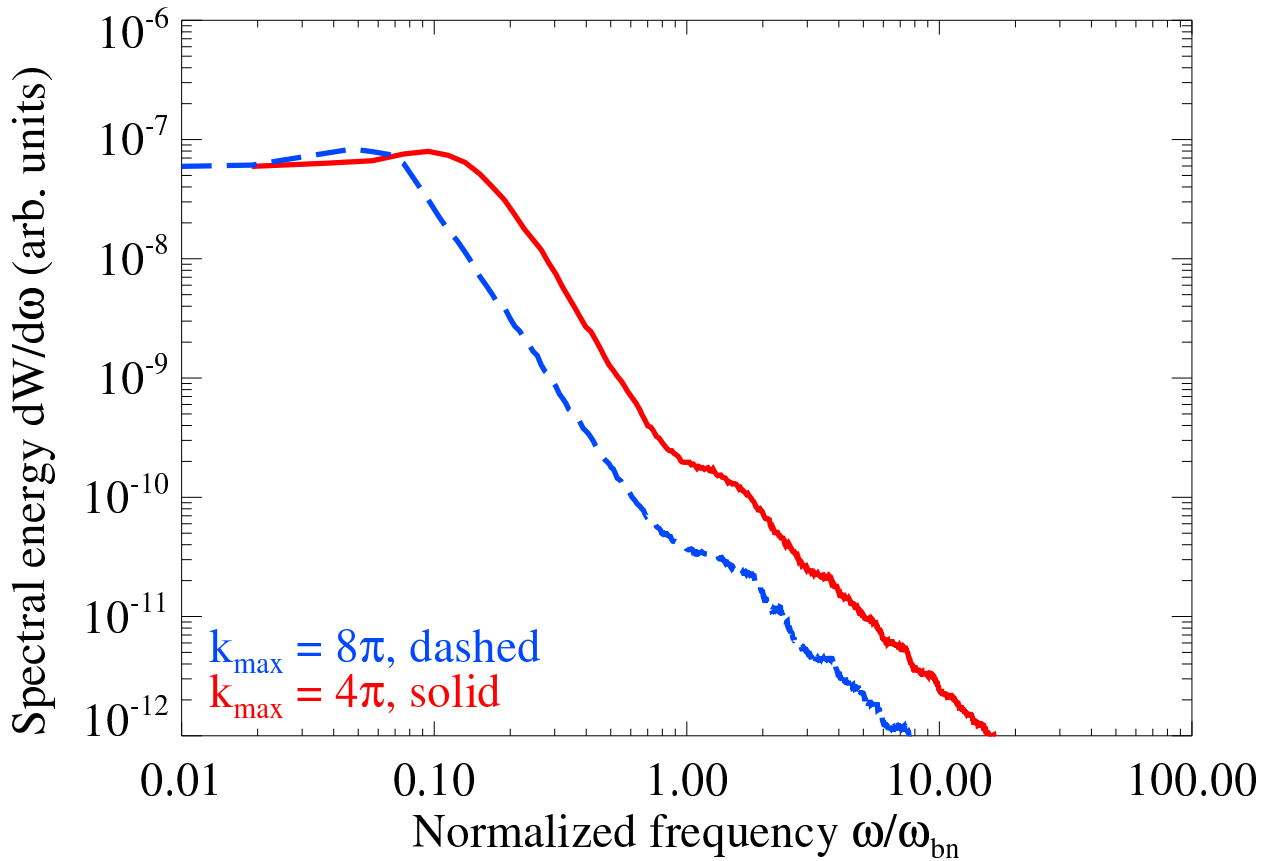


Figure 6.5: Radiation spectra with differing k_{\max} . Some other relevant parameters are $v = 0.25c$, $\rho = 6.34$, $N_p = 2000$, and $\mu = 5$ (for a complete listing, see Table 6.1). The two spectra differ by a factor of 2 in k_{\max} , with k_{\min} the same between them. Roughly, the spectra transition to the “tail” feature near $\omega \sim \gamma_e^2 k_{\max} v = \omega_{bn}$.

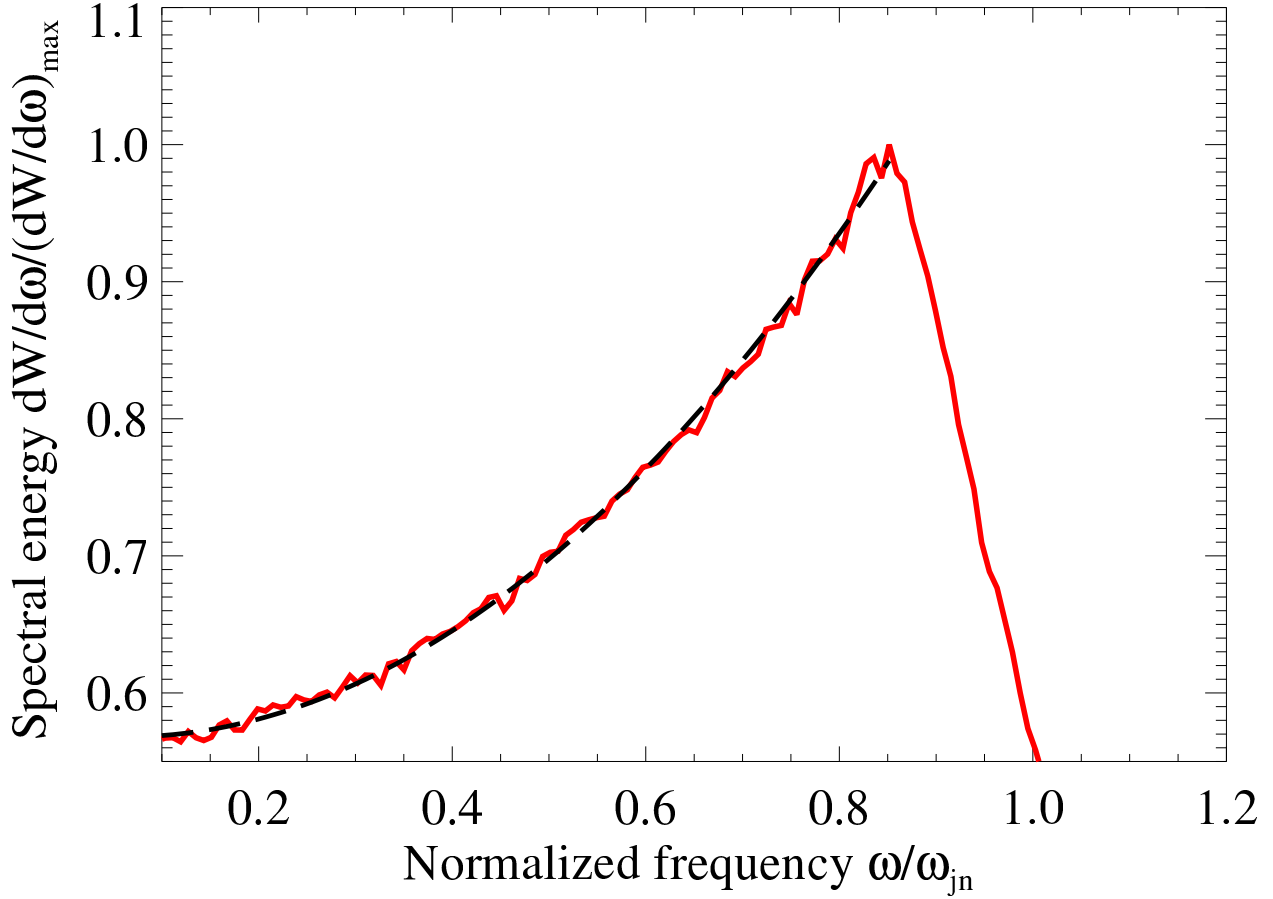


Figure 6.6: Radiation spectrum with $\mu = 100$ ($\beta = 0.125c$). Evidently, the spectral feature presented directly prior to ω_{jn} has a functional form given by $A + D\omega^2$ (dashed line). This is consistent with Eq. (6.20).

a large magnetic spectral index of $\mu = 100$ with $\beta = 0.125c$. Such a large μ makes the feature more prominent, helping to magnify it. As can be seen, the curve that best fits the bump-like feature at $\omega < \omega_{jn}$ is given by a function of the form $A + D\omega^2$.

6.4.2 Jitter Radiation From Monopoles

One may consider the magnetic correlation tensor and its relation to the shape of the radiation spectra. Anisotropic turbulence will alter the shape, but so will a change to the topology of the magnetic field. Motivated by pure curiosity, we consider turbulence that is generated by a distribution of magnetic monopoles. This will result in a magnetic field that is curl-free, but has a divergence given by Gauss's Law for monopoles. This topological

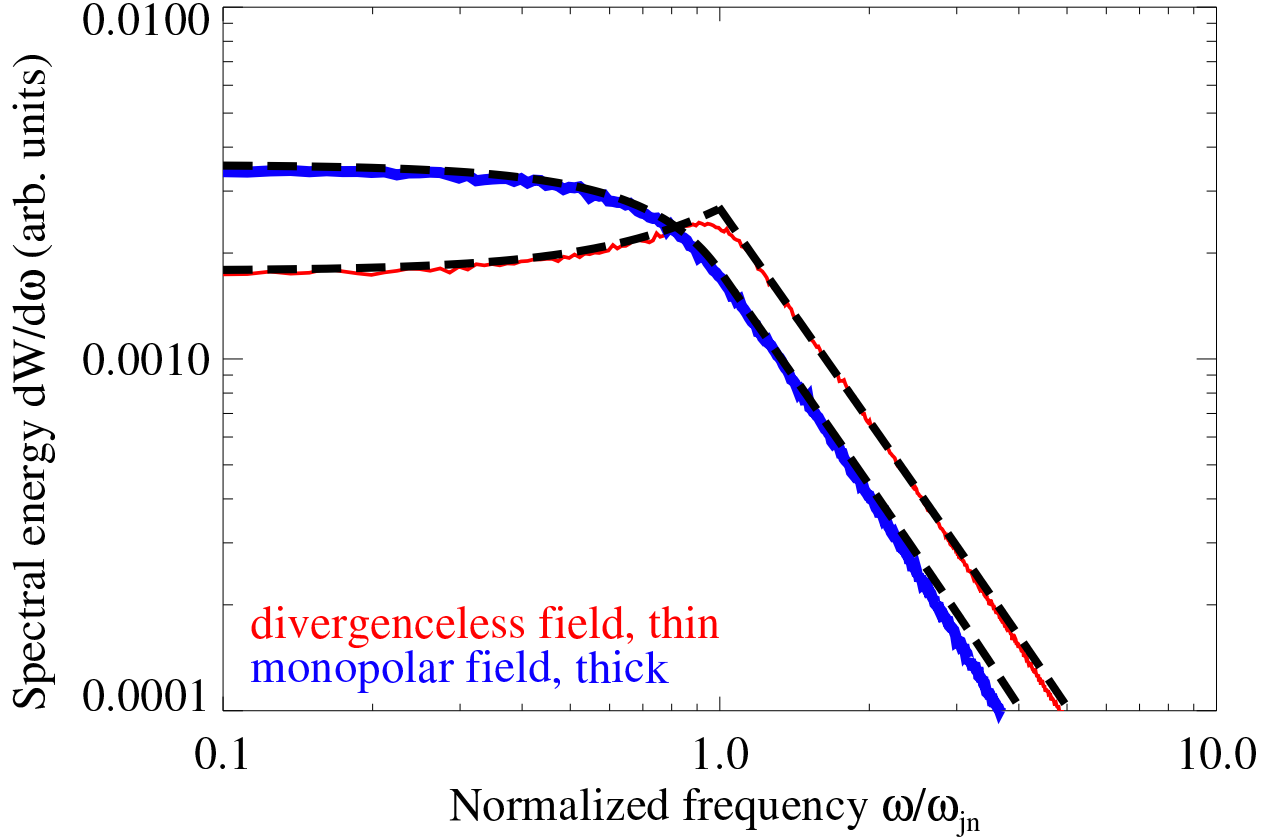


Figure 6.7: Radiation spectrum of non-relativistic electrons moving through small-scale magnetic turbulence generated by a distribution of magnetic monopoles (“thick”, blue), superimposed with the radiation spectrum given a magnetic spectrum (“thin”, red) produced by standard means (i.e. Ampere’s Law). For each run, $\mu = 4$ and $\beta = 0.125c$. Each curve is accompanied by its corresponding analytical solutions (“dashed”, black). The spectral shape for frequencies less than ω_{jn} is $A + D\omega^2$ and $A - D\omega^2$ for the “divergenceless” field and “monopolar” field, respectively.

change will alter the correlation tensor for isotropic and homogeneous turbulence to:

$$\delta B_{\mathbf{k}}^{i*} \delta B_{\mathbf{k}}^j = |\delta \mathbf{B}_k|^2 \hat{k}^i \hat{k}^j, \quad (6.42)$$

which is the form required for an irrotational vector field. Substitution of this correlation tensor into Eq. (6.8) will give a slightly different radiation spectrum for the magnetic spectrum in Eq. (3.62). The principal change will be to the quadratic prefactor $A + D\omega^2$. The “monopolar” field will result in a sign change to D . In Figure 6.7, this difference is clearly indicated. Notice the apparent lack of the quadratic peak feature at ω_{jn} .

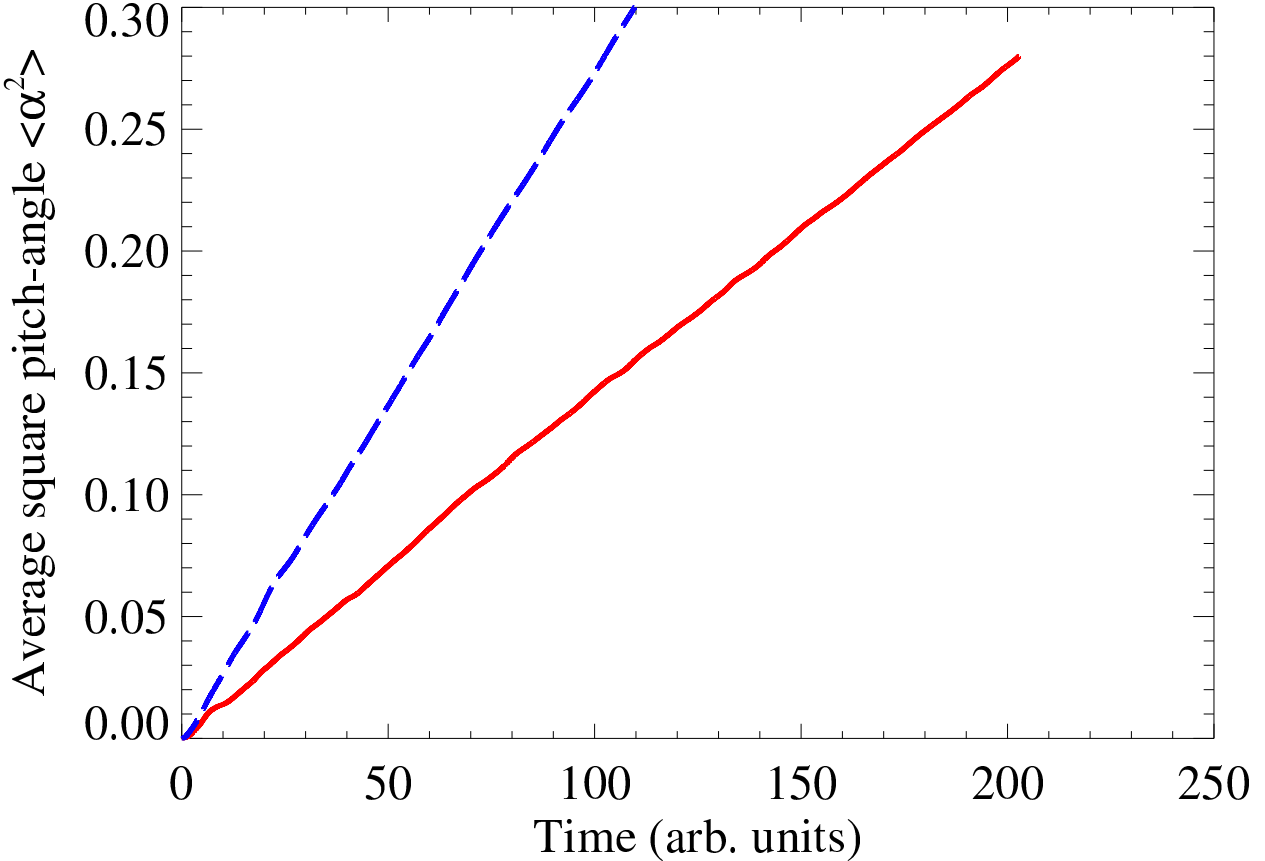


Figure 6.8: Average square pitch-angle growth as a function of time for non-relativistic electrons moving through small-scale magnetic turbulence generated by a distribution of magnetic monopoles “dashed” (blue), superimposed with the otherwise equivalent curve “solid” (red) produced by standard means (i.e. Ampere’s Law). For each run, $\mu = 6$, $N_p = 15420$, $\langle \delta B^2 \rangle^{1/2} = 0.032$, $k_{\min} = \pi$, $k_{\max} = 8\pi$, and $\beta = 0.125c$. Note that the slope of the “monopolar” curve is very nearly twice the slope of the standard curve – in accordance with Eq. (6.43).

The altered correlation tensor will affect the particle diffusion coefficient as well. In fact, as can be seen in Figure (6.8), the pitch-angle diffusion coefficient of particles moving in the monopolar field is twice as large as the divergenceless field equivalent. This follows from the fact that:

$$\lambda_B^{\text{monopole}} = 2\lambda_B^{\text{div. free}}, \quad (6.43)$$

which results from substitution of Eq. (6.42) into Eq. (3.55). It is a noteworthy observation that the preceding results are identical, up to overall multiplicative factors, to the radiation spectra and pitch-angle diffusion coefficient for the more physically plausible situation of

a trans-relativistic monopole moving through “small-scale” electrostatic turbulence, such as Langmuir turbulence.

6.4.3 Jitter Radiation From Magnetized Plasmas

Finally, we consider the radiation spectra when a mean magnetic field is present. As discussed previously, the radiation spectra are expected to be the summation of synchrotron (cyclotron) and jitter (pseudo-cyclotron) components. When calculating the radiation spectrum, however, the presence of the mean magnetic field complicates the process, since a previously non-existent anisotropy now appears. The “summed” spectrum will, as a result, depend upon the location of the observer. However, if the magnetic turbulence is statistically homogeneous/isotropic, then the synchrotron/cyclotron (mean field) component of the spectrum will, alone, possess this dependence. Since the angle-averaged synchrotron spectrum is a known function, we may simply add it to the jitter spectrum, obtained via the “summation” method above. For an ultrarelativistic electron, the angle-averaged synchrotron radiation spectrum is (Landau & Lifshitz, 1975; Jackson, 1998):

$$\frac{dW}{d\omega} = \sqrt{3} \frac{e^2}{c} \gamma_e \frac{\omega}{\omega_c} \int_{\omega/\omega_c}^{\infty} K_{5/3}(x) dx, \quad (6.44)$$

where $K_j(x)$ is a modified Bessel function of the second-kind, and $\omega_c = 3/2\gamma_e^2\Omega_{ce}$ is the critical synchrotron frequency. Strictly, this result applies for an electron moving in the plane transverse to the ambient magnetic field, i.e. when $\alpha = 0$. Nonetheless, we find the expression fits the synchrotron components fairly well; especially when γ_e is decently large. Strictly, this result applies for an electron moving in the plane transverse to the ambient magnetic field, i.e. when $\alpha = 0$. Nonetheless, we find the expression fits the synchrotron components fairly well; especially when γ_e is decently large.

We showcase two numerical spectra here for the case of small-scale Whistler turbulence, along with their corresponding analytical estimates. For cold Whistler waves, the contribu-

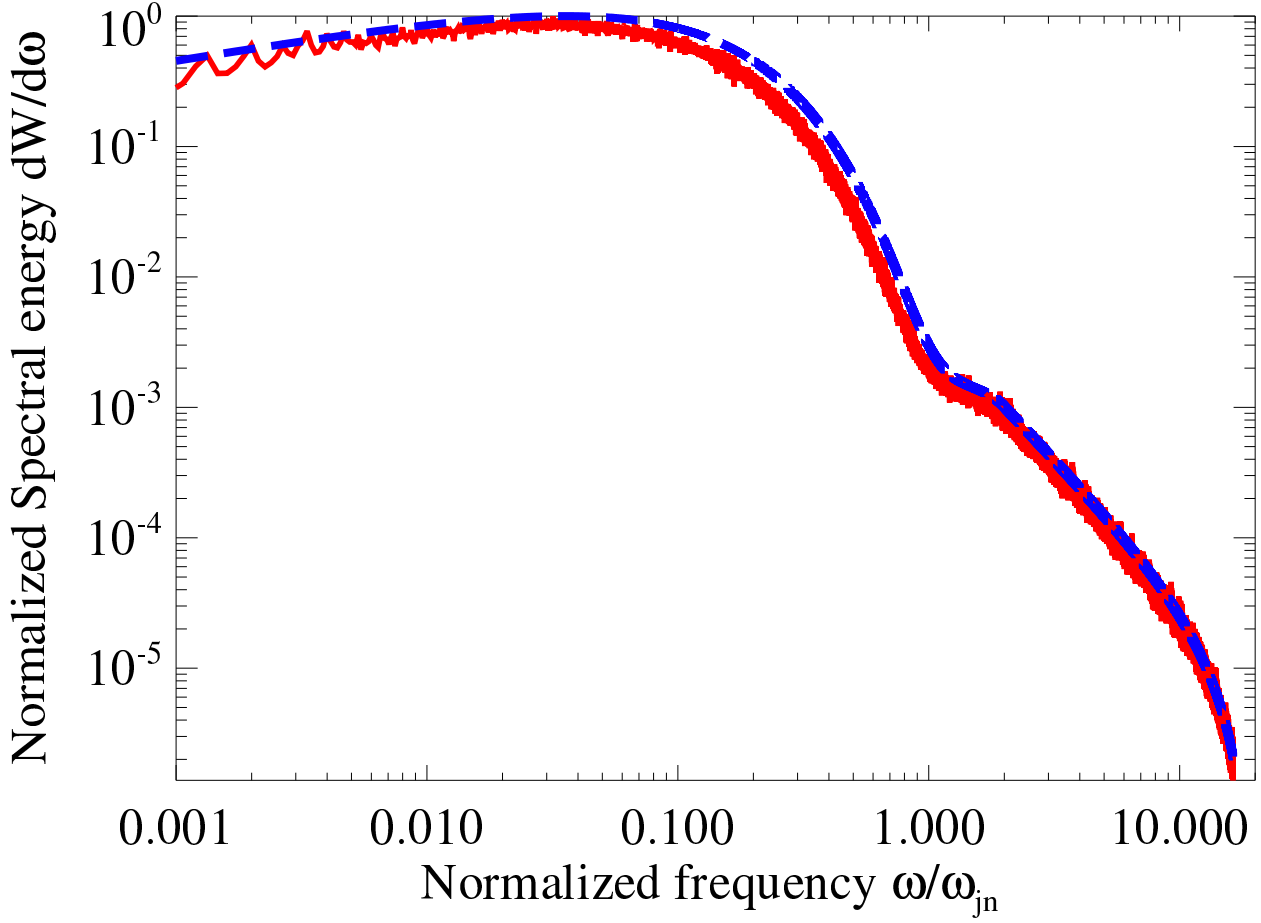


Figure 6.9: Radiation spectrum for a monoenergetic, isotropic distribution of $\gamma_e = 5$ ($\chi \sim 1$; $\rho \approx 928$; $\langle \delta B^2 \rangle^{1/2} / B_0 = 0.1$) electrons moving through small-scale Whistler turbulence. The frequency is normalized by $\omega_{jn} = \gamma_e^2 k_{\min} \beta c$ – the relativistic jitter frequency. The solid (“red”) curve is from simulation data, whereas the dashed (“blue”) curve is the analytic estimate. Clearly, the spectrum is well represented by a superposition of synchrotron+jitter components.

tion due to the electric field may be neglected, since $\langle E^2 \rangle \ll \langle \delta B^2 \rangle$ – hence, the spectrum is wholly determined by the magnetic field.

We considered a $\gamma_e = 5$ electron population for Figure 6.9. In this plot, the relevant parameters are: $N_p = 1000$, $\Delta t = 0.00125$, $k_{\min} = 2\pi$, $k_{\max} = 20\pi$, $\langle \delta B^2 \rangle^{1/2} / B_0 = 0.1$, $\Omega_{ce} = 0.512$, $\mu = 4$, $\rho \approx 928$, $\chi \sim 1$, and the total simulation time was $T = 5T_g$. We see that the synchrotron+jitter fit closely resembles the numerical spectrum.

Next, we explored the non-relativistic regime. In Figure 6.10, we assumed a population of sub-Larmor-scale $\beta = 0.125$ electrons. As expected, a peak in the spectrum may be

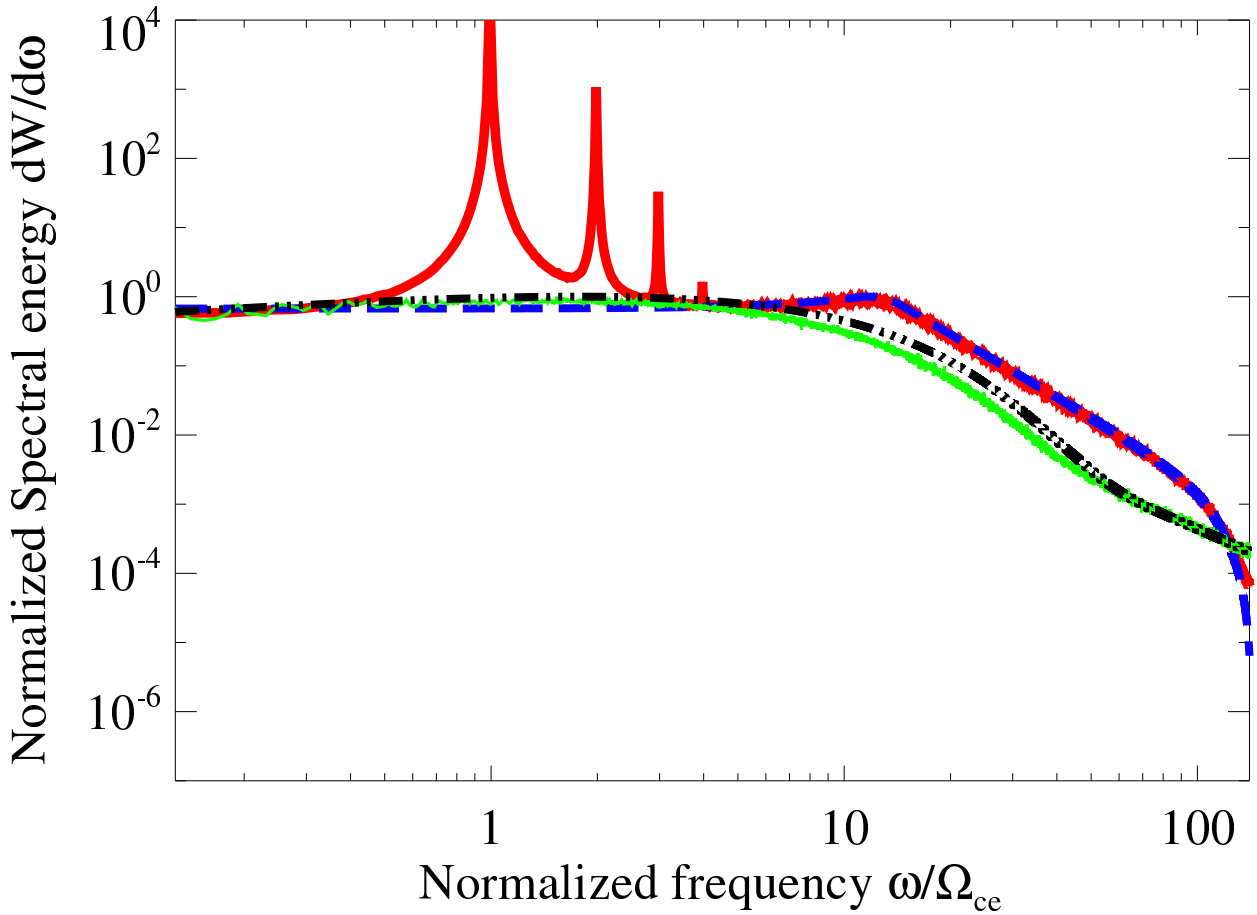


Figure 6.10: Radiation spectrum for a monoenergetic, isotropic distribution of $\beta = 0.125$ electrons ($\chi \sim 0.04$; $\rho \approx 160$; $\langle \delta B^2 \rangle^{1/2} / B_0 = 0.2$; $\Omega_{ce} = 2$; $k_{\min} = 64\pi$; $k_{\max} = 10k_{\min}$; $\mu = 5$; $T = 50T_g$); superimposed with a spectrum given a population of $\gamma_e = 4$ electrons ($\chi \sim 1$; $\rho \approx 367$; $\langle \delta B^2 \rangle^{1/2} / B_0 = 0.1$; $\Omega_{ce} = 0.512$; $k_{\min} = \pi$; $k_{\max} = 10\pi$; $\mu = 4$; $T = 5T_g$). The normalization on the y -axis is arbitrary, whereas the x -axis is normalized to the $\beta = 0.125$ population's cyclotron frequency, i.e. $\Omega_{ce} = 2$. The “thick” solid (“red”) curve is from simulation data for the $\beta = 0.125$ population, the dashed (“blue”) curve is the corresponding analytic estimate for “pure” psuedo-cyclotron radiation, the “thin” solid line is the simulation data for the $\gamma_e = 4$ population, and the “dot-dashed” (“black”) line is the $\gamma_e = 4$ analytic estimate. Notice, for the $\beta = 0.125$ spectrum, that the spectrum peaks near the cyclotron frequency, Ω_{ce} – hence we see the signature of cyclotron radiation. The additional harmonics, which are purely a relativistic effect, are the signature of emerging synchrotron radiation.

observed near the cyclotron frequency Ω_{ce} – confirming that the total spectrum is the hybrid of psuedo-cyclotron+cyclotron radiation. Additionally, to provide a point of comparison, we have superimposed a simulation result for $\gamma_e = 4$ electrons.

6.4.4 Jitter Radiation and Small-Scale Langmuir Turbulence

In Figure 6.11, we have plotted the numerical radiation spectrum for electrons with $v = 0.125c$ and $\gamma_e = 2$ – this corresponds to the scenario explored in Section 5.3.3. The resulting radiation spectrum is analogous to the (mildly) relativistic small-angle jitter spectrum of an electron moving through sub-Larmor-scale magnetic turbulence, but it is morphologically distinct. This is because the electrostatic field, owing to its curl-free presentation, has a different correlation tensor, $\Phi_{ij}(\mathbf{k})$, than the (divergenceless) magnetic equivalent. Thus, we require the substitution:

$$\Phi_{ij}(\mathbf{k}) \propto (\delta_{ij} - \hat{k}_i \hat{k}_j) \rightarrow \hat{k}_i \hat{k}_j. \quad (6.45)$$

The analytical solution, strictly, holds for the ultrarelativistic limit. Nonetheless, as can be seen in Figure 6.11, the numerical solution closely matches the analytic result for mildly relativistic electrons with $\gamma_e = 2$. This is consistent with the result seen in Figure 5.15, which suggests the presence of the small deflection angle regime.

In contrast, the third spectrum in Figure 6.11 differs markedly from the analytic (jitter) prediction. This is the spectrum resolved for a $v = 0.125c$, i.e. $\gamma_e \approx 1$, electron. In accord with Figure 5.15, the deflection angle is large, thus the spectrum is outside the small-angle jitter regime.

It is noteworthy that the $\chi \gg 1$ condition in Langmuir-like turbulence may not be physically realizable, since Landau damping would likely eliminate wave-modes at sub-skin-depth spatial scales too quickly (Teraki & Takahara, 2014). With the field variability time-scales of comparable order to the electric correlation length transit time, it may be necessary to consider the rms electric field as a function of time. Thus, a more realistic model may

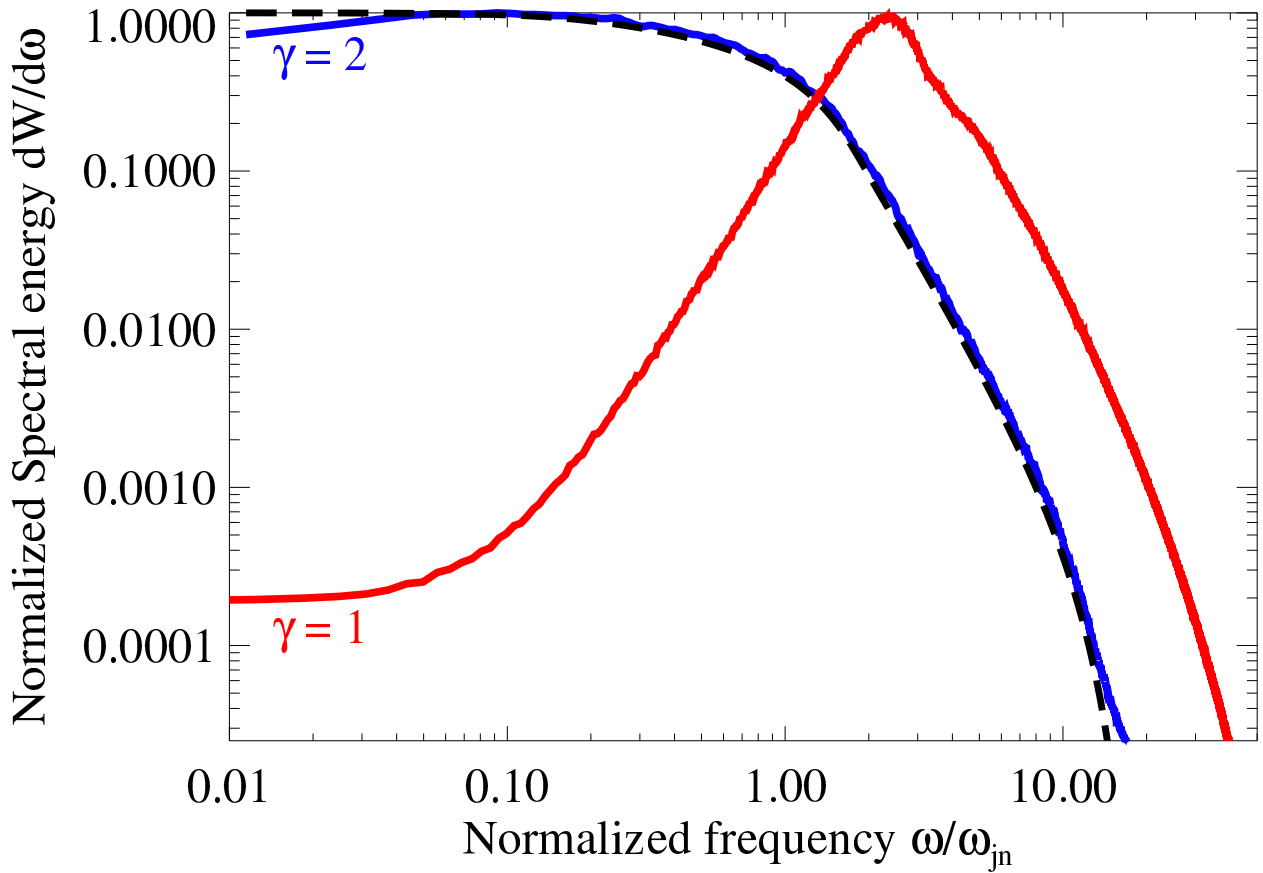


Figure 6.11: Langmuir Radiation spectra for the $\gamma_e = 2$ and $v = 0.125c$ electrons (see Figure 5.15 for details on the simulation parameters). The frequency is normalized by the characteristic jitter frequency, i.e. $\omega_{jn} \equiv \gamma_e^2 k_{\min} \beta c$. The lower (“red”) curve is from simulation data, and it corresponds to the $v = 0.125c$ electron. The upper (“blue”) curve is the simulation result for the $\gamma_e = 2$ electron, and the dashed curve is the analytic estimate. Clearly, the mildly relativistic spectrum is well represented by the (Langmuir) jitter result.

require a time-dependent pitch-angle diffusion coefficient.

6.5 The Jitter/Synchrotron Spectrum of a Thermal Distribution of Particles

In most cases, our sub-Larmor-scale electron distribution will not be composed of mono-energetic electrons. Here, we consider the radiation spectrum one might expect from a Maxwell-Boltzmann (thermal) distribution of electrons in sub-Larmor-scale magnetic fields.

To obtain the jitter component of the spectrum, we must average the single electron spectrum over an appropriate relativistic Maxwell-Boltzmann distribution. We define the jitter *emission coefficient*, which is the total radiated power per frequency per volume, as thusly:

$$\left(\frac{dP}{d\nu dV} \right)^{\text{jitt.}} = n_e \frac{\int P_j(\nu, p) e^{\gamma_e/\Theta} d^3 p}{\int e^{\gamma_e/\Theta} d^3 p}, \quad (6.46)$$

where $\Theta \equiv k_B T_e / m_e c^2$, $\nu = \omega / 2\pi$, and

$$P_j(\nu, p) \equiv \frac{2\pi}{T} \frac{dW}{d\omega}(p), \quad (6.47)$$

is the single electron (power) spectrum with kinetic momentum, $p = \gamma_e m_e v$, and at the observation time, T .

Next, we require an expression for the angle-averaged thermal synchrotron emission coefficient. To that end, we employ:

$$\left(\frac{dP}{d\omega dV} \right)^{\text{syn.}} = \frac{2^{1/6} \pi^{3/2} e^2 n_e \nu}{3^{5/6} c K_2(1/\Theta) \xi^{1/6}} \exp \left[- \left(\frac{9\xi}{2} \right)^{1/3} \right], \quad (6.48)$$

where $\xi \equiv \omega / \Omega_{ce} \Theta^2$. This expression produces the correct total power, up to a factor of 1.05, when $\Theta = 0.6$ (Wardziński & Zdziarski, 2000). With $\Theta = 0.6$, the thermal Lorentz factor, $\gamma_{T_e} = \Theta + 1 = 1.6$. Thus, this corresponds to the trans-relativistic regime.

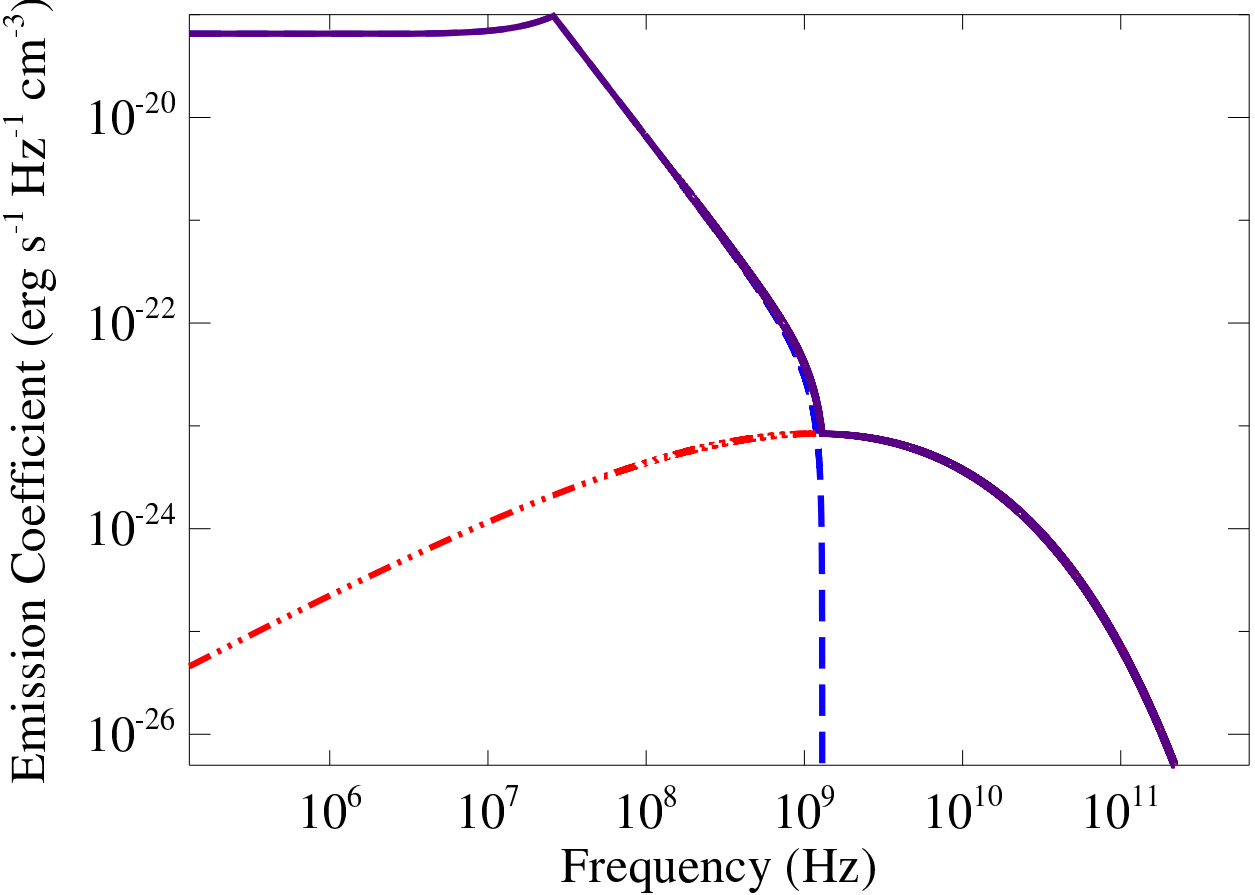


Figure 6.12: Emission coefficient vs. frequency for a thermal distribution of electrons moving through “magnetized”, sub-Larmor-scale magnetic turbulence. Relevant parameters: $n_e = 1 \text{ cm}^{-3}$, $\delta B = B_0 = 1 \text{ G}$, $\gamma_{T_e} = 12$, $k_{\max} = 50k_{\min}$, and $k_{\min}^{-1} = d_e^{\text{rel.}}$ – where $d_e^{\text{rel.}} \equiv c\sqrt{\gamma_{T_e}}/\omega_{pe}$ is the relativistic skin-depth. The jitter component – dashed (“blue”) line – overpowers the synchrotron portion – three-dot-dashed (“red”) line – at frequencies below $\omega_{bn} \sim \gamma_{T_e}^2 k_{\max} v_{T_e}$. This produces a distinctly non-synchrotron feature, at low frequencies, in the total (summed) spectrum, solid (“purple”) line.

When the temperature approaches the ultrarelativistic limit, i.e., $\Theta \gg 1$, Eq. (6.48) gives a fairly accurate result, with a correction factor of order unity.

In figure 6.12, we have plotted the combined emission coefficient for a scenario in which sub-Larmor-scale magnetic turbulence, with a spectrum identical to Eq. (3.62), is embedded in an ambient magnetic field, \mathbf{B}_0 . We suppose the following parameters: $n_e = 1 \text{ cm}^{-3}$, $\delta B = B_0 = 1 \text{ G}$, $\gamma_{T_e} = 12$, $k_{\max} = 50k_{\min}$, and $k_{\min}^{-1} = d_e^{\text{rel.}}$ – where $d_e^{\text{rel.}} \equiv c\sqrt{\gamma_{T_e}}/\omega_{pe}$ is the relativistic skin-depth. These parameters, other than Θ , are not important for determining the overall shape of the spectra; thus, our selection is made only for instructional purposes.

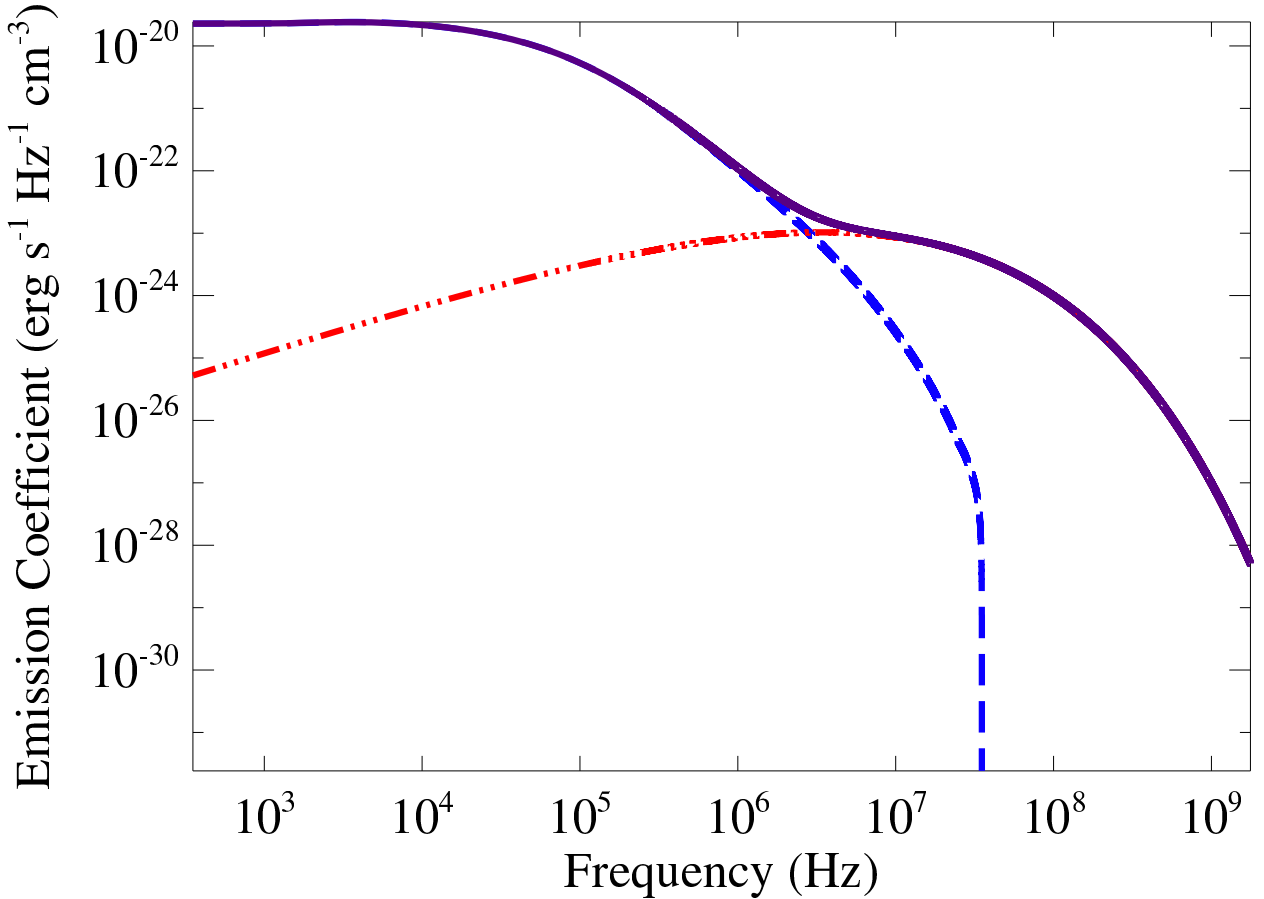


Figure 6.13: Emission coefficient vs. frequency for a thermal distribution of electrons moving through “magnetized”, sub-Larmor-scale magnetic turbulence. Relevant parameters: $n_e = 1 \text{ cm}^{-3}$, $\delta B = B_0 = 1 \text{ G}$, $\gamma_{Te} = 1.6$, $k_{\max} = 50k_{\min}$, and $k_{\min}^{-1} = d_e^{\text{rel}}$. Despite the presence of noticeable thermal spread, the jitter component – dashed (“blue”) line – still overpowers the synchrotron portion – three-dot-dashed (“red”) line – at frequencies below $\omega_{\text{bn}} \sim \gamma_{Te}^2 k_{\max} v_{Te}$. The summed spectrum, solid (“purple”) line, remains distinctly non-synchrotron-like at low frequencies.

As may be readily seen in Figure 6.12, the jitter emission spectrum – dashed (“blue”) line – dominates over the synchrotron component – three-dot-dashed (“red”) line – at low frequencies. This contrasts with the scenario depicted in Figure 6.9, where the jitter portion dominates at high frequencies. Essentially, the ratio: ω_{jn}/ω_c , determines where the jitter component makes an appearance.

Furthermore, the depicted jitter and synchrotron spectra are nearly identical to the mono-energetic equivalents. This is because with $\gamma_{Te} = 12$ – or, equivalently, $\Theta = 11$ – the vast majority of particles are moving ultrarelativistically. Hence, the thermal spread is very small.

In contrast, with $\gamma_{Te} = 1.6$, a considerable degree of thermal spread will be noticeable on inspection. However, as we see in Figure 6.13 – where we consider an identical scenario, with $\Theta = 0.6$ – this spread does not obscure the trans-relativistic jitter (pseudo-cyclotron) feature; the jitter portion is still very clearly distinct from the thermal synchrotron component.

To summarize, the signature of jitter radiation — both in the relativistic and trans-relativistic regimes – remains clearly evident, even given a thermal distribution of electrons.

6.5.1 Plasma Dispersion

Our results do not consider the dispersive effect of the surrounding plasma. An account of dispersion will modify the radiation spectrum by a multiplication of Eq. (6.8) by the square root of the frequency-dependent scalar permittivity, $\epsilon(\omega)$. The scalar dielectric permittivity at high frequencies is (Jackson, 1998; Rybicki & Lightman, 1986):

$$\epsilon(\omega) = 1 - \frac{\omega_{pe}^2}{\omega^2}, \quad (6.49)$$

where ω_{pe} is the plasma frequency. Eq. (6.49) holds formally for $\omega^2 \gg \omega_{pe}^2$ in any dielectric medium; although it holds for cold, non-magnetized, isotropic plasmas for a wide domain of frequencies – including $\omega < \omega_{pe}$ (Rybicki & Lightman, 1986). In a magnetized plasma, additional terms including the ambient “mean” magnetic field appear in the permittivity

tensor. As previously mentioned, the Weibel-like magnetic turbulence can occur in a non-magnetized environment, thus we ignore any “mean” field here. Hence, we will consider an extension of Eq. (6.49) to low frequencies ($\omega \sim \omega_{pe}$).

For simplicity and convenience, we have ignored the plasma dispersion in our numerical simulations. However, we consider a few cases with plasma dispersion intact, both numerically and theoretically, in Appendix C.

6.6 Discussion of Results

In this Chapter, we explored non-relativistic and trans-relativistic particle radiation production in small-scale electromagnetic turbulence. Principally, we demonstrated that in the regime of small deflections, i.e. when the particle’s deflection angle over a correlation length is small $\alpha_\lambda \ll 1$, the produced radiation spectrum is wholly determined by the particle velocity and the statistical/spectral properties of the magnetic turbulence; which is a result most transparently offered by Eq. (6.16).

Just as small-angle jitter radiation strongly differs from synchrotron radiation, so too does the analogous non-relativistic jitter radiation distinguish itself from cyclotron radiation. Given the isotropic 3D power law magnetic spectral distribution from Eq. (3.62), the resulting trans-and non-relativistic radiation spectrum is a piece-wise function of a quadratic equation in frequency, ω up to the characteristic (jitter) frequency, $\omega_{jn} = \gamma_e^2 k_{\min} v$, after which it is the sum of a power law and a quadratic term up to the break frequency, $\omega_{bn} = \gamma_e^2 k_{\max} v$, where it then quickly approaches zero – see Eq. (6.20). We have, furthermore, confirmed our theoretical results via first-principle numerical simulations.

Additionally, we showed that the test particle radiation spectrum in small-scale Whistler turbulence is simply the summation of a small-scale, jitter/pseudo-cyclotron component and a regular, synchrotron/cyclotron component – see Eq. (6.41). We confirmed this via first-principle numerical simulations.

Next, we considered the change in the radiative and transport properties of trans-relativistic particles moving through magnetic turbulence due to a topological change in the field. Namely, we supposed the generation of sub-Larmor-scale magnetic turbulence from a distribution of magnetic monopoles. We showed that the radiation spectra and pitch-angle diffusion coefficient are modified; i.e. the pitch-angle diffusion coefficient doubles in magnitude, *à la* Eq. (6.43), and the shape of the radiation spectrum is dramatically altered for frequencies less than the jitter frequency, ω_{jn} . These results, furthermore, generalize to the case of a magnetic monopole moving through “small-scale” electrostatic turbulence.

Furthermore, we confirmed the result first shown by (Teraki & Takahara, 2014) that the spectrum of relativistic electrons in small-scale Langmuir turbulence is a form of jitter radiation. We, further, expanded upon this result by resolving the spectrum for trans-relativistic velocities – showing that the jitter prescription holds well even down to $\gamma_e \sim 2$.

Finally, we considered the radiation produced by a Maxwell-Boltzmann (thermal) distribution of electrons in a magnetized plasma with sub-Larmor-scale magnetic fluctuations. We demonstrated that the signature of the jitter component clearly remains when the fluctuation field is comparable to the ambient magnetic field – just as it did for the mono-energetic case considered previously.

Chapter 7

Small-Scale Magnetic Turbulence And (Quasi-)Collisionality

7.1 Introduction

Sub-Larmor-scale magnetic turbulence induces particle dynamics reminiscent of binary Coulomb interactions. In this Chapter, we show that this behavior, under certain conditions, is actually equivalent to Coulomb collisions in collisional plasmas. The magnetic pitch-angle diffusion coefficient, which acts as an effective “collision” frequency, may be substantial in these, otherwise, collisionless environments. We show that this “quasi-collisionality” may radically alter the expected radiative transport properties of candidate plasmas.

7.2 General Discussion

As we defined it in 3.5.1, there is a single correlation length for all spatial scales of the magnetic field. Nonetheless, any realization of electromagnetic turbulence may be envisioned as the superposition of “small-scale” and “large-scale” (i.e., the “sub-” and “super-Larmor-scale”) components. Thus, we may roughly define two characteristic spatial scales for the general case, where λ_B^{ssc} and λ_B^{lsc} are the sub-Larmor-scale and super-Larmor-scale correlation

lengths, respectively.

Ignoring the mean magnetic field, there are a number of different regimes that may be enumerated, depending upon the relative significance of the magnetic field at each scale. Firstly, if the correlation length is infinite, then the electrons will follow helical orbits about the axis of a perfectly homogeneous magnetic field. Next, if the magnetic field is “large-scale” — i.e., possessing fluctuations on a finite, though super-Larmor, spatial scale — then the electron’s guiding center will drift, due to slight inhomogeneity in the magnetic field.

Thirdly, an electron moving through purely sub-Larmor-scale magnetic turbulence will not complete a Larmor orbit, because the magnetic field varies on a scale shorter than the Larmor curvature radius. With $\rho \gg 1$, this trajectory is a nearly straight line, with small, random (diffusive) deflections perpendicular to the direction of motion (i.e. the small-angle jitter regime).

Finally, when a range of spatial scales exists, the chaotic trajectory will be a combination of large-scale gyro-motions (though not necessarily complete gyro-orbits) with small-scale diffusive deflections (i.e. the large-angle jitter regime, for ultrarelativistic particles).

We will show that it is these small-scale deflections that induce a *quasi-collisionality* with the pitch-angle diffusion coefficient acting as an effective collision frequency. To this end, we will next turn our attention to the conventional treatment of (Coulomb) collisions in plasmas.

7.3 The Lorentz Collision Model of Electron-Ion Collisions

As the lowest order approximation, Coulomb collisions are considered in a small deflection angle regime. In this approximation, a “test” electron will undergo a slight (transverse) deflection as it passes by an ion. For simplicity, we will neglect electron-electron collisions.

As the binary collisions continue with other ions, several scatterings will occur. These

scatterings are effectively stochastic, if the background of (stationary) ions is randomly distributed. Since the collisions with the fixed ion background are elastic, the total electron energy is conserved.

Nevertheless, the small deflections accumulate, leading to a gradual change in the electron's transverse momentum, Δp_\perp . An electron is deflected by one radian, i.e. $\Delta p_\perp/p \sim 1$, in a single collision time, τ_c . The inverse of the collision time, $\nu_{ei} \equiv \tau_c^{-1}$, is defined as the electron-ion collision frequency.

Given a Maxwellian distribution of electrons, the electron-ion collision frequency assumes the simple form (Kruer, 1988):

$$\nu_{ei} \simeq 3 \times 10^{-6} \ln(\Lambda) \frac{n_e Z_i}{\theta_{\text{eV}}^{3/2}} [s^{-1}], \quad (7.1)$$

where n_e is the electron number density in cm^{-3} , θ_{eV} is the electron temperature in units of electron-volts, Z_i is the atomic ionization number, and $\ln(\Lambda)$ is the Coulomb logarithm.

Here, we employ the Spitzer result for the Coulomb logarithm (Spitzer, 1956):

$$\ln(\Lambda) \approx 25.28 + \ln \left[\frac{\theta_{\text{eV}}}{\sqrt{n_e}} \right], \quad (7.2)$$

which is valid for temperatures above $4 \times 10^5 K \approx 34 eV$.

Next, we will argue that the [small-scale] pitch-angle diffusion coefficient acts as an effective collision frequency in plasmas with sub-Larmor-scale magnetic fluctuations.

7.4 Pitch-angle Diffusion as Effective Collisionality

The small-angle magnetic deflections are analogous to electron-ion collisional deflections in a number of ways, namely they both (i) conserve the particle's energy and (ii) induce deflections transverse to the electron's initial velocity.

Where the two effects differ, however, is in the nature of the stochasticity. In an idealized

scenario, an electron in a collisional plasma is continuously deflected by ions along its trajectory. In contrast, an electron moving through small-scale electric turbulence is deflected on a characteristic spatial scale of finite length: the correlation length. Thus, the two descriptions are only equivalent on a coarse-graining. Indeed, the electron motion in small-scale turbulence resembles electron-ion collisions only on spatial scales greater than – or similar to – the electric correlation length.

Thus, we must require that:

$$L \gtrsim \lambda_B^{ssc}, \quad (7.3)$$

where L is the characteristic length scale of the system. With regard to the propagation properties of plasmas, this dimension is on the order of the wave packet size. For pure plane waves, however, L is unlimited.

Next, we may infer this effective collision frequency directly from Eq. (5.4). The pitch-angle deflections are assumed to be small, hence $\alpha \sim \Delta p_\perp / p$. Thus, at τ_c , the following condition must hold:

$$D_{\alpha\alpha}^{ssc} \tau_c \sim 1, \quad (7.4)$$

where $D_{\alpha\alpha}^{ssc}$ is the (small-scale) pitch-angle diffusion coefficient. Therefore, $D_{\alpha\alpha}^{ssc}$ must be the effective “collision” frequency. Generalizing Eq. (5.4), we write:

$$D_{\alpha\alpha}^{ssc} \sim \left(\frac{e^2}{m_e^2 c^3} \right) \frac{\lambda_B^{ssc}(\mathbf{x}, t)}{\gamma_e^2 \langle \beta^2 \rangle^{1/2}} \langle \delta B_\perp^2 \rangle, \quad (7.5)$$

where $\delta \mathbf{B}_\perp$ is the component of the (small-scale) fluctuation field perpendicular to the electron’s velocity, \mathbf{x} is in the vicinity of the electrons of interest, and $\langle \beta^2 \rangle^{1/2}$ is an appropriate ensemble-average over the electron velocities.

Electron-ion collisions in plasmas are often important too, hence we include them in our study. Consequently, we define the total (effective) collision frequency as:

$$\nu_{\text{eff}} \equiv \nu_{ei} + D_{\alpha\alpha}^{ssc}. \quad (7.6)$$

7.5 A Phenomenological Interpretation

Estimating $D_{\alpha\alpha}$, in real plasmas, may be difficult since it depends upon the small-scale correlation length – a quantity which requires knowledge of the magnetic spectral distribution to obtain. In principle, if the nature of the instability which produces the electromagnetic fluctuations is known, then we may produce a rough estimate of the characteristic spatial scales which ultimately set the correlation length. However, in many cases, the type of turbulent fluctuations may not be known; hence, an *a priori* estimate of the magnetic spectrum may not be available.

Fortunately, charged particles undergoing quasi-collisions in small-scale magnetic fields emit small-angle jitter radiation. This radiation, which is distinct from both cyclotron and synchrotron radiation, has spectral properties which are fully determined by the statistical characteristics of the magnetic turbulence. Furthermore, the pitch-angle diffusion coefficient and the jitter radiation spectrum are intimately related. Thus, the jitter spectrum offers an immediate estimate for the pitch-angle diffusion coefficient, as we will show.

Similarly, electrons undergoing collisions with an ion background will emit Bremsstrahlung radiation. The emission coefficient, j_ω , is directly proportional to the collision frequency. For a Maxwellian (thermal) distribution of electrons in a weakly ionized plasma, the emission coefficient is (Bekefi, 1966):

$$j_\omega^{\text{Brems}} = \Re[n] \left(\frac{\omega_{pe}^2 k_B T_e}{8\pi^3 c^3} \right) \nu_{ei}, \quad (7.7)$$

where $\Re[n]$ is the real part of the plasma's index of refraction. Now, taking into account quasi-collisions, as in Eq. (7.6), by substituting $\nu_{ei} \rightarrow \nu_{\text{eff}}$ in Eq. (7.7), the latter introduces a phenomenological definition for the effective collision frequency.

As we have shown in 6.3.1, the total (dispersion free) jitter power emitted by a single electron is given by:

$$P_{\text{tot}}^{\text{jitter}} = \frac{2}{3} c \beta^2 r_e^2 \gamma_e^2 \langle \delta B_\perp^2 \rangle. \quad (7.8)$$

The small-angle jitter radiation spectrum has the jitter frequency,

$$\omega_{jn} = \gamma_e^2 k_{mag} \beta c, \quad (7.9)$$

where k_{mag} is the dominant wave number of the (small-scale) turbulent fluctuations. Next, we may write the spectral power for a single electron as:

$$P_{jitter}(\omega) \equiv \frac{dP}{d\omega} \sim \frac{P_{tot}^{jitter}}{\omega_{jn}}. \quad (7.10)$$

Substitution of Eq. (9.2) into Eq. (9.9), results in the expression:

$$P_{jitter}(\omega) \sim \frac{2}{3} \lambda_B^{ssc} \beta \left(\frac{e^4}{m_e^2 c^4} \right) \langle \delta B_\perp^2 \rangle, \quad (7.11)$$

where the relation, $k_{mag}^{-1} \sim \lambda_B^{ssc}$. Comparing this result to Eq. (5.4), we find that the power spectrum is directly proportional to the pitch-angle diffusion coefficient:

$$P_{jitter}(\omega) \sim \frac{2}{3} \frac{e^2}{c} \gamma_e^2 \beta^2 D_{\alpha\alpha}. \quad (7.12)$$

Next, if we assume isotropic emission by all plasma electrons, then the jitter emission coefficient may be obtained from Eq. (7.12) with the multiplication of $n_e/4\pi$. Thus:

$$j_\omega^{jitter} \sim \frac{n_e e^2}{6\pi c} \gamma_e^2 \beta^2 D_{\alpha\alpha} = \left(\frac{m_e \omega_{pe}^2}{24\pi^2 c} \right) \gamma_e^2 \beta^2 D_{\alpha\alpha}. \quad (7.13)$$

Finally, the emission coefficient for non-relativistic jitter (pseudo-cyclotron) radiation, given a Maxwellian distribution of electrons, will be:

$$j_\omega^{jitter} \sim \text{Re}[n] \left(\frac{\omega_{pe}^2 k_B T_e}{3\pi^3 c^3} \right) D_{\alpha\alpha}, \quad (7.14)$$

where we have reintroduced the index of refraction, and substituted:

$$\beta c = \langle |\mathbf{v}| \rangle = \left(\frac{8k_B T_e}{\pi m_e} \right)^{1/2}. \quad (7.15)$$

Comparing Eqs. (7.14) and (7.7), we see that they only differ by a numerical factor. Thus, Eqs. (7.13) and (7.14) provide an attractive phenomenological definition for the “jitter” collision frequency, which may be obtained directly from the small-angle jitter radiation emission coefficient.

7.6 Magneto-optic Effects with Small-Scale Magnetic Fields

To explore the properties of electromagnetic (EM) wave propagation in quasi-collisional, “cold” magnetized plasmas, we examine the elements of the dielectric tensor, i.e. Eq. (3.31). As a low-order approximation, collisions may be treated as drag terms, of the form $-\nu_{\text{eff}}\mathbf{v}$, in the Lorentz equation of motion for the charged plasma particles. This introduces the substitution rule: $\omega \rightarrow \omega + i\nu_{\text{eff}}$. Notice that this is equivalent to setting $(\partial f / \partial t)_{\text{coll.}} = \nu \delta f$ in the collisional Boltzmann transport equation, Eq. (2.12). Thus, the elements of the “collisionless” dielectric tensor generalize to (Brambilla, 1998):

$$L = 1 - \sum_s \frac{\omega_{\text{ps}}^2}{\omega(\omega + i\nu_s - \Omega_{\text{cs}})} \quad (7.16a)$$

$$R = 1 - \sum_s \frac{\omega_{\text{ps}}^2}{\omega(\omega + i\nu_s + \Omega_{\text{cs}})} \quad (7.16b)$$

$$P = 1 - \sum_s \frac{\omega_{\text{ps}}^2}{\omega(\omega + i\nu_s)}, \quad (7.16c)$$

In our study, we will assume that only the electron dynamical time-scales are of interest; thus, $s = e$.

The properties of EM wave propagation through a magnetized plasma depends heavily upon the orientation of the wave-vector with respect to the ambient magnetic field, \mathbf{B}_0 –

hence, magnetized plasmas are *gyrotropic media*. We will consider two limiting cases for wave-vector orientation. First, we will treat the propagation along the direction of \mathbf{B}_0 . The difference in the indices of refraction of left- and right-circularly polarized light, as it propagates along this direction, results in the well-known *Faraday Effect*. As we will demonstrate, strong collisions significantly alter the conventional Faraday expressions.

7.7 “Quasi-collisional” Faraday Effect

If the wave-vector is aligned with \mathbf{B}_0 , the solution to Eq. (7.16) assumes the form:

$$\frac{c^2 k^2}{\omega^2} = 1 - \frac{\omega_{pe}^2}{\omega \sigma (1 \pm \frac{\Omega_{ce}}{\sigma})}, \quad (7.17)$$

where $\sigma \equiv \omega + i\nu_{eff}$, and we have assumed the total collision frequency given by Eq. (7.6). The “ \pm ” signs refer to the right-circular and left-circular polarizations, respectively.

Next, we make the standard assumptions that $\omega \gg \Omega_{ce}$ and $\omega^3 \gg \omega_{pe}^3$. The high-order of the latter assumption is needed to keep terms (linearly) proportional to the electron number density, $n_e \propto \omega_{pe}^2$. Next, we expand Eq. (7.17) in the small parameter, Ω_{ce}/σ :

$$\frac{c^2 k^2}{\omega^2} \approx 1 - \frac{\omega_{pe}^2}{\omega \sigma} \left[1 \mp \frac{\Omega_{ce}}{\sigma} \right]. \quad (7.18)$$

Expanding the square root results in the index of refraction:

$$n \approx 1 - \frac{\omega_{pe}^2}{2\omega\sigma} \left[1 \mp \frac{\Omega_{ce}}{\sigma} \right]. \quad (7.19)$$

Faraday rotation is the result of the discrepancy between the wave-vectors of the two polarizations, Δk_{\pm} . From the real part of Eq. (7.19), we get:

$$\Delta k_{\pm} \approx \frac{\omega_{pe}^2 \Omega_{ce}}{2c(\omega^2 + \nu_{eff}^2)^2} [\omega^2 - \nu_{eff}^2]. \quad (7.20)$$

The existence of an imaginary part in Eq. (7.19) indicates the presence of absorption. The absorption coefficient is given by the general relation:

$$\alpha_{\text{absp}} \equiv -2 \frac{\omega}{c} \Im[n] \quad (7.21)$$

Thus, the Faraday (quasi-)collisional absorption coefficient is:

$$\alpha_{\text{absp}}^{\text{Farad}} \equiv -\frac{\omega_{\text{pe}}^2 \nu_{\text{eff}}}{c(\omega^2 + \nu_{\text{eff}}^2)} \left[1 \mp \frac{2\Omega_{\text{ce}}\omega}{(\omega^2 + \nu_{\text{eff}}^2)} \right]. \quad (7.22)$$

Finally, the total change in the polarization phase angle, $\Delta\Psi$ is obtained by the integration of Δk_{\pm} along the path of the EM wave. Operationally, Ω_{ce} and ω_{pe} are functions of position, z . The latter depending, straightforwardly, upon the electron density, $n_e(z)$. There is subtlety in the interpretation of the gyro-frequency, however. Traditionally, it is defined here as:

$$\Omega_{\text{ce}} \equiv \frac{eB_{\parallel}(z)}{m_e c}, \quad (7.23)$$

where $B_{\parallel}(z)$ is the component of the magnetic field, at z , parallel to \mathbf{k} . It is implicitly assumed that \mathbf{B}_0 is super-Larmor-scale, which is an underlying assumption of the (linear) cold plasma approximation.

Thus, the proper physical interpretation of our result is that $B_{\parallel}(z)$ refers only to the large-scale component of the magnetic field, whereas ν_{eff} is the result of small-scale magnetic fluctuations. Hence, using Eq. (7.20), we may write the collision-corrected expression for the Faraday rotation angle as:

$$\Delta\Psi = \frac{2\pi e^3}{m_e^2 c^2} \int \frac{[\omega^2 - \nu_{\text{eff}}(z)^2]}{[\omega^2 + \nu_{\text{eff}}(z)^2]^2} n_e(z) B_{\parallel}(z) dz. \quad (7.24)$$

Formally, the collision frequency may be a function of z ; which is why we have included it in the integrand. To simplify the treatment even further, we assume a constant (or averaged)

collisional frequency ν_{eff}^* throughout the entire plasma. Then, Eq. (7.24) can be written as:

$$\Delta\Psi \simeq \frac{(1 - Z^2)}{(1 + Z^2)^2} \lambda^2 RM, \quad (7.25)$$

where $\lambda = 2\pi c/\omega$ is the radiation wavelength, $Z \equiv \nu_{\text{eff}}^*/\omega$ is a normalized collision frequency, and

$$RM \equiv \frac{e^3}{2\pi m_e^2 c^2} \int n_e(z) B_{\parallel}(z) dz, \quad (7.26)$$

is the standard collisionless *rotation measure*.

In the absence of (quasi-)collisions, when $Z = 0$, Eq. (7.25) gives the conventional result. Thus, the ratio:

$$\frac{\Delta\Psi}{\lambda^2 RM} = \frac{(1 - Z^2)}{(1 + Z^2)^2} = \frac{\Delta\Psi_{\text{collisional}}}{\Delta\Psi_{\text{collisionless}}}, \quad (7.27)$$

illuminates a possible, (quasi-)collisionality-induced, discrepancy.

In Figure 7.1, we have plotted Eq. (7.27) as a function Z . The curve has a number of interesting properties. Firstly, when $Z = 1$ (i.e., $\omega = \nu_{\text{eff}}^*$), zero rotation occurs. Evidently, in this case, (quasi-)collisions have effectively nullified Faraday Rotation.

Secondly, the rotation angle remains negative for $Z > 1$; obtaining a minimum value of $-1/8$ at $Z = \sqrt{3}$. Finally, as $Z \rightarrow \infty$, the rotation angle approaches zero.

How much do standard Coulomb collisions affect Faraday rotation observations/measurements? For example, in the interstellar medium with density $n_e \sim 1 \text{ cm}^{-3}$, the electron-ion collisional frequency is about $\nu_{ei} \simeq 7 \times 10^{-5} \text{ s}^{-1}$. The strongest effect is expected at the observation frequency $\omega \sim \nu_{ei}$, which is well below any viable frequency range for Faraday polarimetry. Thus, for this reason, Coulomb collisions are generally neglected in astrophysical environments. Nevertheless, quasi-collisionality may be significant where high-amplitude electromagnetic turbulence is suspect. Thus, the observation of a Faraday rotation discrepancy (as described above) may indicate the presence of small-scale magnetic fields.

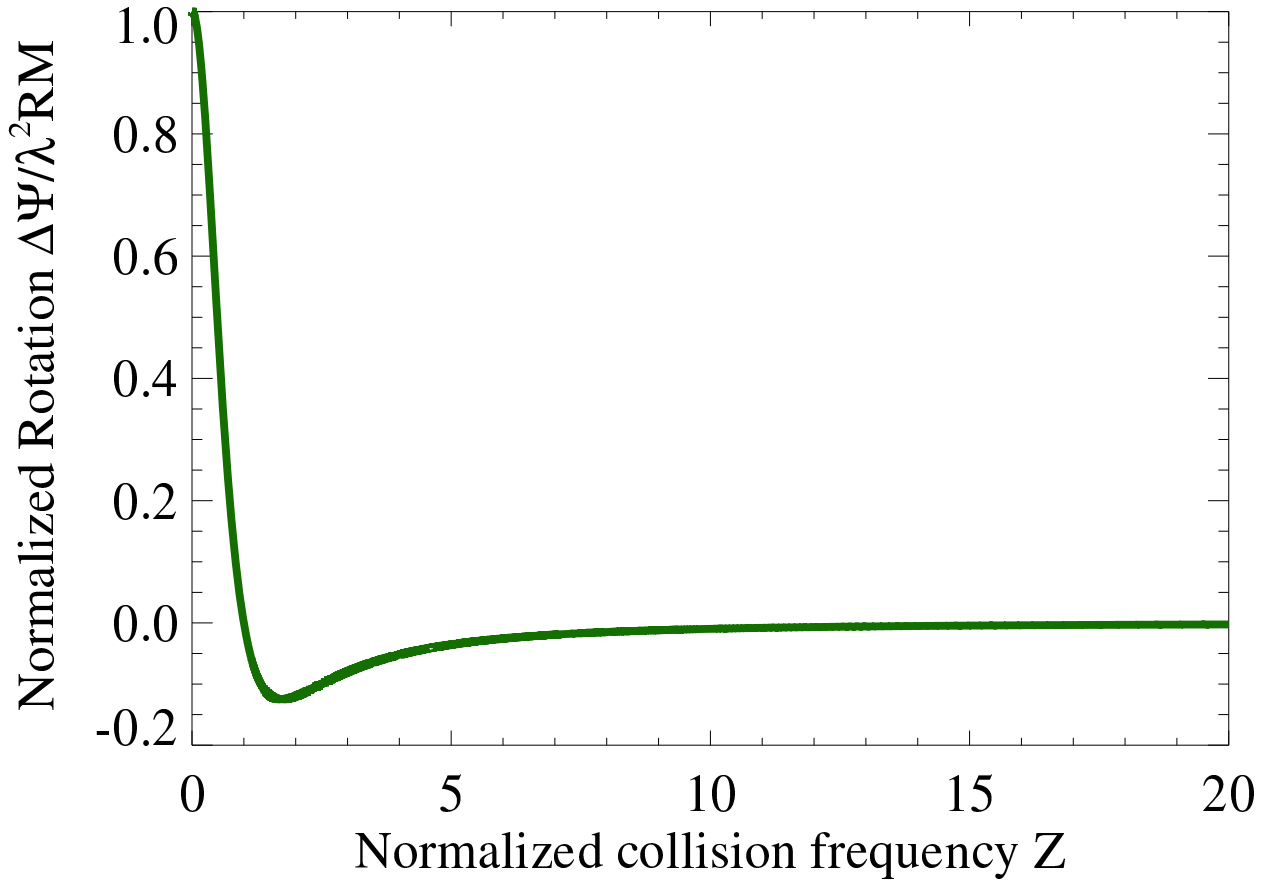


Figure 7.1: Normalized Faraday rotation angle vs. the normalized collision frequency. Notice that at $Z \equiv \nu_{\text{eff}}^*/\omega = 1$ zero Faraday rotation occurs. Collisions have effectively nullified Faraday Rotation.

7.8 Ordinary and Extraordinary Mode Propagation in “Quasi-collisional” Solid-density Laser Plasmas

In the plane perpendicular to \mathbf{B}_0 , two distinct wave modes may propagate. The first of these is the *Ordinary mode* (or *O-mode*), which is equivalent to the electromagnetic wave solution for a non-magnetized plasma. The index of refraction for the *O*-mode, accounting for collisions, is:

$$n_O^2 = 1 - \frac{X}{1+Z^2} + iZ \frac{X}{1+Z^2}, \quad (7.28)$$

where $X \equiv \omega_{pe}/\omega$. Since we cannot safely assume that $Z \ll 1$, Eq. (7.28) must be solved exactly. This results in a real part (Ma, 2005):

$$\Re[n_O] = \frac{1}{4} \left(\epsilon_r + \sqrt{\epsilon_r^2 + \epsilon_i^2} \right)^2, \quad (7.29)$$

and an imaginary part:

$$\Im[n_O] = \frac{1}{2\Re[n_O]} \epsilon_i, \quad (7.30)$$

where $\sqrt{\epsilon_r} \equiv \Re[n_O]$ and $\sqrt{\epsilon_i} \equiv \Im[n_O]$. As before, the presence of an imaginary index of refraction implies absorption. Consequently, the *O*-mode absorption coefficient is given by the substitution of Eq. (7.30) into Eq. (7.21).

Notice that $\Re[n_O] > 0$, for all ω . This means, physically, that the mode has no true cutoff frequency. For $Z \ll 1$, the approximate cutoff will be at the plasma frequency, ω_{pe} , that is where $\Re[n_O]$ quickly approaches zero. In the general case, however, an effective cutoff may not be present.

The *Extraordinary mode* (or, *X*-mode) has a considerably more complicated dispersion

relation. The exact solution of which is (Yesil et al., 2008):

$$n_X^2 = 1 - \frac{X [(1-X)(1-X-Y^2) + Z^2]}{[1-X-Z^2-Y^2]^2 + Z^2[2-X]^2} \\ + iZ \frac{X [(1-X)^2 + Z^2 + Y^2]}{[1-X-Z^2-Y^2]^2 + Z^2[2-X]^2}, \quad (7.31)$$

where $Y \equiv \Omega_{ce}/\omega$ and $X \equiv \omega_{pe}/\omega$. Due to complexity, we will not present an analytical analysis of this case.

Now, we will explore the implications of strong quasi-collisions for O -mode and X -mode propagation in laser-generated solid-density plasmas. We consider a metal target irradiated by a laser at normal incidence, with an intensity of $10^{18} W cm^{-2}$ (the threshold of relativistic intensity). Next, we estimate the relevant plasma parameters, assuming a fully ionized aluminium target ($Z_i = 13$) and a laser wavelength of $\lambda_l = 800 nm$. A decent estimate for the electron temperature is suggested by (Hatchett et al., 2000):

$$k_B T_e \sim U_{\text{pond}} \sim 1 MeV \times \sqrt{\frac{I \lambda_l^2}{10^{19} [W cm^{-2} \mu m^2]}}, \quad (7.32)$$

where U_{pond} is the ponderomotive potential of the incident laser beam. Substitution of our laser parameters gives an electron temperature of $253 keV$.

Assuming that the small-scale magnetic turbulence is the result of a Weibel-like instability, the magnetic field will roughly have the maximum value (Belyaev et al., 2008):

$$B_{\max}^{\text{Weibel}} \sim \frac{m_e \omega_{pe} c}{e}, \quad (7.33)$$

which is consistent with the theoretical saturation condition $\Omega_{ce} \sim \omega_{pe}$.

Next, we must select a model for the plasma frequency profile. We suppose an exponential profile for the electron density in the direction of the laser beam, i.e.,

$$n_e(z) = n_c e^{(z/\lambda_l - 1)}, \quad (7.34)$$

where $n_c \equiv m_e\omega^2/4\pi e^2$ is the *collisionless* critical electron density, and z is along \mathbf{k} . We furthermore assume that the density is uniform in the transverse plane. From this profile, we choose $\omega_{pe}(z = 0)$ for substitution into Eq. (7.33). The result is a magnetic field, $B_{\max}^{\text{Weibel}} \approx 81.2 \text{ MG}$. We will suppose the existence of a large-scale magnetic field in the metal target. For simplicity, we assume that this field is approximately uniform, and that it is situated perpendicular to the angle of normal incidence, which is typical of the laser-induced (ordered) Biermann battery fields seen in ICF experiments, although these fields assume a more complex azimuthal profile (Huntington et al., 2015).

Additionally, we suppose that $B_0 = B_{\max}^{\text{Weibel}}$, and treat δB (the small-scale component) as a free parameter.

Furthermore, the electron-ion collisions are computed using Eq. (7.1), that is we ignore any non-uniformity in the electron temperature.

Lastly, we consider an effective pitch-angle diffusion coefficient for the entirety of the target. We assume that $\lambda_B \sim \lambda_l$, since for Weibel magnetic fields: $\lambda_B \sim d_e$, where $d_e = c/\omega$ is electron skin-depth at the critical surface. In practice, the correlation length should be significantly shorter than the laser wave packet size, so that Eq. (7.3) will hold.

In Figure 7.2, five solutions for the O -mode index of refraction are plotted as a function of the depth into the target (represented by the electron density). These solutions differ by the assumed δB . The effective quasi-collision frequency is significantly large for $\delta B \sim B_0$: $\nu_{\text{eff}} \approx 3.3 \times 10^{15} \text{ s}^{-1}$, which is comparable to the laser frequency. This is in stark contrast to the much weaker electron-ion contribution: $\nu_{ei} \approx 7.1 \times 10^9 \text{ s}^{-1}$, at the critical surface, n_c .

For $\delta B/B_0 = 0.001$, $\nu_{ei} \gg D_{\alpha\alpha}^{ssc}$, and the expected weakly-collisional dependence is realized. Here, there is a steep drop in the index of refraction towards zero near n_c . Physically, this indicates that most of the O -mode wave is reflected back from the critical surface – as, otherwise, anticipated. As the effective collision frequency increases, the reflectivity at the critical surface quickly drops. In fact, when $\delta B/B_0 = 1$, the entirety of the metal target is virtually transparent.

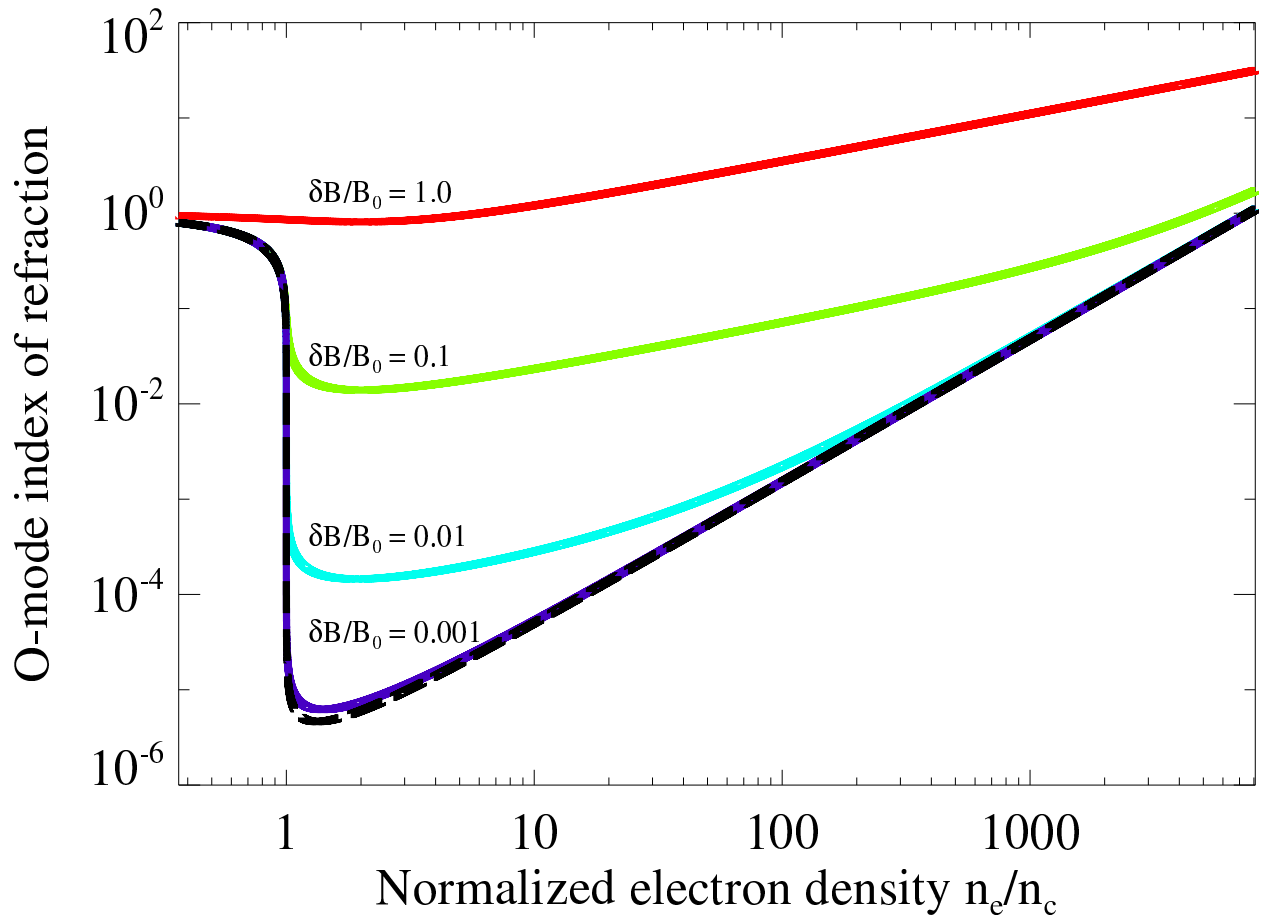


Figure 7.2: Index of refraction for the *O*-mode as a function of depth (in terms of the electron density). Displayed here are five solutions, all differing by the ratio, $\delta B/B_0$. Notice that for $\delta B/B_0 = 0.001$, $\nu_{ei} \gg D_{\alpha\alpha}^{ssc}$, and the expected weakly-collisional dependence is realized; i.e., a steep approach of the index of refraction towards zero at n_c . In contrast, $\delta B = B_0$ leads to a virtually transparent target. Included in this plot is the solution for $\nu_{\text{eff}} = \nu_{ei}$ — the dashed black line.

The steep increase in the index of refraction, for all the curves, at high-density is a result of the density dependence in Eq. (7.1). Since the metal target is of limited extent, this asymptote of the solution may not be experimentally viable.

Next, the *X*-mode has a considerably more complicated index of refraction. The *collisionless* dispersion relation includes two cutoff frequencies and a resonance. The first cutoff,

$$\omega_R = \frac{1}{2} \left(\Omega_{ce} + \sqrt{\Omega_{ce}^2 + 4\omega_{pe}^2} \right), \quad (7.35)$$

is slightly less than ω . Its presence, as the first steep drop in the index of refraction, can be seen Figure 7.3. Next, a resonance occurs at the *upper-hybrid* frequency, i.e.

$$\omega_{UH} = \sqrt{\omega_{pe}^2 + \Omega_{ce}^2}. \quad (7.36)$$

The upper-hybrid resonance, similarly, occurs slightly prior to n_c (see Figure 7.3). Lastly, a second cutoff frequency occurs at:

$$\omega_L = \frac{1}{2} \left(-\Omega_{ce} + \sqrt{\Omega_{ce}^2 + 4\omega_{pe}^2} \right), \quad (7.37)$$

which is slightly beyond the critical surface, n_c .

The behavior similar to the *O*-mode profile may be observed in Figure 7.3. What is noteworthy here is that collisions essentially connect the cutoff frequencies to the resonance, allowing access by ω_{UH} and ω_L . Nonetheless, when quasi-collisions dominate the dispersion, as they do for $\delta B \sim B_0$, the cutoffs and resonance disappear completely.

Next, the *X*-mode index of refraction depends upon the ambient magnetic field via Ω_{ce} . In Figure 7.4, we have plotted three solutions for which $\delta B/B_0 = 0.1$, but B_0 differs by orders of magnitude. As expected, the solution approaches the *O*-mode profile for $B_0 \rightarrow 0$.

Finally, the quasi-collisional absorption is a very important consideration as well. Ignoring reflection and refraction, the intensity, I , falls off exponentially while traversing a lossy

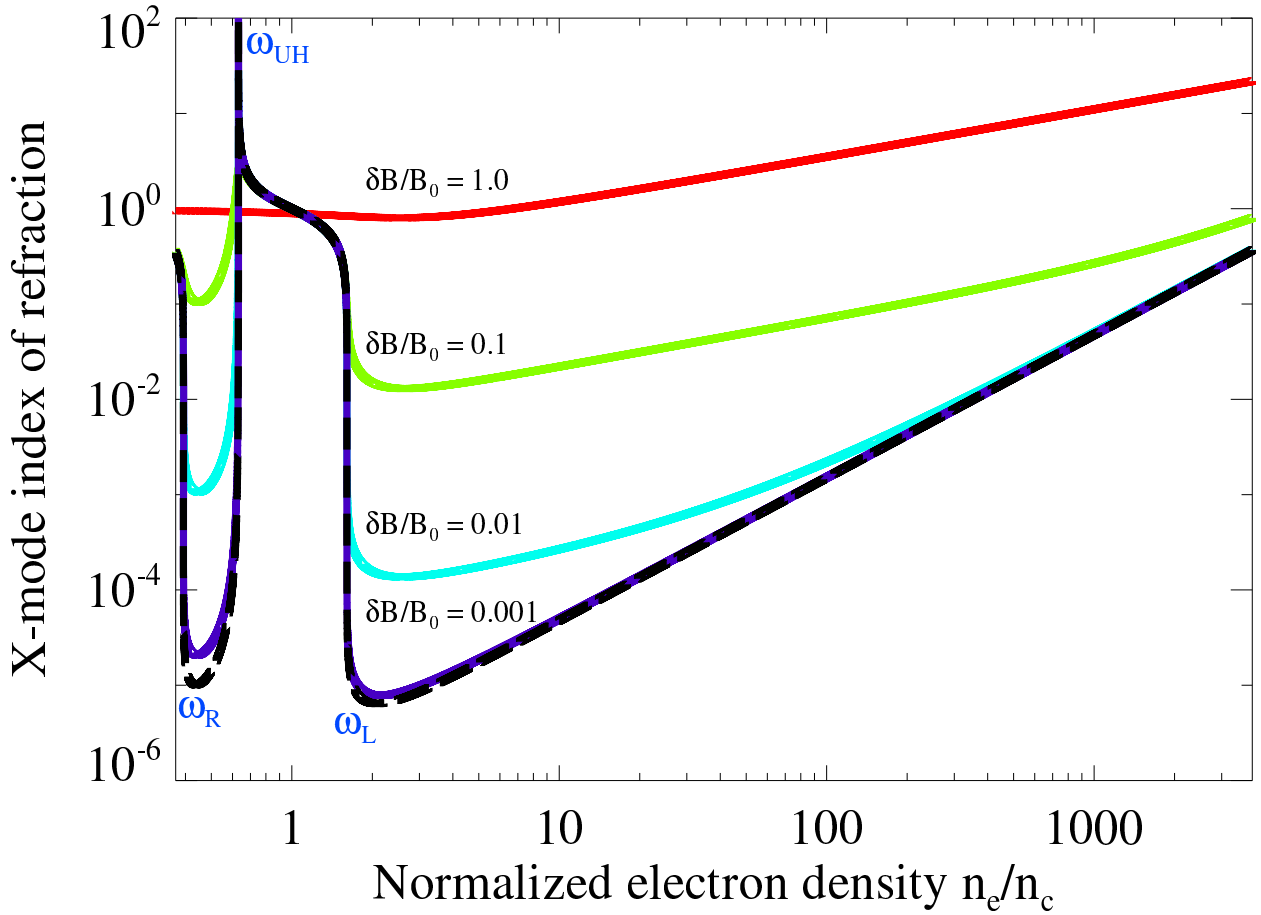


Figure 7.3: Index of refraction for the X -mode as a function of depth (in terms of the electron density). Displayed here are five solutions, all differing by the ratio, $\delta B/B_0$. Notice that for $\delta B/B_0 = 0.001$, $\nu_{ei} \gg D_{\alpha\alpha}^{ssc}$, and the expected weakly-collisional dependence is realized; i.e., a steep approach of the index of refraction towards zero at ω_R , a resonance at ω_{UH} , and another cutoff at ω_L . Collisions effectively connect the cutoff frequencies to the resonance, allowing access to ω_{UH} and ω_L . Nonetheless, for $\delta B \sim B_0$, the cutoffs and resonance disappear completely. Included in this plot is the solution for $\nu_{\text{eff}} = \nu_{ei}$ — the dashed black line.

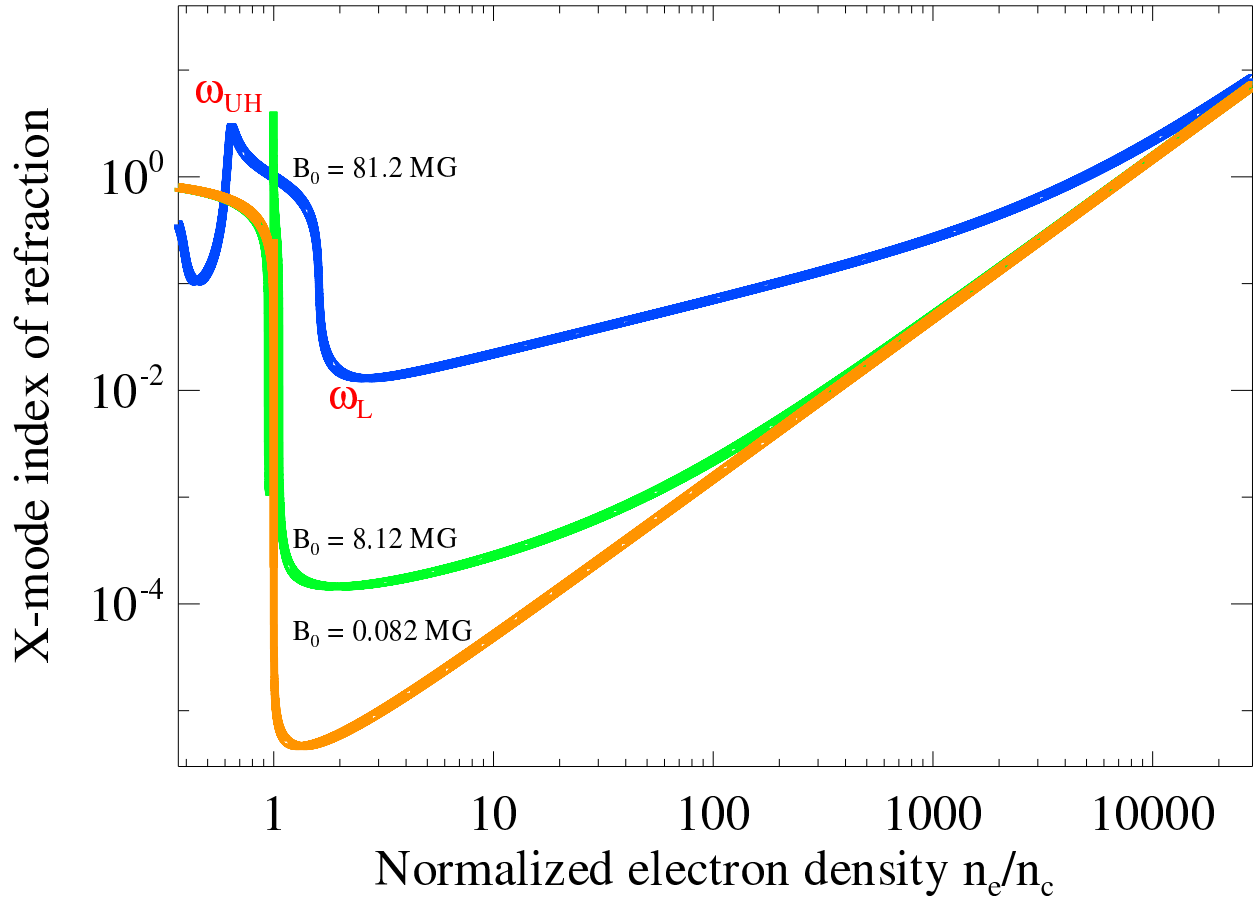


Figure 7.4: Index of refraction for the X -mode as a function of depth (in terms of the electron density). Here, three solutions for which $\delta B/B_0 = 0.1$ are plotted with a variable B_0 . As expected, the solution approaches the O -mode profile for $B_0 \rightarrow 0$.

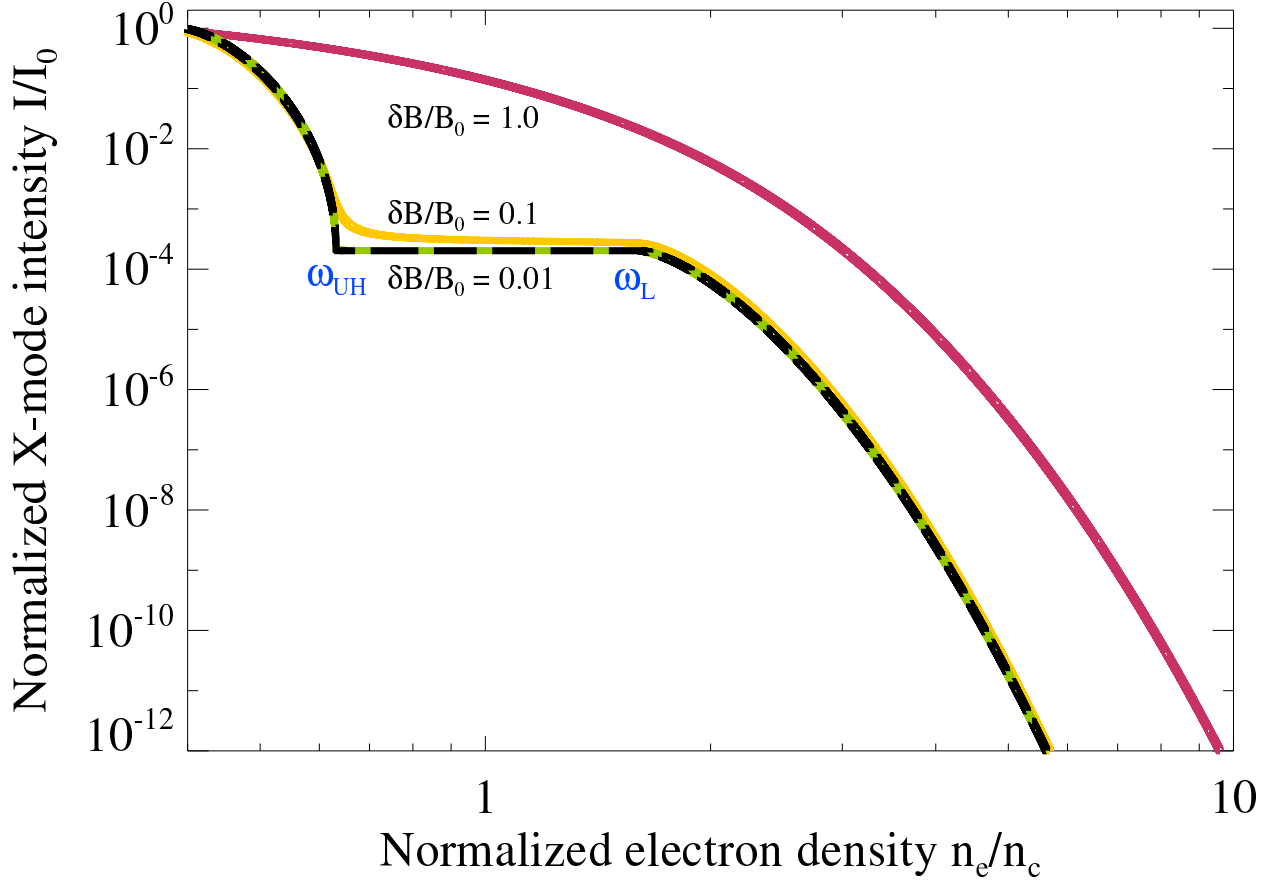


Figure 7.5: X -mode laser intensity as a function of the target depth (in terms of the electron density). Despite the relative transparency for $\delta B \sim B_0$, the laser intensity quickly decays beyond the critical surface. Interestingly, the laser intensity is relatively fixed from ω_{UH} to ω_L , for low- Z . Additionally, there is initial drop near ω_{UH} that is not present in the high- Z case. Included in this plot is the solution for $\nu_{\text{eff}} = \nu_{ei}$ — the dashed black line.

medium, i.e.,

$$I(z) = I_0 e^{-\int |\alpha_{\text{absp}}(z)| dz}, \quad (7.38)$$

where I_0 is the vacuum intensity. In Figure 7.5, we have used Eqs. (7.21) and (7.38) to plot the X -mode intensity as a function of depth for the same conditions as in Figure 7.3 (excluding $\delta B/B_0 = 0.001$).

Despite the relative transparency of the plasma for $\delta B \sim B_0$, Figure 7.5 shows that the laser intensity quickly decays beyond the critical surface. Interestingly, the laser intensity is relatively fixed from ω_{UH} to ω_L , for low quasi-collisionality, i.e., low- Z . Figure 7.6 displays the same scenario for the O -mode case. Once more, we see a relatively fixed laser intensity up

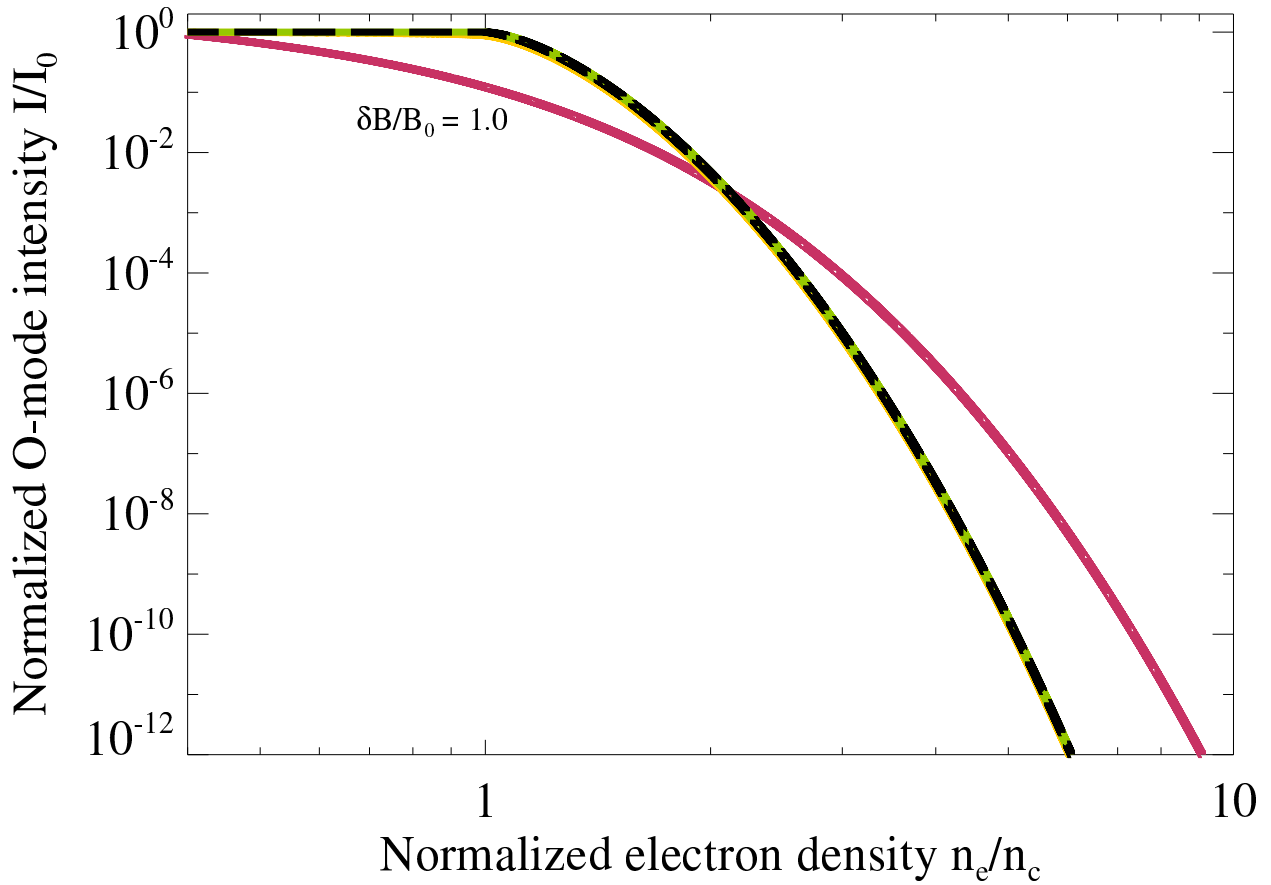


Figure 7.6: *O*-mode laser intensity as a function of the target depth (in terms of the electron density). Once more, we see a relatively fixed laser intensity up to the critical surface, for low- Z . The high- Z curve is identical to the *X*-mode equivalent. Included in this plot is the solution for $\nu_{\text{eff}} = \nu_{ei}$ — the dashed black line.

to the critical surface, for low- Z . The high- Z (i.e., $\delta B \sim B_0$) curve is identical to the X -mode equivalent, thus demonstrating the dominance of quasi-collisions over the “magnetization” effect from B_0 at large δB .

From Figures 7.2-7.6, it is clear that effective quasi-collisionality in solid-density laser plasmas may be significant. Although the high- Z scenario of $\delta B \sim B_0$ is unlikely, the presence of small-scale magnetic fields (especially near the critical surface) may, unanticipatedly, impact the reflectivity and absorption. The effect may be critically important to certain setups, such as the inertial confinement fusion (ICF) experiments or experiments that exploit the *Cotton-Mouton effect* for magnetic field diagnostics.¹

7.9 Discussion of Results

In this Chapter, we investigated the implications the quasi-collisionality induced by small-scale magnetic turbulence in, otherwise, collisionless plasma environments. Our results demonstrate that radiative transport is dramatically affected by the presence of strong effective collisions.

Particularly, our analysis shows that sub-Larmor-scale magnetic fluctuations in magnetized plasmas may sharply attenuate Faraday rotation measures (RM). In fact, with the effective quasi-collision frequency on the same order as the wave frequency, the Faraday rotation effect may be completely canceled, hence $RM = 0$. In an unexpected turn, with $\nu_{\text{eff}} > \omega$, we predict *negative* RM values in these environments. These results are crucial for Faraday rotation-based laboratory plasma diagnostics and interpretation of the results of astronomical observations of Faraday rotation measures of magnetized astrophysical and space plasmas, e.g., of the interstellar and intracluster media.

In the laboratory setting, we find that small-scale turbulence may complicate the prop-

¹The Cotton–Mouton effect refers to the change in the ellipticity of a light wave, which is a combination of X/O -modes, as it propagates transverse to a magnetic field in a plasma medium. The ellipticity change results from the difference in the phase velocities of the two modes – i.e. it is the “transverse” analog of the Faraday effect.

agation of EM waves through high-intensity laser-plasmas; specifically, solid-density laser-plasmas. Namely, the reflectivity and absorption of *X*- and *O*-modes is largely affected when the plasma is highly “collisional”. In fact, for sufficiently high (quasi-)collisionality, the plasma cutoff frequencies cease to exist.

These effects can have crucial implications for the ICF performance. Indeed, the high quasi-collisionality regime occurs when the Weibel instability or other kinetic filamentation instabilities are excited to produce strong sub-Larmor magnetic (or possibly fully electromagnetic) fields. In this regime, the plasma may happen to be transparent so that the critical surface ceases to exist. The impulse delivered to the imploding plasma by radiation pressure halves in the case (cf. reflection vs. absorption), which greatly affects ICF performance. For the same reason, the absorption coefficient reduces too, so that the depth through which radiation can penetrate into the target increases, which changes the energy deposition profile in the target. How theis affect the ICF performance remains to be seen from dedicated theoretical analyses and numerical simulations. On the other hand, we stress that the performance, being affected by quasi-collision-induced transparency which depends on $\delta B/B_0$, can be controlled by the ambient magnetic field, B_0 , both via the Weibel instability suppression (by lowering δB) and the reduction of the effective quasi-collisionality of the plasma (by increasing B_0 for a fixed δB).

We propose that quasi-collisional magneto-optic effects may be exploited for diagnostic purposes. Since the effective quasi-collision frequency — the pitch-angle diffusion coefficient, Eq. (5.4) — is proportional to the magnetic field correlation length and the square of the small-scale magnetic fluctuations, it provides a novel means by which the statistical properties of the small-scale magnetic turbulence may be identified. Additionally, the jitter radiation spectrum readily provides a phenomenological definition for the effective collision frequency, *à la* Eq. (7.13). Jitter radiation may be directly observable in several of these plasma environments.

Chapter 8

(Quasi-)collisionality and Small-scale Electric Fields

8.1 Introduction

In this Chapter, we investigate the realization of quasi-collisionality in small-scale electric fields. In particular, we will explore Faraday rotation in magnetized plasmas with small-scale electric fluctuations.

8.2 Pitch-Angle Diffusion in Small-Scale Langmuir-like Turbulence

The small-angle electric deflections are analogous to electron-ion collisional deflections in a number of ways; they both approximately conserve particle energy, and they both induce deflections that are approximately transverse to the electron's initial velocity.

Thus, in accord with our previous work, we propose that the pitch-angle diffusion coefficient, given by Eq. (5.11), is the electric quasi-collision frequency, ν_E .

8.3 A Phenomenological Definition of the [Electric] Quasi-Collision Frequency

Since relativistic electrons in small-scale electric turbulence, also, emit jitter radiation, we may offer a phenomenological definition for the electric quasi-collision frequency – as we did previously. First, we must consider the total radiated power of the electron. To this end, we use the general Larmor formula, which is given by (Jackson, 1998):

$$P_{\text{tot.}} = \frac{2e^2\gamma_e^6}{3c} \left[\dot{\beta}^2 - (\boldsymbol{\beta} \times \dot{\boldsymbol{\beta}})^2 \right]. \quad (8.1)$$

For purely electric fields, we have the acceleration:

$$\dot{\boldsymbol{\beta}} = -\frac{1}{\gamma_e} [\boldsymbol{\Omega}_E - \boldsymbol{\beta}(\boldsymbol{\beta} \cdot \boldsymbol{\Omega}_E)]. \quad (8.2)$$

However, we are assuming that the transverse acceleration dominates, hence:

$$\dot{\boldsymbol{\beta}} \approx -\frac{1}{\gamma_e} \boldsymbol{\Omega}_E^\perp, \quad (8.3)$$

and, therefore:

$$P_{\text{tot}}^{\text{jitter}} \approx \frac{2}{3} c r_e^2 \gamma_e^2 E_t^2, \quad (8.4)$$

Next, we may write the spectral power for a single electron as:

$$P_{\text{jitter}}(\omega) \equiv \frac{dP}{d\omega} \sim \frac{P_{\text{tot}}^{\text{jitter}}}{\omega_{\text{jn}}}. \quad (8.5)$$

Thus:

$$P_{\text{jitter}}(\omega) \sim \frac{2}{3} \lambda_E^t \beta^{-1} \left(\frac{e^4}{m_e^2 c^4} \right) E_t^2. \quad (8.6)$$

Comparing this result to Eq. (5.11), we find that the power spectrum is directly proportional to the pitch-angle diffusion coefficient:

$$P_{\text{jitter}}(\omega) \sim \frac{2}{3} \frac{e^2}{c} \gamma_e^2 \beta^2 D_{\alpha\alpha}^{\text{elec.}}, \quad (8.7)$$

which is equivalent to the magnetic expression, Eq. (7.12).

Finally, if we assume isotropic emission by all plasma electrons, then the jitter emission coefficient may be obtained from Eq. (7.12) with the multiplication of $n_e/4\pi$. Thus:

$$j_{\omega}^{\text{jitter; elec.}} = \left(\frac{m_e \omega_{\text{pe}}^2}{24\pi^2 c} \right) \gamma_e^2 e^2 \beta^2 D_{\alpha\alpha}^{\text{elec.}}. \quad (8.8)$$

Thus, Eq. (8.8) – once again – provides an attractive phenomenological definition for the “jitter” collision frequency, which may be obtained directly from the small-angle jitter radiation emission coefficient.

8.4 “Quasi-collisional” Faraday Effect in Electric Turbulence

In the previous Chapter, we showed that magnetically-induced quasi-collisionality alters the expected form of this Faraday rotation, $\Delta\Psi$, for magnetized plasmas. The obtained results, formally, hold for a non-relativistic, “cold” plasma with $\omega \gg \Omega_{\text{ce}}$ and $\omega^3 \gg \omega_{\text{pe}}^3$. Consequently, it fails for the scenario considered here, since Eq. (5.8) implies that the electron population is relativistic.

Fortunately, the Faraday expression for relativistic velocities is a straightforward generalization of Eq. (7.24) (Shcherbakov, 2008):

$$\Delta\Psi_{\text{collisionless}} \approx \frac{K_0(\sigma)}{K_2(\sigma)} \lambda^2 R_M, \quad (8.9)$$

where $\sigma \equiv m_e c^2 / k_B T_e$. Thus, under the first-order substitution rule for including the effects of collisions, i.e. $\omega \rightarrow \omega + i\nu_{\text{eff}}$, Eq. (7.27) will hold for the relativistic regime as well. Likewise,

$$\alpha_{\text{absp}}^{\text{Farad}} \rightarrow \frac{K_0(\sigma)}{K_2(\sigma)} \alpha_{\text{absp}}^{\text{Farad}}. \quad (8.10)$$

Finally, we will assume that the small-scale electric fluctuations are predominantly along the direction of the ambient magnetic field, \mathbf{B} . This assumption allows us to disregard additional complications, such as diffusion induced by “E cross B” drifts.

In Figure 8.1, we have plotted Eq. (7.27) as a function of the electric fluctuation strength (the “rms” value of the electric field) for mildly relativistic electrons ($\gamma_e \sim 2$). As we have shown in Section 5.3.3, the small deflection angle regime holds well even at these mildly relativistic speeds. Five curves appear in Figure 8.1, each differing by the electric correlation length, which is chosen to be equal to the relativistic electron skin-depth, $d_e = c\sqrt{\gamma_e}/\omega_{\text{pe}}$ (the reasons for this choice will become more apparent in the following section). The electron number densities are: $n_e = 1, 10^2, 10^4, 10^6$, and 10^8 cm^{-3} ; the electromagnetic wave frequency, $\omega/2\pi$, is 10 GHz.

The curves in Figure 8.1 exhibit a universal feature: the rotation angle reverses sign when the electric fluctuation field is sufficiently strong. As $\langle E^2 \rangle^{1/2} \rightarrow \infty$, the rotation is completely nullified. Notice that, for typical interstellar densities ($n_e \sim 1 \text{ cm}^{-3}$), a noticeable effect can be seen for electric field strengths $> 1.0 \text{ G}$.

Next, since strong quasi-collisions imply strong “collisional” absorption, we must consider the result of Eq. (8.10) – which will, in turn, constrain the strength of the ambient magnetic field. In Figure 8.2, the e-folding distance (i.e. $1/\alpha_{\text{absp}}^{\text{Farad}}$) is plotted as function of B_0 for the $n_e = 10^8 \text{ cm}^{-3}$ case from Figure 8.1. We see that the “collisional” absorption occurs on a many kilometer length scale. With $B_0 = 10 \text{ G}$, the signal would be reduced to a factor of 0.01 around 44 km. Thus, the limiting factor in the possible observation of the quasi-collisional Faraday effect is this absorption; which is, necessarily, strong when the

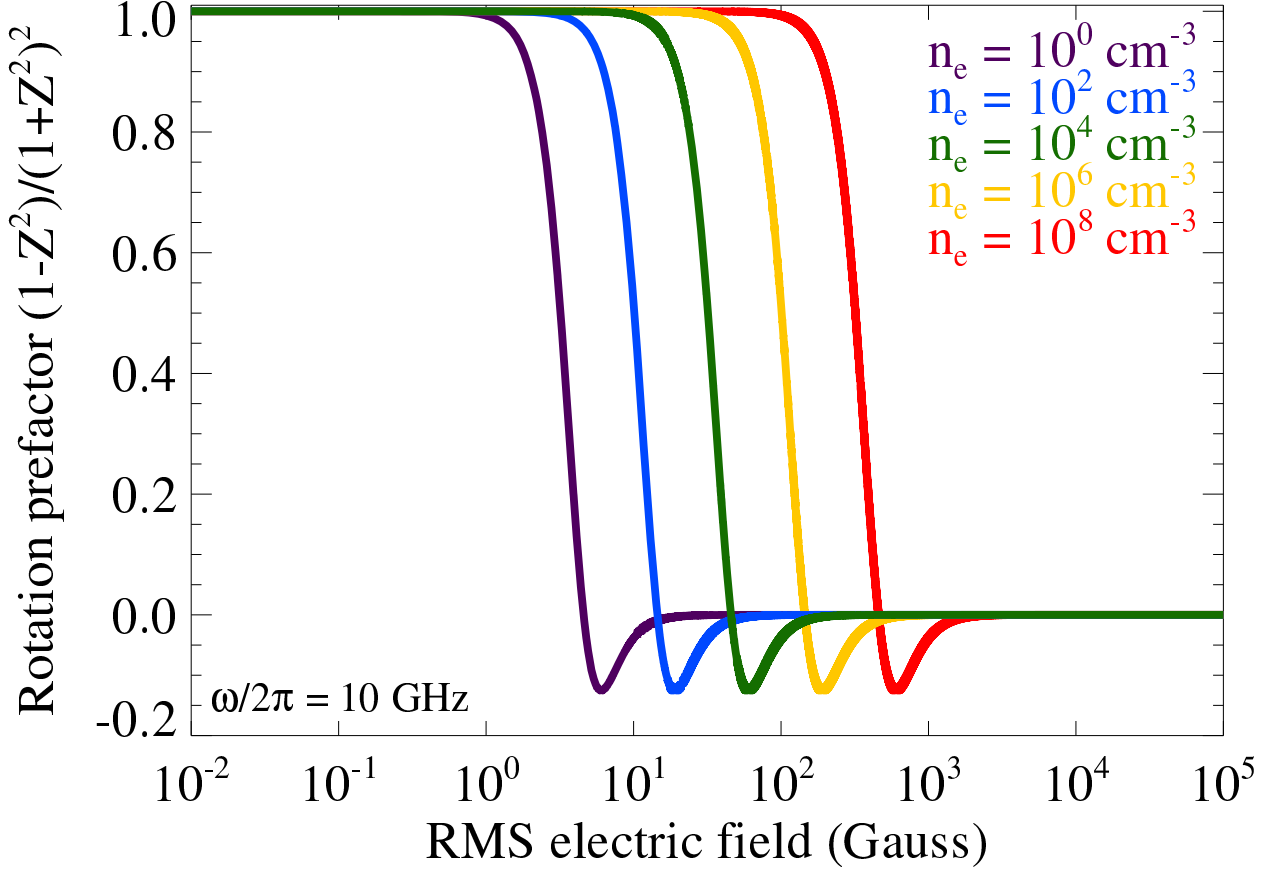


Figure 8.1: Normalized Faraday rotation angle – i.e. Eq. (7.27) – vs. the electric fluctuation strength for various electron densities. The electron number densities are (from right to left): $n_e = 1, 10^2, 10^4, 10^6$, and 10^8 cm^{-3} ; the electron temperature is 0.511 MeV (or $\gamma_e \sim 2$), and $\omega/2\pi = 10 \text{ GHz}$. These curves exhibit a universal feature; namely, the rotation angle will reverse sign when the electric fluctuation field is sufficiently strong. As $\langle E^2 \rangle^{1/2} \rightarrow \infty$, the rotation is completely nullified.

quasi-collision frequency is large. In the next section, we will argue that small-scale ion acoustic turbulence may present the ideal realization of electric quasi-collisionality in actual space, astrophysical, and laboratory plasmas.

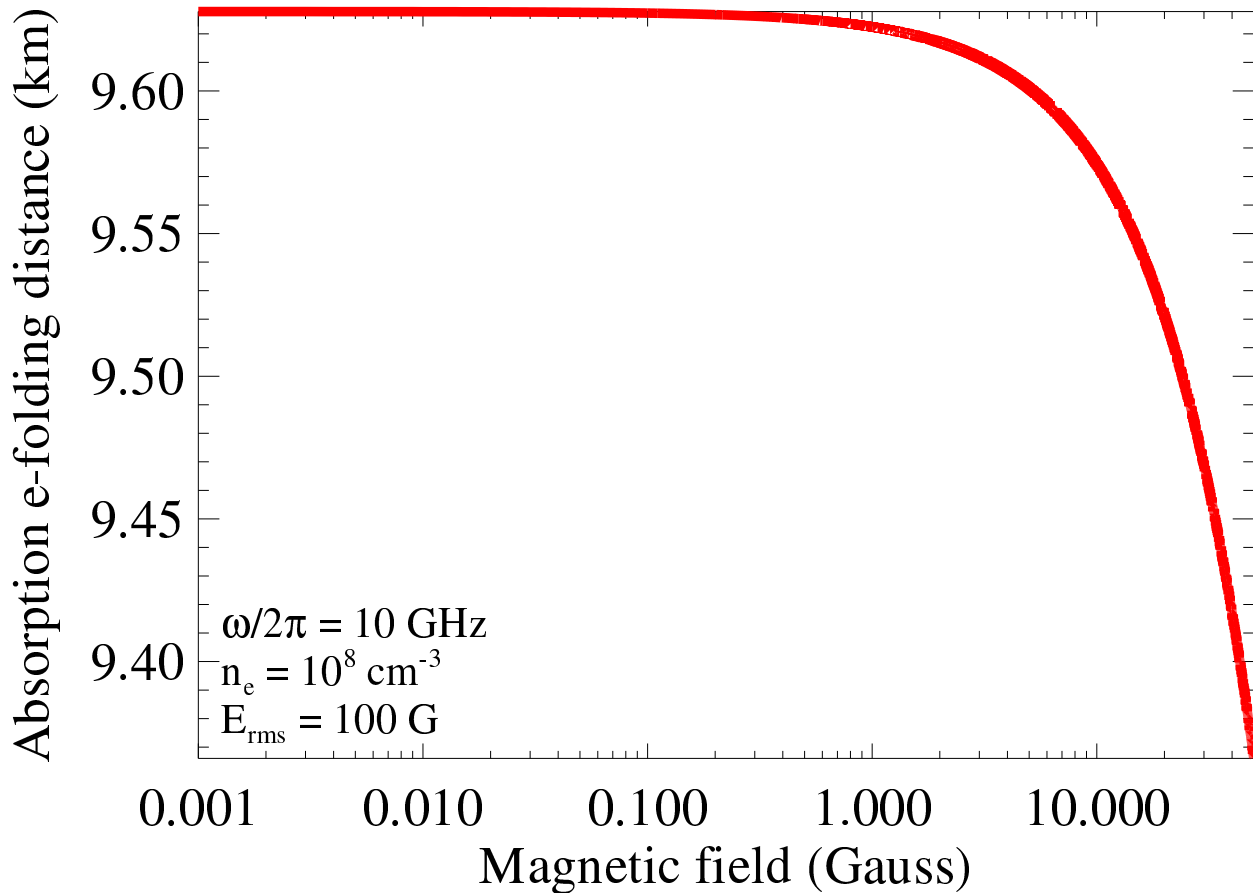


Figure 8.2: Quasi-collisional absorption e-folding distance vs. the ambient magnetic field. The instance depicted here is the $n_e = 10^8 \text{ cm}^{-3}$ case from Figure 8.1. We see that the “collisional” absorption occurs on a many kilometer length scale. With $B_0 = 10 \text{ G}$, the signal would be reduced to a factor of 0.01 around 44 km.

8.5 Small-Scale Electric Turbulence in Real Plasmas

For the realization of small-scale electric turbulence, the second condition from Eq. (5.8) is most difficult to satisfy. Using $\tau_E \sim c/\lambda_E^t$ and $\lambda_E^t \sim k_E^{-1}$, this condition is equivalent to:

$$\frac{k_E^2 c^2}{\Omega_r^2} \gg 1. \quad (8.11)$$

In accord with (Teraki & Takahara, 2014), we may be inclined to choose “cold” electron langmuir waves to mediate the turbulence. The dispersion relation, in this case, would be $\Omega_r = \omega_{pe}^{rel.}$ – where $\omega_{pe}^{rel.} \equiv \omega_{pe}/\sqrt{\gamma_e}$, is the relativistic plasma frequency. Thus, Eq. (8.11) would require that:

$$k_E c \gg \omega_{pe}^{rel.}, \quad (8.12)$$

or, equivalently, that the correlation length is smaller than the electron skin-depth. However, this is problematic. The thermally corrected, ultra-relativistic, dispersion relation for electron langmuir waves is(Bergman & Eliasson, 2001):

$$\Omega_r^2 = \frac{\sigma}{3} \omega_{pe}^2 + \frac{9}{5} k^2 c^2. \quad (8.13)$$

Thus, the condition that $\Omega_r \simeq \omega_{pe}^{rel.}$ contradicts Eq. (8.12), since these “cold” plasma waves require that $(27/5)k^2 c^2 \ll \sigma \omega_{pe}^2 \sim \omega_{pe}^2/\gamma_e$. Therefore, electron Langmuir turbulence may not self-consistently satisfy all the conditions that we require.

Alternatively, we may consider turbulence mediated by the ion population. In this case, we must be careful to specify electric fluctuations that exist on spatial scales comparable to the Debye length, λ_D , since the ion time-scales will be sufficiently long enough that electrons will effectively screen out these fields on electron scales; i.e. these “large-scale” electric fields have very little effect on the electron population.

When electric fluctuations exist on scales smaller than the Debye shielding length, then “quasi-neutrality” can be broken. Thus, with $m_i \gg \gamma_e m_e$ (where m_i is the ion mass), we

require that:

$$k_E \lambda_D \gtrsim 1, \quad (8.14)$$

where $\lambda_D = v_{\text{the}}/\omega_{\text{pe}}$, and $v_{\text{the}} \sim c$ is the electron thermal velocity.

One possible realization of this condition is provided by the very short wavelength branch of the ion acoustic mode. These modes can exist in magnetized plasmas, and we assume for our purposes that the wave-vector is nearly aligned with the direction of the ambient magnetic field. For a non-relativistic, “cold” plasma, If $k_E \lambda_D \gtrsim 1$, the ion acoustic mode has the frequency (Luo & Chian, 1997):

$$\Omega_r = \frac{\omega_{\text{pi}}}{1 + (k \lambda_D)^{-2}}, \quad (8.15)$$

where ω_{pi} is the ion plasma frequency. From this, we see that $\Omega_r \approx \omega_{\text{pi}}$ when $k \lambda_D \gg 1$. Ion acoustic turbulence may be strongly excited when the electron temperature far exceeds the ion temperature (Luo & Chian, 1997) – a scenario which is required here, since the ions are being treated as non-relativistic, while the electrons are – at least – mildly relativistic (i.e. $m_i \gg \gamma_e m_e$).

8.6 Discussion of Results

we explored the consequences of high electrically-induced quasi-collisionality for Faraday rotation in magnetized plasmas. We found – as we did, previously, for magnetically-induced quasi-collisionality – that the Faraday rotation measure, R_M , may obtain negative values, in this case. In fact, as the quasi-collision frequency becomes sufficiently large, $R_M \rightarrow 0$.

We, furthermore, speculated upon the most likely set of plasma parameters that would allow for direct observation of this, modified, Faraday effect. We found that quasi-collisional absorption may severely limit possible space and astrophysical applications of our model – since strong quasi-collisionality, also, implies strong “collisional” absorption.

Chapter 9

Jitter Radiation and Solid-Density Laser-Plasma Experiments

9.1 Introduction

The direct observation of mildly relativistic jitter radiation may be feasible in the laboratory setting. We will focus our attention upon the Mondal experiment (Mondal et al., 2012). This experiment provides a concrete example of an applicable laser plasma. Additionally, the Mondal experiment constructed, directly from data, the magnetic (spatial) power spectrum. A considerable amount of what is explored here is applicable to (short duration) relativistic laser-plasma experiments, in general.

9.2 The Weibel Instability in Laser-Plasma Experiments

In the Mondal experiment, conducted at the Tata Institute of Fundamental Research (TIFR), an aluminum coated, BK-7 glass target was irradiated by a 10^{18} W/cm^2 (800 nm , 30 fs duration) laser pump beam – thereby creating a plasma in the aluminum layer (with thickness several times larger than the electron skin-depth) of the target. A low-intensity probe beam (400 nm , 80 fs) was then introduced at a delay to the initial pump beam. This probe beam

was then reflected by the corresponding critical plasma surface. By exploiting the Cotton–Mouton effect, the strength, spatial, and temporal evolution of the generated magnetic fields were inferred by measuring the ellipticity induced in the probe beam’s polarization.

The observed magnetic fields were very intense, with a maximum value $\sim 63\text{ MG}$. Additionally, the fields were relatively long-lived – existing on a several picosecond time-scale – which is about a hundred times longer than the laser duration time-scale. These fields initially grow on a femtosecond time-scale and on spatial scales comparable to the electron skin-depth, $d_e \equiv c/\omega_{pe} \sim 0.1\text{ }\mu\text{m}$ – which is smaller than the probe spatial resolution of a few microns; consequently, their initial development was not directly observable. Nonetheless, the Weibel fields further evolved via mechanisms such as Kelvin-Helmholtz (KH) like instabilities (driven by fluid-like velocity shears). Finally, the random magnetic filamentary structures eventually exist on a picosecond time-scale and on a many micron spatial-scale – allowing their detection.

In the Mondal experiment, it was reported that the spatial spectrum of the magnetic field (in the target’s transverse plane) is well approximated by an inverse power-law which extends to spatial scales below the electron skin-depth. Furthermore, the spectral shape remains largely unchanged over a $\sim 10\text{ ps}$ time-scale. This result was additionally confirmed by 2D Particle-in-Cell (PIC) simulations. The PIC simulations further indicated that the magnetic field development is largely insensitive to the initial electron (10 eV) and ion (1 eV) temperatures. The final PIC ion temperatures were in the range 4–8 keV. The final electron temperature (300 – 600 keV; $t \sim 10\text{ ps}$) implies that the electrons are mildly relativistic; i.e. $\gamma_e \sim 2$, where $\beta \equiv v/c$ is the normalized electron velocity, and c is the speed of light.

9.3 Jitter Radiation

The question we address here is whether or not the plasma electrons emit jitter radiation in setups similar to the Mondal plasma experiment. Furthermore, is this radiation directly

observable in the framed experiment? Firstly, we must determine if the jitter prescription is appropriate, given the experimental parameters. We know that three principal parameters determine the jitter regime: the magnetic field strength, the electron velocities, and the magnetic field correlation length. The first two parameters are known scaling functions of the laser intensity, I and wavelength, λ . For a given intensity and wavelength, the (final) “forward” electron temperatures are given by Eq. (7.32). Substitution of the Mondal parameters gives the electron temperature of 253 keV. This is comparable to the PIC simulation (final) electron temperature 300 – 600 keV.

Likewise, the order of the laser generated Weibel magnetic field is indicated by Eq. (7.33), which suggests $B_{\text{Weibel}}^{\max} \approx 171 \text{ MG}$ (for $d_e \sim 0.1 \mu\text{m}$); this is similar to the maximum experimental value of $\sim 100 \text{ MG}$.

Next, the correlation length of the magnetic field is indicated by the characteristic wave number of the turbulent spectrum, k_{mag} . Given an inverse power-law spectrum for the magnetic fluctuations, k_{mag} is the minimum wave number, k_{\min} . This corresponds to a spatial-scale $\sim d_e$, thus we take $k_{\min} \sim d_e^{-1}$.

Now, electrons moving in a random, static, magnetic field \mathbf{B} will produce radiation in the small-deflection jitter regime if:

$$\rho \sim k_{\text{mag}} \frac{\gamma_e m_e \beta c^2}{e B}, \quad (9.1)$$

is greater than unity. Where B is an appropriate statistical average of the magnetic fluctuations. In the Mondal experiment, the spatially/temporally averaged magnetic field ($\approx 100 \text{ MG}$) was slightly larger than the maximum value of 63 MG. We have elected to take $B \sim B_{\max} \approx 63 \text{ MG}$.

Lastly, ρ will necessarily be small in the initial stages of the electron acceleration. So, we consider only the final time velocities (obtained from the PIC simulations) which are $v/c \equiv \beta \approx 0.78 - 0.89$. Then, finally, considering $\beta_{\min} \equiv 0.78$, the gyro-number, $\rho \approx 4$.

Thus, since ρ is slightly greater than unity, the radiation regime will be predominantly characteristic of the, mildly relativistic, jitter regime.

Nonetheless, the observability of the radiation is subject to a number of conditions. In the following subsections, we will outline and roughly estimate these limiting factors. Obviously, this list may not be exhaustive, but we will address the most apparent concerns.

9.3.1 The Jitter Frequency

Is the jitter radiation production time-scale small enough to temporally resolve the spectrum? This question may be answered by considering the jitter frequency:

$$\omega_{jn} \equiv \gamma_e^2 k_{\min} \beta c. \quad (9.2)$$

Considering only the final electron temperatures (i.e. the velocities $\beta = 0.78, 0.89$), the jitter frequency is

$$\omega_{jn} \sim 6 \times 10^{15} - 1 \times 10^{16} \text{ rad/s}, \quad (9.3)$$

indicating that the radiation is in the Extreme Ultraviolet (EUV) part of the EM spectrum. To avoid shielding by the plasma, ω_{jn} must be greater than the electron plasma frequency, ω_{pe} . The electron plasma density, at the critical surface, is indicated by the skin-depth, $d_e \sim 0.1 \mu m$. The corresponding plasma frequency is

$$\omega_{pe} \sim 3 \times 10^{15} \text{ rad/s}. \quad (9.4)$$

Thus, the jitter frequency is slightly larger than the plasma frequency. This indicates that plasma dispersion will play an important role in determining the spectral shape of the radiation, but the signal will nonetheless propagate throughout the entirety of the plasma. In contrast, non-relativistic electrons would emit cyclotron radiation in large-scale (i.e., weakly inhomogeneous or uniform) magnetic fields. In this case, the mean magnetic field (acting in

place as an ambient, uniform field) will admit a slightly broadened cyclotron component due to mild relativistic effects. With $\langle B \rangle \sim 100 \text{ MG}$, the cyclotron frequency is roughly:

$$\Omega_{ce} \sim 2 \times 10^{15} \text{ rad/s}, \quad (9.5)$$

This is slightly below the plasma cutoff, ω_{pe} . Thus, this cyclotron feature may not be readily observable – while, in contrast, the jitter frequency will be larger by a factor of a few. Furthermore, The isotropic jitter spectrum has a high-frequency break at

$$\omega_{bn} = \gamma_e^2 k_{max} \beta c, \quad (9.6)$$

where k_{\max} is the maximum turbulent wave number; i.e., the inverse of the turbulent wavelength at the shortest spatial-scale. The jitter and the break frequencies determine the window where most of the radiation is emitted.

Next, in order to well-resolve the radiation spectrum, one must observe the signal over several characteristic time-scales. Given a mildly relativistic electron, this time-scale must be several ω_{jn}^{-1} . In this case, $\omega_{jn}^{-1} \sim 0.1 \text{ fs}$. The magnetic field lifetime ($\sim 10 \text{ picoseconds}$) is many orders of magnitude larger than a femtosecond, thus the magnetic field will exist sufficiently long enough so that the jitter spectrum may be resolved. Furthermore, since the field-variability time-scale is $\sim \text{picoseconds}$, which is much longer, the magnetic field may be treated as static.

9.3.2 The Jitter Power

Now, we will estimate the volumetric power of jitter radiation to ascertain its observability using current instrumentation. We will ignore any magnetic anisotropy, statistical inhomogeneity, and plasma dispersion effects. We will consider a distribution of mono-energetic electrons that radiate isotropically. Since the characteristic wavelength of the emitted radiation by a single electron is smaller than the volume dimensions considered, we will assume

that the radiation of the individual electrons add incoherently. Thus, with these assumptions, and the experimental values used previously, the volumetric radiated power is:

$$\frac{dP}{dV} \sim \frac{2}{3} n_e c (r_e \gamma_{min} \beta_{min} B_{max})^2. \quad (9.7)$$

where n_e is the number density of electrons in volume dV , and $r_e = e^2/m_e c^2$ is the classical electron radius. We expect the Weibel fields to predominantly reside at scales comparable to the electron skin-depth. Since the fields will, likely, be strongest at the site of laser absorption, i.e. the critical surface, we may very roughly estimate the jitter power by substituting $n_e \sim n_c$ – where the n_c is the critical density, i.e.

$$n_c = \frac{m_e \omega^2}{4\pi e^2}, \quad (9.8)$$

where ω is the laser frequency. Thus, we estimate the volumetric jitter power as:

$$\frac{dP^{jitter}}{dV} \sim 10^{22} \text{ erg cm}^{-3} \text{ s}^{-1}. \quad (9.9)$$

Finally, we should compare this result to estimates for any competing radiation mechanisms. We believe that *thermal Bremssrahlung* (Bremss.) due to electron-ion collisions is the only likely complication. In the next subsection, we will make an attempt to roughly estimate the Bremss. contribution.

9.4 Thermal Bremssrahlung

To estimate the electron-ion Bremss. component, we will assume a thermal distribution of electrons. We will assume, as before, the estimate for the “effective” electron temperature, i.e. $T_e = 300 - 600 \text{ keV}$, obtained from the Mondal PIC simulations (Mondal et al., 2012). At these temperatures, the aluminum coating layer will be fully ionized, meaning $Z = 13$.

Ignoring the particle escape from the aluminum layer (either into the vacuum or the BK-7 glass), the number density of ions $n_i = n_e/Z$. Thus, neglecting self-absorption (which only occurs at small frequencies), the electron Bremss. power per unit volume (in cgs units) will be (Rybicki & Lightman, 1986):

$$\frac{dP}{dV} \sim 1.4 \times 10^{-27} T_e^{1/2} n_e n_i Z^2. \quad (9.10)$$

Now, we suspect that Bremss. radiation will be emitted throughout the entirety of the plasma. Nonetheless, owing to the square dependence on the plasma density, the regions of high-density will dominate the total emission power.

Thus, we need an estimate of the density profile. To that end, we adopt the electron density supposed by the Mondal PIC simulations. This was an exponential profile, in the longitudinal direction, of the form:

$$n_e(z) = \exp(z/L - 1), \quad (9.11)$$

where $L = 2\lambda$ is the scale length, and z is the longitudinal coordinate. The profile was uniform in the transverse plane. This longitudinal trend continued up to a plateau at $n_e = 140n_c$. Then, the simulation box ended at $z = 16\lambda$. We adopt this profile here.

Finally, for our estimate of the Bremss. component, we will suppose that $n_e = 140n_c$. With this substitution, we have:

$$\frac{dP^{Bremss.}}{dV} \sim 10^{26} \text{ erg cm}^{-3} \text{ s}^{-1}. \quad (9.12)$$

This value is four orders of magnitude larger than the jitter radiation power. However, this estimate does not account for the variation in the power across the frequency domain. For this, we will need to estimate the radiation spectrum. As we will show, the jitter spectrum dominates at low frequencies.

As a final consideration, we must ensure that these radiative processes are not obscured by the inevitable loss of particle energy via *radiative cooling*. This requires that we estimate the cooling time-scales.

9.5 Radiative Cooling

First, we consider the Bremss. cooling time. Considering the electrons as a classical monoatomic gas, the Bremss. cooling time, with $n_e = 140n_c$, is

$$t_{\text{cool}}^{\text{Bremss.}} \sim \frac{3n_e k_B T_e}{\left(\frac{dP^{\text{Bremss.}}}{dV} \right)} \sim 100 \mu\text{s}, \quad (9.13)$$

which is a few orders of magnitude larger than all other time-scales in this experiment. Thus, Bremss. cooling is negligible.

The jitter cooling time-scale may be estimated by considering the time at which the radiated power, for a given electron, is comparable to that electron's initial kinetic energy, i.e.

$$P_{\text{single}}^{\text{jitter}} t_{\text{cool}}^{\text{jitter}} \sim (\gamma_e - 1)m_e c^2, \quad (9.14)$$

where $P_{\text{single}}^{\text{jitter}}$ is the power emitted by a single particle – i.e. Eq. (9.7) divided by n_e . Using $\gamma_e \approx 1.59$, the jitter cooling time is

$$t_{\text{cool}}^{\text{jitter}} \sim 0.1 \mu\text{s}, \quad (9.15)$$

which is, also, sufficiently long enough to be ignored. We may conclude that, neither Bremss. nor jitter cooling, is significant.

9.6 The Radiation Power Spectrum

Finally, we make predictions for the spectral profile of the emitted radiation. We retain our initial assumptions that the magnetic turbulence is statistically isotropic, that the electron density has the exponential (longitudinal) profile – Eq. (9.11) – that plateaus at $n_e = 140n_c$, and that the electron velocities are thermally distributed.

Next, the thermal Brems. power spectral density (i.e., radiated power per frequency per unit volume) is a well known function:

$$\frac{dP}{d\omega dV} = \frac{8\sqrt{2}}{3\sqrt{\pi}} \sqrt{\epsilon(\omega)} [Z^2 n_i n_e r_e^3] \frac{(m_e c^2)^{3/2}}{(k_B T_e)^{1/2}} \bar{G}(\omega, T_e), \quad (9.16)$$

where $\sqrt{\epsilon(\omega)}$ is the scalar dielectric permittivity, and $\bar{G}(\omega, T_e)$ is the velocity-averaged Gaunt factor. For high-temperature, though non-relativistic, electrons (Bekefi, 1966):

$$\bar{G}(\omega, T_e) = \ln \left(\frac{4}{\gamma} \frac{k_B T_e}{\hbar \omega} \right), \quad (9.17)$$

where $\gamma \approx 0.5772$ is the Euler–Mascheroni constant. Since the electron velocities are only mildly relativistic, the relativistic correction to Eq. (9.17) will be relatively small – a factor of a few.

We may obtain the total Brems. spectral flux by integrating Eq. (9.16) over the length of z , i.e.

$$\frac{dP}{d\omega dA} = \frac{8\sqrt{2}}{3\sqrt{\pi}} \frac{(m_e c^2)^{3/2}}{(k_B T_e)^{1/2}} \bar{G}(\omega, T_e) Z^2 r_e^3 \int \sqrt{\epsilon(\omega(z))} n_i(z) n_e(z) dz, \quad (9.18)$$

where dA is the differential cross-section, and dP is the differential radiant power.

Next, to obtain the total jitter spectrum from a thermal distribution of electrons, we must average the single electron spectrum over the appropriate Maxwell-Boltzmann distribution, à la Eq. (6.46). Thus, assuming the jitter prescription for the entirety of the plasma length,

the spectral flux of jitter radiation will be:

$$\frac{dP}{d\omega dA} = \int n_e(z) \frac{\int P_j(\omega, \omega_{pe}(z), p) e^{\sigma(1-\gamma_e)} d^3p}{\int e^{\sigma(1-\gamma_e)} d^3p} dz, \quad (9.19)$$

Due to non-perturbative effects, the low-frequency end of the jitter radiation spectrum will differ slightly from the jitter prescription by the addition of an $\omega^{1/2}$ power-law asymptote (Teraki & Takahara, 2014). Given $\rho \sim 4$ and $\omega_{pe} \sim \omega_{jn}$, this deviation will be present near ω_{pe} ; it has no effect, however, on the high-frequency end of the spectrum. Consequently, we have elected to ignore this feature.

As stated previously, a cyclotron/synchrotron component, corresponding to the mean magnetic field, will be present. However, since this component is largely screened out by plasma dispersion, and its effect is already well known, we omit it here.

Additionally, we safely ignore the damping effect of Coulomb collisions, since the experimental Reynold's number is $Re_{exp} \sim \omega_{pe}/\nu_{ei} \sim 10^6$ – where ν_{ei} is the electron-ion collision frequency (Mondal et al., 2012). From this, we may infer that $\omega_{jn} \gg \nu_{ei}$.

Finally, we neglect the plasma gyrotropy. Since $\omega_{ce} < \omega_{pe}$, the gyrotropy will not be critically important to the plasma dispersion at high frequencies, i.e. near ω_{bn} .

Thus, we consider an isotropic, collisionless plasma. The scalar dielectric permittivity is, consequently

$$\epsilon(\omega) = 1 - \omega_{pe}^2/\omega^2. \quad (9.20)$$

Finally, we may construct the radiation power spectrum. In each plot, the relevant parameters are: $\mu = 4$, $\omega_{pe} = 3 \times 10^{15} \text{ rad/s}$, $k_{min} = 0.5\omega_{pe}/c$, $k_{max} = 10k_{min}$, $n_e = 3 \times 10^{21} \text{ cm}^{-3}$, $n_i = n_e/Z$, $k_B T_e = 300 \text{ keV}$, and $\langle B^2 \rangle^{1/2} = 63 \text{ MG}$. The jitter spectrum was constructed using a logarithmically spaced, discretized range of electron velocities from $\beta_{min} = 0.1$ to $\beta_{max} = 0.99$.

In Figure 9.1, the total spectral flux is plotted (“purple”, solid line) alongside the individual thermal Bremsstrahlung (“red”, lower-left dashed line) and jitter (“blue”, upper-left

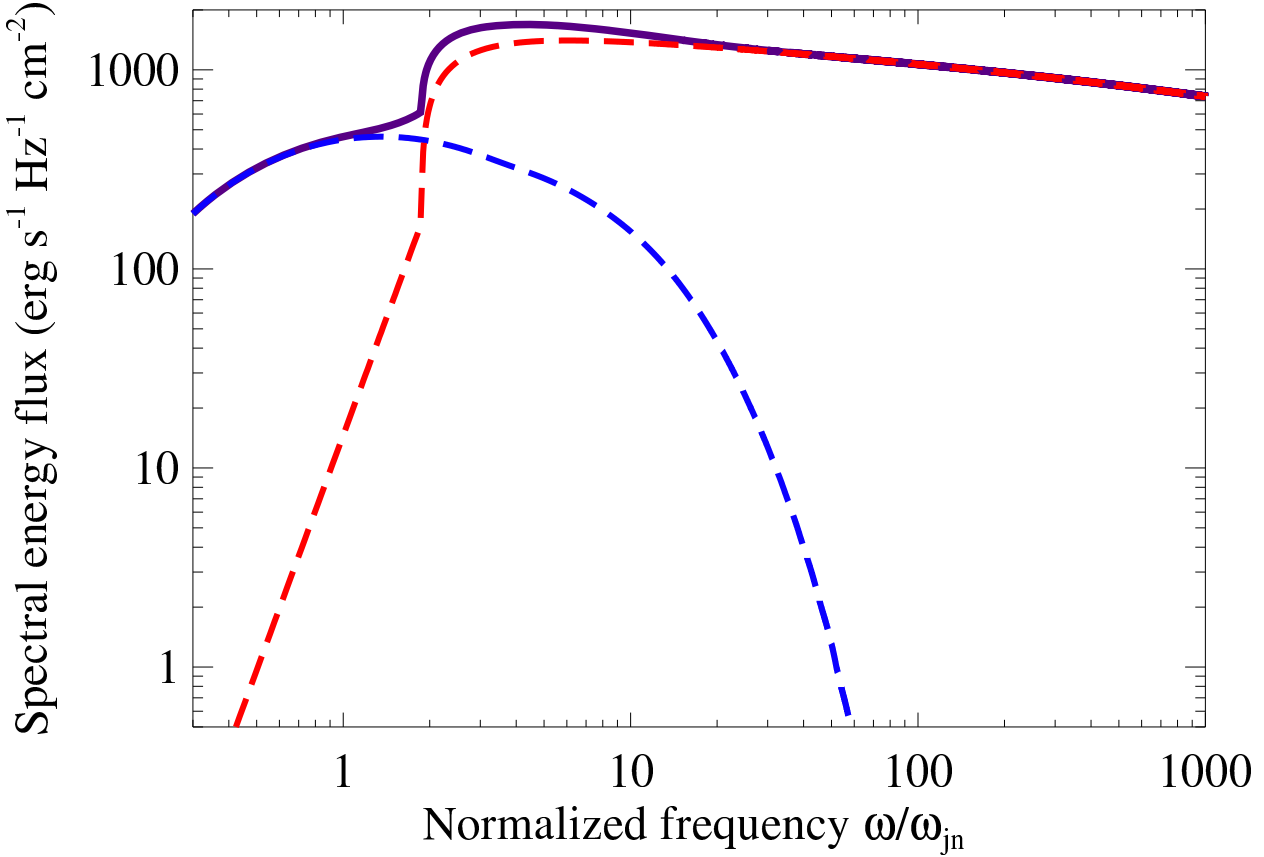


Figure 9.1: Spectral flux (differential flux per differential frequency) of the total emitted radiation vs normalized frequency. The frequency is normalized to the jitter frequency, i.e. Eq. (9.2). The total power (“purple”, solid line) is the sum of the individual jitter (“blue”, upper-left dashed line) and Bremssrahlung (“red”, lower-left dashed line) components. Clearly, the jitter component dominants near the jitter frequency (here defined as $f = \omega/2\pi$).

dashed line) components. Notice that the jitter component dominants at frequencies near the jitter frequency, $\omega_{jn} \sim \gamma_e^2 k_{min} \beta c$ – where $1/\sqrt{1 - \beta^2} = \gamma_e$ and $(\gamma_e - 1)m_e c^2 \sim k_B T_e$.

Next, Figure 9.2 displays the photon flux at each frequency; i.e., Figure 9.1 divided by the the photon energy, $\hbar\omega$. By integrating these curves over the complete frequency range, we may estimate the total photon flux for each component. These are 2×10^{29} (*photons*) $cm^{-2} s^{-1}$ and 10^{30} (*photons*) $cm^{-2} s^{-1}$ for jitter and Bremss., respectively. Thus, it would appear that the Bremss. flux is only an order of magnitude larger than the jitter flux. Since Bremss. emission is easily and routinely detectable in plasma experiments, it should be easy to observe jitter radiation too. It is the very distinct spectral shapes of the two, along with the high

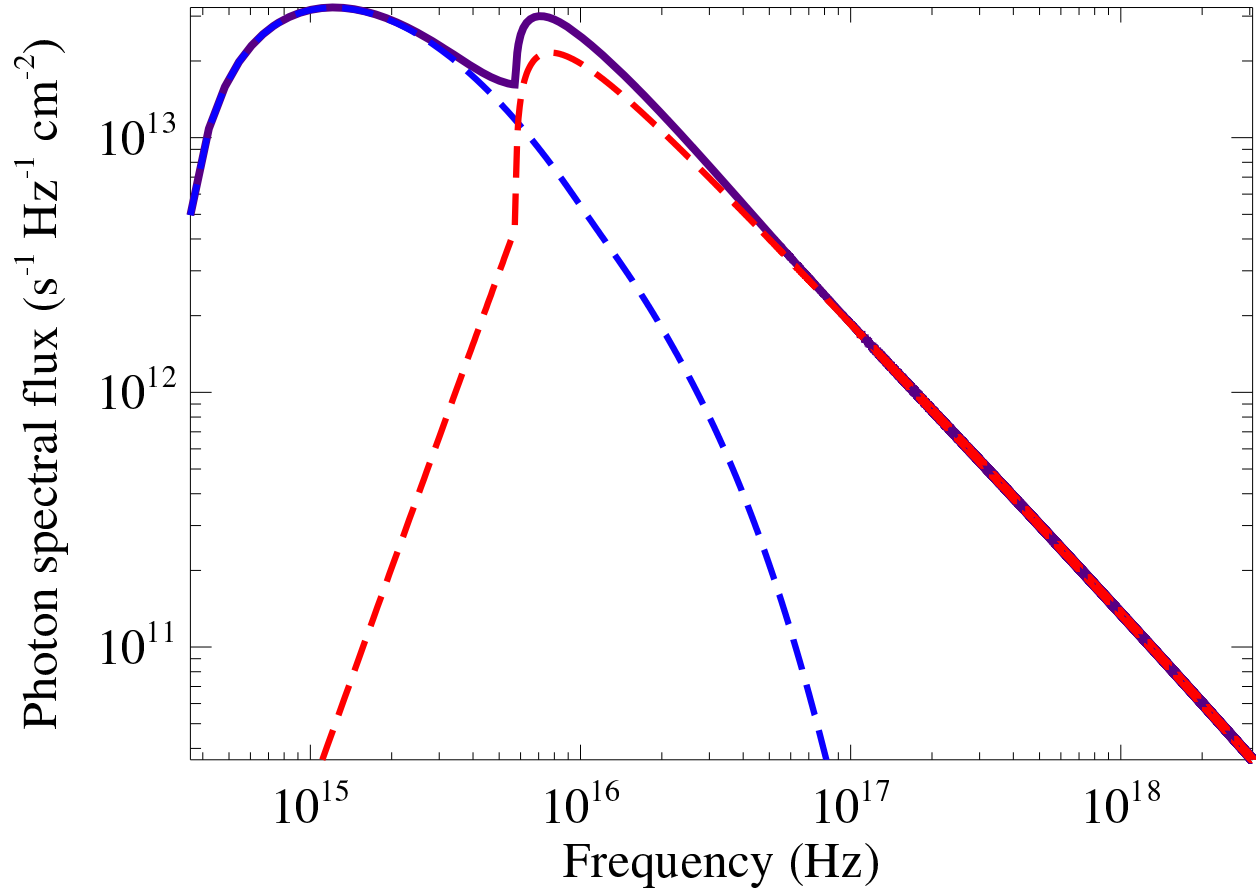


Figure 9.2: The photon flux at each frequency; i.e. Figure 9.1 divided by the the photon energy, $\hbar\omega$. We see that the majority of the jitter flux is at frequencies slightly below the jitter frequency, ω_{jn} .

fluxes, that make Bremss. and jitter radiation easily distinguishable from one another and allows one to resolve their spectral features well – the key factor of a good plasma diagnostic tool.

9.7 Discussion of Results

In this Chapter, we have investigated the prospects for the direct radiative diagnostics of a mildly relativistic, solid-density laser plasmas produced in current lab experiments. Our results demonstrate the feasibility of such an approach. Particularly, our analysis shows that a sub-relativistic laser-plasma setup, such as the experiment described in Mondal, et al. (Mondal et al., 2012), is a promising candidate for the direct observation of mildly relativistic jitter radiation.

A very important feature of our model, as an advanced radiative diagnostic tool, is the ability to probe plasmas at different locations (depths). Indeed, Bremss. is a quadratic function of the density, so this radiation probes the plasma conditions in the densest parts of the plasma, i.e., deep into the “core”. In contrast, jitter radiation probes the region with the strongest small-scale fields, which occur where the laser energy/momentum deposition is most efficient, i.e., near the critical surface. The location of this region depends on both plasma density and the laser frequency, which opens up a possibility to do some sort of “plasma tomography” by using different laser frequencies. We believe these provide sufficient impetus for experimental exploration.

Chapter 10

General Conclusions

In this Chapter, we present our general conclusions. We discuss the limitations inherent in our model, and speculate upon how we may address these weaknesses in the future. We, furthermore, speculate upon the possible applications of our model to real plasmas. We, finally, consider the physical questions still remaining – concluding, ultimately, that a considerable amount of work is still needed to answer these questions definitively.

10.1 Assumptions Concerning Turbulence

The theoretical and numerical models applied throughout this work have a proper domain of application. The assumptions we have made about the electromagnetic turbulence, in particular, presents a strict constraint.

For example, in real plasmas, the turbulence dissipation time-scale, growth rate, time-evolution, and spatial-scale are important considerations. Throughout much of this work, we have particularly highlighted the Weibel-like turbulence because of its favorable properties. As stated previously, the Weibel instability is aperiodic (i.e. real frequency $\Omega_r \sim 0$), and thus allows for the static field treatment – a fact that we have exploited many times. More precisely, the growth rate $\Omega_i \gg \Omega_r$.

Additionally, the Weibel-filamentation fluctuations are long-lived, dying out only when

the driving free energy (provided by the kinetic energy of streaming particle filaments) of the system is converted by particle isotropization (i.e. the depletion of the anisotropy in the streaming particle distribution function). In short, the generated fields are approximately stationary on a time-scale which exceeds the growth/stabilization rate times (Treumann & Baumjohann, 2012).

All of these properties suggest that there will be adequate time for radiation production in the jitter regime, given by our prescription, in these “quasi-static” Weibel magnetic fields. A conclusion that is well supported by the time-scale arguments made in Chapter 9, concerning solid-density laser-plasmas.

Nonetheless, Whistler-like instabilities, for example, may be more likely to take hold in “pre-magnetized” media. Their complete description, furthermore, may extend beyond the “cold plasma” approximation – requiring “thermal” corrections to the dielectric tensor, and therefore, the dispersion relation. Nonetheless, we suspect, in the static limit, that our results will deviate only quantitatively in these cases.

10.2 The Applicability of the Radiation Perturbation Theory

We may reiterate that our treatment of pseudo-cyclotron radiation assumes small deflections; an assumption that allowed the use of the, so called, perturbation theory. Recent work (Kelner et al., 2013) has considered a formal treatment of the perturbation theory that exclusively requires that the deflection angle over a correlation length is small, i.e. $\alpha_\lambda \ll 1$. Due to continued diffusive scatterings of the electron, its path will eventually deviate strongly from its initial trajectory. The traditional perturbative approach, regardless, remains valid so long as the trajectory remains approximately straight over the radiation formation length, at least for the considered domain of frequencies (i.e. lower frequencies will, inevitably, require a non-perturbative treatment). In the non-relativistic limit, the formation length is $\sim k^{-1}$.

This must be less than, or comparable to, the magnetic correlation length, λ_B . With the characteristic frequency, ω_{jn} , this length is $\sim \lambda_B/\beta$. Consequently, as long as the particle velocity is not arbitrary small, the perturbative approach will be valid; if α_λ is, indeed, small. By way of numerical simulation, we demonstrated that this condition holds as long as $\rho > 1$ (i.e. the turbulence is sub-Larmor in scale).

Concerning our realization of Langmuir turbulence, it is noteworthy that the $\chi \gg 1$ condition may not be physically realizable, since Landau damping would likely eliminate wave-modes at sub-skin-depth spatial scales too quickly (Teraki & Takahara, 2014). With the field variability time-scales of comparable order to the electric correlation length transit time, it may be necessary to consider the rms electric field as a function of time. Thus, a more realistic model may require a time-dependent pitch-angle diffusion coefficient.

10.3 Plasma Dispersion and Pseudo-Cyclotron Radiation

The fact that plasma dispersion may play a significant role in the non-relativistic limit should be thoroughly considered. The plasma dispersion effect is only important for frequencies $\omega \ll \gamma_e \omega_{pe}$ – below which, suppression of relativistic beaming (due to the Razin effect) occurs (Jackson, 1998; Rybicki & Lightman, 1986). Electron driven Weibel-like turbulence occurs on a very small-scale, with $\lambda_B \sim d_e$. Consequently, in the ultra-relativistic regime, the jitter frequency is many orders of magnitude larger than the plasma frequency – by a factor $\sim \gamma_e^2$.

However, in the non-relativistic and trans-relativistic regimes, dispersion can play a considerable role. This will especially be so for $\beta \ll 1$. In this case, a considerable portion of the radiation spectrum may fall below ω_{pe} , and thus be unobservable.

Furthermore, via subsequent non-linear evolution, the electron-generated Weibel magnetic fields may grow to larger spatial-scales – including the ion skin-depth. Additionally, the Weibel fields may “seed” the growth of further MHD turbulence via a process of inverse-

cascade – once more, residing at larger spatial-scales. Thus, in the non-relativistic regime, the jitter radiation spectrum may be effectively screened out when the turbulent magnetic fields predominantly exist at scales much larger than the electron skin-depth. Consequently, non-relativistic jitter radiation, as a diagnostic of Weibel turbulence, may have a limited applicability.

Nonetheless, kinetic instabilities in magnetized plasma can produce turbulent magnetic spectra at the appropriate length scales as well. Anisotropic whistler turbulence may provide a promising candidate – which is why we have selected it for a detailed study. In fact, the cold collisionless Whistler spectrum (perpendicular to the mean magnetic field) may be rather broadband – a (stationary) piece-wise set of power-laws extending to scales much smaller than the electron skin-depth (Saito et al., 2010).

Lastly, the effect of quasi-collisions, in principle, should be included in the plasma dispersion relation for jitter radiation as well. However, this would amount to be a second-order correction to the jitter perturbation theory, since the jitter radiation-producing electrons would, themselves, be the particles that attenuate the “jitter radiation fields”. Self-consistency with the perturbation theory requires that only first-order corrections to the electron trajectories must suffice to account for their accelerations. Hence, any “second-order” corrections by the introduction of radiation fields of other particles would be negligibly small.

Furthermore, if these radiation fields were strong enough to significantly affect the trajectories of the electrons, then the assumption that radiative cooling may be ignored would also fail – since the energy contained in the “jitter fields” would necessarily be comparable to each electron’s kinetic energy.

10.4 Small-Scale Whistler/Langmuir Turbulence and “Cold” Plasmas

Our model implicitly considered a scenario whereby a turbulent magnetic field was generated in a cold, magnetized, background plasma. We then imagined the existence of a “hot” population of sub-Larmor-scale electrons that served as our test particles. We suggested that the motion of high-energy, supra-thermal, “super-Halo” electrons through the magnetized solar wind is a promising candidate for the physical realization of our model. Indeed, despite the fact that this population only accounts for a small fraction of a percent of the solar wind, its high energy ($2 - 20 \text{ keV}$) makes it very significant (Wang et al., 2015; Yoon, 2015).

Additionally, the super-Halo population is largely insensitive to solar activity, and it is likely constantly present in the interplanetary plasma (Wang et al., 2015) – thus, it is a relatively fixed source of high-energy particles. In fact, recent work has suggested that the super-Halo electrons may mediate Weibel-like instabilities in the solar wind plasma – facilitating the development of Kinetic-Alfvén wave (KAW) and/or Whistler-mode turbulence at sub-electron spatial scales (Che et al., 2014).

The nature of this wave turbulence, in the solar wind plasma, is a matter of contention. Conflicting accounts implicate either KAW or Whistler-modes (or both) (Mithaiwala et al., 2012; Salem et al., 2012). A number of reasons for this ambiguity have been given. For example, in situ measurements of these waves must be done in the spacecraft frame – which is usually moving at super-Alfvénic speeds with respect to the plasma (Salem et al., 2012). Furthermore, the solar wind hosts a permanent source of turbulence; hence, many results implicating Whistler waves – via, for example, the observed power spectrum – may be the erroneous signature of the, ever present, background turbulence (Lacombe et al., 2014).

However, a more detailed analysis of the turbulent spectrum may provide a means by which Whistlers and KAW may be distinguished. In fact, the degree of anisotropy has been found to significantly differ between the two types of wave turbulence (Salem et al., 2012).

With regard to our model, the presence of anisotropy will result in diffusion coefficients that differ perpendicular and parallel to the anisotropy axis (which is typically the direction of the ambient magnetic field), since the correlation lengths will depend upon the structure of the correlation tensor.

Hence, we may imagine that the transport properties of “hot” electrons (e.g. sub-Larmor-scale, super-Halo electrons) may be different for Whistler-mode and KAW turbulence. The radiation spectrum would, additionally, distinguish these forms of turbulence – as the anisotropy, which features into the field correlation tensor, would alter the shape of the radiation spectrum in a characteristic way.

Other cases where this work is of great interest include the upstream of collisionless shocks in astrophysical and interplanetary systems. The “hot” population, in this case, would be Cosmic Rays (CRs) – which are both non-relativistic and relativistic in astrophysical systems. Relativistic CRs are radiatively efficient and radiation from them is observed in supernova remnant shocks (Tycho, Chandra, 1003, etc) pulsar wind nebulae, termination shocks, GRBs (internal and reverse shocks, if the ejecta is magnetized) and GRB remnants. In the latter case, the external shock may become weak and non-relativistic. Consequently, the ambient interstellar field may become significant, and Whistler-like instabilities may develop from an initial Weibel “seed”.

Concerning Whistler turbulence and our energy diffusion coefficient, our model’s principal limitation is the essential assumption of the “cold” plasma approximation. In many cases, thermal effects must be accounted for; i.e. the plasma “beta” is non-negligible. Nonetheless, under certain conditions, the underlying plasma may be considered “cold”. As an example, the plasma outflow in ultrarelativistic “collisionless” shocks is beam-like, with very little dispersion; this permits a cold plasma treatment (Lemoine & Pelletier, 2010). Therefore, since these shocks may be mediated in part by small-scale Whistler-modes, our rough estimates concerning the diffusive transport of electrons may provide some insight into the process of shock acceleration.

10.5 Quasi-collisions in Real Plasmas

In Chapter 7, we once more considered Weibel-like turbulence as the ideal candidate for quasi-collisionality. Nonetheless, strong Weibel-like magnetic fluctuations are not likely present in all collisionless or weakly collisional plasmas. Of course, the leading candidates for the existence of strong fluctuations include: collisionless shocks in gamma-ray bursts and early moments of supernova explosions, high-intensity laser plasmas, and turbulent solar wind and magnetosphere/magnetotail plasmas.

Our principal assumption that the wave packet spatial scale is much greater than the small-scale magnetic correlation length, however, seems to rule out most interstellar and intergalactic plasmas, where the magnetic correlation lengths are believed to be $\sim 100\text{ pc}$ and $\sim kpc - Mpc$, respectively (Beck & Grave, 1987; Neronov et al., 2013). Allowing for hidden small-scale components (with smaller correlation lengths) in these environments requires unrealistically large magnetic fields to keep the absorption *e-folding* distance at parsec to kiloparsec scales; this is required so that a signal may not be completely absorbed in transit.

Finally, we argued in Chapter 8 that plasmas with high-frequency, small-scale, ion-acoustic turbulence – where $T_e \gg T_i$ – offer the most likely environment in which electrically-induced quasi-collisional effects may be physically realized. Supernova remant (SNR) shocks, for example, may host ion-acoustic instabilities that may drive the required strong, turbulent fluctuations (Dieckmann et al., 2000). Acoustic modes have, additionally, been implicated in the phenomenon of pulsar eclipsing, and astrophysical accretion flows where $T_i \neq T_e$ (Luo & Chian, 1997). Thus, a number of astrophysical environments may be favorable candidates.

However, owing to the high “collisional” absorption that accompanies high quasi-collisionality, the Faraday signature of these plasmas may be completely obscured. For this reason, space and laboratory plasmas may be better suited for the direct observation of this unique signature. Laser-plasmas, specifically, are an attractive candidate – since sufficiently intense laser pulses can quickly heat an electron population and separate it from an ion background.

Such a plasma configuration is especially susceptible to ion-acoustic instabilities.

10.6 Jitter Radiation and Laser-Plasmas

In Chapter 9, in order to produce results, we had to make a number of assumptions. The most important of these concerns isotropy – both in the magnetic turbulence and the emission of radiation. The turbulent magnetic fields produced by Weibel-like instabilities are typically characterized by anisotropy. This is because the distribution function of particles that produce Weibel fields is, itself, anisotropic. Thus, our assumption that an isotropic Maxwell-Boltzmann distribution, with a given “effective” temperature for the entire plasma, is not likely to hold on initial time-scales.

Similarly, our assumption that the magnetic turbulence is statistically homogeneous – i.e. characterized by a single spectral distribution throughout the plasma – is suspect. The correlation length throughout the plasma is likely, itself, a function of the electron density. For this reason, there may be regions within the solid target where the magnetic field is not sub-Larmor-scale; hence, the small-angle jitter prescription fails there.

Nevertheless, we believe our model is reasonable. Our model illustrates two key features that we expect will be present in real lab experiments. First, the Weibler spectrum peaks near the frequency, $\omega_{jn} = \gamma_e^2 k_{\min} \beta c$, where k_{\min} is the characteristic wave-number of the magnetic turbulence. Thus, we may directly extract the correlation length, $\lambda_B \sim k_{\min}^{-1}$, from the radiation spectrum. Lastly, the jitter spectrum takes a sharp drop near the second break, $\omega_{bn} = \gamma_e^2 k_{\max} \beta c$. Similarly, k_{\max} denotes the minimum spatial scale. Although this feature may be concealed by the Bremss. component, we may extract it by subtracting the predicted Bremss. spectrum.

It is worthwhile to note that the scale of the magnetic field is dictated by the electrons in these solid-density plasma experiments. In contrast, the Weibel instability in (laser ablated) plasma flows is mediated by the ions. Consequently, the spatial scale of these Weibel

magnetic fields will be on the order of the ion skin-depth. For this reason, these magnetic fields will not be sub-Larmor-scale with respect to the electrons; thus, the electrons will not emit radiation in the small-deflection jitter regime. Therefore, the magnetic fields are not so easily identifiable by the internal radiation production of the plasma electrons. Rather, proton-radiography or Thomson scattering, via the injection of external particles, is the prescribed diagnostic tool (Huntington et al., 2015; Sakawa et al., 2013).

In principle, the sub-Larmor-scale ions should emit jitter radiation, but this will be orders of magnitude less intense (because of their higher mass) than the radiation produced by electrons via alternative radiation mechanisms. In addition, plasma dispersion would certainly screen out any ion jitter radiation, since the characteristic emission frequencies will be well below the electron plasma cutoff frequency. Thus, we do not anticipate that our results will be immediately applicable to the laser setups, such as NIF and OMEGA/OMEGA EP, as they stand currently. These experiments would, rather, likely require a modification of the setup to realize the creation of a solid-density plasma.

10.7 Future Studies

Small-scale electromagnetic turbulence is a rich phenomenon that plays an important role in many plasma environments. Second, there is still much to learn about plasma physics at these smallest scales. In this work, we have shed considerable light upon the matter of sub-Larmor-scale magnetic fields. Nonetheless, a more general treatment may prove necessary to answer some of physical questions that spurred interest in small-scale turbulence.

Astrophysical plasmas, for example, contain a number of spatial/temporal scales. Included in these settings are “cold”, “thermal”, and relativistic plasmas. Thus, their complete kinetic treatment must appeal to this larger picture. Only then will be able to definitively answer questions, such as, “how do small-scale fields precisely affect the Fermi acceleration prescription for collisionless shocks?”. Or, “can we observe the signature of small-scale

turbulence in the Faraday rotation measures of interplanetary, interstellar, and/or cosmic magnetic fields?”.

Similarly, as the existence of “Superhalo” electrons demonstrates, the mixing of scales is very important to some solar system plasmas, as well. It is possible that small-scale effects may be important for solar plasma turbulence. It is likely, however, that these effects reside on ion, rather than electron, scales.

Some important questions concerning, specifically, laboratory plasma experiments remain. Perhaps the most significant one is this: “do small-scale field effects impact ICF experiments?”. “Do they potentially inhibit, or promote, ignition?” Only a detailed study may provide any conclusive resolution.

10.8 Final Remarks

In short, despite a number of physical limitations, the results obtained here reveal strong inter-relation of transport and radiative properties of plasmas turbulent at small spatial scales – which may be readily exploited for plasma diagnostics. Furthermore, concealed in this turbulence is a “collisional” signature, which may provide a useful radiative diagnostic of magnetic micro-turbulence in laboratory, astrophysical, space and solar plasmas, as well as significantly affect performance of inertial confinement fusion and laser plasma experiments.

Bibliography

- Ren, C., Tzoufras, M., Tsung, F. S., et al. 2004, Physical Review Letters, 93, 185004
- Tatarakis, M., Beg, F. N., Clark, E. L., et al. 2003, Physical Review Letters, 90, 175001
- Guo, F., Li, S., Li, H., et al. 2012, ApJ, 747, 98
- Mao, J., Wang, J. 2007, ApJ, 669, L13
- Gurnett, D. A., Neubauer, F. M., & Schwenn, R. 1979, Journal of Geophysical Research, 84, 541
- McAteer, R. T. J., Gallagher, P. T., & Conlon, P. A. 2010, Advances in Space Research, 45, 1067
- Treumann, R. A., & Baumjohann, W., *Advanced Space Plasma Physics* (Imperial College Press, London, 1997).
- Weibel, E.S. 1959, PRL, 2, 83
- Fried, B. D. 1959, Physics of Fluids, 2, 337
- Medvedev, M. V., & Loeb, A. 1999, ApJ, 526, 697
- Silva, L. O., Fonseca, R. A., Tonge, J. W., et al. 2003, ApJL, 596, L121
- Nishikawa, K.-I., Hardee, P., Richardson, G., et al. 2003, ApJ, 595, 555
- Frederiksen, J. T., Heddal, C. B., Haugbølle, T., & Nordlund, Å. 2004, ApJL, 608, L13

- Spitkovsky, A. 2005, *Astrophysical Sources of High Energy Particles and Radiation*, 801, 253
- Spitkovsky, A. 2008, *ApJL*, 673, L39
- Medvedev, M. V. 2006, *ApJ*, 637, 869
- Fiuza, F., Fonseca, R. A., Tonge, J., Mori, W. B., & Silva, L. O. 2012, arXiv:1204.5914
- Medvedev, M. V. 2000, *ApJ*, 540, 704
- Medvedev, M. V., Frederiksen, J. T., Haugbølle, T., & Nordlund, Å. 2011, *ApJ*, 737, 55
- Mizuno, Y., Nishikawa, K.-I., Hardee, P., Fishman, G. J., & Preece, R. 2008, *American Institute of Physics Conference Series*, 1000, 393
- Frederiksen, J. T., Haugbølle, T., Medvedev, M. V., & Nordlund, Å. 2010, *ApJL*, 722, L114
- Medvedev, M. V. 2006, *ApJL*, 651, L9
- Preece, R. D., Briggs, M. S., Mallozzi, R. S., et al. 1998, *ApJL*, 506, L23
- Medvedev, M. V., Pothapragada, S. S., & Reynolds, S. J. 2009, *ApJL*, 702, L91
- Keenan, B. D., & Medvedev, M. V. 2013, *PRE*, 88, 013103
- Keenan, B. D., Ford, A. L., & Medvedev, M. V. 2015, *PRE*, 92, 033104
- Keenan, B. D., Medvedev, M. V. 2016, arXiv:1512.01284
- Keenan, B. D., & Medvedev, M. V. 2015, *Physics of Plasmas*, 22, 113110
- Keenan, B. D., Ford, A. L., & Medvedev, M. V. 2015, *PRE*, 92, 053102
- Keenan, B. D., Medvedev, M. V. 2016, arXiv:1601.00983
- Palodhi, L., Califano, F., & Pegoraro, F., *Plasma Physics and Controlled Fusion*, 52, 095007 (2010)

Fairfield, D. H., Journal of Geophysical Research, 79, 1368 (1974)

Tsurutani, B. T., Smith, E. J., & Jones, D. E., Journal of Geophysical Research, 88, 5645 (1983)

Ramírez Vélez, J. C., Blanco-Cano, X., Aguilar-Rodriguez, E., et al., Journal of Geophysical Research (Space Physics), 117, A11103 (2012)

Lengyel-Frey, D., Hess, R. A., MacDowall, R. J., et al., Journal of Geophysical Research, 101, 27555 (1996)

Lin, N., Kellogg, P. J., MacDowall, R. J., et al., Journal of Geophysical Research, 103, 12023 (1998)

Sandhu, A. S., Dharmadhikari, A. K., Rajeev, P. P., Kumar, G. R., Sengupta, S., Das, A., Kaw, P. K. 2002, PRL, 89, 225002

Sarri, G., Macchi, A., Cecchetti, C. A., Kar, S., Liseykina, T. V., Yang, X. H., Dieckmann, M. E., Fuchs, J., Galimberti, M., Gizzi, L. A., Jung, R., Kourakis, I., Osterholz, J., Pegoraro, F., Robinson, A. P. L., Romagnani, L., Willi, O., Borghesi, M. 2012, PRL, 109, 205002

Wagner, U., Tatarakis, M., Gopal, A., Beg, F. N., Clark, E. L., Dangor, A. E., Evans, R. G., Haines, M. G., Mangles, S. P. D., Norreys, P. A., Wei, M.-S., Zepf, M., Krushelnick, K. 2004, PRE, 70, 026401

Gopal, A., Minardi, S., Burza, M., Genoud, G., Tzianaki, I., Karmakar, A., Gibbon, P., Tatarakis, M., Persson, A., Wahlström, C.-G. 2013, Plasma Physics and Controlled Fusion, 55, 035002

Mondal, S., Narayanan, V., Ding, W. J., Lad, A. D., Hao, B., Ahmad, S., Wang, W. M., Sheng, Z. M., Sengupta, S., Kaw, P., Das, A., Kumar, G. R. 2012, Proceedings of the National Academy of Science, 109, 8011

Belyaev, V. S., Krainov, V. P., Lisitsa, V. S., & Matafonov, A. P. 2008, Physics Uspekhi, 51, 793

Medvedev, M. V., Fiore, M., Fonseca, R. A., Silva, L. O., & Mori, W. B. 2005, ApJL, 618, L75

Polomarov, O., Kaganovich, I., & Shvets, G. 2008, PRL, 101, 175001

Shvets, G., Polomarov, O., Khudik, V., Siemon, C., & Kaganovich, I. 2009, Physics of Plasmas, 16, 056303

Medvedev, M. V. 2007, Astrophysics and Space Science, 307, 245

Medvedev, M. 2008, Bulletin of the American Astronomical Society, 40, 192

Medvedev, M. V., & Spitkovsky, A. 2009, ApJ, 700, 956

Fox, W., Fiksel, G., Bhattacharjee, A., Chang, P.-Y., Germaschewski, K., Hu, S. X., Nilson, P. M. 2013, PRL, 111, 225002

Sakawa, Y., Kuramitsu, Y., Morita, T., Kato, T., Tanji, H., Ide, T., Nishio, K., Kuwada, M., Tsubouchi, T., Ide, H., Norimatsu, T., Gregory, C., Woolsey, N., Schaars, K., Murphy, C., Gregori, G., Diziere, A., Pelka, A., Koenig, M., Wang, S., Dong, Q., Li, Y., Park, H.-S., Ross, S., Kugland, N., Ryutov, D., Remington, B., Spitkovsky, A., Froula, D., Takabe, H. 2013, European Physical Journal Web of Conferences, 59, 15001

Bret, A., Stockem, A., Narayan, R., & Silva, L. O. 2014, Physics of Plasmas, 21, 072301

Huntington, C. M., Fiuzza, F., Ross, J. S., Zylstra, A. B., Drake, R. P., Froula, D. H., Gregori, G., Kugland, N. L., Kuranz, C. C., Levy, M. C., Li, C. K., Meinecke, J., Morita, T., Petrasso, R., Plechaty, C., Remington, B. A., Ryutov, D. D., Sakawa, Y., Spitkovsky, A., Takabe, H., Park, H.-S. 2015, Nature, 11, 2, 173-176

Park, H.-S., Huntington, C. M., Fiuzza, F., Drake, R. P., Froula, D. H., Gregori, G., Koenig, M., Kugland, N. L., Kuranz, C. C., Lamb, D. Q., Levy, M. C., Li, C. K., Meinecke, J., Morita, T., Petrasso, R. D., Pollock, B. B., Remington, B. A., Rinderknecht, H. G., Rosenberg, M., Ross, J. S., Ryutov, D. D., Sakawa, Y., Spitkovsky, A., Takabe, H., Turnbull, D. P., Tzeferacos, P., Weber, S. V., Zylstra, A. B. 2015, Physics of Plasmas, 22, 056311

Rechester, A. B., & Rosenbluth, M. N. 1978, Physical Review Letters, 40, 38

Chandran, B. D. G., & Cowley, S. C. 1998, Physical Review Letters, 80, 3077

Narayan, R., & Medvedev, M. V. 2001, ApJL, 562, L129

Malyshkin, L., & Kulsrud, R. 2001, ApJ, 549, 402

Malyshkin, L. 2001, ApJ, 554, 561

Medvedev, M. V. 2007, ApJL, 662, L11

Landau, L. D., & Lifshitz, E. M. 1975, Course of theoretical physics - Pergamon International Library of Science, Technology, Engineering and Social Studies, Oxford: Pergamon Press, 1975, 4th rev.engl.ed.

Lifshitz, E. M., & Pitaevskii, L. P. 1981, Course of theoretical physics, Oxford: Pergamon Press, 1981

Cravens, T. E. 1997, Physics of solar system plasmas /Thomas E. Cravens. Cambridge : Cambridge University Press, 1997. QB 529 C72 1997. DA,

Brambilla, M. 1998, Kinetic theory of plasma waves : homogeneous plasmas, Publisher: Oxford, UK: Clarendon, 1998, Series: International series of monographs on physics, vol. 96, ISBN: 0198559569

Whistler-mode Waves in a Hot Plasma (Cambridge Atmospheric and Space Science Series)
(Cambridge University Press, Cambridge, 1993)

Verkhoglyadova, O. P., Tsurutani, B. T., & Lakhina, G. S. 2010, Journal of Geophysical Research (Space Physics), 115, A00F19

Yoon, P. H., & Davidson, R. C. 1987, PRA, 35, 2718

Medvedev, M. V., Silva, L. O., & Kamionkowski, M. 2006, ApJL, 642, L1

Tsytovich, V. N. 1977, Trends in Theoretical Physics

Batchelor, G. K. 1982, The Theory of Homogeneous Turbulence, by G. K. Batchelor, pp. 197. ISBN 0521041171. Cambridge, UK: Cambridge University Press, June 1982.

McNally, C. P. 2011, MNRAS, 413, L76

Tautz, R. C., & Dosch, A. 2013, Physics of Plasmas, 20, 022302

Jackson, J. D. 1998, Classical Electrodynamics, 3rd Edition, by John David Jackson, pp. 832. ISBN 0-471-30932-X. Wiley-VCH, July 1998.

Heddal, C. 2005, Ph.D. Thesis

Reville, B., & Kirk, J. G. 2010, ApJ, 724, 1283

Teraki, Y. & Takahara, F. 2011, ApJ, 735, L44

Teraki, Y., & Takahara, F. 2014, ApJ, 787, 28

Stix, T. H. 1992, Waves in plasmas , by Stix, Thomas Howard.; Stix, Thomas Howard. New York : American Institute of Physics, c1992.

Chen, F. F., Introduction to Plasma Physics and Controlled Fusion, Volume 1 (2nd Edition), Plenum, 1984.

Toptygin, I. N., & Fleishman, G. D. 1987, *Astrophysics and Space Science*, 132, 213

Reville, B., & Kirk, J. G. 2010, *ApJ*, 724, 1283

Wardziński, G., & Zdziarski, A. A., *MNRAS*, 314, 183 (2000)

Rybicki, G. B., & Lightman, A. P. 1986, *Radiative Processes in Astrophysics*, by George B. Rybicki, Alan P. Lightman, pp. 400. ISBN 0-471-82759-2. Wiley-VCH , June 1986.

Medvedev, M. V. 2009, *Astrophysics and Space Science*, 322, 147

Kruer, W. L. 1988, Reading, MA, Addison-Wesley Publishing Co. (Frontiers in Physics. Volume 73), 1988, 199 p., 73

Spitzer, L. 1956, *Physics of Fully Ionized Gases*, New York: Interscience Publishers

Bekefi, G. 1966, *Radiation Processes in Plasmas* (New York: Wiley).

Ma, J. X. 2005, *Physica Scripta*, 71, 540

Yesil, A., Aydogdu, M., Elias, A. G. 2008, *Progress In Electromagnetics Research Letters*, Vol. 1, 93-99

Hatchett, S. P., Brown, C. G., Cowan, T. E., Henry, E. A., Johnson, J. S., Key, M. H., Koch, J. A., Langdon, A. B., Lasinski, B. F., Lee, R. W., Mackinnon, A. J., Pennington, D. M., Perry, M. D., Phillips, T. W., Roth, M., Sangster, T. C., Singh, M. S., Snavely, R. A., Stoyer, M. A., Wilks, S. C., Yasuike, K. 2000, *Physics of Plasmas*, 7, 2076

Shcherbakov, R. V., *ApJ*, 688, 695 (2008)

Bergman, J., & Eliasson, B., *Physics of Plasmas*, 8, 1482 (2001)

Luo, Q., & Chian, A. C.-L., *MNRAS*, 289, 52 (1997)

Treumann, R. A., & Baumjohann, W. 2012, *Annales Geophysicae*, 30, 427

Kelner, S. R., Aharonian, F. A., & Khangulyan, D. 2013, ApJ, 774, 61

Saito, S., Gary, S. P., & Narita, Y. 2010, Physics of Plasmas, 17, 122316

Wang, L., Yang, L., He, J., et al., ApJL, 803, L2 (2015)

Che, H., Goldstein, M. L., & Viñas, A. F., Physical Review Letters, 112, 061101 (2014)

Yoon, P. H., J. Phys.: Conf. Ser., 642, 012030 (2015)

Mithaiwala, M., Rudakov, L., Crabtree, C., & Ganguli, G., Physics of Plasmas, 19, 102902 (2012)

Salem, C. S., Howes, G. G., Sundkvist, D., et al., ApJL, 745, L9 (2012)

Lacombe, C., Alexandrova, O., Matteini, L., et al., ApJ, 796, 5 (2014)

Lemoine, M., & Pelletier, G. 2010, MNRAS, 402, 321

Beck, R., & Grave, R. 1987, Interstellar magnetic fields : observation and theory : proceedings of a workshop held at Schloss Ringberg, Tegernsee September 8-12, 1986, Berlin ; New York : Springer-Verlag, c1987.

Neronov, A., Taylor, A. M., Tchernin, C., & Vovk, I. 2013, Astronomy and Astrophysics, 554, A31

Dieckmann, M. E., Chapman, S. C., McClements, K. G., Dendy, R. O., & Drury, L. O., Astronomy and Astrophysics, 356, 377 (2000)

Appendix A

The Spectral Tail

As can be seen in Figure 6.2 and Figure 6.5, there is additional structure to the radiation spectra beyond the break frequency, $\sim \gamma^2 k_{\max} v$. This feature is, in fact, a numerical artifact that is magnified by the use of a log-log plot. Here we have plotted Figure 6.2 on a linear scale, and have normalized the frequency axis by the spectral break frequency $\omega_{bn} = \gamma^2 k_{\max} v$.

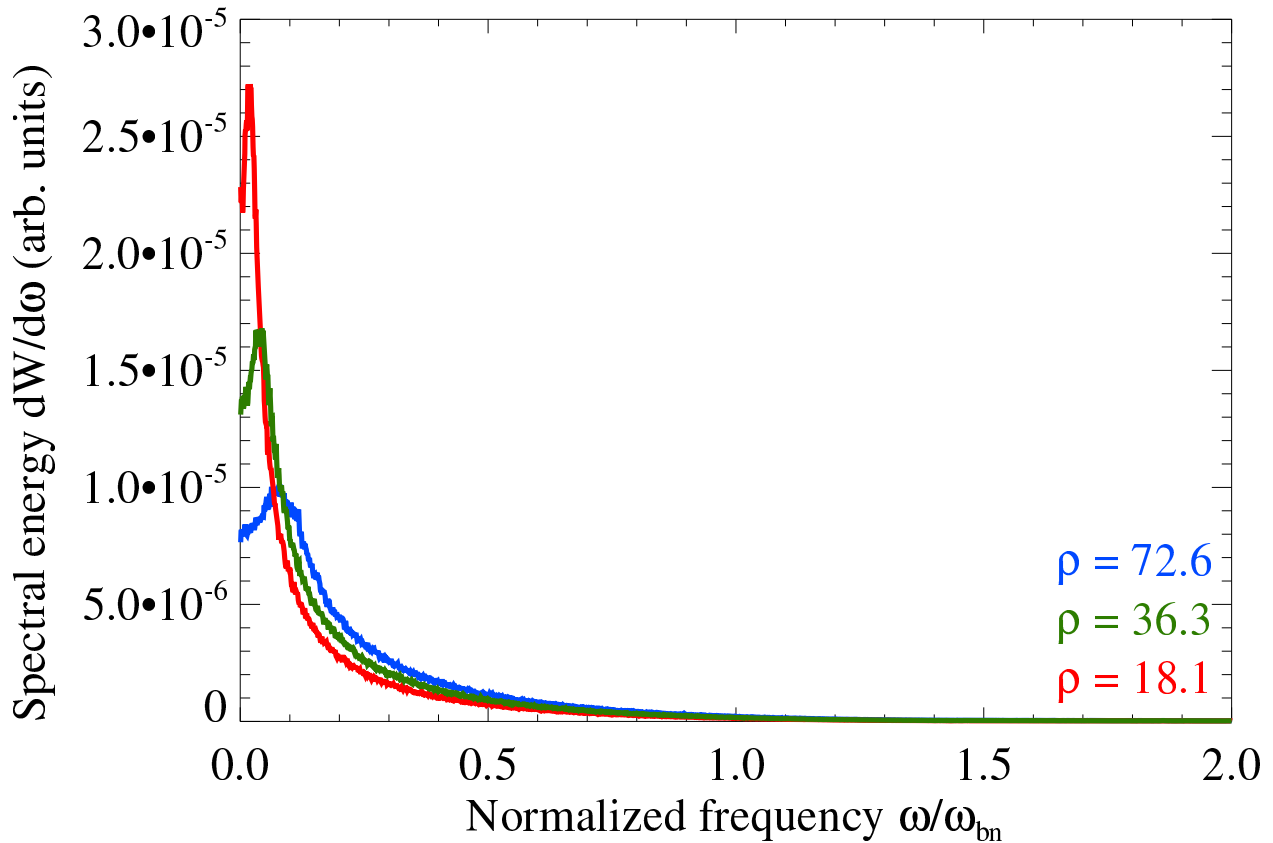


Figure A.1: Radiation spectra of Figure 6.2, with linear abscissa. We see that the power spectrum quickly approaches zero around the “break” frequency, $\gamma^2 k_{max} v$ – in accord with Eq. (6.20). This numerical approach to zero, since it is not instantaneous, appears readily in a log-log plot which magnifies features on an orders of magnitude scale.

Appendix B

Interpolation of the Magnetic Field

One might consider the importance of using a divergenceless set of interpolants for the magnetic field. In Figure B.1, we show a spectrum obtained via the divergenceless radial-basis interpolants of Eq. (4.2) with a spectrum obtained using a simple, non-divergenceless, trilinear interpolation of the magnetic field. For small frequencies, there is little disagreement between the two spectra. However, as the curves approach the break frequency $\omega_{bn} = \gamma^2 k_{max} v$, considerable deviation between the trilinear and radial basis interpolants occurs. In our previous work on the relativistic small-angle jitter regime (Keenan & Medvedev, 2013), little deviation in these spectra was observed in our test runs. One possible explanation is that, since the particle velocities were $\sim c$, the total distance traveled by a particle in one time step was $\Delta x \sim c\Delta t$. The spacing between lattice points is, typically, within an order of $c\Delta t$. In this case, the interpolant should not play an important role in determining the particle trajectories. If, however, v is much less than c , then the difference may be significant. In Figure B.1, $v = 0.125c$, thus $\Delta x \sim 0.125c\Delta t$ (an order of magnitude smaller). In this case, frequencies in the radiation spectrum at scales comparable to the grid resolution (i.e. large k 's) will suffer the most from this deviation.

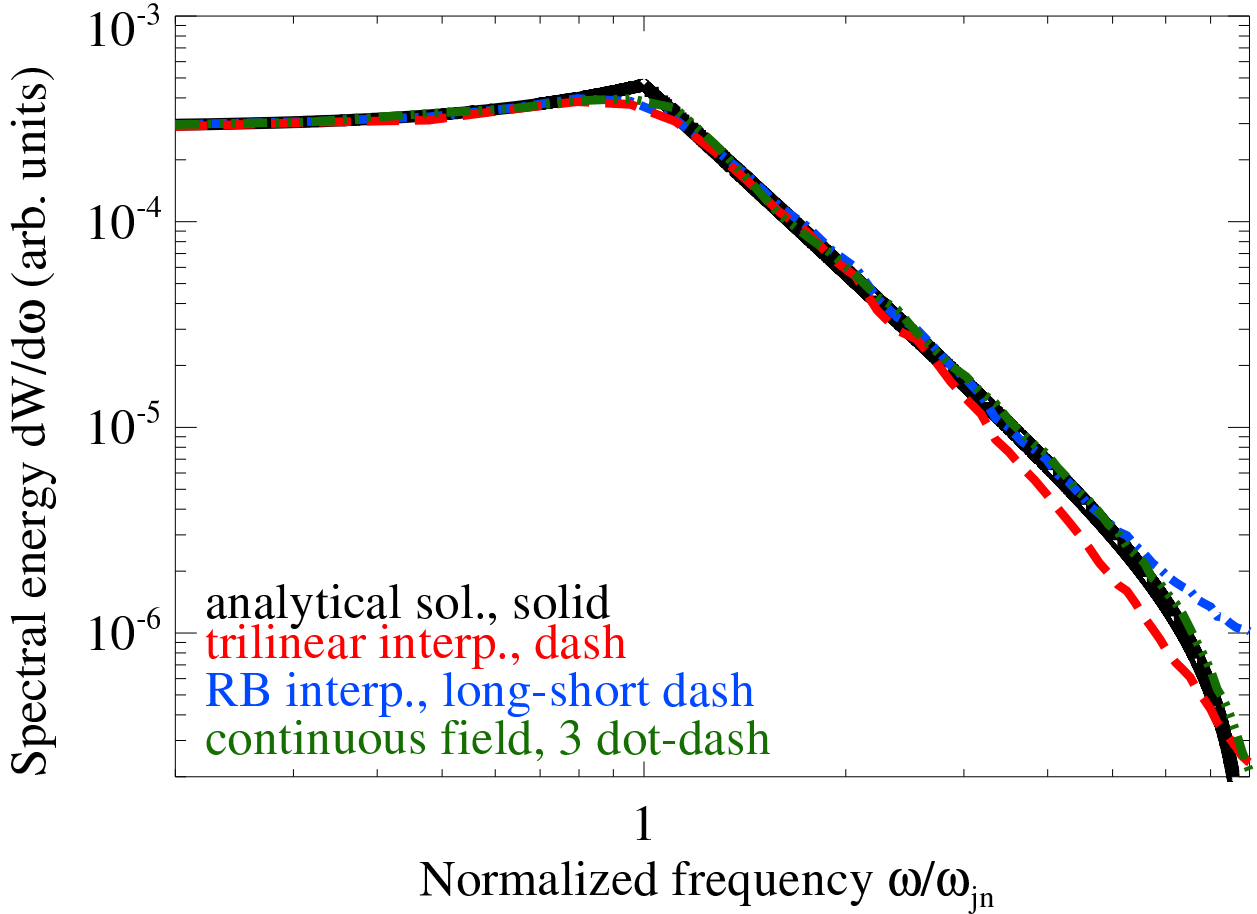


Figure B.1: Radiation spectra given two different interpolations of the magnetic field and a “continuous” field. Relevant parameters are $v = 0.125c$, $\rho = 24.7$, $N_p = 2000$ (for a complete listing, see Table 6.1). The number of wave modes employed to produce the “continuous” magnetic field was $N_m = 10000$. For small frequencies, there is little deviation between the spectra. It is only near the “break” frequency (i.e. $\omega_{bn} = \gamma^2 k_{max} v$) that the three differ considerably. Both of the interpolation derived spectra largely deviate from the analytical solution at the high frequency end; however, the “continuous” field derived spectrum differs noticeably only at the outermost frequencies. Whether or not this deviation is solely to blame on the quality of the interpolant or the discrete nature of lattice derived field, has yet to be determined. At any rate, both interpolants fail to preserve the slope of the spectra up to ω_{bn} , and there is considerable difference between the divergence-free and trilinear cases.

Another question worth addressing is the influence of the discrete implementation of the magnetic field on the spectral shape. Recall that the random magnetic field is initially generated on a lattice in k -space, after which it is subsequently transformed by FFT to real space. The interpolation is then applied on the lattice of points. Due to memory limitations, the lattice dimensions are limited to $\sim 500^3$; this can be a very severe limitation on the

spatial resolution of the magnetic field.

In Figure B.1, we also included a radiation spectrum obtained by electrons moving in the “continuous” magnetic field (with, otherwise, identical properties). Evidently, the “continuous” field derived spectrum closely matches the analytical solution, Eq. (6.20) – preserving the high-frequency end better than the interpolation derived spectra.

Appendix C

The Effect of Plasma Dispersion on the Radiation Spectra

As mentioned previously, inclusion of plasma dispersion changes the non-relativistic radiation spectrum to

$$\frac{d^2W}{d\omega d\eta} = \frac{e^2}{4\pi^2 c^3} \sqrt{\epsilon(\omega)} |\mathbf{w}_\omega|^2 \sin^2 \Theta, \quad (\text{C.1})$$

where $\epsilon(\omega) = 1 - \omega_{pe}^2/\omega^2$, is the plasma scalar permittivity. Since this amounts to a multiplicative factor, the jitter spectrum Eq. (6.20) will be modified simply by an extra frequency-dependent coefficient. The effect will, however, further complicate the relativistic regime. Fortunately, a Lorentz transformation can be applied, once more, to obtain the relativistic spectrum.

Consider a relativistic electron moving with velocity β in the (unprimed) plasma rest frame. In this frame, the plasma frequency is ω_{pe} ; additionally, the index of refraction is $n \equiv \sqrt{\epsilon}$. Conversely, the electron rest frame will be the site of a plasma in motion, with velocity $-\beta$. In this frame, $\omega'_{pe} = \omega_{pe}/\sqrt{\gamma}$. In a plasma medium, the radiation spectra are connected by the generalized relation

$$\frac{1}{n\omega^2} \frac{d^2W}{d\omega d\eta} = \frac{1}{n'\omega'^2} \frac{d^2W'}{d\omega' d\eta'}, \quad (\text{C.2})$$

where n' is the index of refraction in the electron rest frame. Via Lorentz transformation, n' is (?)

$$n'^2 - 1 = (\omega/\omega')^2(n^2 - 1), \quad (\text{C.3})$$

from which one may obtain the generalization of the relativistic Doppler effect

$$\omega' = \gamma\omega(1 - \mathbf{N} \cdot \boldsymbol{\beta}), \quad (\text{C.4})$$

where $\mathbf{N} \equiv n\hat{\mathbf{n}}$. Using the reverse transformation, i.e. *prime* \leftrightarrow *unprimed* and $\beta \rightarrow -\beta$, the angle cosines are related by

$$\cos\theta' = \frac{n\cos\theta - \beta}{n'(1 - n\beta\cos\theta)}. \quad (\text{C.5})$$

Using these results, along with Eqs. (6.35) and (6.36), the dispersion corrected relativistic jitter spectrum becomes

$$\frac{dW}{d\omega} = \frac{3n}{8\gamma^2} \int_{-1}^1 dx \left[\frac{1}{(1 - n\beta x)^2} + \frac{(nx - \beta)^2}{n'^2(1 - n\beta x)^4} \right] I(\omega_0), \quad (\text{C.6})$$

with $\omega_0 \equiv \omega(1 - n\beta x)$ and

$$n' = \frac{\sqrt{n^2 - 1 + \gamma^2(1 - n\beta x)^2}}{\gamma(1 - n\beta x)}. \quad (\text{C.7})$$

Next, the numerical spectrum is obtained from the generalizations of Eqs. (4.3) and (4.4)

$$\frac{d^2W}{d\omega d\eta} = \sqrt{\epsilon(\omega)} \frac{e^2}{4\pi^2 c} \left| \int_{-\infty}^{\infty} \mathbf{A}_{\mathbf{k}}(t) e^{i\omega t} dt \right|^2, \quad (\text{C.8})$$

where

$$\mathbf{A}_{\mathbf{k}}(t) \equiv \frac{\hat{\mathbf{n}} \times [(\hat{\mathbf{n}} - \boldsymbol{\beta}) \times \dot{\boldsymbol{\beta}}]}{(1 - \sqrt{\epsilon(\omega)}\hat{\mathbf{n}} \cdot \boldsymbol{\beta})^2} e^{-i\sqrt{\epsilon(\omega)}\mathbf{k} \cdot \mathbf{r}(t)}. \quad (\text{C.9})$$

In Figure C.1, we consider a $\beta = 0.5$ electron moving through a plasma medium with a plasma frequency $\omega_{pe} = k_{min}c/10$. The plot includes the equivalent dispersion-free jitter

spectrum, along with the analytical spectrum, from Eq. (C.6), and a spectrum obtained numerically. The numerical spectrum was produced given magnetic turbulence prescribed by the model described in Appendix B. Since the wave number becomes imaginary when $\omega < \omega_{pe}$, we have set a cut-off for frequencies below the plasma frequency. From the plot, we see that the spectrum differs largely from the dispersion-free equivalent for frequencies near ω_{pe} . However, as anticipated, the high-frequency end is largely unaffected.

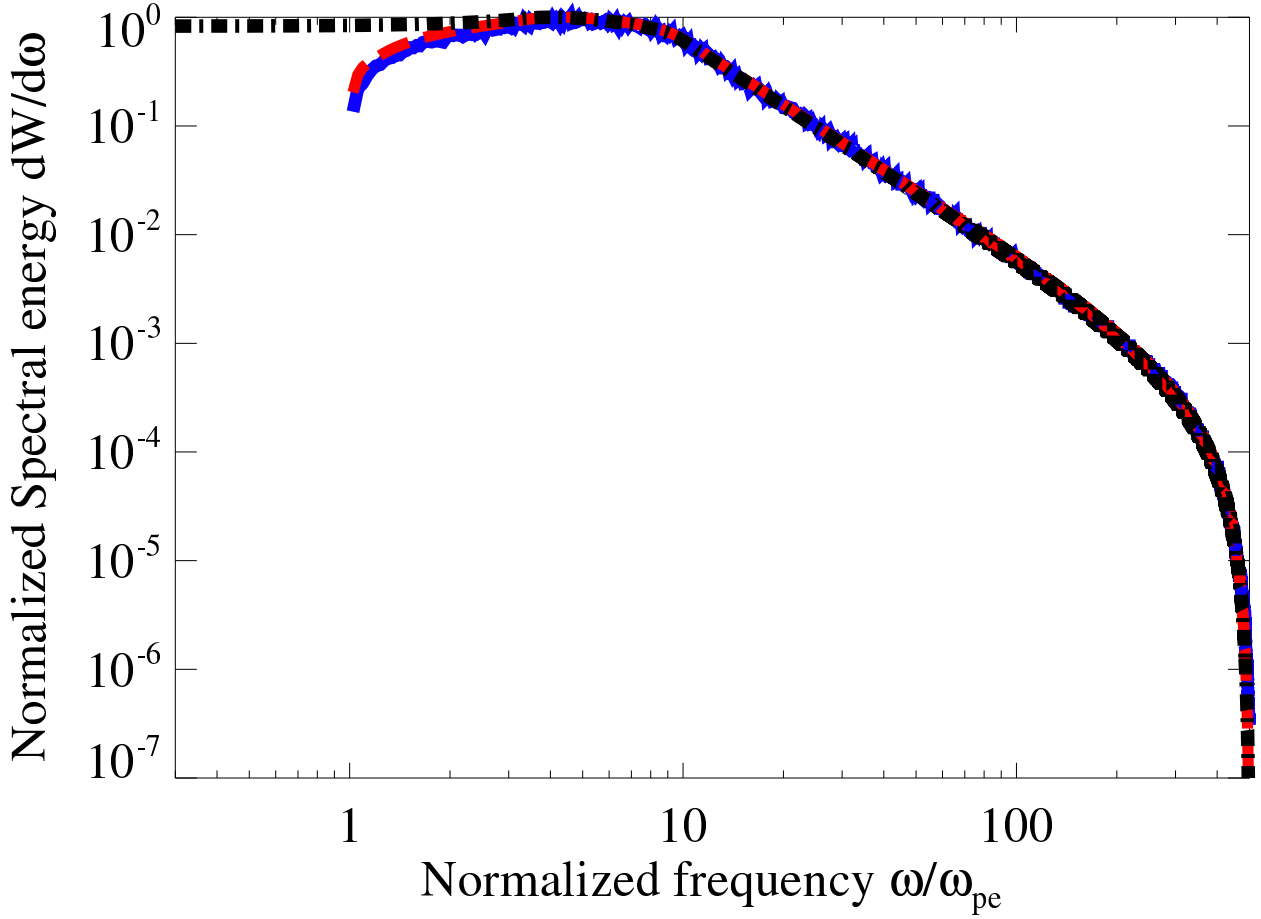


Figure C.1: Numerical radiation spectrum given a $\beta = 0.5$ electron moving through sub-Larmor-scale magnetic turbulence in a dispersive plasma (“thick”, blue), superimposed with the analytical spectrum from Eq. (C.6) (“dashed”, red) and the “dispersion-free” spectrum (“long-short dash”, black). For these runs, $\mu = 4$, $\rho = 14.2$, and $\omega_{pe} = k_{min}c/10$ (see Table 6.1 for a complete listing of simulation parameters). All spectra are normalized to their respective maximum values. As can be readily seen, the high-frequency end remains largely unchanged by the inclusion of plasma dispersion.

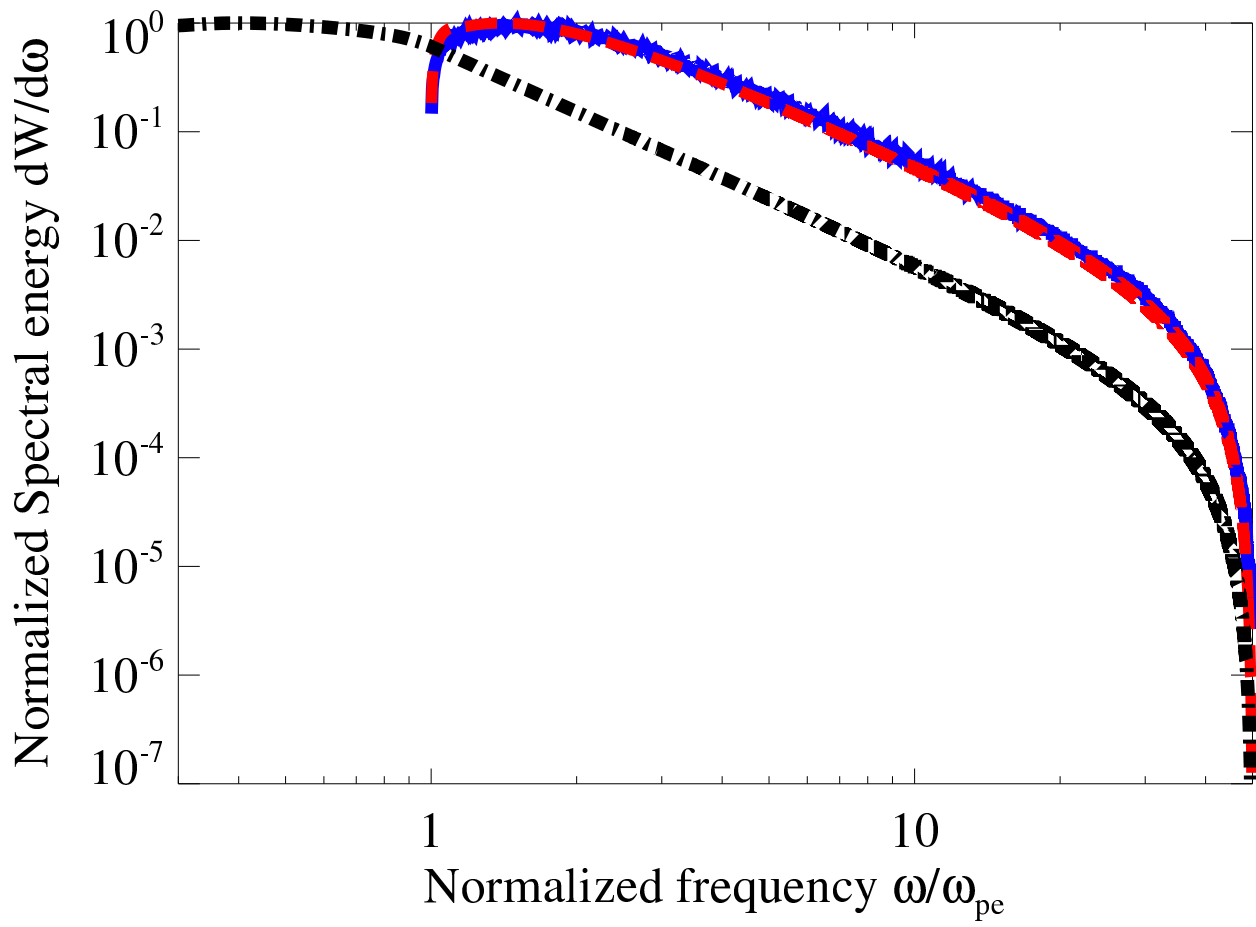


Figure C.2: Radiation spectra, identical to Figure C.1, with the exception that $\omega_{pe} = k_{min}c$. With $\omega_{pe} \sim \omega_{jn}$, the dispersion plays a more prominent role. Nonetheless, the overall shape of the spectrum is unaffected.

However, as can be seen in Figure C.2, the spectrum is altered in a more dramatic way when $\omega_{pe} = k_{min}c$. The low-frequency end remains distinctly concave, but now the high-frequency end is shifted to the right. The overall shape of the spectrum, nevertheless, remains the same.

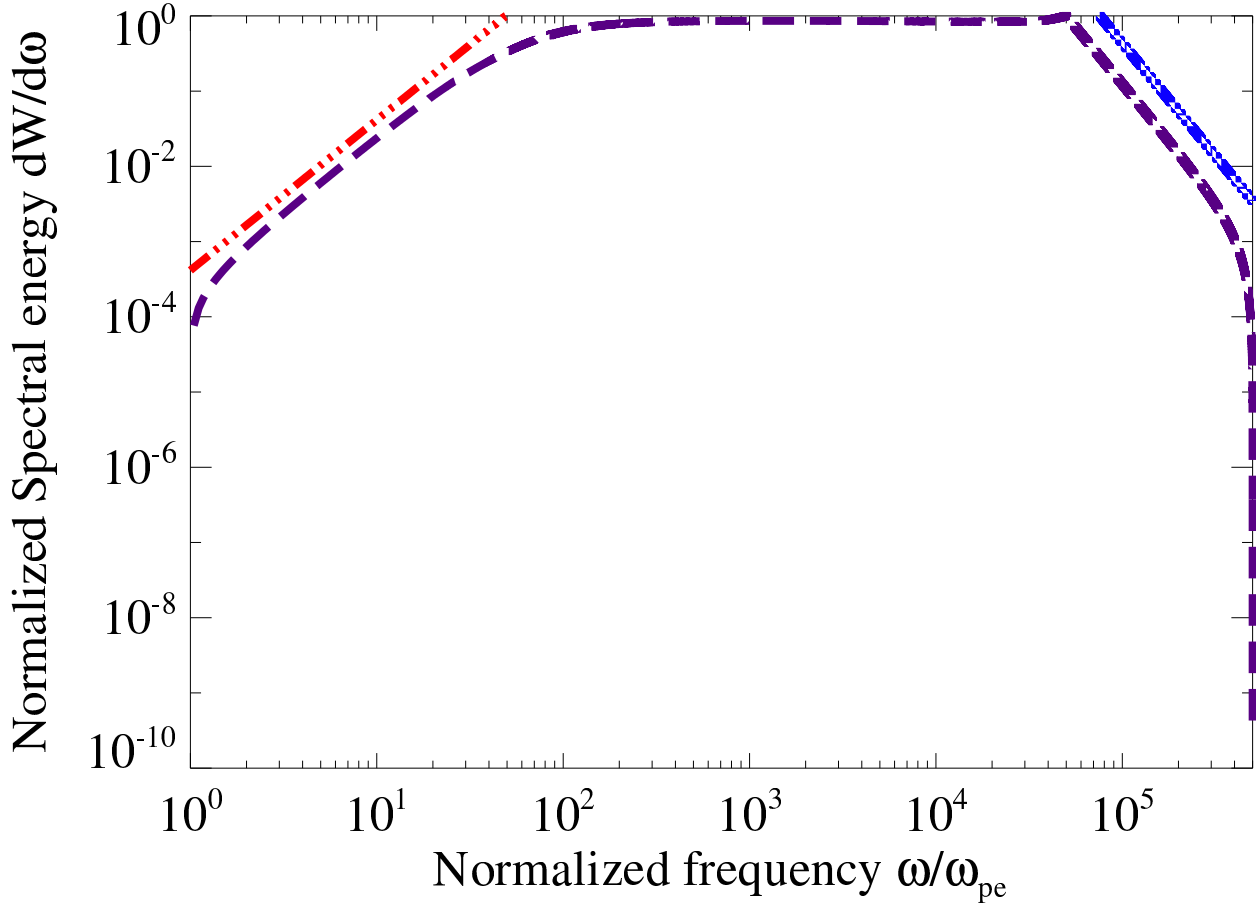


Figure C.3: Dispersion adjusted analytical radiation spectrum for a $\gamma = 50$ electron. Relevant parameters are $\rho = 153.4$ and $\mu = 5$. Two power laws appear. The ω^2 (“long-three-dash”, red) power law, which extends up to $\omega \sim \gamma\omega_{pe}$, is a consequence of the Razin effect. Additionally, we have included $\omega^{-\mu+2}$ (“long-two-dash” blue) on the right. As expected from Eq. (6.3), the high-frequency end is a power law, with a very steep drop beyond $\omega_{bn} \approx \omega_b$.

As a final test of Eq. (C.6), we consider an extreme relativistic case, $\gamma = 50$. The ultra-relativistic jitter spectrum, with plasma dispersion included, contains an additional ω^2 asymptote at low-frequencies (a hint of this was seen in the previous, trans-relativistic, plots). In Figure C.3, we see the emergence of this low-frequency asymptote. Additionally, we see that the jitter spectrum falls off dramatically for frequencies beyond $\omega_{jn} = \gamma^2 k_{\max} v \approx \gamma^2 k_{\max} c$ – hence, the correspondence to the ultra-relativistic hard cut-off at ω_b , from Eq. (6.3), is made apparent.